

1-1-2012

A Study on Radial and Axial Temperature Effects on the Growth of Bulk Single Crystal of SixGe1-x in Bridgman Setting

Mehdi Mohammadi Shemirani
Ryerson University

Follow this and additional works at: <http://digitalcommons.ryerson.ca/dissertations>



Part of the [Mechanical Engineering Commons](#)

Recommended Citation

Shemirani, Mehdi Mohammadi, "A Study on Radial and Axial Temperature Effects on the Growth of Bulk Single Crystal of SixGe1-x in Bridgman Setting" (2012). *Theses and dissertations*. Paper 1353.

This Dissertation is brought to you for free and open access by Digital Commons @ Ryerson. It has been accepted for inclusion in Theses and dissertations by an authorized administrator of Digital Commons @ Ryerson. For more information, please contact bcameron@ryerson.ca.

**A STUDY ON RADIAL AND AXIAL TEMPERATURE
EFFECTS ON THE GROWTH OF BULK SINGLE
CRYSTAL OF $\text{Si}_x\text{Ge}_{1-x}$ IN BRIDGMAN SETTING**

By

MEHDI M. SHEMIRANI

**Bachelor of Technology, McMaster University, Hamilton, Canada
M.A.Sc., Mechanical Engineering, Ryerson University, Toronto, Canada**

A dissertation presented to

Ryerson University

In partial fulfillment of the requirements for the degree of

DOCTOR OF PHILOSOPHY

in the Program of

MECHANICAL ENGINEERING

Toronto, Ontario, Canada, 2012

© Mehdi M. Shemirani 2012

Author's Declaration

I hereby declare that I am the sole author of this dissertation.

I authorize Ryerson University to lend this dissertation to other institutions or individuals for the purpose of scholarly research.

Mehdi M. Shemirani

I further authorize Ryerson University to reproduce this dissertation by photocopying or by other means, in total or in part, at the request of other institutions or individuals for the purpose of scholarly research.

Mehdi M. Shemirani

Abstract

A Study on Radial and Axial Temperature Effects on the Growth of Bulk Single Crystal of $\text{Si}_x\text{Ge}_{1-x}$ in Bridgman Setting

Doctor of Philosophy

MEHDI M. SHEMIRANI

Mechanical Engineering

Ryerson University

2012

This research explores simulation of the growth of large diameter single bulk crystals of silicon and germanium alloy from its melt utilizing Bridgman method. Producing homogeneous single bulk crystals requires a good understanding of the thermo-solutal behavior in the solvent region. This study also suggests certain fundamental scientific aspects of this alloy system which are not well considered to date, and which underlie both the homogeneity and obtaining relatively flat solid liquid interface of the $\text{Si}_x\text{Ge}_{1-x}$ alloy. These aspects are the diffusion and transport of silicon and germanium in the molten alloy. Both three and two dimensional numerical simulations of thermo-solutal convection in solvent region were examined. The whole simulation scheme was applied to a cylindrical model representing the sample to investigate the aforementioned phenomena in the entire process. It was found that the application of axial magnetic field had no significant effect on the buoyancy driven convection in the solvent region. However, conducting the microgravity environment simulation has shown that the removal of the gravitational force on the solvent region would result in a homogeneous

solidification. As an alternative, this study has found that both axial and radial temperature gradients play a role in the solidification process. Controlling this phenomenon, along with two other factors such as applied uniform temperature and reduced pulling rate, would help achieve a homogeneous single bulk crystal with more uniform silicon distribution in the solvent region, more specifically near the solid liquid interface and produce a flat shape interface which is most desired shape in industry.

Acknowledgements

I would like to thank Professor Ziad Saghir, my supervisor, for his guidance during my PhD program; I am grateful to him for his unconditional support and all countless precious advices.

I would also like to thank Mechanical/Industrial Engineering Department of Ryerson University for providing the opportunity for me to work on this research.

I would also like to thank Professor Daniel Labrie, from Dalhousie University for experimental support.

I acknowledge the financial support of the Canadian Space Agency (CSA), the Natural Sciences and Engineering Research Council of Canada (NSERC) and the School of Graduate Studies in Ryerson University.

Table of Contents

Author's Declaration	iii
Abstract	v
Acknowledgements	vii
Table of contents	ix
List of Tables	xiii
List of Figures	xv
Nomenclature	xix
 Chapter 1 (Introduction)	
1.0 Research Objectives	2
1.1 Motivation and need for this Research.....	3
1.2 Importance of Microgravity Application	5
1.3 Complications and defects	6
1.4 Dissertation Organization.....	9
 Chapter 2 (Literature Review)	
2.0 Introduction	11
2.0.1 Silicon.....	11
2.0.2 Germanium.....	12
2.0.3 Bulk Single Crystal of $\text{Si}_{0.25}\text{Ge}_{0.75}$	13
2.1 Methods or Techniques	15
2.1.1 Bridgman method	15

Chapter 3 (Theoretical approach and Numerical Solution)

3.0 Introduction	37
3.1 Numerical Solution Techniques	37
3.1.1 Boussinesq Approximation	38
3.1.2 Finite Element Analysis (FEA)	39
3.2 Dimensional Governing Equations	41
3.2.1 Navier-Stokes Equation	41
3.2.2 Energy Equation	42
3.2.3 Continuity Equation	42
3.2.4 Mass Transport Equation	43
3.2.5 Latent Heat Equation	43
3.2.6 Growth Velocity Equation	43
3.3 Dimensional Analysis	44
3.3.1 Dimensional Variables	44
3.4 Finite Volume Analysis (FVA)	46
3.4.1 Momentum Equation	48
3.4.2 Continuity Equation	48
3.4.3 Energy Equation	48
3.4.4 Transport Equation	49
3.5 Model Geometrics & Boundary Conditions	50
3.6 Mesh Sensitivity and Solution Technique	52

Chapter 4 (Two & Three dimensional modeling with different heating profile)

4.0 Introduction	55
4.1 3-D Model under non-linear temperature, terrestrial condition, (FEA)	56
4.2 Experimental results under non-linear temperature profile.....	62
4.3 3-D Model under non-linear temperature, microgravity condition, (FEA)	64
4.4 2-D axi-symmetric under non-linear temperature, microgravity, (FEA)	68
4.5 2-D axi-symmetric under non-linear temperature, microgravity, (FVA)	69
4.6 2-D Model under non-linear temperature, terrestrial, (FEA)	71
4.7 Applied axial magnetic field under non-linear temperature profile, (FEA)	75
4.8 2-D Model under linear temperature, terrestrial, (FEA)	82
4.9 Applied axial magnetic field under linear temperature profile, terrestrial, (FEA) ..	86

Chapter 5 (The effects of axial and radial temperature gradient)

5.0 Introduction	93
5.1 Application of different axial temperature gradient	93
5.2 Detail analysis of 35K/cm axial temperature gradient case	111

Chapter 6 (Summary, Conclusion, and Future Work)

6.0 Summary	121
6.1 Conclusion	122
6.2 Future Work	125

Appendix A

Physical Properties and Raw Data	129
--	-----

Appendix B

Non-dimensionalization	133
------------------------------	-----

Appendix C

Simulation Input Files	147
------------------------------	-----

References	193
-------------------------	-----

List of Tables

Description	Page
=====	
2.1 Physical properties	14
3.1 Some dimensionless parameters	46
3.2 Mesh sensitivity analysis	53
5.1 Radial temperature differences at different axial level, 35K/cm case	112
A.1 Complete physical properties	129
A.2 Silicon atomic %, density, segregation coefficient, melt temperature	130

List of figures

Description	Page
=====	=====
2.1 $\text{Si}_x\text{Ge}_{1-x}$ phase diagram	14
2.2 Schematic view of vertical Bridgman	16
2.3 Schematic view of horizontal Bridgman	16
3.1 Bridgman model under the investigation	40
3.2 Solvent region meshed model	50
3.3 Non-linear temperature profile	52
3.4 Mesh density vs. heat flux	53
4.1 Flow velocity contours, under terrestrial condition	57
4.2 Flow velocity plotlines, under terrestrial condition	57
4.3 Temperature distribution contours, under terrestrial condition	59
4.4 Temperature distribution plotlines, under terrestrial condition	59
4.5 Silicon distribution contours, under terrestrial condition	60
4.6 Silicon distributions, terrestrial, a comparison between FEA & experiment	61
4.7 Radial & Axial silicon compositions, by simulation, terrestrial condition	62
4.8 Axial silicon compositions, by experiment, terrestrial condition	63
4.9 Silicon Distributions at different axial level, by Experiment, terrestrial	63
4.10 Flow velocities in solvent region in microgravity condition, (FEA)	64
4.11 Flow velocities along vertical axis, microgravity condition , (FEA)	65
4.12 Temperature distributions in solvent region under microgravity condition, (FEA) ..	66

4.13 Silicon distributions in solvent region in microgravity condition, (FEA)	67
4.14 Results of the axi-symmetric model, microgravity condition, (FEA)	68
4.15 Temperature distribution, microgravity condition, (FVA)	69
4.16 Silicon composition, microgravity condition, (FVA)	70
4.17 Flow velocity contours, terrestrial condition, (FVA)	70
4.18 Full 2-D model, non-linear temperature profile, terrestrial condition, (FEA)	71
4.19 Line plots, with non-linear temperature profile, terrestrial condition, (FEA)	73
4.20 Radial line plots, non-linear temperature, terrestrial condition, (FEA)	74
4.21 Flow velocities, under different magnetic intensities, (FEA)	77
4.22 Radial line plots, under B=1mT axial static magnetic field, (FEA)	78
4.23 Radial line plots, under B=20mT axial static magnetic field, (FEA)	79
4.24 Radial line plots, under B=200mT axial static magnetic field, (FEA)	80
4.25 Radial line plots, under B=1T axial static magnetic field, (FEA)	81
4.26 Full 2-D model, under linear temperature profile, terrestrial condition, (FEA)	83
4.27 Line plots, with linear temperature profile, terrestrial condition, (FEA)	84
4.28 Radial line plots, linear temperature, terrestrial condition, (FEA)	85
4.29 Flow velocities, under different magnetic intensities, linear temperature, (FEA)	87
4.30 Radial line plots, under B=1mT axial static magnetic field, (FEA)	88
4.31 Radial line plots, under B=20mT axial static magnetic field, (FEA)	89
4.32 Radial line plots, under B=200mT axial static magnetic field, (FEA)	90
4.33 Radial line plots, under B=1T axial static magnetic field, (FEA)	91
5.1 Contour plots with $Gr_T = 2.29E + 05$, terrestrial condition, (FEA)	97

5.2 Line plots with $Gr_T = 2.29E + 05$, terrestrial condition, (FEA)	98
5.3 Contour plots with $Gr_T = 1.91E + 05$, terrestrial condition, (FEA)	99
5.4 Line plots with $Gr_T = 1.91E + 05$, terrestrial condition, (FEA)	100
5.5 Contour plots with $Gr_T = 1.53E + 05$, terrestrial condition, (FEA)	101
5.6 Line plots with $Gr_T = 1.53E + 05$, terrestrial condition, (FEA)	102
5.7 Contour plots with $Gr_T = 1.34E + 05$, terrestrial condition, (FEA)	103
5.8 Line plots with $Gr_T = 1.34E + 05$, terrestrial condition, (FEA)	104
5.9 Contour plots with $Gr_T = 1.22E + 05$, terrestrial condition, (FEA)	105
5.10 Line plots with $Gr_T = 1.22E + 05$, terrestrial condition, (FEA)	106
5.11 Contour plots with $Gr_T = 1.18E + 05$, terrestrial condition, (FEA)	107
5.12 Line plots with $Gr_T = 1.18E + 05$, terrestrial condition, (FEA)	108
5.13 Contour plots with $Gr_T = 1.15E + 05$, terrestrial condition, (FEA)	109
5.14 Line plots with $Gr_T = 1.15E + 05$, terrestrial condition, (FEA)	110
5.15 Schematic of solvent region under applied 35K/cm axial thermal gradient	111
5.16 Two zones of radial temperature gradient variations, under applied 35K/cm	114
5.17 Radial temperature difference at the first 5 mm above interface, (35K/cm)	115
5.18 Radial temperature difference from 10 to 50 mm above interface, (35K/cm)	116
5.19 Radial temperature difference from 60 to 89 mm above interface, (35K/cm)	117
5.20 Silicon radial distribution with $Gr_T = 1.34E + 05$, (35K/cm)	118
B.1 Control volume grids for two dimensional models	138
B.2 Location of the control volume in the grids	138
B.3 Nodes for the bilinear interpolation	142

B.4 Cylindrical coordinate system	143
B.5 Magnetic field vectors orientation	144

Nomenclature

at %	Atomic percentage
B	Magnetic field Induction (Tesla)
B_1	Magnetic field Induction, “r” direction (Tesla)
B_2	Magnetic field Induction, “ φ ” direction (Tesla)
B_3	Magnetic field Induction, “z” direction (Tesla)
B^*	Dimensionless magnetic field induction
c	Solute concentration (at %)
c_0	Reference solute concentration (at %)
c_p	Specific heat (J/g. K)
C	Dimensionless concentration
g	Gravitational acceleration
κ	Thermal conductivity(cal/s.cm.K)
L	Reference length
mT	milli-Tesla (1/1000 Tesla)
p	Pressure (Pa)
P	Dimensionless pressure
r	Radial direction (cm)
R	Dimensionless radial coordinate
t	Time (s)
T	Temperature ($^{\circ}$ C)
T	Tesla
u	Velocity in “ r ” direction (cm/s)
U	Dimensionless Velocity in “r” direction
v	Velocity in “ φ ” direction (cm/s)
V	Dimensionless Velocity in “ φ ” direction
w	Velocity in “ z ” direction (cm/s)

W	Dimensionless Velocity in “z” direction
z	Axial direction (cm)
Z	Dimensionless axial coordinate

Greek Symbols

α_c	Solutal (mass) diffusivity of the specie (cm ² /s)
β_c	Solutal expansion coefficient (1/at % Si)
β_T	Thermal expansion coefficient (1/°C)
φ	Circumferential direction
ϕ	Dimensionless circumferential direction
μ	Dynamic viscosity (g/cm.s)
ρ	Density (g/cm ³)
σ	Electric conductivity (S/cm)
τ	Dimensionless time
θ	Dimensionless temperature
ν	Kinematic viscosity (cm ² /s)

Subscript

◦	Reference
<i>eff</i>	Effective
<i>int</i>	Interface
<i>m</i>	Melt
s	Solid/Solidification

Superscript

M Magnetic field

Dimensionless Numbers

Gr Grashof number $\left(\frac{\beta_T \Delta T g \rho^2 L^3}{\mu^2} \right)$

Ha Hartmann number $\left(|B_0| L \sqrt{\frac{\sigma}{\mu}} \right)$

Pe Peclet number $\left(\frac{Lv}{\alpha} \right)$

Pr Prandtl number $\left(\frac{c_p \mu}{k} \right)$

Re Reynolds number $\left(\frac{\rho u_0 L}{\mu} \right)$

Sc Schmidt number $\left(\frac{\nu}{\alpha_c} \right)$

CHAPTER ONE

Introduction

Crystal growth of multi-component alloys like $\text{Si}_x\text{Ge}_{1-x}$ is an inherently complex process since it involves coupled and non-linear interactions of fluid flow, heat and mass transport, phase diagrams, phase changes, surface and interface phenomena, and other micro- and macro-level interactions. Most of these are affected by the presence of gravity. Particularly, the convective heat, momentum and mass transport processes in the melt result in significant uncertainties in the experimental measurement of physical parameters such as diffusion coefficients, and affect the evolution of the growth interface, crystal composition uniformity, impurity and inclusions, interface kinetics, surface curvature, etc. Such information is essential for the optimization of crystal growth systems for commercial applications.

An extensive research has been carried out on heat and mass transport in semiconductor melts of the silicon-germanium (Si-Ge) system. The interplay of diffusion, structure, and thermodynamics in this system is important and is of great interest. The availability of new knowledge in these areas will open new horizons in the development of needed devices for human use and for addressing the environmental issues such as renewal energy conversion and climate change, and others like medical and security applications. The proposed research will be carried out in two main parts: a) the study of silicon distribution in the melt under diffusion-dominated conditions, and b) the investigation of the role of mass transport and gravity in single crystal growth of

bulk $\text{Si}_x\text{Ge}_{1-x}$ alloys. Experiments were carried out in terrestrial condition in order to validate those of the numerical simulations.

1.0 Research Objectives

The available microgravity platforms on the orbiters will be utilized for the study of fundamental and technical issues related to diffusion mass transport in semiconductor systems with the aim of developing new knowledge in this field and of making it available for the use of the relevant industry for optimization. In this regard, there were few questions needed to be responded to such as; can buoyancy driven convection in the solvent region be suppressed by the external forces such as axial magnetic field? What is the role of the gravity force on mass transport and silicon distribution in the solvent region of the model? Which one of the applied linear or non-linear temperature profile generates better results? And what is the interplay between the axial and radial temperature during the solidification process? The research has the following objectives:

- To suppress the buoyancy driven convection in the solvent region by an external force such as axial magnetic field.
- To observe the role of the gravity force on mass transport and silicon distribution in the solvent region of the model under this study.
- To study the behavior and the effect of the axial temperature during the solidification process.
- To study the behavior and the effect of the radial temperature gradient during the solidification process.

- To simulate the growth of a large diameter single bulk crystals with the selected method.
- For optimization and verification of the process parameters involved in the selected crystal growth technique, sophisticated modeling and numerical simulations are necessary and will be carried out.
- The data obtained from microgravity simulations will be compared to the ground-based (terrestrial) results.

1.1 Motivation and Need for this Research

The choice of SiGe is motivated by two considerations: first, SiGe represents a class of pseudo-binary materials with non-isothermal growth interface, second, there is an increasing interest in the bulk growth of this material which is not produced with satisfactory compositional and crystalline quality to-date. Although researches and studies on the $\text{Si}_x\text{Ge}_{1-x}$ alloy system date back to as early as 1954 [1], an extensive body of research associated with the growth of high quality $\text{Si}_x\text{Ge}_{1-x}$ bulk single crystals, epitaxial techniques leading to thin $\text{Si}_x\text{Ge}_{1-x}$ layers, and methods relating to $\text{Si}_x\text{Ge}_{1-x}$ -based microelectronic semiconductor devices began to emerge about two decades ago. The $\text{Si}_x\text{Ge}_{1-x}$ alloy system offers very promising features since the band structure and thus the effective mass and mobility of electrons and holes are significantly affected by alloy composition, temperature and strain. For instance, the incorporation of a small amount of Si into Ge considerably increases carrier mobility, hence leading to the possibility of creating devices with improved frequency and computational speeds. Most

importantly, the material composition can be tailored to afford the desired electrical or optical properties in accordance with the performance specifications of the targeted device application. Furthermore, the $\text{Si}_x\text{Ge}_{1-x}$ alloy system offers a feasible integration into the well-developed, long-established silicon-based technologies. These features make the $\text{Si}_x\text{Ge}_{1-x}$ system a very promising candidate to support a variety of micro-electronics and opto-electronic device applications.

These applications include the use of $\text{Si}_x\text{Ge}_{1-x}$:

- i) As a base in Si/SiGe hetero-junction bipolar transistors (HBT) [1-3] and high electron-mobility field-effect transistors [4],
- ii) For photo-detector [5-6] and solar cell applications [7-11] because of its superior light sensitivity and high solar cell response in the infrared region of the solar spectrum,
- iii) As a substrate to fabricate perfectly lattice-matched GaAs/SiGe hetero-structures, thereby enabling higher efficiency solar cell applications, and
- iv) In thermoelectric power generators [12-13], tunable neutron and X-ray monochromators [14], high-speed temperature sensors in the range of 20-400°C, and X-ray detectors [15]. $\text{Si}_x\text{Ge}_{1-x}$ single crystal substrates of a specific composition (x) are required for these applications.

Due to difficulties associated with band-gap engineering techniques, the growth of bulk crystals with desired compositions is necessary. However, it is very difficult to grow $\text{Si}_x\text{Ge}_{1-x}$ single crystals of uniform compositions and low defect densities since $\text{Si}_x\text{Ge}_{1-x}$ has a large miscibility gap, and its components (Si and Ge) have significant differences in their physical properties (density, and melting temperature). Because of the large

miscibility gap, any small changes in the solidification rate lead to significant composition variations, and growth striations [16-19]. In addition, in crystal growth while it is necessary to establish a high axial temperature gradient to prevent constitutional under-cooling, a low radial temperature gradient must be maintained for crystal perfection. Any curvature of the liquid-solid interface leads to very large radial chemical heterogeneity [20-21]. Modeling crystal growth of the alloy Ge-Si system requires accurate diffusion coefficient values in the melt and the understanding of fundamental relations between diffusive mass transport, nucleation, and crystal growth. The lack of diffusion data in Ge-Si melts yields to an insufficient description, for instance as observed in the phase field models developed for the Czochralski crystal growth process [22-24].

1.2 Importance of Microgravity Application

Crystal growth of multi-component systems is an inherently complex process since it involves coupled and non-linear interactions of fluid flow, heat and mass transport, phase diagrams, and other micro- and macro-level interactions. Most of these are affected by the presence of gravity. During the crystallization processes mentioned earlier there are many issues that require microgravity experimentation for a better understanding of these processes. For instance, gravity driven convection in the melt causes fluctuation in the crystal composition [25]. When the component concentrations are equal, crystal lattice parameter fluctuations occur and consequently crystal quality (perfection) and its range of applications are reduced [26]. Furthermore, the effect of convective flow on the evolution of the growth interface, crystal composition uniformity, impurity and inclusions, interface

kinetics, surface curvature, etc must be studied. Under microgravity conditions the chemical segregation, the solvent inclusions and their interaction with the moving crystallization front can be studied under almost purely diffusive transport conditions. Controlled convective conditions can be achieved by the usage of time-dependent magnetic fields under microgravity conditions where available; leading to crucial information on the effect of convection on the incorporation of inclusions and their distribution in the grown crystals. Although to a certain degree the use of strong static magnetic fields may lead to satisfactory results in some systems, the microgravity environment is still the most viable option to obtain accurate results for the optimization of many crystal growth techniques for commercialization [27].

1.3 Complications and Defects

The reliability of the aforementioned products is highly depending on the performance of the semiconductors being used in them. This reliance is based on the consistency of internal arrangement of atoms of three dimensional crystal structure and the characteristics such as uniformity and purity of bulk single crystal. Every crystal structure consists of single unit cell which can be classified as the smallest configuration of arranged atoms which makes each material's distinguishable characteristics. The specific arrangement of these unit cells in an array format creates the crystal lattice. The ultimate goal is to achieve a high level of purity, uniformity, homogeneity and a perfect crystalline. These crystals, of course should be produced under specific circumstances in order to ensure high quality and satisfy the ever growing demand. There are many different methods and techniques for

crystal growth. Among those, the crystallization from the melt is the most practiced one. Inevitably, this way of crystal growth has some complications which baffle the process of obtaining a perfect arrangement of molecules or atoms of crystals as mentioned above. It should be noted that these complications are generally known as the growth defects. Growth defects as shown by Muller et al [28] can be categorized as; substitutions which is a replacement of an atom with the atom of the crystal lattice, grain boundaries which happens when two small grains of crystal have different crystallographic orientations, vacancies which refers to the missing atom in the crystal lattice, dislocations which is referring to misalignment of the crystal lattice, and interstitial which happens when an atom is being squeezed into the crystal lattice and stacking which is a disturbance in the regularity of the arrangement of the plane of atoms in a crystal lattice.

Voronkov [29] showed that grown-in micro-defects in dislocation-free silicon are distributed in banded patterns that result from a spatial variation in the type and concentration of the incorporated point defects; vacancies (at V/G larger than some critical value) or self-interstitials otherwise (V is the growth rate, G is the axial temperature gradient). The incorporated point defects agglomerate into micro-defects upon lowering the temperature; particularly the vacancies are agglomerated into voids. However, it should be noted that oxygen plays an important role in the Czochralski crystals by assisting the void formation, by producing joint vacancy-oxygen agglomerates (oxide particles) and by trapping vacancies into vacancy-oxygen species. The critical ratio depends on the point defect parameters taken at T_m as expressed by Voronkov. The dependency of the micro-defect type on V/G was explained by Voronkov assuming that the vacancy (V) and self-

interstitial (I) in silicon coexist, at the crystallization temperature (T_m) in comparable equilibrium concentrations. Another essential point is that the recombination rate of (V) and (I) is sufficiently high, at least close to (T_m), to support the product $C_V C_I$ of the two actual concentrations close to the equilibrium value. This product decreases very fast upon lowering temperature (T) (By moving away from the crystal-melt interface, into the crystal bulk). Therefore, either only one type of the defects, V or I can survive at a lower T while the concentration of the partner defect will be reduced to a negligible value. Voronkov also concluded that at V/G exceeding the critical value, the incorporated point defects are mainly vacancies. And at V/G below the critical value, the incorporated point defects are self-interstitials and the incorporated concentration increases upon reducing V/G .

Necking technique is one way to overcome the dislocation in silicon single crystals. Dash [30] has shown how necking, which was one of the problems to deal with at the beginning of the silicon single crystal-growing era, can help reduce dislocations. However, it was discovered that the dislocation-free crystals are not all perfect; they contained some grown-in micro-defects as addressed by Plaskett [31] and Abe et al. [32].

The gravity has a great influence on the growth process since it is the major cause of the buoyancy force, which in turn affects on the mass and heat transport mechanisms in each system (melt) of crystal growth. It is a known fact that under the terrestrial (on the earth surface or ground-based) condition, the hot fluid with less density in the crystal melt rises and the denser cool fluid falls down. This obviously, known as convective flow, causes the irregular distribution of the dopant and into a larger extent affects on the perfection of the crystal growth. Many attempts have been made to minimize or overcome

this problem, such as the use of either axial or rotating magnetic field, the rotating crucible and under the microgravity condition.

1.4 Dissertation Organization

This work consists of six chapters and three appendices. Chapter one is a detailed introduction, research objectives, motivation, need for the research, importance of microgravity application, complications and defects in crystal growth. Chapter two would present a comprehensive literature review, methods and techniques. In chapter three, governing equations, mesh sensitivity, solution techniques along with model geometry and boundary conditions would be discussed in detail. Chapter four presents two and three dimensional modeling with different heating profiles and applied different magnetic field intensities. Chapter five would show the effect of axial and radial temperature gradient results and discussions. Finally, Chapter six presents the summary, and conclusions of this study along with the recommendations and future works. All the additional information such as necessary tabulated data, non-dimensional equations, and sample of CFD input programs would be presented in Appendices A, B, and C.

CHAPTER TWO

Literature Review

2.0 Introduction

Since this study is focusing on the growth of the bulk single crystals of SiGe alloy, it is inevitable to look into each component of this alloy and the chosen combination of this alloy which is $\text{Si}_{0.25}\text{Ge}_{0.75}$ in more details.

2.0.1 Silicon (Si)

Silicon with atomic number of 14 is the second most abundant element (after oxygen) in the earth crust, making up 25.7% of the crust by mass. Silicon crystal structure is cubic diamond. Silicon has many industrial uses. It is the principal component of most semiconductor devices, most importantly integrated circuits or microchips. Silicon is widely used in semiconductors. In its crystalline form, pure silicon has a gray color and a metallic luster. It is similar to glass in that it is rather strong, very brittle, and prone to chipping [33]. Pure silicon is used to produce ultra-pure silicon wafers used in the semiconductor industry, in electronics and in photovoltaic applications. Ultra-pure silicon can be doped with other elements to adjust its electrical response by controlling the number and charge (positive or negative) of current carriers. Such control is necessary for transistors, solar cells, semiconductor detectors and other semiconductor devices which are used in electronics and other high-tech applications, and of large-area, low-cost thin-film solar cells [34]. Most

notable physical properties of silicon for this study are as follow; Density (2329 kg/m³), Thermal expansion coefficient ($2.6 \times 10^{-6}/\text{K}$), Melting temperature (1687.15 K), Boiling temperature (3538.15 K), Thermal conductivity (148 W/m K), and Heat capacity (705 J/kg.K).

2.0.2 Germanium (Ge)

Germanium with atomic number of 32 is a hard, grayish-white element that has a metallic luster and the same crystal structure as diamond. Germanium is a semiconductor, with electrical properties between those of a metal and an insulator. In its pure state, this metalloid is crystalline, brittle and retains its luster in air at room temperature. Germanium crystal structure is also cubic diamond. The development of the germanium transistor opened the door to countless applications of solid-state electronics. From 1950 through the early 1970's, this era provided an increasing market for germanium, but then high purity silicon began replacing germanium in transistors, diodes, and rectifiers. Meanwhile, demand for germanium in fiber optics communication networks, infrared night vision systems, and polymerization catalysts increased dramatically. The recent rise in energy cost has improved the economics of solar panels, a potential major new use of germanium. Germanium is also a good substrate of the wafers for high-efficiency multi-junction photovoltaic cells for space applications [35]. Because germanium is transparent in the infrared it is a very important infrared optical material, that can be readily cut and polished into lenses and windows. It is especially used as the front optic in thermal imaging cameras working in the 8 to 14 micron wavelength range for passive thermal imaging and for hot-spot detection

in military, night vision system in cars, and fire fighting applications [36]. Germanium is also used in infrared spectrometers and other optical equipment which require extremely sensitive infrared detectors [37]. Physical properties of germanium which have been taken into the consideration are as follow; density (5323 kg/m^3), thermal expansion coefficient ($5.9 \times 10^{-6} / \text{K}$), melting temperature (1214.4-K), boiling temperature (3106.15 K), thermal conductivity (59.9 W/m.K), and Heat capacity (320 J/kg.K).

2.0.3 Bulk Single Crystal of $\text{Si}_{0.25}\text{Ge}_{0.75}$

Silicon-germanium alloys are rapidly becoming an important semiconductor material, for use in high speed integrated circuits. Circuits utilizing the properties of SiGe junctions can be much faster than those using silicon alone. Silicon-germanium is beginning to replace gallium arsenide (GaAs) in wireless communications devices. The SiGe chips, with high-speed properties, can be made. One of the purposes of this study is to find a proper condition in which SiGe chips can be obtained from a defect free single crystal of SiGe. Although the pure silicon and germanium are chemically similar, crystallize in the same lattice structure, and are completely miscible in the solid and liquid phase, the growth of mixed crystals is very complicated because of the differences in some physical properties especially when the combination is in the wider range in the phase diagram [38]. The chosen combination of silicon and germanium under this study is benefiting of the large amount of silicon which enhances the performance of the semiconductors at the same time utilizes the large amount of germanium which carries a lot of aforementioned characteristics.

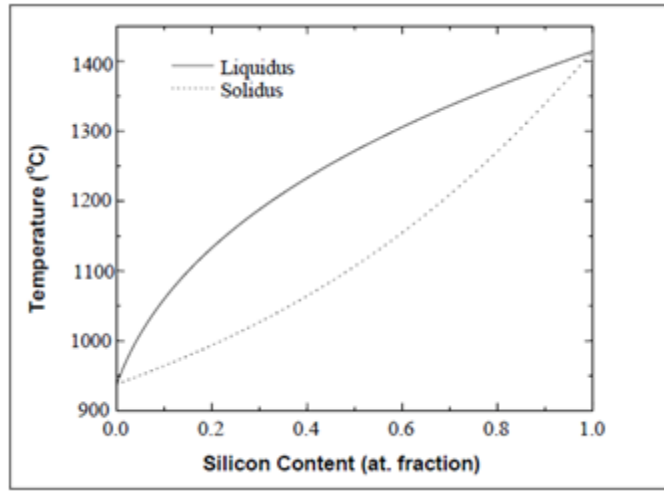


Figure 2.1 $\text{Si}_x\text{Ge}_{1-x}$ phase diagram [38]

Table -2.1 represents the employed physical properties of the mixture used in this study.

The comprehensive list of physical properties can be found in Appendix “A”

Table 2.1 Physical properties of the SiGe in the Solvent Region

Physical Properties of $\text{Si}_{0.25}\text{Ge}_{0.75}$			
Description	Symbol	Values	Units
Melting Temperature	T_m	1057.5	$^{\circ}\text{C}$
Density	ρ	4.843	g/cm^3
Mass Diffusivity	α_c	1.65×10^{-4}	cm^2/s
Kinematic Viscosity	ν	8.8×10^{-4}	cm^2/s
Solutal Expansion Coeff.	β_c	0.0051	/ at% Si
Thermal Conductivity	κ	0.294	$\text{W}/\text{cm}/\text{K}$
Thermal Expansion Coeff.	β_T	5.075×10^{-6}	$1/^{\circ}\text{C}$
Dynamic Viscosity	μ	4.3×10^{-3}	$\text{g}/\text{cm.s}$
Electrical Conductivity	σ	2.5×10^4	S/cm
Specific Heat	c_p	0.4145	$\text{J}/\text{g.K}$

2.1 Methods or Techniques

There are many different methods and techniques which have been used for the crystal growth purposes, from early twentieth century, among which the four most practiced ones are; Czochralski technique (Cz), Bridgman method, Floating zone technique (FZ) and traveling solvent method (TSM) also known as traveling heater method (THM). Each method or technique tries to achieve and fulfill the need of a homogeneous purified single crystal growth. The Cz and FZ methods due to their limitations for this type of semiconductor alloys is not of our interest and TSM has been utilized and discussed in my masters research [39], therefore in this study, the emphasis is on the Bridgman method.

2.1.1 Bridgman Method

This method uses a tubular furnace, which has three zones, Figures 2.1-2.2. Each heated at a different temperature. The "hot" zone is held at a temperature above the melting point of the material, while the "cold" zone is kept at a temperature below the melting point. The sample material is usually placed in a container made of an inert material (such as quartz).

Once a region of the sample is melted, the sample is slowly moved, and directional solidification takes place. The interface between the liquid and solid material, the solidification front, is particularly interesting to scientists. It is here that the flows in the molten material affect the final composition and structure of the solid and its properties.

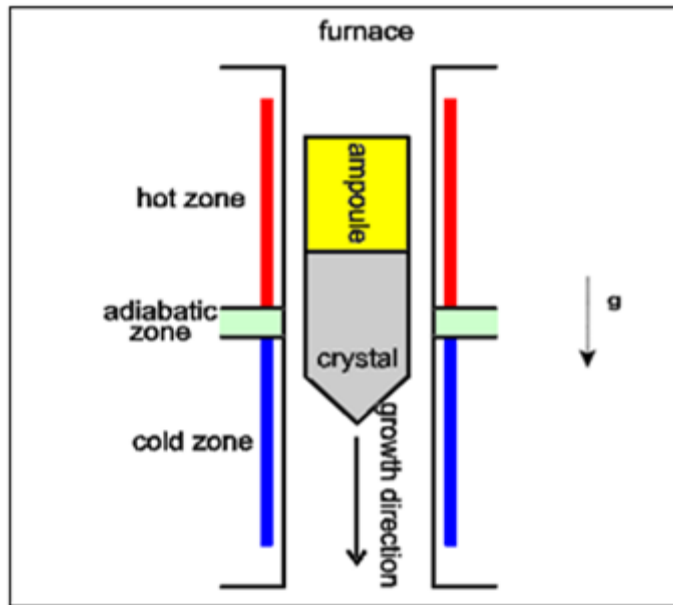


Figure 2.2 Schematic view of a vertical Bridgman method [40]

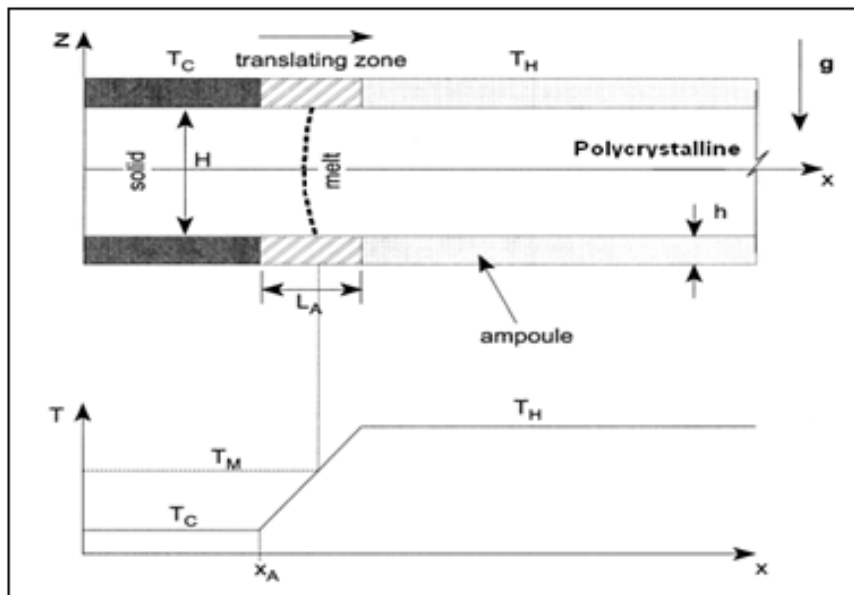


Figure 2.3 Schematic view of a horizontal Bridgman method [41]

The ampoule contains the melt which moves through the axial temperature gradient in a furnace. This ampoule is necessary to support the melt, because in contrast to the float-zone method, the completely feed material (feed-rod) is molten as shown by Helmers et al. [40]. This method has its own advantages such as; simplicity, containers can be evacuated and sealed, control of shape and size of crystals and stabilized thermal gradients. Disadvantages are such as; confinement, thermal expansion of container versus the crystals, can handle small melt volume and process is not visible. Helmers et al. [40] conducted a Bridgman growth of non-dilute $\text{Si}_x\text{Ge}_{1-x}$ mixed crystals and reported four samples of different composition. Fluctuations of growth rate and or composition result in strong striation patterns. The spacing of the striae is found to be similar for all melt volumes, compositions and thermal environments used in this experiment. The crystal quality is generally poor. All samples show the grain structure. It was found that if the seed is of higher Si content than the first part of the grown crystal, formation of grain is considerably reduced. It was shown in the phase diagram that an increase of the Si content in the solid changes the equilibrium temperature at the phase boundary during solidification up to 10K/at%.

Schilz et al. [41] in a review of this method state that in contrast to Czochralski technique, directional solidification, i.e. mostly the Bridgman process, can handle only a small melt volume, since heat flow should always be perpendicular to the phase boundary. Because of this problem and also due to the inevitability of the non-uniform composition profile after solidification, the Bridgman method has neither ever been applied for the growth of technically exploitable Si-Ge semiconductor material, nor has been a subject to intense research in this field. Experiment suggested that in bottom-seeded vertical

Bridgman growth, the damping power of the solute field is predominant over the thermal influence. Also, observed segregation profiles exhibit a typical diffusion controlled shape.

Considering the fixed thermal field of a Bridgman facility, a changing Si concentration will move the position of the solid/liquid interface with respect to the furnace, and the growth rate differs from the velocity at which the cartridge passes through the heater. Thus, the monotonic decrease of Si concentration is accompanied by a slowing down of the growth velocity. The thermal environment can cause the striae only if the temperature accidentally fluctuates with the same frequency as presented by Dold et al. [42].

Dold et al. utilized the Bridgman method in a radiation heated mirror furnace. The growth velocity was 1.3mm/h. GeSi crystal in a range (Si \leq 15 at %) grown on a seed crystal with the diameter of 9mm and length from 30 to 40 mm. Si-concentration was restricted for the given set-up to about 10-15 at%. Axial and radial macro-segregation measured by X-ray (EDAX). The average Electrophoretic deposition (EPD) was in the range 6×10^4 to 1×10^5 and was enhanced at the seed/crystal interface and in the part grown in the vicinity of the container wall. The full-width at half-maximum (FWHM) values of 20-40 arcsec obtained via Bartel's five crystal diffractometer of the (111) peak is best result reported up until this experiment. Although the quartz crucible is the best container for single crystal growth but the interaction between the silicon and the ampoule wall leads to sticking of the crystal to the wall. During the cool down process, the grown crystal is subjected to heavy mechanical stress. Together with tension because of lattice mismatch

due to concentration gradients, this might lead to cracking of the crystal or the ampoule wall.

Walker [43] carried out an experiment utilizing the Bridgman method for crystal growth with a strong, low-frequency, rotating magnetic field. The study shows the motion of the melt driven by a low-frequency, spatially uniform, rotating magnetic field that is perpendicular to the axis of a cylindrical Bridgman ampoule. Since the magnetic force is so strong, the inertial effects are negligible and that viscous effects are confined to thin boundary layers which are adjacent to the ampoule surfaces and the crystal-melt interface. Outside the boundary layers, the melt nearly rotates as a rigid body with the angular velocity of the rotating magnetic field. Because of non-electrical conductivity, the static crystal acts as a generator in the rotating magnetic field and drives electric currents through the crystal-melt interface boundary layer, these currents from the slightly conducting crystal interact with the magnetic field to accelerate the azimuthally velocity. A strong, low frequency, rotating magnetic field would produce poor crystals with severe rotational striations. They conclude that a rotating magnetic field may produce beneficial mixing, but it may also produce potentially deleterious (harmful) deviations from axisymmetry in the melt motion. With a rotational magnetic field, it is not appropriate to treat the crystal as an electrical insulator. The importance of the nonaxisymmetric radial and axial velocities inside the interface layer lies in their potential effects on the mass transport of dopants or species. Walker also showed in his study that constitutional super-cooling and a high silicon concentration increase at the growth beginning due to the use of Germanium seed-crystal could not be avoided.

Feonychev et al. [44] also studied the Bridgman method by showing that the flow arising in a conducting liquid under the effect of a rotating magnetic field as well as under its interaction with gravitational and thermo-capillary convection, region of mixed flows, in which the impurity in crystal growth were found. Application of magnetic fields in semiconductor crystal growth is an efficient solution to control the convection in the liquid, the micro and macro segregation, and to improve the material quality. Nowadays, growth installations can be equipped with different magnetic field configurations. Transverse, axial and cusp static magnetic fields are used to eliminate thermal fluctuations and to damp thermal convection in the liquid in order to obtain stable transport regimes as shown by Okano et al. [45]. It has been observed that the intensity of the melt convection has a significant influence on both radial and axial segregation of species and interface shape during crystal growth. Studies of natural convection in the melt demonstrated that the magnitude of radial segregation is lower than the axial one and is due to either; a) diffusion-controlled growth such as convection free or b) intense mixing in the melt as shown by Martinez-Tomas et al. [46] and Labrie et al. [47]. The radial segregation reaches a maximum for intermediate values of flow intensity, which results in relatively thick solute boundary layers that have a non-uniform thickness Labrie et al. [48]. When crystals are grown in the Bridgman configuration, forced convection is difficult to produce, because the crystal cannot be moved relative to the ampoule. The intensity of the natural convection which cannot be avoided scales with the Grashof (thermal) number. It is obvious that the intensity of the buoyancy driven convection depends highly on the melt height and thus changes as the melt is depleted as studied by Makriyannis et al. [49]. In the vertical

Bridgman configuration for crystal growth, the interface shape is a factor that greatly influences the yield of single crystals. The shape of the interface is mainly determined by the temperature field near the interface and the level of natural convection in the melt as shown by Saghir et al. [50]. The shape of the interface can range from concave to convex. Slightly convex interface shape is most desirable because it eliminates most problems with spontaneous nucleation at the crucible wall and improves grain selection which results in higher yield of single crystals. However, the efforts of obtaining convex interface shapes in growth experiments have been of limited success as stated by Lan et al. [51]. A planar interface shape has the beneficial effect of minimizing thermal stresses and the intention of the present work is to establish a desirable interface shape by controlling the convection in the melt and the directional heat flux near the interface by means of the static magnetic field.

Yeckel et al. [52] in their study which is a three-dimensional simulation of the flow induced by transient acceleration (g-jitter) in microgravity crystal growth, showed the effect of g-jitter in both axial and transverse directions in a vertical Bridgman setting. It was also presented the effects of applying steady magnetic field oscillations, but for transverse jitter at intermediate frequencies, flow oscillations are increased. This counter-intuitive effect is a dynamic one, in which boundary layer formation under the influence of a magnetic field shortens the time scale of momentum transfer, allowing the flow to respond more quickly to the time variation of acceleration. The effect of the magnetic field on an enclosed flow with electrically insulating boundary conditions is to preferentially suppress the velocity component tangential to the magnetic field. The ability to filter a

single component by application of a specified magnetic field could be useful for simultaneously improving both axial and radial segregation in semiconductor crystal growth as shown by Saghir et al. [53].

Yesilyurt et al. [54] conducted a study to investigate the effect of thermo-electromagnetic convection (TEMC) on the Bridgman growth of $\text{Si}_x\text{Ge}_{1-x}$ in which they have shown that the thermoelectric currents at the growth interface of GeSi during Bridgman growth technique, promote convection when a low-intensity axial magnetic field is applied. TEMC, typically, is characterized by a meridional flow driven by the rotation of the fluid. Meridional convection alters the composition of the melt, and the shape of the growth interface substantially. TEMC effect is more important in micro-gravity environment than the terrestrial one, and can be used to control convection during directional solidification of GeSi. TEMC is based on the principle that in any material a temperature gradient, ∇T , produces a Seebeck electromotive forces $S\nabla T$ where S is the thermoelectric power of the material. If the gradients of S and T are not parallel, then a thermoelectric current is generated in the system. They have also shown that the following points should be met in order to have strong enough thermoelectric currents to create TEMC:

- 1) In systems where the melt and solid have different thermoelectric powers, and the solid-melt interface is not isothermal; e.g. binaries and pseudo-binaries such as GeSi and HgCdTe.
- 2) In systems where the thermoelectric power is a function of the liquid-phase composition which is *non-uniform* due to segregation at the growth interface.

3) In systems where the melt and the container have different thermoelectric powers, and melt-container interface is not isothermal (e.g. the Bridgman growth of Ge in a graphite crucible). As per their findings two remarks should be pointed out;

- i) the azimuthal velocity does not influence the composition directly, and
- ii) meridional flows can only be sustained at low magnetic field strengths, typically of the order of 10-100mT and the Lorentz force, $\mathbf{u} \times \mathbf{B}$ weakens the meridional flow as the field strength is increased further. Lehoczky et al. [55] showed that the thermo electromagnetic is also a function of the square of the difference of the thermoelectric powers of the melt and crystal, which is assumed to be $1\mu\text{V/K}$. For semiconductors, this value varies between 1 and $100\mu\text{V/K}$ as shown by Muller et al. [56].

Marin et al. [57] worked on a 6 cm diameter Ga-doped $\text{Si}_{0.02}\text{Ge}_{0.98}$ crystal by utilizing the vertical Bridgman method with a submerged baffle in which they removed the baffle after 3 cm of growth and let the solidification continue. By using the baffle in vertical Bridgman setting, axially uniform concentration of Si and Ge in $\text{Si}_{0.02}\text{Ge}_{0.98}$ alloy was obtained. In contrast, non-uniform segregation typical of full mixing was obtained when the baffle was removed from the melt. Li et al. [58] shown that the baffle has reduced the extent of micro-segregation.

Mitric et al. [59] in their experimental study of the Alternating Magnetic Field (AMF) effect on the crystal growth by vertical Bridgman technique showed that a modification of classical growth set-up is required. A preliminary evaluation of the appropriate parameters for an efficient electromagnetic stirring with minimum of heat released in the sample was performed. The estimation of both magnetic field frequency and

intensity (approximately $B=30T$) was achieved by both experimental and theoretical approaches. The thermal field modification in the sample due to the additional quantity of heat released by induction in the melt, near the solid-liquid interface and by Joule effect (when an alternating electrical current is applied to the inductor, heat dissipation by Joule effect occurs in the coil as well as in the molten sample due to the eddy currents) in the coil was calculated. In their experiment a $50K/cm$ temperature gradient was also used. The solidification interface shape is at the origin of the thermal convection in the liquid and, in consequence, will have an influence on the solutal distribution. The knowledge of the interface deflection allows a first estimation of the flow intensity order of magnitude, which is important for the further choice of AMF values. The interface shape is the result of thermal, latent heat and solutal condition. In their experiment (GaInSb sample), it was found that the diffusive layer (δ_D = has approximately 1 cm thickness) and the viscous layer (δ_v = reaches approximately 400 μm). For an interface deflection of 1mm and a thermal gradient of $50K/cm$, an AMF with an intensity of 3mT and a frequency around 8000Hz was found to be sufficient for an efficient mixing of the liquid.

The solid-liquid interface curvature results from differences of the thermal conductivity of semiconductor alloys in the liquid and solid state, and depends also on the geometry and conductivity of the crucible as stated by Naumann et al. [60].

Meyer et al. [61] have shown the application of the submerged heater method (SHM) in a vertical Bridgman configuration to grow Ge single crystals doped with Ga. It was found that when SHM is used without rotation, the submerged heater drastically reduces convection at the solid-liquid interface. When SHM is set into rotation or

oscillatory rotation, it acts as a centrifugal viscous pump, inducing forced convection (radial-inward flow) along the interface. The flow produced by a rotation and oscillatory rotation of the submerged heater was visualized using a 1:1 scale model. They have shown that the vigorous mixing produced by the oscillatory rotation creates a nearly perfect stirred melt, and yields a uniform lateral distribution of the dopant. The crystals were free of unintentionally produced striae. It was also mentioned that the intensity of the natural convection, which cannot be avoided, scales with the dimensionless Grashof number which describes the aforementioned intensity, depends strongly on the melt height, and thus changes as the melt is depleted. Therefore, the electrical and optical properties of the crystals grown from unstirred Bridgman melts are expected to change axially and radially. They also found that the Grashof number (Gr) of the zone was approximately 50,000 which was three orders of magnitude lower than the (Gr) of the conventional vertical Bridgman. Meyer et al. also showed that when crystals are grown in the Bridgman configuration, forced convection is difficult to produce, because the crystal cannot be moved relative to the ampoule.

Ruiz et al. [62] studied the impact of the g-pulses on the semiconductor solid segregation in a generic μg Bridgman growth arrangement in a computational point of view with the help of a time-dependent computer code. It was pointed out that the present calculations indicate that segregation is weakly dependent on the geometry of the pulse if the g-dose, at equal activity time is the same. However, solid dopant patterns as well as the magnitude of the relative variation with regard to a basic state are different for each semiconductor (Ge with Ga-doped, GaAs with Se-doped, Sn with Bi-doped) analyzed.

They used a 2D transient model in which all the walls of the ampoule stay at rest except the solidification front, defined as a flat moving interface. Ermakov et al. [63] showed that liquid phases at high temperature have been defined as Boussinesq Newtonian ones and the transport of mass, momentum and heat has been considered to be time-dependent because of the continuous decreasing of melt volume and the built-up of solute caused by the continuous decreasing length of the ampoule. They have concluded that longitudinal segregation profiles are practically independent of the pulse shape, rectangular or half-sinusoidal applied and simplified their analysis by only taking into account the g-dose applied to the growth system. Depending on the magnitude of this g-dose, the axial segregation remains practically constant along the crystal but not the radial one, knowing that by its definition, radial segregation is the most sensitive parameter against this kind of external impulsive force. In addition, it has been clearly stated that the dynamic and thermal responses are dependent on the shape of the external impulsive force.

Volz et al. [64] have grown a series of (1 0 0)-oriented Gallium-doped Ge crystals by the vertical Bridgman method and under the influence of a rotating magnetic field (RMF). They have found that the time-dependent flow instabilities occur when the critical magnetic Taylor number (T_m^c) is exceeded, and this can be observed by noting the appearance of striations in the grown crystals. (T_m^c) decreases as the aspect ratio of the melt increases, and approaches the theoretical limit expected for an infinite cylinder. Intentional interface demarcations introduced by switching the RMF on and off. The RMF has a marked effect on the interface shape, changing it from concave to nearly flat as the RMF strength is increased. They have stressed that the key issue is that of stability, since

unstable melt flow during the growth of doped semiconductors and semiconductor alloys will lead to striations and compositionally inhomogeneous material. If the magnetic field strength is too large, the RMF itself will cause unstable flow. The critical value for instability will depend on the aspect ratio of the melt and coupling to buoyancy-induced flows. They also observed in their study that without the RMF, there is a concave shape at the interface, this concavity results primarily from the heat flow, which is determined by the differences in thermal conductivity between the melt, solid, and the ampoule. However, this concave shape changed to convex shape near the end of the growth. Finally they have stated that it might be difficult to use RMF to both control the interface shape and at the same time maintain time-dependent melt flow with the Bridgman technique.

Duhanian et al. [65] have shown, in their experimental study, the solid-liquid interface dynamics and chemical segregation in concentrated semiconductor alloy in a vertical Bridgman setting (in the advanced gradient heating facility, AGHF, of the European Space Agency) which incorporated three samples of $\text{Ga}_{1-x}\text{In}_x\text{Sb}$ with compositions of $x=0.04$, 0.1 , and 0.2 . The position and shape of the solid-liquid interface has been marked by electrical pulses all along the growth direction and revealed by subsequent metallographic procedure. The axial and radial segregation of the (In) has been measured by chemical analysis of the solid. The result show that the effect of the chemical segregation, coupled to thermo-solutal convection, leads to huge deformations of the solid-liquid interface, with interface curvature even larger than the sample diameter. They observed a sharp increase of the chemical composition as well in the most concentrated samples and interface destabilization occurred quickly. Bulk crystal growth experiments

began with Wagner [66] on GaAs-InAs, and by Plaskett et al. [67] on GaSb-InSb, and by Capper et al. [68] on HgTe-CdTe, then extended to numerous other alloys. Comprehensive surveys of the experimental difficulties and resulting properties were published by Foster et al. [69] and Lendvay [70] and it appeared that the main problems in the growth of semiconductors crystals were related to the conjunction of high concentration and wide liquidus-solidus interval in the phase diagram. This leads to strong axial and radial chemical segregations, with large lattice parameter variations and associated with mechanical stress, so that the sample are generally heterogeneous and cracked. However, some other times as shown by Andrews et al. [71] and Cobb et al. [72], the crystals were found unexpectedly homogeneous. It should be noted here that several technical methods and attempts have been developed, such as micro-gravity condition and application of magnetic field to deal with aforementioned problems. It should also be pointed out that in every crystal growth procedure, aside from the main materials of the alloys, the size and the pulling rate or solidification rate are those of the importance. Duhanian et al. utilized the same setting for their experiment as in [73-75], the furnace pulling rate of 1.1 $\mu\text{m/s}$ (which is approximately 4mm/h, this is almost 8 times faster than that of the conditions used in this study) and thermal gradient of 60K/cm in the adiabatic zone of the furnace. The diameter of their sample was 12mm, the length of the seed was 63mm, and the length of the feed was 152mm.

Corriel et al. [76] and Barat et al. [77] showed that this setting was compromised between several constraints, including interface stability, end effects and measurable interface curvature. It was also concluded by Duhanian et al. [65] that from structural point

of view, the samples were of rather good quality with grain sizes in the millimeter and centimeter range, except of course where some destabilization occurred. They also mentioned that the quality immediately improved compared to the seed. The grain boundaries are roughly perpendicular to the interface. At some grain boundaries, the interface demarcation line is strongly distorted. With a 60K/cm thermal gradient, the difference in under-cooling from one grain boundary to other can reach 6K. The fact that was observed in the diluted alloy as well suggests that it is due to surface orientation effect rather than to a different segregation coefficient and then to liquid composition variations along the interface. They also found and listed the following findings:

- i) There is a strong correlation between the interface curvature and the radial segregation along the interface.
- ii) Interface curvature is directly related to the concentration variation on its surface, obviously through the liquidus slope in the phase diagram.
- iii) The interface velocity decreases when the concentration increases, especially on the crucible axis. And finally,
- iv) The radial effects are of primary importance in compare with those of the axial.

Detached solidification is one of the characteristic of vertical Bridgman crystal growth. This is referred to where the melt forms a meniscus between the crucible wall and the solid-liquid interface making the crystal grow without contact with the crucible wall. Duffar et al. [78] in their study focused on the equilibrium at the meniscus between the crystal-melt interface and the crucible wall under terrestrial conditions. The principle is to impose a gas pressure at the cold part (seed side) of the crucible, approximately equal to the

hydrostatic pressure of the molten sample, in order to get a small liquid meniscus between the solid-liquid interface and the crucible wall. A first-order capillary stability analysis shows that stable conditions can be reached for the growth of semiconductors by this technique. Dewetting is the specific phenomenon, originally observed under micro-gravity conditions, which generates a thin and constant gap between a crystal and the container in which it has been grown. This leads to a dramatic increase of crystal structure quality, due to the absence of thermal and mechanical interactions between the solid and the crucible. The classical explanation of the mechanism involves wetting considerations, hydrostatic pressure and gas pressures. A number of developments of this theory have been published in the last few years. Some experiments under micro-gravity conditions also permitted a better understanding of the physical phenomena involved in the dewetting process. Following these developments, the way of obtaining dewetting on the earth has been found and successfully applied to the growth of III-V and II-VI semiconductor crystals. Duffar [79] stressed that one point should be kept in mind that stability of dewetted growth is of the importance. Once dewetting is obtained, it is necessary to insure that the growth conditions, including the gap thickness, will remain constant all along the solidification.

Palosz et al. [80] in their experimental studies on detached growth of germanium (Ge) under controlled pressure condition, examined the conditions of detached solidification in an uncoated graphite crucible as well as in a BN-coated silica and pBN ampoule. Detached and partly detached growth was achieved in pBN and BN-coated crucibles respectively. The results of their experiment are based on the Duffar's theory which states the key factors in detached solidification are the growth and contact angles.

Palosz et al. theoretically calculated the dependency of the gap width on the pressure differential across the meniscus by the following formula; $\Delta P_m = P_{\text{cold}} - P_{\text{hot}} - P_{\text{hydro}}$ where ΔP_m is the pressure differential, P_{cold} and P_{hot} are the gas pressure in the inner and outer chamber, respectively and P_{hydro} is the hydrostatic pressure rate at the crystal-liquid junction. They indicated that the stable growth is possible only below $\Delta P_m = -1$ mbar. Under this condition the gap width is normally more than 100 μm wide which easily leads to melt run-down in terrestrial condition.

Steian et al. [81] by utilizing numerical simulation studied the thermosolutal convection during vertical Bridgman directional solidification of $\text{Ga}_{1-x}\text{In}_x\text{Sb}$ alloys. From the transient modeling of the heat, momentum and species transport it is found that, in the case of vertical Bridgman configuration, the heavier InSb solute rejected at the interface leads to a continuous damping of the thermally driven convection. The modeling of low-doped alloy solidification shows that the solutal effect cannot be neglected for high pulling rates. They reminded that the morphological interface stability criterion allows great values of the pulling rate for low-doped alloys (as for example $V_{\text{max}} \approx 10 \mu\text{m/s}$ for a $\text{Ga}_{0.99}\text{In}_{0.01}\text{Sb}$ alloy solidified in a thermal gradient $G_T \approx 50\text{K/cm}$). However, they warned that the use of such high rates is not advisable for the experiments because, after the damping of the melt convection, the poor mixing of solute at the interface leads to a strong increase of the radial and axial chemical segregations in the samples grown in such conditions. They concluded that in the case of concentrated alloys solidified at $V=1.0 \mu\text{m/s}$, this effect becomes dramatic because of the dependency of the melting point on the interface composition which produces a significant increase of interface curvature. They also proposed an

analytical expression to compute a critical value of the growth rate V_{cr} for which the thermosolutal effect must be considered. Because the damping of the thermally driven convection has undesirable effects on the crystals quality, this phenomenon can be avoided if the condition $V < V_{cr}$ is respected. Steian et al in their modeling performed for the horizontal Bridgman solidification of concentrated GaInSb alloys under microgravity conditions showed an inverse but lower solutal effect on the melt convection, leading to a small increase of the flow intensity during the solidification. The solute distribution in the sample and the interface shape are essentially affected by the thermal convection, which depends on the gravity level. From the numerical simulation, they found that a modification of g values between 2×10^{-6} and $2 \times 10^{-5} g_o$, which is the gravity level measured onboard Spacelab during STS 78/LMS mission, has no significant influence on the chemical segregations in the solidified sample, and residual accelerations lower than $10^{-7} g_o$ are necessary to get diffusive conditions.

Ruiz [82] studied the impact of short impulsive forces on the semiconductor segregation patterns inside a generic μg Bridgman growth arrangement with the help of a time-dependent 2D numerical scheme. Impulses applied parallel to the growth interface, equivalently, orthogonal to the external thermal gradient. The present results indicate that for each one of the three semiconductors (GeGa, GaAsSe, SnBi) considered, the reduced longitudinal and radial segregation are practically insensitive to the pulse (impulse) shape, rectangular or half-sinusoidal. The reduced longitudinal segregation only depends on the growth velocity for constant g -dose impulses. The reduced radial segregation depends on both the interface growth velocity and very weakly on the activity time of the constant g -

dose impulse externally applied. The thermal flux across the interface is shape-dependent and does not act synchronically with half-sinusoidal external impulses. Ruiz also mentioned that as before, this flux depends on the activity time and on the growth velocity for constant g-dose impulses.

Li et al. [83] presented a full three dimensional (3D) transient finite element analysis of the complex fluid and heat and mass transfer phenomena in a simplified Bridgman crystal growth configuration under the influence of g-jitter perturbations and magnetic field to grow Ga-doped germanium single crystal in space. Numerical results and findings showed that g-jitter drives a complex, 3D, time-dependent thermal convection and that velocity spikes in response to real g-jitter disturbances in space flights, resulting in irregular solute concentration distributions. An applied magnetic field provides an effective means to suppress the deleterious convection effects caused by g-jitter. Based on the simulations with applied magnetic fields of various strength and orientations, the magnetic field aligned with the thermal gradient provides an optimal damping effect, and the stronger magnetic field is more effective in suppressing the g-jitter induced convection. Magnetic damping of the motion of an electrically conducting fluid stems from the interaction between the convection and an applied magnetic field, which generates an opposing Lorentz force to suppress the flow. The intensity of the natural convection which cannot be avoided scales with the Grashof (thermal) number. It is obvious that the intensity of the buoyancy driven convection depends highly on the melt height and thus changes as the melt is depleted. Hoshikawa [84] showed that for higher Rayleigh number ($Ra \geq 10^6$) stronger axial static magnetic fields are needed to eliminate thermal fluctuations and to

suppress convection and reach to a symmetric flow. Nikitin et al. [85] conducted a mathematical simulation of impurity distribution in crystals prepared under microgravity condition and found since $Gr.Pr \ll 10^3$, the motion in the melt produces practically no effect on the temperature field. Chang et al. [86] showed in their studies the influence of natural convection in the melt/solid interface on radial dopant segregation (gallium-doped germanium) in a vertical Bridgman crystal growth system. When the crystal diameter is large and the velocity field is similar along the radius of the melt/solid interface, convection only alters the concentration field perpendicular to the interface. Burton et al. [87] states that the radial segregation reaches a maximum for intermediate values of flow intensity, which results in relatively thick solute boundary layers that have a non-uniform thickness. Fu et al. [88] expressed that in the vertical Bridgman configuration for crystal growth, the interface shape is a factor that greatly influences the yield of single crystals. The shape of the interface is mainly determined by the temperature field near the interface and the level of natural convection in the melt. The shape of the interface can range from concave to convex. Slightly convex interface shape is most desirable because it eliminates most problems with spontaneous nucleation at the crucible wall and improves grain selection, which results in higher yield of single crystals. However, as Jasinsky et al. [89] showed, the efforts of obtaining convex interface shapes in growth experiments have been of limited success.

CHAPTER THREE

Theoretical Approach and Numerical Solution

3.0 Introduction

The model is cylindrical; therefore all the equations are considered in cylindrical coordinates and introduced in a transient condition. This chapter presents the numerical solution technique and the governing equations and boundary conditions by using Finite Element Analysis which will be used in the computer simulations. The discretized form which is utilized in Finite Volume also has been used for computer simulations. The calculation of the flow field by utilizing “Semi-Implicit Method for Pressure-Linked Equations” (SIMPLE) [90], which is a Finite Volume method, is incorporated to verify those of Finite Element results. Model description, and mesh sensitivity analysis will be discussed as well.

3.1 Numerical Solution Technique

Since this study focuses on the solution zone (solvent region), the full non-linear Navier-Stokes equations for laminar (since Reynolds number (Re) = 340), incompressible Newtonian flows in transient condition are solved, by taking the Boussinesq approximation Equation 3.1 into the consideration. Convective heat and mass transfer along with the external forces such as axial magnetic field in terrestrial and microgravity condition are also taken into the consideration. The applied axial temperature is calculated by utilizing

the experimental field temperature, done by Dalhousie University, for this model along with the radial temperature. There are some assumptions which put forward into the input files for the computational simulations. The input files for several cases are presented in Appendix-C. The aforementioned assumptions are as follow:

1. The flow is laminar
2. The fluid is Newtonian
3. The flow is viscous
4. The solvent is electrically conductive
5. Except density, all other thermo-physical properties are constant
6. Ampoule's translational speed is set to very minimal speed
7. Non-slip condition for velocity on the side walls and dissolution boundaries

3.1.1 Boussinesq Approximation

The Boussinesq approximation, Equation 3.1, states that the fluid density is a linear function of the temperature and concentration. This approximation can only be applied where the product of the coefficient of thermal expansion (β_T) and temperature difference (ΔT) is much less than 1 ($\beta_T \cdot \Delta T \ll 1$), in this study the aforementioned product equates to 0.0063 which perfectly satisfies the requirement.

$$(\rho - \rho_0) = -\rho_0 [\beta_T(T - T_0) - \beta_c(C - C_0)] \quad (3.1)$$

Where; $\beta_T = -\frac{1}{\rho} \left(\frac{\partial \rho}{\partial T} \right)_c$, and $\beta_c = -\frac{1}{\rho} \left(\frac{\partial \rho}{\partial C} \right)_T$ while the norm $|\circ|$ indicates the reference value on density, temperature and concentration respectively.

3.1.2 Finite Element Analysis (FEA)

Solving the governing equations for the purpose of modeling and simulation can be carried out with several methods such as control volume or better known as Finite Volume Analysis (FVA) and Finite Element Analysis (FEA). In this study, FEA is utilized which is very effective and accurate for solving all kinds of partial differential equations. By applying FEA, we try to minimize the infinite number of degrees of freedom (DoF) in a given problem to a manageable finite number of DoF by a system of algebraic equations. A model under study and analysis is then divided into smaller areas known as elements. Each element is defined by a finite number of points known as nodes by which all the variables in the analysis, such as velocity, concentration, pressure and temperature to name a few, can be evaluated and analyzed. In the model under study for this thesis, which has over fourteen thousand nodes, the Galerkin finite element method approximation [91] has been employed for silicon concentration and velocity in the solvent region along three axes (u , v , w and C) as well as the solvent temperature and pressure (T and P). This was done to reduce partial differential equations and boundary conditions to a set of algebraic equations, as mentioned above. This is completed by using the segregated algorithm to solve those equations [91].

A commercial software (GAMBIT) has been used to make a three dimensional geometry of the model under this study. Once the eight-node hexahedron elements produced via meshing the model, the geometry and the associated mesh are exported to another commercial software which is computational fluid dynamics (CFD), FIDAP and FLUENT software and runs on the Finite Element Analysis and is used to numerically

model the crystal growth of $\text{Ge}_{0.75}\text{Si}_{0.25}$ in this study [91]. Along with the finite element analysis, the author of this study has utilized the Finite Volume Analysis in order to validate the accuracy of the results obtained by Finite Element Analysis; the outcome of the Finite Volume Analysis conform those of the Finite Element Analysis and is presented in the Appendix-C. The Figure 3.1 depicts the geometry and finite mesh of the model in this study.

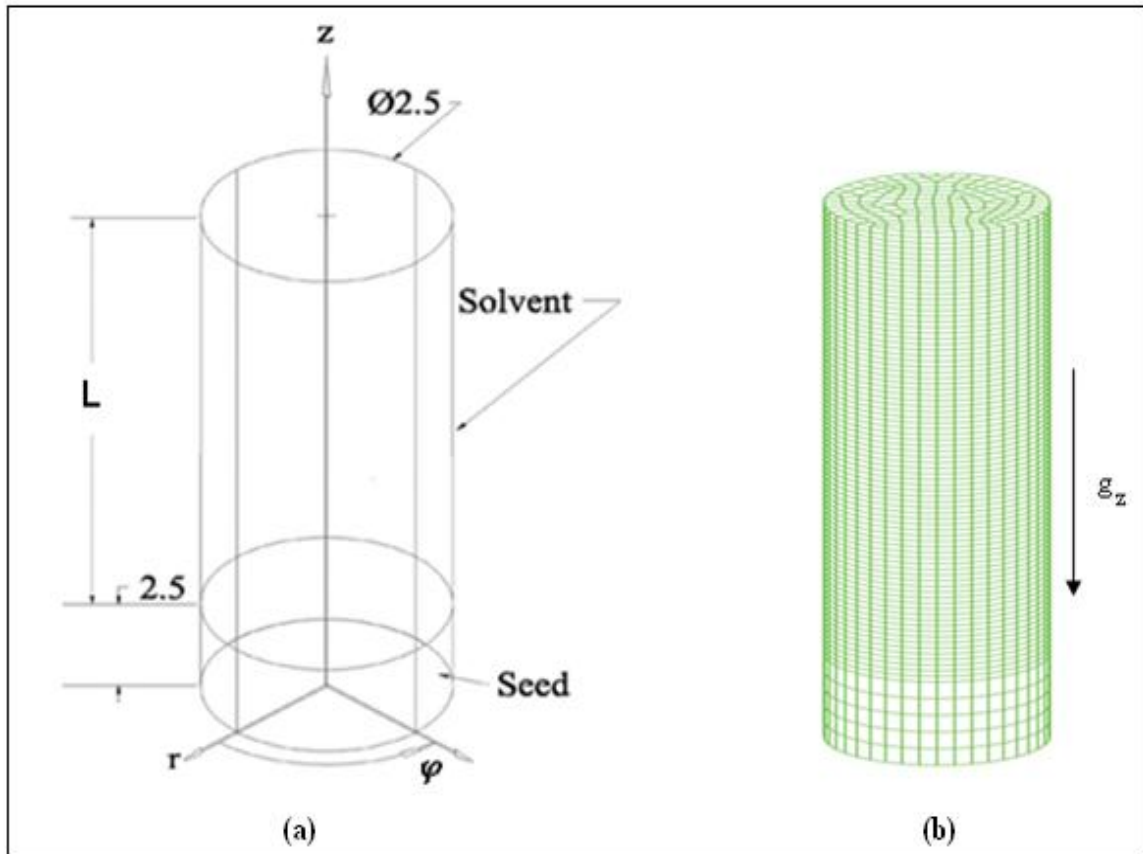


Figure 3.1 Bridgman model, solvent region under investigation

a) Model geometry

b) Meshed Model

3.2 Dimensional Governing Equations

3.2.1 Navier-Stokes Equations:

The full set of Navier-Stokes equations for laminar, transient condition incompressible Newtonian flows, by taking the Boussinesq approximation is defined for radial, circumferential and vertical axis respectively as:

r-component:

$$\rho \left(\frac{\partial u}{\partial t} + u \frac{\partial u}{\partial r} + \frac{v}{r} \frac{\partial u}{\partial \varphi} + w \frac{\partial u}{\partial z} - \frac{v^2}{r} \right) = -\frac{\partial p}{\partial r} + \mu \left(\nabla^2 u - \frac{u}{r^2} - \frac{2}{r^2} \frac{\partial v}{\partial \varphi} \right) + F_r^M + \rho g_r [\beta_T (T - T_0) - \beta_C (C - C_0)] \quad (3.2)$$

φ -component:

$$\rho \left(\frac{\partial v}{\partial t} + u \frac{\partial v}{\partial r} + \frac{v}{r} \frac{\partial v}{\partial \varphi} + w \frac{\partial v}{\partial z} + \frac{uv}{r} \right) = -\frac{1}{r} \frac{\partial p}{\partial \varphi} + \mu \left(\nabla^2 v - \frac{v}{r^2} + \frac{2}{r^2} \frac{\partial v}{\partial \varphi} \right) + F_\varphi^M + \rho g_\varphi [\beta_T (T - T_0) - \beta_C (C - C_0)] \quad (3.3)$$

z-component:

$$\rho \left(\frac{\partial w}{\partial t} + u \frac{\partial w}{\partial r} + \frac{v}{r} \frac{\partial w}{\partial \varphi} + w \frac{\partial w}{\partial z} \right) = -\frac{\partial p}{\partial z} + \mu (\nabla^2 w) + F_z^M + \rho g_z [\beta_T (T - T_0) - \beta_C (C - C_0)] \quad (3.4)$$

Where the Laplacian (del) operator is defined as:

$$\nabla^2 = \left(\frac{1}{r} \frac{\partial}{\partial r} \left(r \frac{\partial}{\partial r} \right) + \frac{1}{r^2} \frac{\partial^2}{\partial \varphi^2} + \frac{\partial^2}{\partial z^2} \right) \quad (3.5)$$

The melt temperature (T_0) of Germanium (Ge) and the Silicon (Si) concentration (c_0) are used as the reference temperature and concentration respectively. Equations (3.2), (3.3) and (3.4) satisfy the momentum equations (Navier-Stokes) in the solvent region in all three directions of radial (r), angular (φ) and axial (z) respectively. Three external forces ; F_r^M , F_φ^M , and F_z^M represent the magnetic body force components along the r , φ and z direction respectively and are defined as;

$F_r^M = -\sigma B_r^2 u$, $F_\varphi^M = -\sigma B_\varphi^2 v$, and $F_z^M = 0$ [92], [93], and Appendix-B. It is clear that the magnetic body force components, acting on the solvent region, are only effective in the radial and angular directions respectively.

3.2.2 Energy Equation:

Energy equation for the solvent region (liquid phase) is presented as:

$$\rho c_p \left(\frac{\partial T}{\partial t} + u \frac{\partial T}{\partial r} + \frac{v}{r} \frac{\partial T}{\partial \varphi} + w \frac{\partial T}{\partial z} \right) = k \left(\frac{1}{r} \frac{\partial}{\partial r} \left(r \frac{\partial T}{\partial r} \right) + \frac{1}{r^2} \frac{\partial^2 T}{\partial \varphi^2} + \frac{\partial^2 T}{\partial z^2} \right) \quad (3.6)$$

Where c_p and κ are specific heat and thermal conductivity of the solvent respectively.

3.2.3 Continuity (mass conservation) Equation:

The continuity equation is expressed as:

$$\frac{\partial \rho}{\partial t} + \frac{1}{r} \frac{\partial}{\partial r} (ru) + \frac{1}{r} \frac{\partial v}{\partial \varphi} + \frac{\partial w}{\partial z} = 0 \quad (3.7)$$

3.2.4 Mass Transport Equation:

$$\frac{\partial c}{\partial t} + u \frac{\partial c}{\partial r} + \frac{v}{r} \frac{\partial c}{\partial \varphi} + w \frac{\partial c}{\partial z} = \alpha_c \left(\frac{1}{r} \frac{\partial}{\partial r} \left(r \frac{\partial c}{\partial r} \right) + \frac{1}{r^2} \frac{\partial^2 c}{\partial \varphi^2} + \frac{\partial^2 c}{\partial z^2} \right) \quad (3.8)$$

Where c and α_c are silicon concentration and solutal diffusivity respectively.

3.2.5 Latent Heat Equation:

The model also utilizes the latent heat of the material and the continuity of the velocities and temperature to be exchanged along the solid-liquid interface and is described by:

$$\rho_s L_f (w_s - w_{int}) = k \frac{\partial T}{\partial z} - k_s \frac{\partial T_s}{\partial z} \quad (3.9)$$

Where, L_f is the latent heat and " w_s " is the axial velocity along the vertical axis of the solvent region and " w_{int} " is the axial velocity of the solid-liquid interface.

3.2.6 Growth Velocity Equation:

The growth velocity (the interface displacement rate) is a modified version of Helmers et al. [94] which is computed by solving the mass balance equation coupled with the GeSi binary phase diagram.

$$v_{eff} = \frac{v_z}{2} \left[1 - \frac{\nabla c_s}{\nabla \theta} \left(\frac{\partial T_L}{\partial c} \right)_{c_s/k} \right]^{-1} \quad (3.10)$$

Where v_z is the pulling rate (same as w_s in equation 3.9), ∇c_s is the dimensionless concentration gradient, $\left(\frac{\partial T_L}{\partial c}\right)_{c_s/k}$ is the slope of the liquidus, $\nabla \theta$ is the dimensionless temperature gradient. For this study, the typical values give $v_{eff} \approx v_z$, considering the pulling rate is set to 0.25mm per hour (0.069 $\mu\text{m/s}$). This is well below ($1/4^{\text{th}}$) of the Helmers et al. study.

3.3 Dimensional Analysis

Dimensional analysis, simply put, is another useful tool of modern fluid mechanics. It is basically the mathematics of dimensions of quantities [93]. This method is used to reduce the number and complexity of experimental variables which affect a given physical phenomenon, by using a kind of compacting technique [94]. Reynolds number, Prandtl number and Grashof number are a few examples of dimensionless parameters which are used in this study as shown in Table-3.1. All the non-dimensionalization steps are presented in Appendix-B.

3.3.1 Dimensionless Variables

The dimensionless variables are used to achieve the aforementioned goals. They are used to help make all the governing equations such as Navier-Stokes equations to become non-dimensional which further on enhance and expedite the computation processes.

These variables can be defined as follow;

$$R = \frac{r}{L}, \quad U = \frac{u}{u_0}, \quad V = \frac{v}{u_0}, \quad W = \frac{w}{u_0}, \quad Z = \frac{z}{L}, \quad \theta = \frac{T-T_0}{\Delta T},$$

$$C = \frac{C-C_0}{\Delta C}, \quad P = \frac{pL}{\mu u_0}, \quad B^* = \frac{B}{|B_0|}, \quad \tau = \frac{tu_0}{L}$$

Where R and Z are considered as non-dimensional radial and axial coordinates, respectively. U , V and W are dimensionless radial, angular and axial velocity, respectively. θ (theta) is the non-dimensional temperature, T_0 is the reference temperature (melt temperature of $\text{Si}_{0.25}\text{Ge}_{0.75}$), C is the dimensionless solute concentration, P is dimensionless hydrodynamic pressure, B^* is dimensionless variable of magnetic field induction, and τ is referred to the dimensionless variable of time (t).

The reference velocity (u_0) is defined as; $u_0 = \sqrt{gL\beta_T\Delta T}$

Where g is the earth gravity, L is the characteristic (reference) length, β_T is the coefficient of the thermal expansion, and ΔT is set equal to one for simplicity.

Table 3.1 Some dimensionless parameters, excerpted from [95].

Parameter	Definition	Qualitative Ratio	Application
Reynolds Number	$Re = \frac{\rho u_0 L}{\mu}$	$\frac{Inertia}{Viscosity}$	Almost Always
Schmidt Number	$Sc = \frac{\nu}{\alpha_c}$	$\frac{Viscous}{Solutal\ diffusivity}$	Mass transfer
Prandtl Number	$Pr = \frac{c_p \mu}{k}$	$\frac{Dissipation}{Thermal\ Conductivity}$	Heat Convection
Peclet Number (Thermal)	$(Pe)_T = \frac{Lv}{\alpha} = Re \cdot Pr$	$\frac{Inertia}{Thermal\ diffusivity}$	F.E.A Heat transfer
Peclet Number (Diffusion)	$(Pe)_c = \frac{Lv}{D} = Re \cdot Sc$	$\frac{Inertia}{Mass\ diffusivity}$	F.E.A Fluid Flow
Hartmann Number	$Ha = B_0 L \sqrt{\frac{\sigma}{\mu}}$	$\frac{Magnetic\ Force}{Viscous\ Force}$	Magnetic field effect
Grashof (Thermal)	$(Gr)_T = \frac{\beta_T \Delta T g \rho^2 L^3}{\mu^2}$	$\frac{Buoyancy}{Viscosity}$	Natural Convection
Grashof (Solutal)	$(Gr)_c = \frac{\beta_c \Delta C g \rho^2 L^3}{\mu^2}$	$\frac{Buoyancy}{Viscosity}$	Natural Convection

3.4 Finite Volume Analysis (FVA)

As mentioned earlier, discretized equations for two dimensional models in Finite Volume Analysis have been employed for verification of the result shown by the Finite Element Analysis. Input programs for velocities, temperature, concentrations (species), and

pressure would be presented in Appendix “C”. In control volume the calculation domain is divided into a number of non-overlapping control volumes such that there is one control volume surrounding each grid points. The differential equation is integrated over each control volume. Piecewise profiles expressing the variation of ϕ (which is referring to any variable under evaluation such as; velocity, temperature, etc. in the formulas) between the grid points are used to evaluate the required integrals. The result is the discretization equation containing the values of ϕ for a group of grid points [90]. The discretization equation obtained in this manner expresses the conservation principle for ϕ for the finite control volume, just as the differential equation expresses it for an infinitesimal control volume; Appendix-B shows the set up for the grids.

For the seed or solid section (which only was used in preliminary model) the energy equation is defined as:

$$\rho c \frac{\partial T}{\partial t} = \frac{\partial}{\partial x} \left(k \frac{\partial T}{\partial x} \right) + \frac{\partial}{\partial y} \left(k \frac{\partial T}{\partial y} \right) + S \quad (3.21)$$

And can be turned into discretization equation as follow:

$$a_P T_P = a_E T_E + a_W T_W + a_N T_N + a_S T_S + b \quad (3.22)$$

Where

$$a_E = \frac{k_e \Delta y}{(\partial x)_e}, \quad a_W = \frac{k_w \Delta y}{(\partial x)_w}, \quad a_N = \frac{k_n \Delta y}{(\partial x)_n}, \quad a_S = \frac{k_s \Delta y}{(\partial x)_s}, \quad b = S_C \Delta x \Delta y + a_P^0 T_P^0, \text{ and}$$

$$a_P = a_E + a_W + a_N + a_S + a_P^0 - S_P \Delta x \Delta y \text{ in which } a_P^0 = \frac{\rho c \Delta x \Delta y}{\Delta t}. \text{ It should be noted}$$

that the product of $\Delta x \Delta y$ is the volume of the control volume in which the z value is considered as the unity.

3.4.1 Momentum Equation:

$$\frac{\partial}{\partial t}(\rho u) + \frac{\partial}{\partial x}\left(\rho uu - \mu \frac{\partial u}{\partial x}\right) + \frac{\partial}{\partial y}\left(\rho vu - \mu \frac{\partial u}{\partial y}\right) = -\frac{\partial p}{\partial x} + \rho g_x \quad (3.23)$$

Where the terms $\rho uu - \mu \frac{\partial u}{\partial x} = J_x$ and $\rho vu - \mu \frac{\partial u}{\partial y} = J_y$ are the flux in x and y direction respectively. Equation (3.23) then can be written in discretized form as:

$$(\rho_e u_e - \rho_e^0 u_e^0) \frac{\Delta y(\delta x)}{\Delta t} + J_E - J_P + J'_n - J'_s = (P_P - P_E)\Delta y + \rho g_x \Delta y \delta x \quad (3.24)$$

Where

$$J_E = \int_s^n J_x|_e dy; J_P = \int_s^n J_x|_p dy; J'_n = \int_p^E J_x|_n dy; J'_s = \int_p^E J_x|_s dy$$

3.4.2 Continuity Equation

$$\frac{\partial \rho}{\partial t} + \frac{\partial}{\partial x}(\rho u) + \frac{\partial}{\partial y}(\rho v) = 0 \quad (3.25)$$

This in discretized form becomes:

$$(\rho_e - \rho_e^0) \frac{\Delta y(\delta x)}{\Delta t} + F_E - F_P + F'_n - F'_s = 0 \quad (3.26)$$

Where

$$F_E = (\rho u)_E y; F_P = (\rho u)_P \Delta y; F'_n = (\rho v)_n \delta x; F'_s = (\rho v)_s \delta x$$

3.4.3 Energy Equation

$$\frac{\partial}{\partial x}(\rho T) + \frac{\partial}{\partial x}(\rho u T) + \frac{\partial}{\partial y}(\rho v T) = \frac{\partial}{\partial x}\left(\Gamma \frac{\partial T}{\partial x}\right) + \frac{\partial}{\partial y}\left(\Gamma \frac{\partial T}{\partial y}\right) + S \quad (3.27)$$

Where; $S=0$, and $\Gamma = \frac{k}{c_p}$

The discretized form reads as:

$$a'_W T_W + a'_S T_S + a'_P T_P + a'_E T_E + a'_N T_N = b \quad (3.28)$$

where

$$b = a_P^0 T_P^0 ; \quad a_P^0 = \frac{\rho_P^0 \Delta x \Delta y}{\Delta t} , \quad \text{and} \quad a_P = -(a'_E + a'_W + a'_N + a'_S) + a_P^0$$

By considering Power-Law scheme for a_E when $0 \leq P_e \leq 10$, (P_e is the local Peclet number), We have $\frac{a_E}{D_e} = (1 - 0.1P_e)^5$, again the details can be found in Appendix-B.

3.4.4 Mass Transport (Species) Equation

$$\begin{aligned} \frac{\partial}{\partial t}(\rho r c) + \frac{\partial}{\partial r}(\rho r u c) + \frac{\partial}{\partial z}(\rho r w c) \\ = \frac{\partial}{\partial r} \left[\rho r \left(D_c \frac{\partial c}{\partial r} + D_r \frac{\partial T}{\partial r} \right) \right] + \frac{\partial}{\partial z} \left[\rho r \left(D_c \frac{\partial c}{\partial z} + D_r \frac{\partial T}{\partial z} \right) \right] \end{aligned} \quad (3.29)$$

And by integrating in transient mode, we will have;

$$\begin{aligned} \iiint_t^{t+\Delta t} \frac{\partial}{\partial t}(\rho r c) dt dr dz + \iiint_t^{t+\Delta t} \frac{\partial}{\partial r}(\rho r u c) dr dz dt + \iiint_t^{t+\Delta t} \frac{\partial}{\partial z}(\rho r w c) dz dr dt = \\ \iiint_t^{t+\Delta t} \frac{\partial}{\partial r} \left(\rho r c D_c \frac{\partial c}{\partial r} \right) dr dz dt + \\ \iiint_t^{t+\Delta t} \frac{\partial}{\partial z} \left(\rho r D_c \frac{\partial c}{\partial z} \right) dz dr dt + \iiint_t^{t+\Delta t} \frac{\partial}{\partial r} \left(\rho r D_r \frac{\partial T}{\partial r} \right) dr dz dt + \\ \iiint_t^{t+\Delta t} \frac{\partial}{\partial z} \left(\rho r D_r \frac{\partial T}{\partial z} \right) dz dr dt \end{aligned} \quad (3.30)$$

3.5 Model Geometrics and Boundary Conditions

The model consists of a fixed cylindrical coordinate system of (r, ϕ, z) with its origin located at the center of the solid section (seed). The model is 11.5 cm long with a uniform diameter of 2.5 cm and consists of two segments as; seed (Silicon) 2.5 cm, the solvent region 9.0 cm which is a mixture of silicon (Si) and germanium (Ge) initially set as $\text{Ge}_{0.75}\text{Si}_{0.25}$, the solvent region is the upper segment. The model in this study is focusing only on the solvent region. The vertical Bridgman method is the technique being chosen for this study. Both sections, introduced earlier in model description, are held in a quartz ampoule (the ampoule is neither shown nor modeled).

A linear temperature gradient with minimal temperature difference between top and the bottom of the model is applied on the outer face of the crucible. Since the melt temperature of the solvent region is much lower than that of the quartz, therefore there would be no oxygen penetration from quartz into the melt and consequently no contamination or impurity occurs which is a great advantage of low temperature gradient in this technique. Figure 3.2 depicts the meshed model of the solvent region in this study.

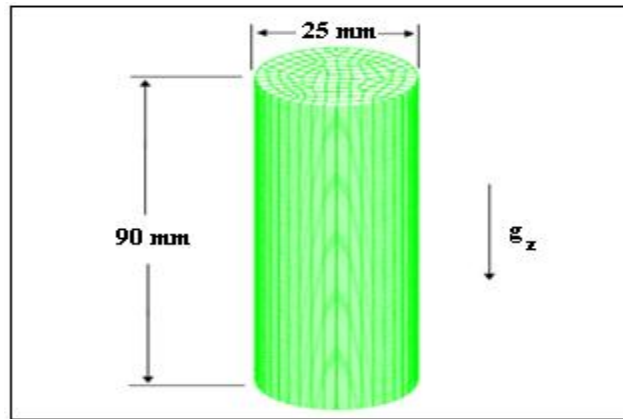


Figure 3.2 Solvent region meshed model

Boundary Conditions

In this model, the boundary conditions associated with the governing equations are:

- a) At the ampoule side wall (solid);

$$u=0, v=0 \text{ and } w=0 \text{ (Non-slip condition), and } \frac{\partial c}{\partial r} = 0$$

- b) Silicon concentration at the dissolution interface which is on the top horizontal plane:

$$c=c_1=0 \text{ (Chapter Four) and (Proposed 0.34 for Chapter Five)}$$

- c) Silicon concentration in the solvent region and facing the growth interface is:

$$c=c_2=0.75 \text{ (Chapter Four) and (Proposed 0.25 for Chapter Five)}$$

- d) Silicon concentration in the substrate (seed which is Si-rich and used in the preliminary model) is: $c=1.0$

Where c_1 and c_2 are representing the silicon concentration at the dissolution, in the solvent region, and seed interface respectively. These values for the silicon concentration are obtained from the phase diagram [38].

As for the temperature, the boundary conditions are defined as follow;

- a) At the external surface of the quartz ampoule (not shown in the Figure 3.1) a non-linear temperature distribution, Figure 3.3, is applied in the axial direction. This temperature profile is computed based on the measured profile which was experimented at Dalhousie University.

- b) At the bottom horizontal plane of the model $T = T_o = T_m = 1057.5 \text{ } ^\circ\text{C}$

- c) and at the top horizontal plane of the model $T = T_H = 1100 \text{ } ^\circ\text{C}$

It should be noted that these boundary conditions for temperature (both non-linear and linear) are only for Chapter four of this research. Later on different linear temperature gradients were applied in Chapter Five of this research.

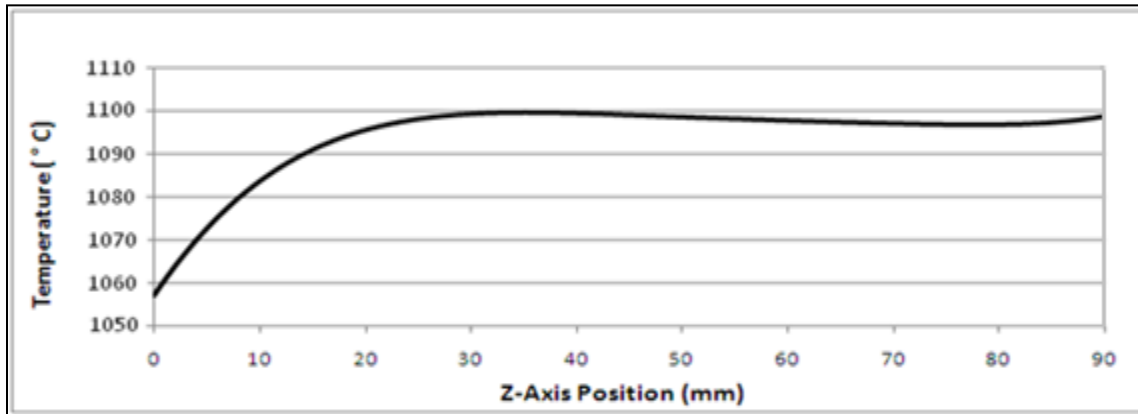


Figure 3.3 Non-linear temperature profile, data acquired from Professor Labrie at D.U.

3.6 Mesh Sensitivity and Solution Technique

In order to have the best and most reliable results, an optimum number of nodes and elements should be defined, therefore, mesh sensitivity analysis was carried out and ideal numbers of nodes on both circumferential and axial edges were selected based on the heat flux across the dissolution interface in solvent region. As it can be read from the Figure 3.4, and Table-3.2 a mesh with 1 to 2 aspect ratio of circumferential to axial nodes is made where heat flux does not change across the dissolution interface as the mesh becomes finer. For this reason and the aforementioned reasons, the 40 x 288 mesh combination reasonably meets the computational need and simulation becomes satisfactory for the analysis in this

study on the solvent region only. It should be noted that this mesh configuration was applied for Finite Element Analysis.

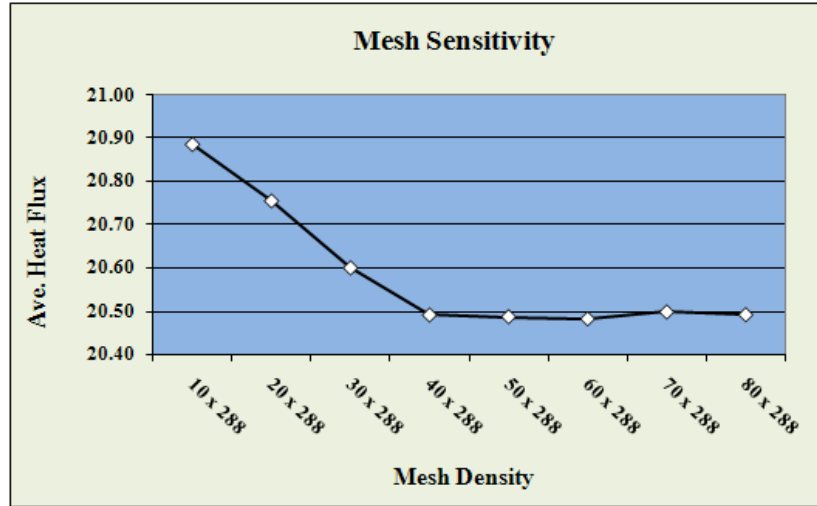


Figure 3.4 Mesh densities vs. heat flux at dissolution interface

Table 3.2 Mesh Sensitivity analysis

Item	Mesh Density (Grids) (circumferential x Axial)	Average Heat Flux
		Dimensionless Values From FIDAP
1	10 x 288	20.8806
2	20 x 288	20.7635
3	30 x 288	20.6014
4	40 x 288	20.4918
5	50 x 288	20.4909
6	60 x 288	20.4940
7	70 x 288	20.4978
8	80 x 288	20.4956

Finite element method is utilized and the model is divided into elements and subsequently nodes by which all the variables, which are the three velocities, concentration, pressure and

the temperature can be evaluated and analyzed. In this model, which has over fourteen thousands nodes, the Galerkin finite element method approximation has been employed for silicon concentration and velocity in the solvent region along three axes (u, v, w). The governing equations then solved simultaneously and criteria for the convergence considered for the aforementioned variables. For convergence checking between two successive time steps the following equations are set to be met; $\frac{\|\Delta u_i\|}{\|u\|} \leq \varepsilon_u$, $\Delta u_i = u_i - u_{i-1}$ and $\frac{\|R_i\|}{\|R_0\|} \leq \varepsilon_F$ are used where “u_i” represents the pressure, temperature, velocities and silicon concentration, along “r, φ and z” directions for each node and “R₀” is reference vector, typically R(u_i) which is the residual force vector. ε_u is the convergence tolerance based on the relative error and ε_F is the residual convergence tolerance for each variable at each iteration. Since both Δu_i and R(u_i) tend to zero near the solution therefore problem is assumed converged when system satisfies the above criteria which was specified as 10^{-4} for both solution vector and residual force vector. For our study the maximum number of nonlinear iterations for both fluid and structural problem is set to 450. The norm $\| \cdot \|$ is a root mean square norm summed overall the equations for the model [91].

CHAPTER FOUR

Two and Three Dimensional Modeling with Different Heating Profile and Applied Axial Magnetic Field

4.0 Introduction

As mentioned earlier on the main purpose of growing single bulk crystals is to control and to have the uniformity of solution-zone composition in the growth process, since the quality of the single bulk crystal is essentially affected by the fluid flow strength and characteristics, the silicon distribution in the solvent region along with the flow velocity are studied. To achieve the aforementioned uniformity, it is required to have no convection in the solvent region. One proven method is to eliminate the effect of gravity force. This can be and have been shown in the microgravity condition where gravity vector (g) is set to ($10^{-6} g_0$). Another way to suppress the effect of the gravity force is to apply magnetic force. This chapter presents the results obtained with non-linear temperature profile (a polynomial of sixth-order) which experimentally obtained by Professor Labrie at Dalhousie University, and linear temperature profile when applied to the model in different conditions. These are; terrestrial, microgravity and terrestrial with different applied axial magnetic field and under two temperature profile regimes, linear and non-linear, using Vertical Bridgman Method (VBM). The VBM process of $\text{Si}_{0.25}\text{Ge}_{0.75}$ is considered utilizing the physical properties which are presented in Appendix “A”. All the results are obtained through numerical simulation by applying Finite Element Analysis (FEA) and in order to verify these results, they were compared with both the results obtained through simulation

by volume control analysis known as Finite Volume Analysis (FVA) and those of obtained through experimental settings.

4.1 3-D Model under Non-Linear Temperature Profile in Terrestrial Condition

A polynomial of the sixth order temperature profile is used in the terrestrial condition where the gravity (g_0) is not suppressed. All the figures shown in this study are representing the end of the solidification real time which is $t = 360$ hours or 15 days and the time steps are set for every 12 minutes with a total of 1800 time steps. Figure 4.1 represents the flow velocity in the solvent region, where Figure 4.1-a, is the vertical cross section of the model and Figure 4.1-b is the horizontal cross section at 1 millimeter above the growth interface. It is clear to see that the flow is creating almost three distinct areas, but in terms of the flow speed near the growth interface, two distinct areas marked as “e” and “f” with 0.82 mm/s and 2.17 mm/s respectively and “d” with 0.15 mm/s. These velocities have an impact on the shape of the interface ultimately and result in not having nearly flat shape of the interface which is desired and sought after. The flow velocities are induced due to the buoyancy driven convection effect. Figure 4.1-a also reveals that there is a stronger flow cell in the middle of the region near the interface along with two weaker cells near the wall of the model. Figure 4.2 represents the flow velocity plotline along the vertical axis passing through the center of the model. It shows that there is a strong flow cell near the growth interface. Figure 4.3-a reveals the temperature distribution in the solvent region which is under a non-linear polynomial temperature applied on the outer surface of the model. Figure 4.3 which shows an increment of 1.42 °C describes the temperature contour lines. The purpose of heating the model is to create a mushy zone known as solvent region which

is hot enough to obtain a mixture of the two semiconductors but at the same time not too hot so the seed, which is not shown is being melted.

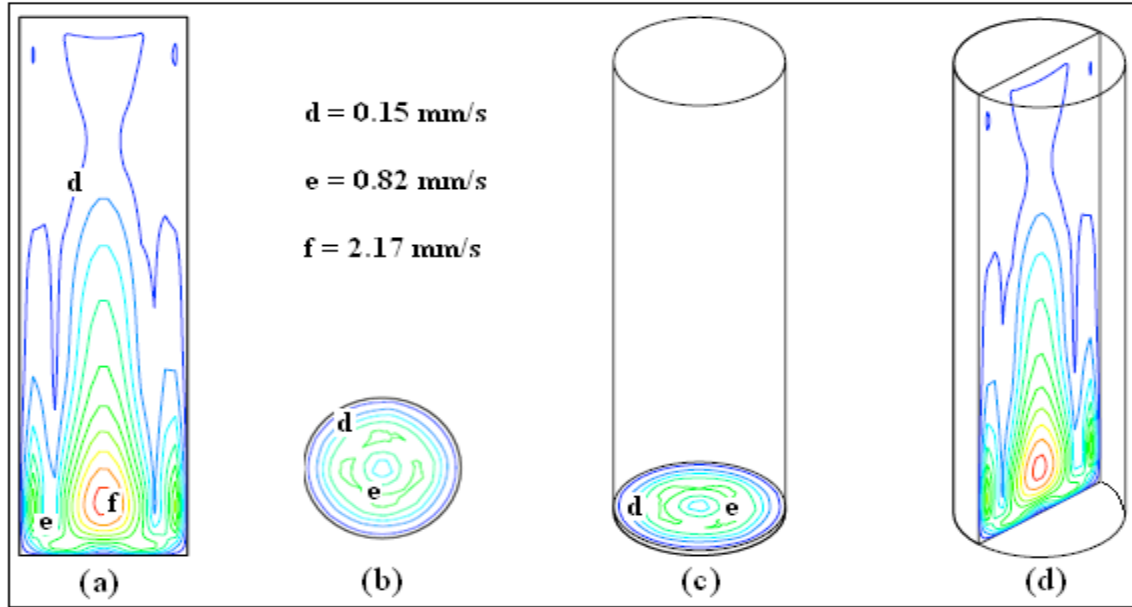


Figure 4.1 Flow velocities in solvent region under terrestrial condition

- a- Vertical cross section passing through the centre of the model
- b- Horizontal cross section at 1 mm above growth interface
- c- 3-D view of horizontal cross section
- d- 3-D view of the vertical cross section

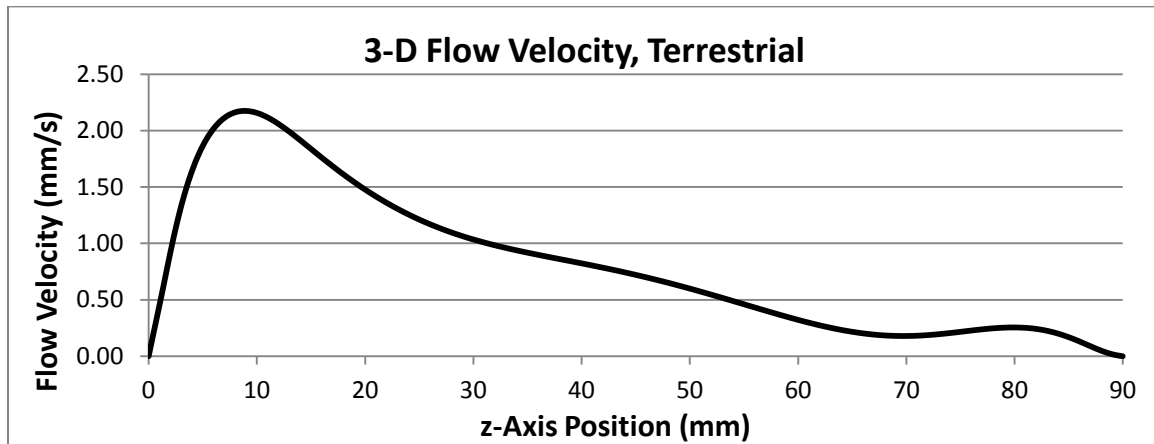


Figure 4.2 Flow velocities along vertical axis under terrestrial condition

The idea is to diffuse the silicon into the solvent zone. By having such a temperature profile, it might be expected to have a convection pattern with hot molten particle moving to the top of the model and the cold particles down from the center of the solvent region. Figure 4.3-b shows the temperature distribution in the solvent region at 1 millimeter above the growth interface. It can be seen that there is a radial temperature gradient; however the variation is small because the heat transfer process in the semiconductor materials is dominated by conduction more than the convection. This has also been addressed by [97] and [98].

Since the material (alloy, for the solvent region) used in this study is a mixture of silicon and germanium and both are semiconductors and has a relatively low Prandtl number ($6.06E-3$). Therefore, for these materials, natural convection is not strong enough to have any impact on the temperature distribution. Generally speaking, in materials with low Prandtl number, the effects of convection heat transfer on temperature distribution and on the thermally-driven buoyant convection are very weak, and therefore, negligible [99]. As can be seen in Figure 4.3-a, which is in the vertical cross section plane passing through the center of the model. Temperature variations, based on the applied non-linear temperature profile as shown in Figure 4.4, are from as low as $1058.6\text{ }^{\circ}\text{C}$ shown in “g” to “h” zone with $1077.9\text{ }^{\circ}\text{C}$ and as high as $1100\text{ }^{\circ}\text{C}$ shown in “i” in the solvent region. This temperature profile reveals that there is a steep gradient at the first three centimeter on the vertical axis of the model. Also this temperature profile generates a thermal Grashof number (Gr_T) of the order of approximately 150k which is a typical value for the vertical Bridgman setting and reveals a natural convection in the system as well [61].

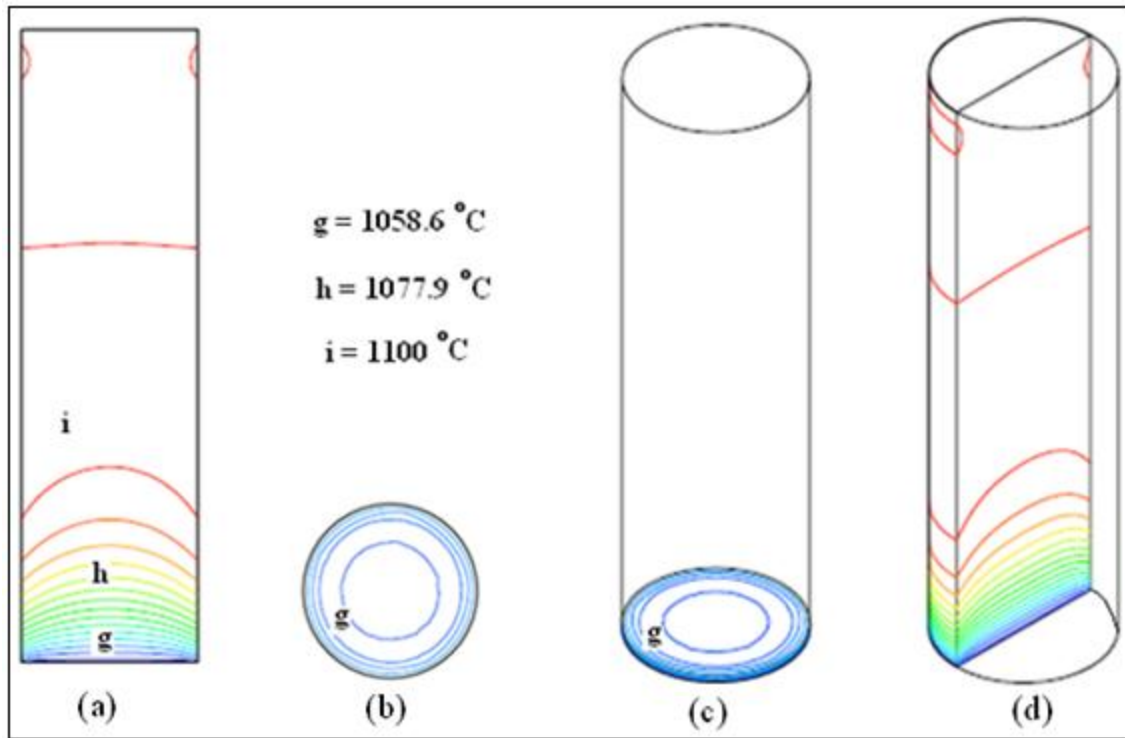


Figure 4.3 Temperature distributions in solvent region under terrestrial condition

- a- Vertical cross section passing through the centre of the model
- b- Horizontal cross section at 1 mm above growth interface
- c- 3-D view of horizontal cross section
- d- 3-D view of the vertical cross section

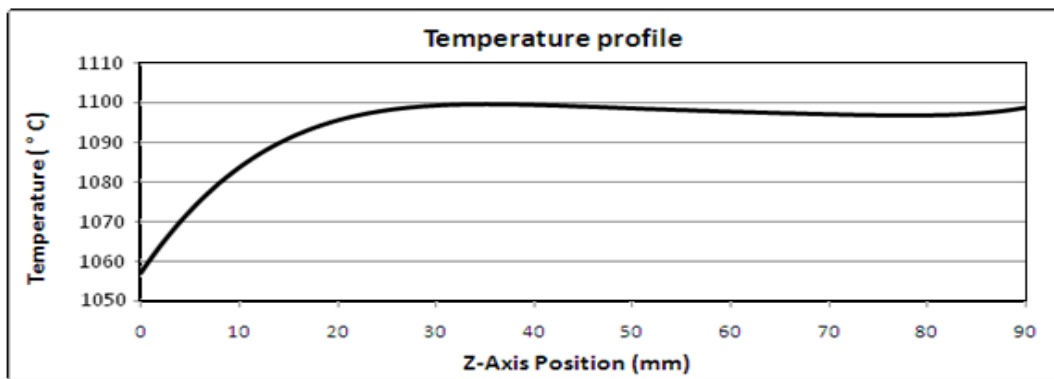


Figure 4.4 Non-linear temperature profile under terrestrial condition

As mentioned earlier on this model is a mimic of the experimental setting in which the silicon concentration at growth interface was measured to be 62.3%. Figure 4.5 shows the silicon distribution in the solvent region. It can be observed from Fig. 4.5-a that the silicon distribution contours are not uniformly parallel to the growth interface and show a concave in the middle of the model from just above the interface where it is marked with “l” to upper middle part of the model marked with “k”. This is as a direct influence of the flow pattern in the solvent region under the flow velocity.

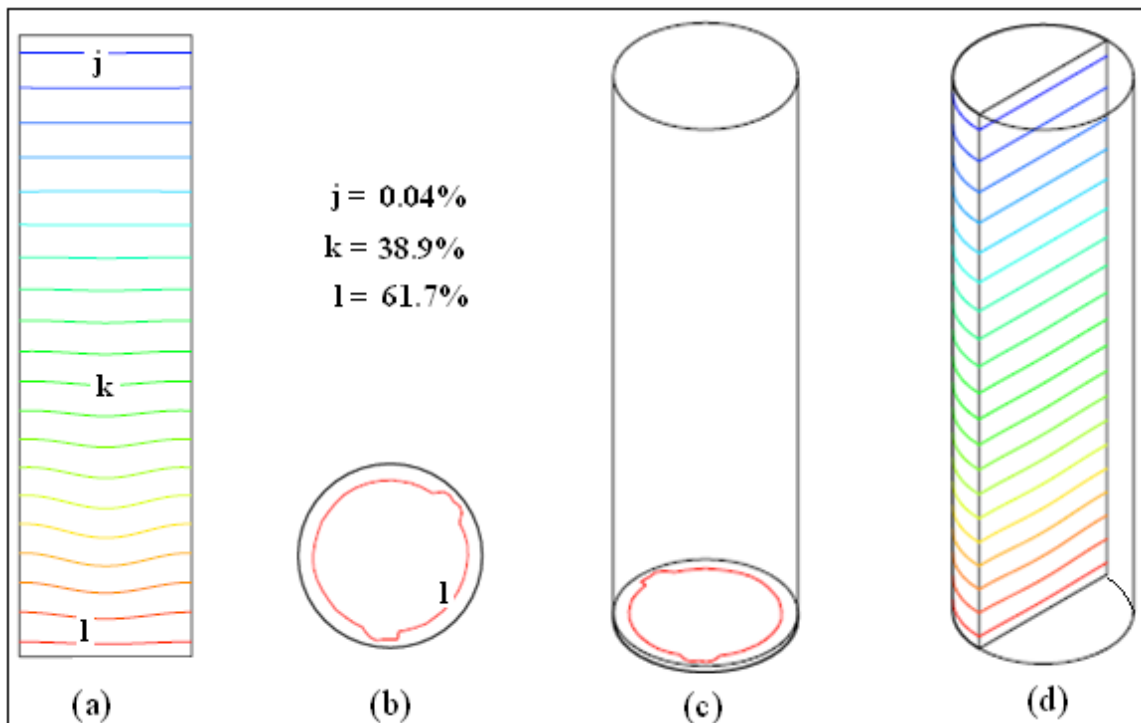


Figure 4.5 Silicon distributions in solvent region under Terrestrial condition

- a- Vertical cross section passing through the centre of the model
- b- Horizontal cross section at 1 mm above growth interface
- c- 3-D view of horizontal cross section
- d- 3-D view of the vertical cross section

Figure 4.6 shows the silicon distribution along the vertical axis of the model. This is shown to purely have a comparison with the results obtained experimentally, which are also being

shown Figure 4.8 in the next section, and those obtained by FEA. The results are in a good agreement with each other since the difference is 0.0003% this is shown by “R” squared value. This difference can be due to the reading off the sample in the experiment. Figure 4.7 depicts the results on silicon distribution in FEA. Figure 4.7-a, shows the silicon composition across the diameter of the model (radially) on three different positions on the vertical axis of the model. Figure 4.7-b presents the silicon distribution along the vertical plane passing through the center of the model. It is clear that there are also good agreements between the simulation results shown in Figure 4.7 and that of shown in Figure 4.8 and Figure 4.9 which were shown in the experiment.

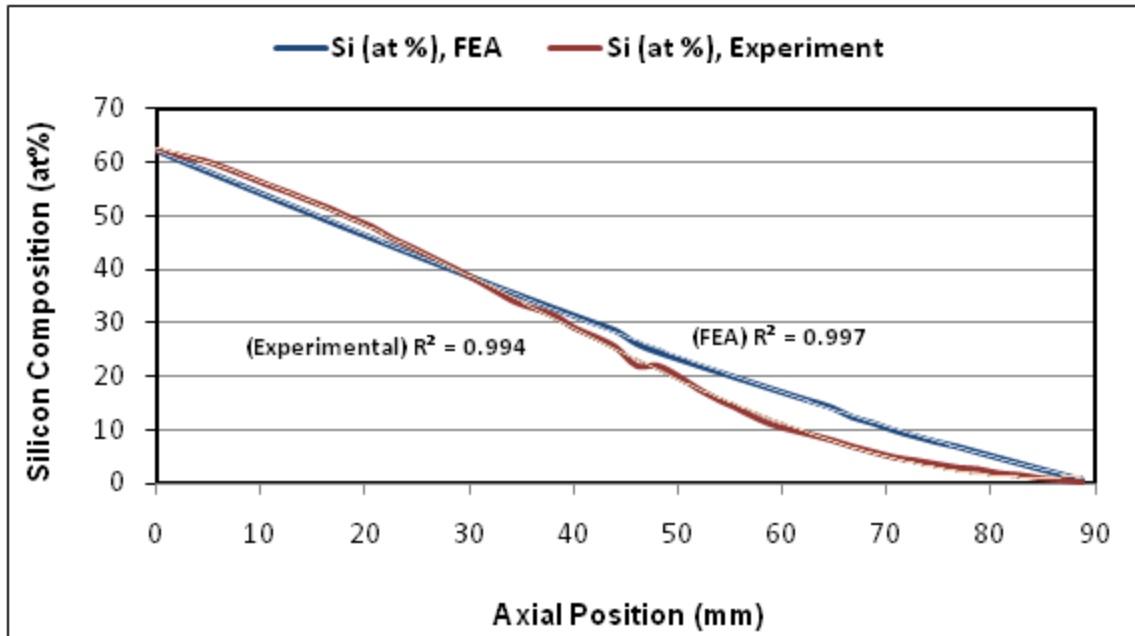


Figure 4.6 Silicon distributions along the vertical axis of the model, a comparison between simulation by FEA and experiment, terrestrial condition.

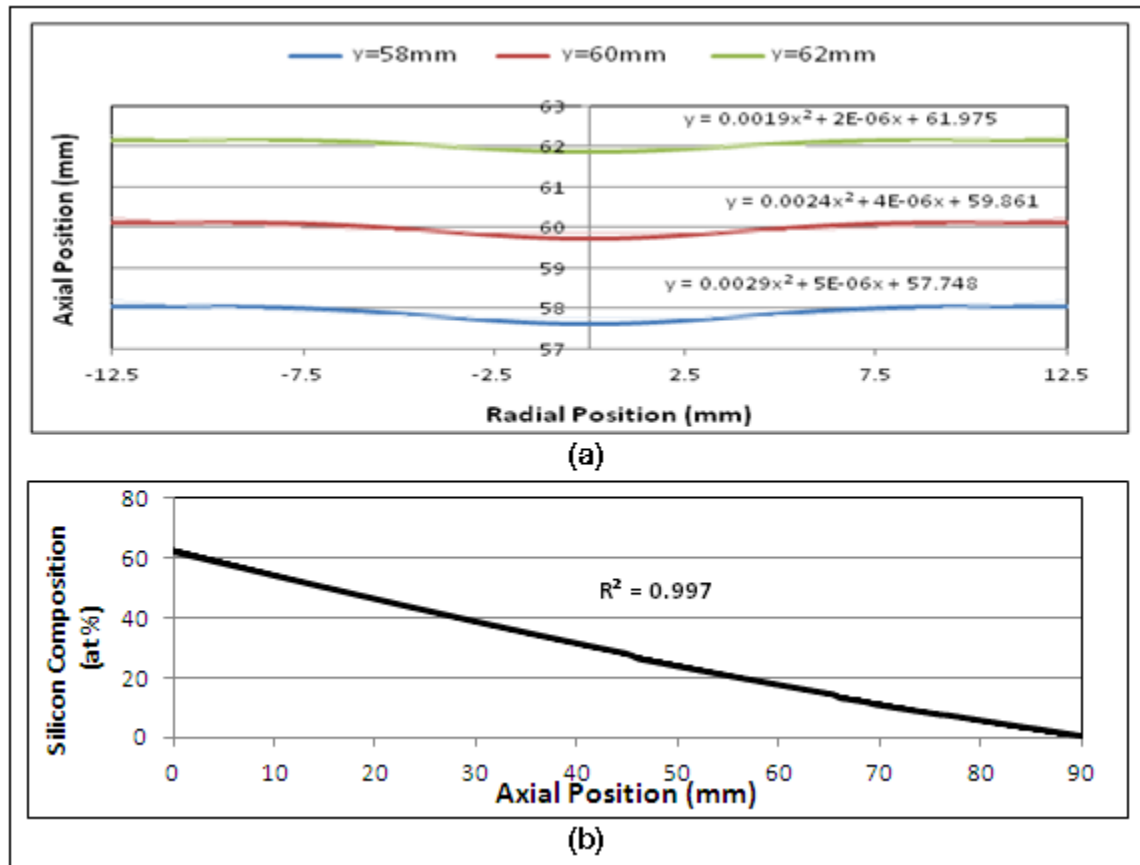


Figure 4.7 Radial and axial silicon compositions, under terrestrial condition
 (a) Radial silicon concentration at three different level on the vertical axis
 (b) Axial Silicon concentration along the vertical axis of the model

4.2 Experimental results under Non-Linear Temperature Profile

These results obtained through the experiments done at Dalhousie University (D.U.), the model was set under the non-linear temperature profile and ran for 15 days to complete the solidification process for the entire 90 millimeter length of the model. Figure 4.8 represents the compositional distribution of silicon at the center of the model along with the vertical axis of the model passing through the center.

Figure 4.9 represents the silicon distribution in both horizontal (radial) and vertical (axial) directions at interfaces in different axial position of the model. It is obvious that the pattern resembles a parabolic curve. These distributions define the concavity of the interface shape in the solidification process.

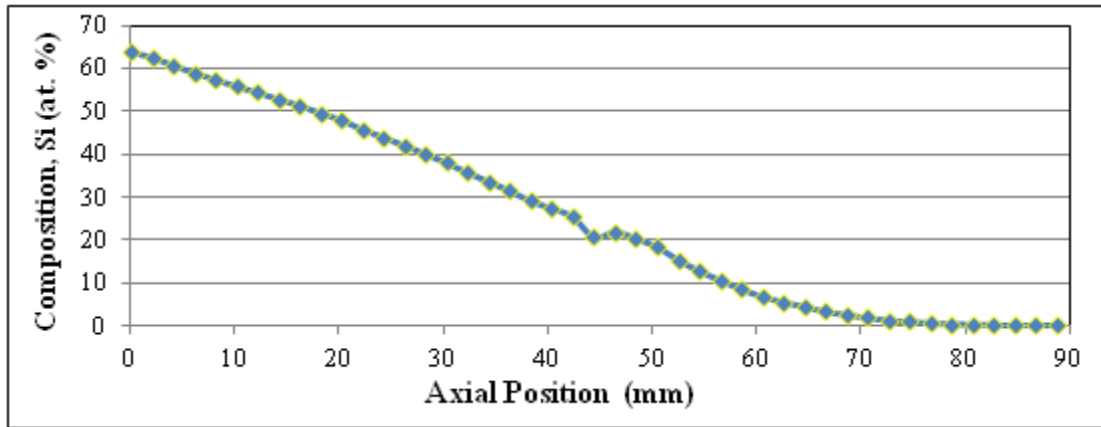


Figure 4.8 Axial silicon compositions, experimental data by Professor Labrie at D.U.

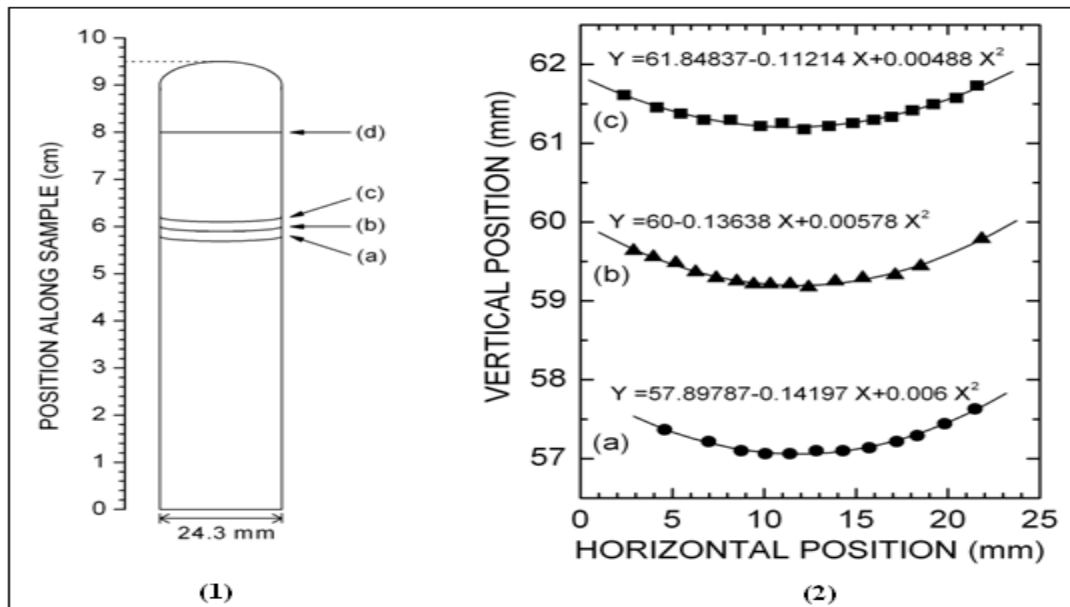


Figure 4.9 Silicon distributions at different axial level, experimental data
 (1) Schematic view of the solvent region in vertical plane
 (2) Closer view of the silicon distribution at three different levels

4.3 Three Dimensional Model under Non-linear Temperature Profile in Microgravity Condition, by simulation in (FEA)

Microgravity is referred to the condition where the gravity force is extremely minimized; and the model is practically under no external forces so the flow phenomenon within the solution region can be observed differently. Figure 4.10 shows the flow behavior, the flow velocity is in the range of the nanometer per second and as it can be seen in Figure 4.10-b the velocity contours near the interface (1 mm above the growth interface) are uniform. Again this low speed causes no impact on the temperature distribution within the solvent.

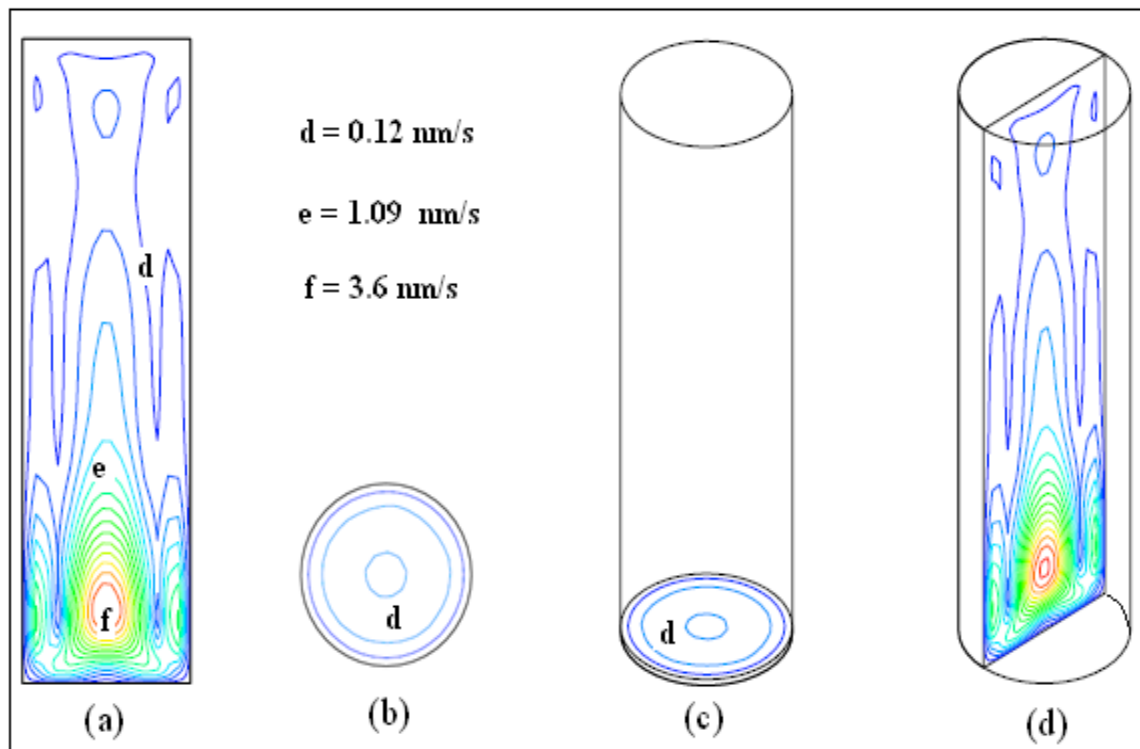


Figure 4.10 Flow velocities in solvent region in microgravity condition

- a- Vertical cross section passing through the centre of the model
- b- Horizontal cross section at 1 mm above growth interface
- c- 3-D view of horizontal cross section
- d- 3-D view of the vertical cross section

It can be seen in Figure 4.10-a that there is a stronger flow, although in the nanometer range, cell in the middle of the region near the interface along with two weaker cells near the wall of the model. This is nothing but the effect of a residual gravity force pushing the flow downward. Figure 4.11 represents line plot of the flow velocity along the vertical plane passing through the center of the solvent region.

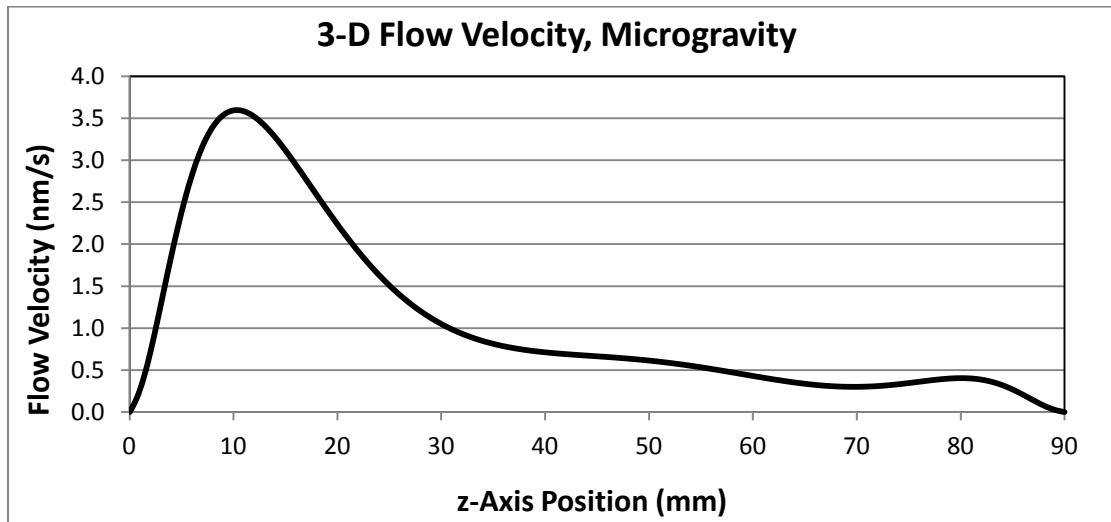


Figure 4.11 Flow velocities along vertical axis in microgravity condition

Figure 4.12 shows the temperature distribution in the solvent region, again the temperature has been distributed the same way as seen in the terrestrial condition and clearly can be seen that the flow has not disrupted the temperature contours. The symmetrical patterns evolved in the solvent region for flow, temperature and silicon concentration respectively. It should be noted that this happens as a direct result of the uniform heating which is also reported by other researchers such as that reported in [100]. This effect was also seen in the terrestrial condition.

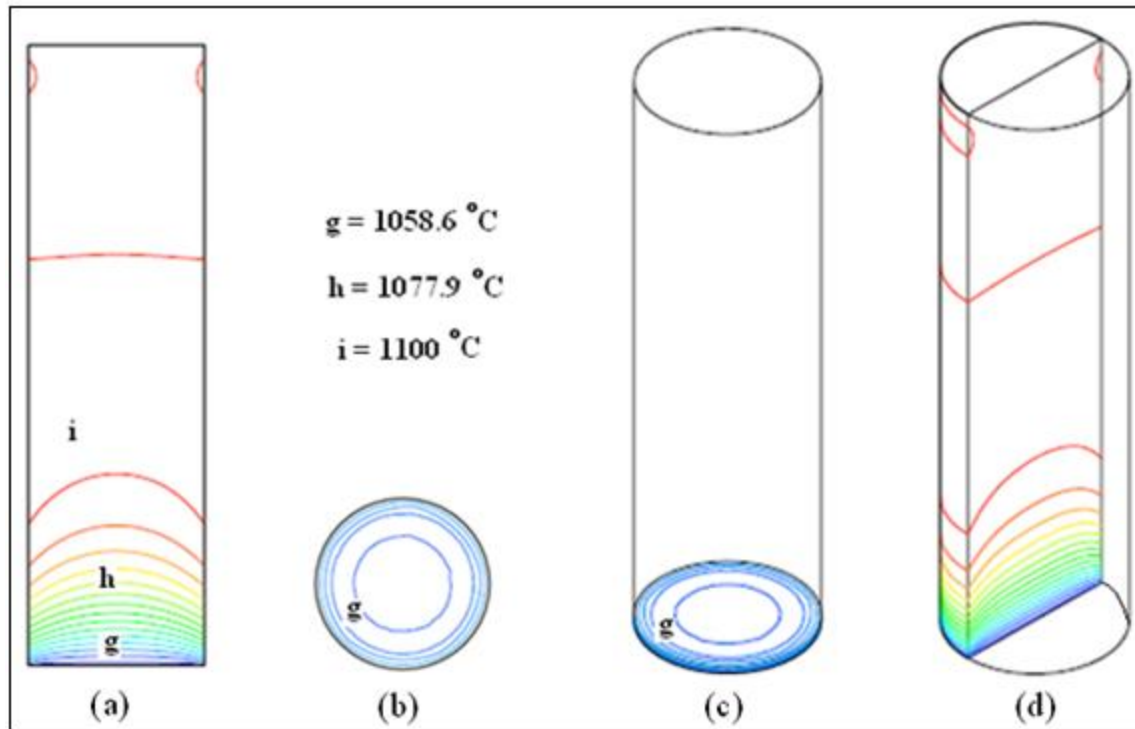


Figure 4.12 Temperature distributions in solvent region under microgravity condition
a- Vertical cut passing through the centre of the model
b- Horizontal cut 1 mm above growth interface
c- 3-D view of horizontal cross section
d- 3-D view of the vertical cross section

Figure 4.13 displays silicon concentration contours in microgravity condition. It is clear that the uniform and perfect flat concentration contours are formed which is an indication of the absence of buoyancy convection. Figure 4.13-b depicts no variation of concentration at the horizontal plane cut 1 millimeter above the growth interface. With this condition, the perfect parallel concentration contour lines reveals that the convective motion has diminished and the growth is convection free and the diffusion has the dominant effect in the process.

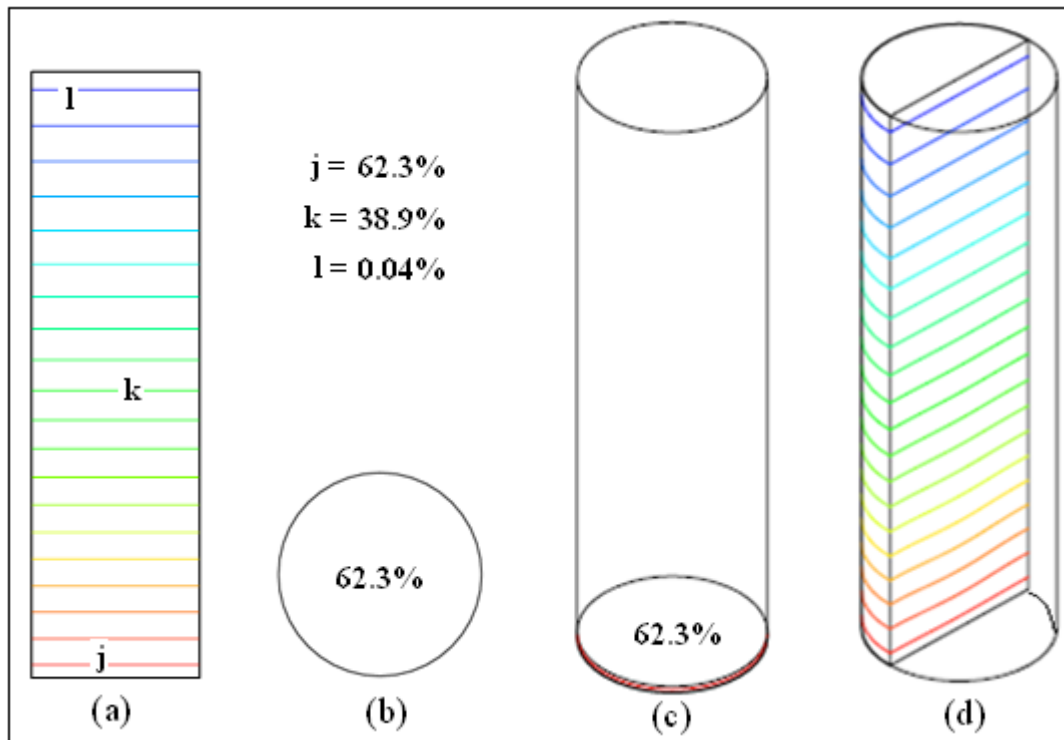


Figure 4.13 Silicon distributions in solvent region in microgravity condition

- a- Vertical cross section passing through the centre of the model
- b- Horizontal cross section at 1 mm above growth interface
- c- 3-D view of horizontal cross section
- d- 3-D view of the vertical cross section

4.4 Two Dimensional Axisymmetric Model under Non-Linear Temperature Profile in Microgravity Condition, by simulation in (FEA)

Since the model is a cylindrical model, an axi-symmetrical model has been utilized to investigate the solidification processes. This step was taken to account for the sole purpose of comparison with that of made through Finite Volume Analysis. In this setting, the results were presented by Shemirani et al. at IAC-09 conference [101].

Figure 4-14 shows flow velocities, temperature distribution, and the silicon composition in the solvent region of the model. These results not only are in good agreement with those of the three dimensional model but also are backed by those of the finite volume control model which are to be presented in the next section.

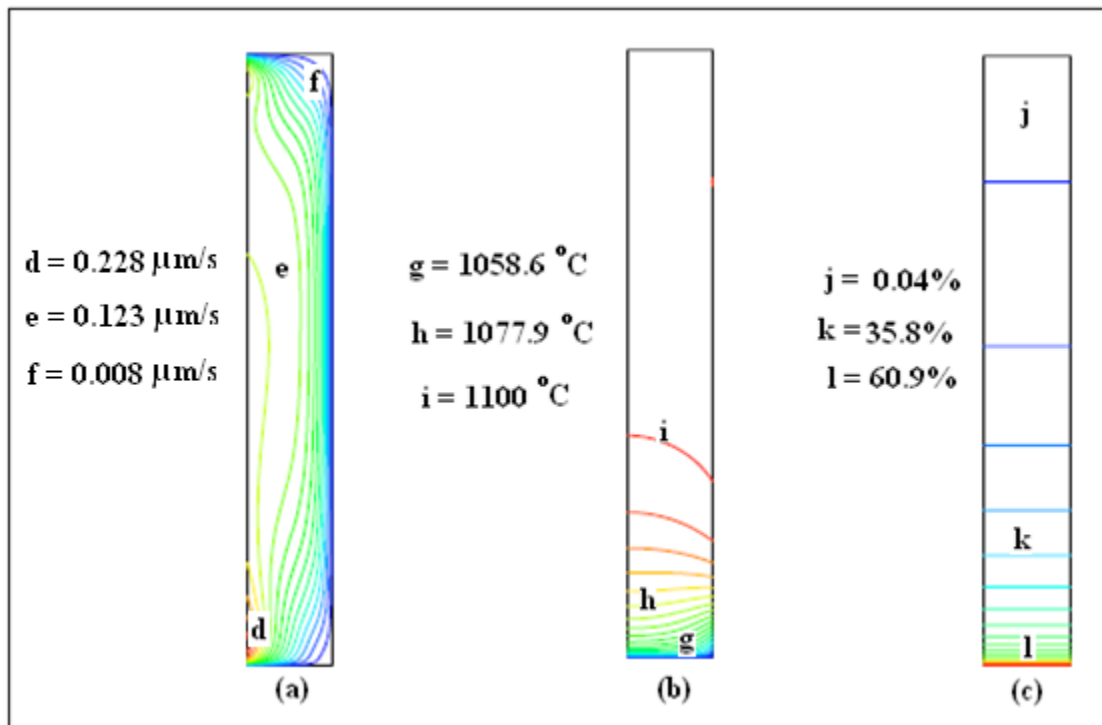


Figure 4.14 Results of the axi-symmetric model in microgravity condition
a- Flow velocities in vertical plane through the centre of the model
b- Temperature distribution
c- Silicon composition

4.5 Two Dimensional Axisymmetric Model under Non-Linear Temperature Profile in Micro-gravity Condition, by simulation in (FVA)

The results obtained through simulation by finite volume control which is temperature distribution, silicon composition and flow condition of the model are presented in Figures 4.15 to 4.17. It is clear that these results support those obtained by Finite Element Analysis. The input files for this analysis can be found in Appendix “C”.

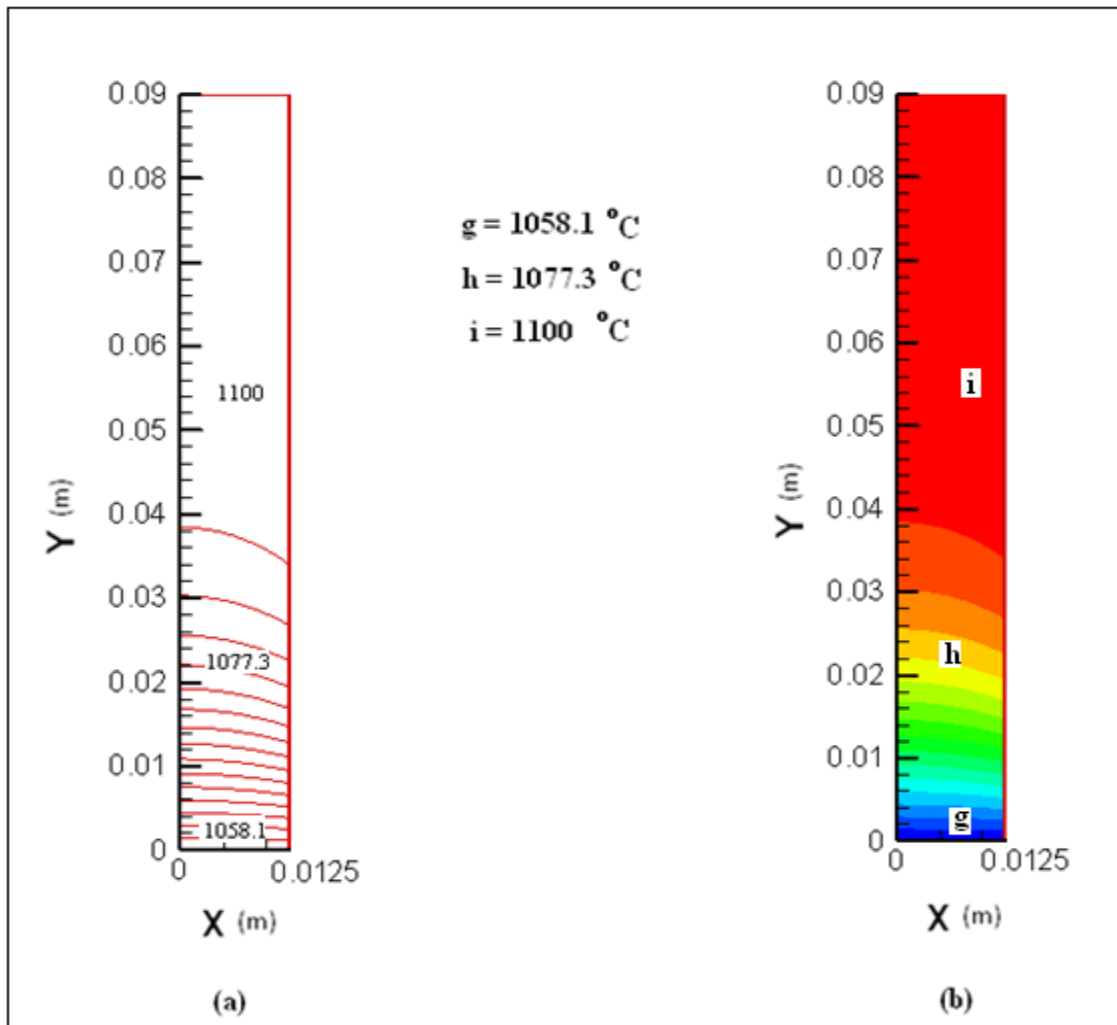


Figure 4.15 Temperature distribution, finite volume simulation, microgravity condition
(a) By contour lines
(b) By color variations

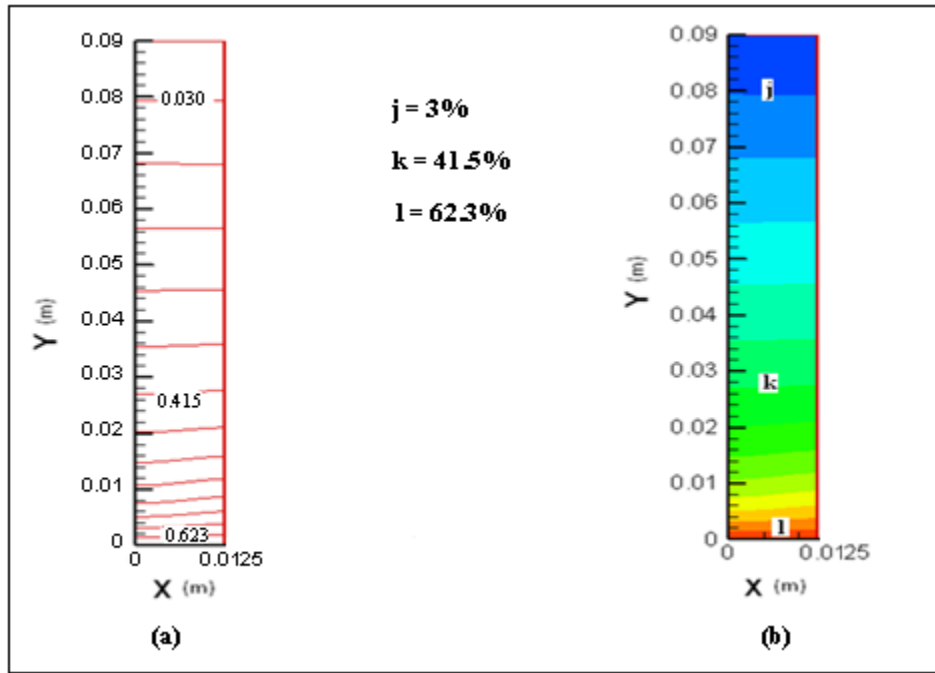


Figure 4.16 Silicon composition, finite volume, microgravity condition
a- By contour lines
b- By color variations

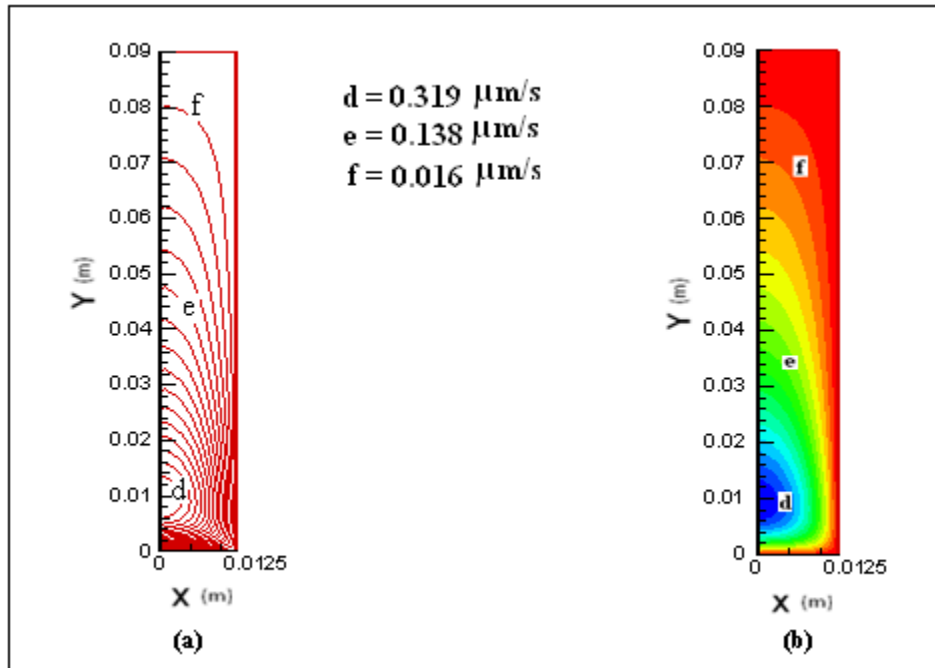


Figure 4.17 Flow velocity, finite volume, microgravity condition
a- By contour lines
b- By color variations

4.6 Two Dimensional Model under Non-Linear Temperature Profile in Terrestrial Condition, by simulation in (FEA)

Since it has been shown that results obtained through two dimensional axis-symmetric model are extremely close to those of three dimensional and those of achieved by finite control model, from this point on in this study, the focus would be on the two dimensional full model, this had tremendously saved time of computation. Figure 4.18 shows three vertical planes passing through the center of the model. Figure 4.18-a represents flow pattern in the solvent region, again the flow velocity varies from 0.1 millimeter per second to as high as 2.18 millimeter per second at the lower middle central flow cell along with two weaker flow cells near the wall. All are relatively close to the growth interface. Figure 14.18-b depicts the temperature distribution throughout the solvent region.

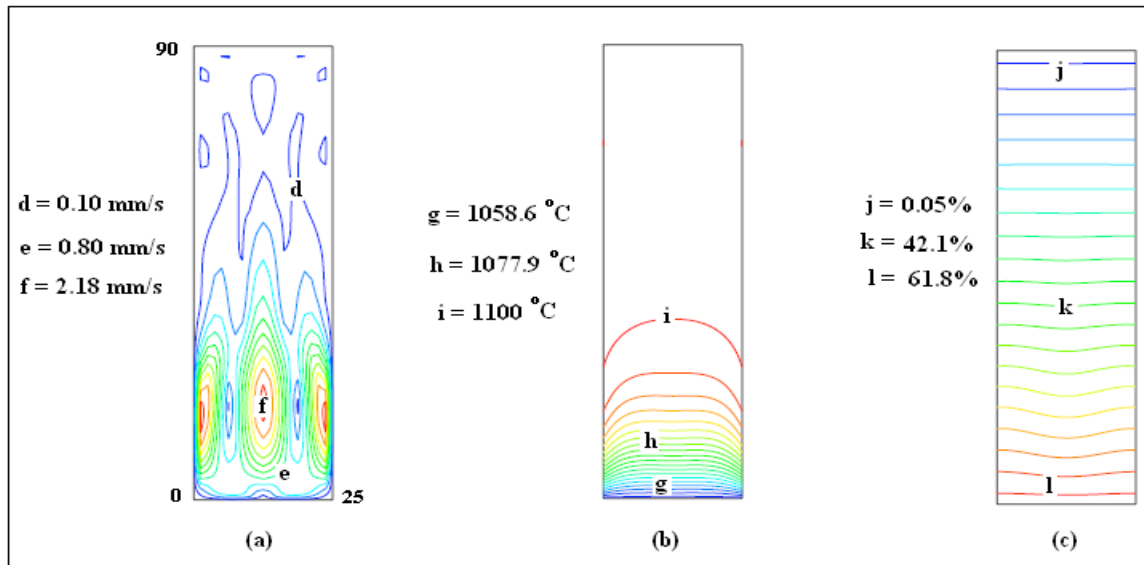


Figure 4.18 Full 2-D model, non-linear temperature profile and terrestrial condition

- a- Flow velocities in vertical plane passing through the centre of the model
- b- Temperature distribution
- c- Silicon composition

Again as it is seen, the contour lines are formed uniformly with a minor flatten part in the lower level, this is as a result of a minimal convection due to the buoyancy. Figure 4.18-c which displays the silicon concentration distribution also shows the concavity in the middle of the contours for the aforementioned reasons.

Figure 4.19 displays three line plots of; a) flow velocity, b) temperature distribution, and c) silicon composition along the vertical axis passing through the center of the solvent region. The maximum flow velocity happens at 19 mm above interface. Figure 4.19-b, reflects the applied non-linear temperature profile in the center line of the model. Figure 4.19-c, shows the silicon composition along the vertical axis of the model. This concentration distribution is extremely similar to that of obtained by the three dimensional model. Figure 4.20 represents the three line plots of; a) flow velocity, b) temperature distribution, and c) silicon composition at the horizontal plane cut through the model at 1 millimeter above the interface in the solvent region. It can be seen that the flow velocity corresponds to those flow cells that was shown in Figure 4.18. The speed variation in radial flow is approximately 0.5 mm/s, this clearly defines the instability of the solvent especially near the interface which is not desirable in solidification process. Figure 4.20-b reveals an approximately 1°C/cm temperature distribution radially. The silicon composition variation shows about 0.12% difference between center and near the wall of the model.

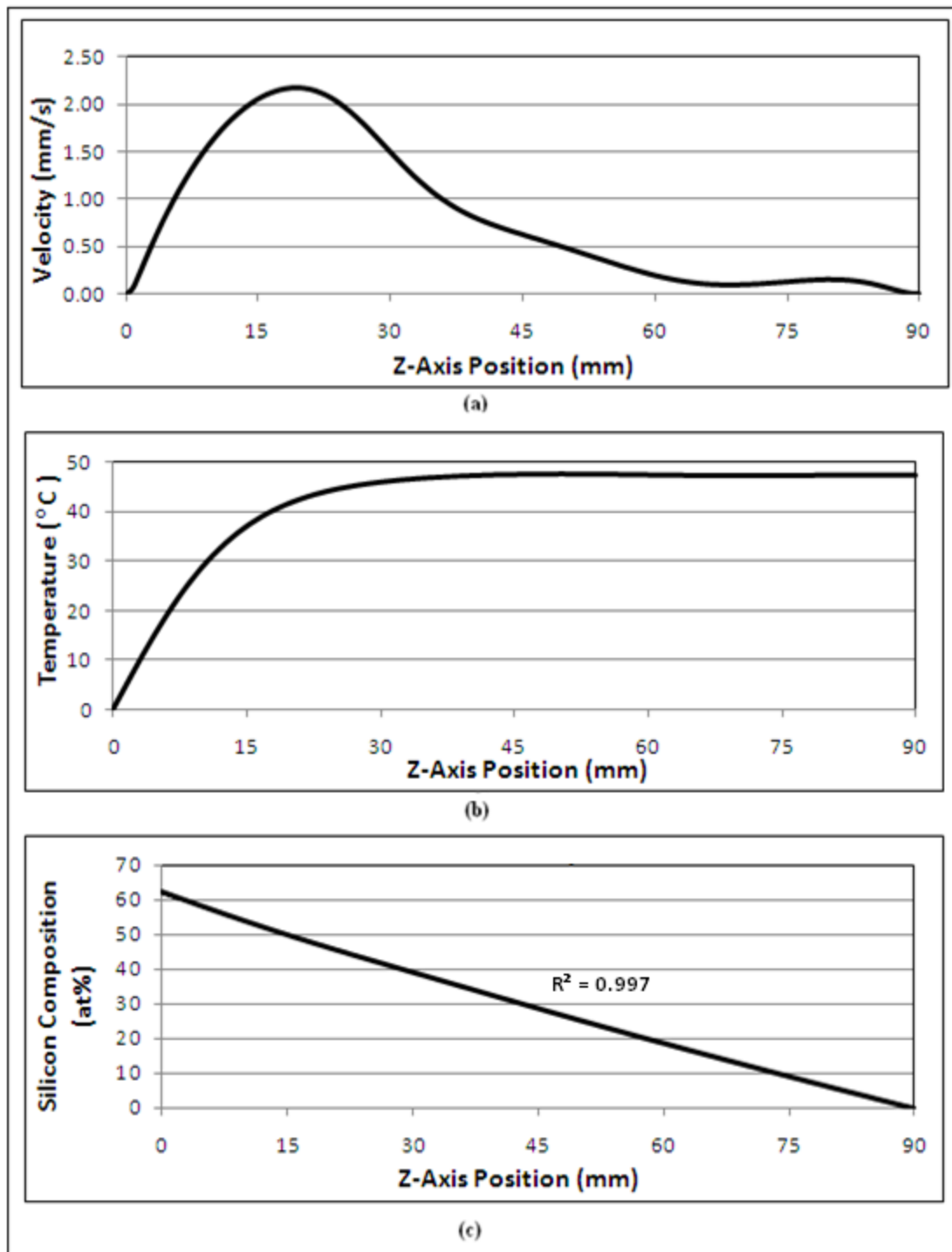


Figure 4.19 Line plots, with non-linear temperature profile terrestrial condition
a- Flow velocities in vertical plane passing through the centre of the model
b- Temperature distribution
c- Silicon composition

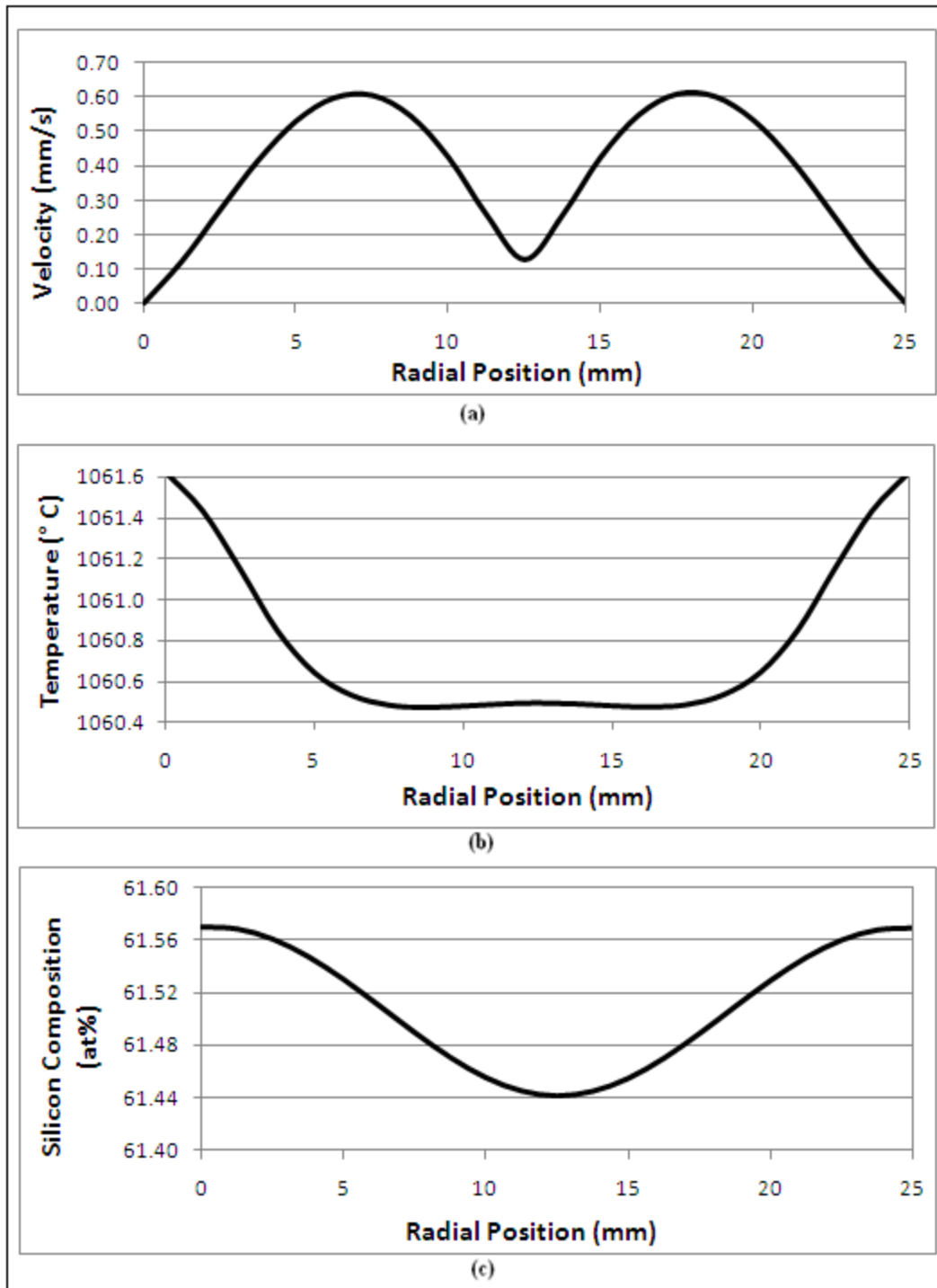


Figure 4.20 Radial line plots, non-linear temperature, terrestrial condition
a- Flow velocities in horizontal plane at 1 mm above interface
b- Temperature distribution
c- Silicon composition

4.7 Applied Axial Magnetic Field under Non-Linear Temperature Profile, (FEA)

The application of magnetic field as an external force on the solvent region has been widely practiced for producing single bulk crystals of the semiconductor alloys. It has been reported that the presence of the axial magnetic field smoothen the concentration profile [102]. Some have shown that the magnetic field had a significant influence on the flow structure and can also damp and or enhance the mixing process so it can be a tool for tuning the melt flow [103]. Other researchers have stated that there has been an improved stability as far as the dissolution interface when static magnetic field was utilized [104].

In this section, different static magnetic field intensities (from 1milli-Tesla to 1 Tesla, which is translated to the non-dimensional Hartmann numbers from 21.7 to 21700.93) are examined and the effects would be presented. The purpose is to see the effect of this external body force on the fluid flow since this body force supposedly works in the opposite direction to the buoyancy convection in the solvent region of the model. The goal is to find the acceptable level of applied axial static magnetic field for an alternative to the microgravity condition with vertical Bridgman technique. It should be noted that there have been many variation of intensities utilized in this study, but only these four distinguished levels are presented here. They are getting 20, 10, 5 times larger in each setting respectively. Figure 4.21 displays a comparison of flow velocities line plots along the vertical plane passing through the central axis of the model. It is noticeable that in spite of a slight difference in the maximum velocities, but generally speaking there is not a significant effect of applied static magnetic field.

Figure 4.22 displays the effect of the applied magnetic field on the flow velocity, temperature, and silicon concentration on the plane cut at 1 millimeter above the interface. It is clear that this intensity is not strong enough and the results are almost the same as those obtained without the magnetic field being applied. Figure 4.23 shows the result of the applied axial static magnetic field with 20 milli-Tesla intensity. The flow velocity, Figure 4.23-a, has been reduced only by less than 0.05 mm/s which is not significant. As for the temperature variation and silicon concentration, the results remain unchanged. As it is revealed in Figure 4.24, the results are not significantly different from those which obtained in previous cases, in spite of increase in magnetic force. Figure 4.25 displays the result of applied 1 Tesla axial static magnetic field and once again, it is not showing any significant changes with respect to those discussed in previous cases. The results of this section have been shown by Shemirani et al. in both CHMT-09 conference [105], and HEFAT-2011 conference [106].

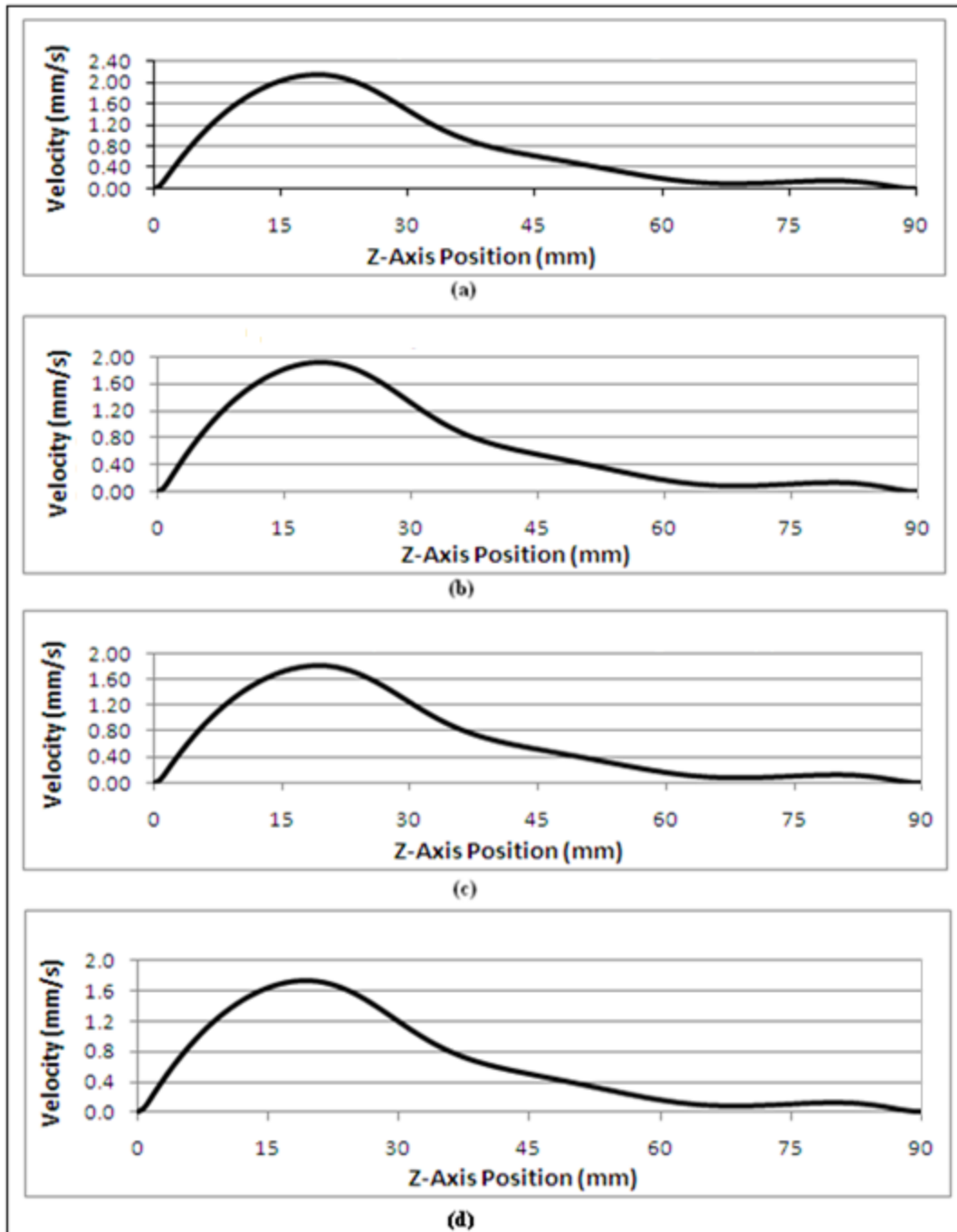


Figure 4.21 Flow velocities along vertical axis, under different magnetic intensities,
a- $B = 1\text{mTesla}$, or $Ha = 21.70$
b- $B = 20\text{mTesla}$, or $Ha = 434.02$
c- $B = 200\text{mTesla}$, or $Ha = 4340.19$
d- $B = 1\text{Tesla}$, or $Ha = 21700.93$

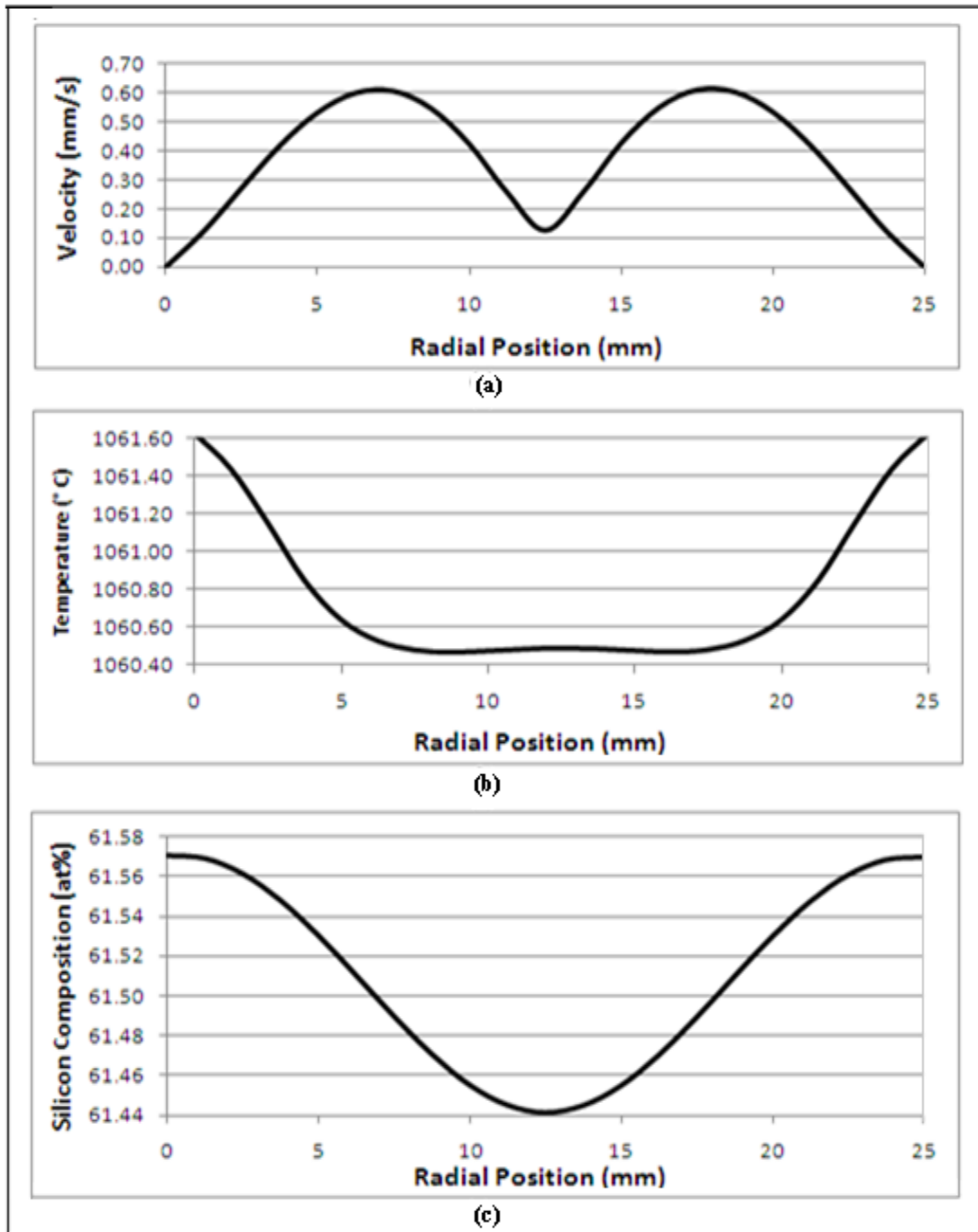


Figure 4.22 Radial line plots, under $B=1\text{mT}$ axial static magnetic field
a- Flow velocities in horizontal plane at 1 mm above interface
b- Temperature distribution
c- Silicon composition

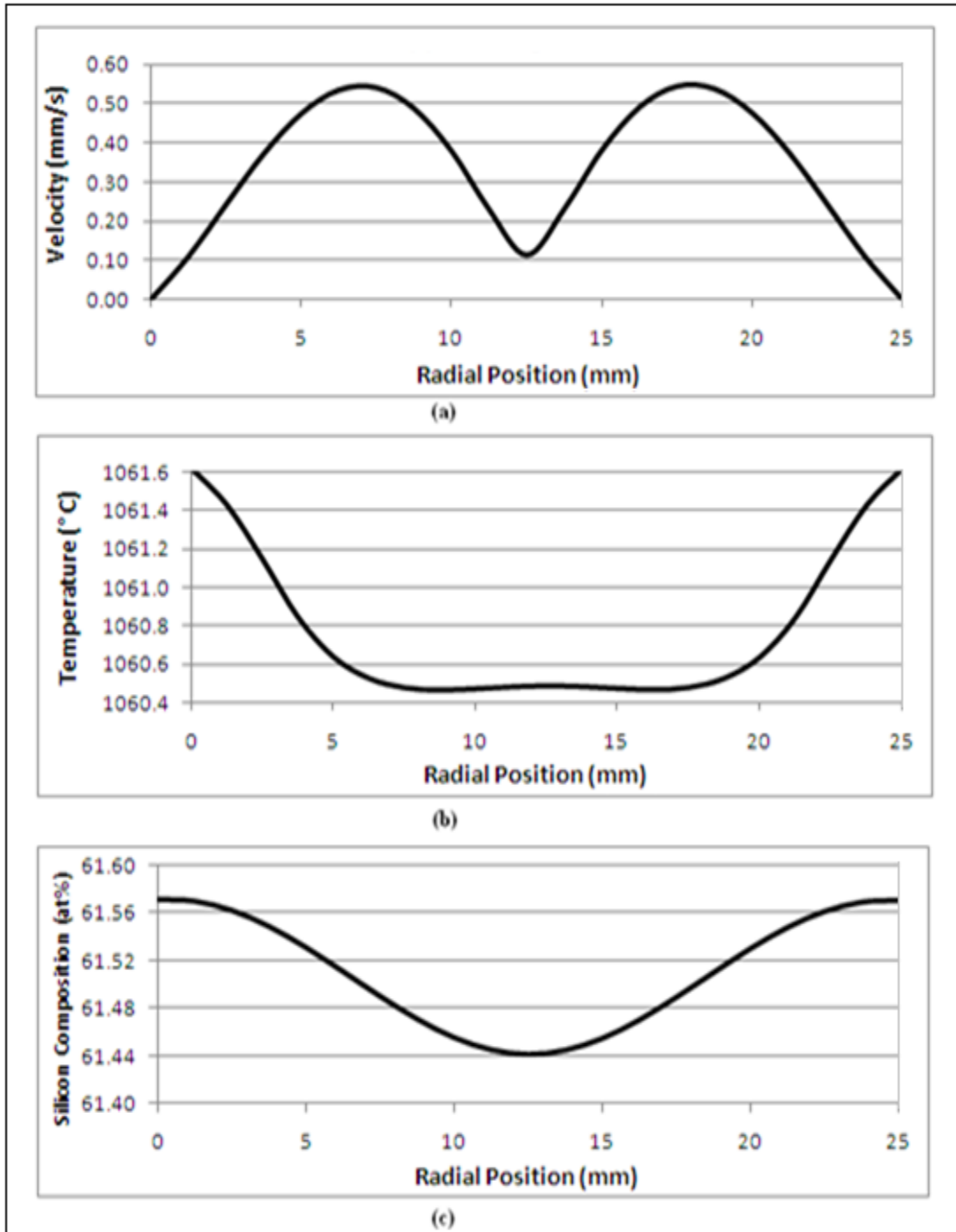


Figure 4.23 Radial line plots, under $B=20\text{mT}$ axial static magnetic field
a- Flow velocities in horizontal plane at 1 mm above interface
b- Temperature distribution
c- Silicon composition

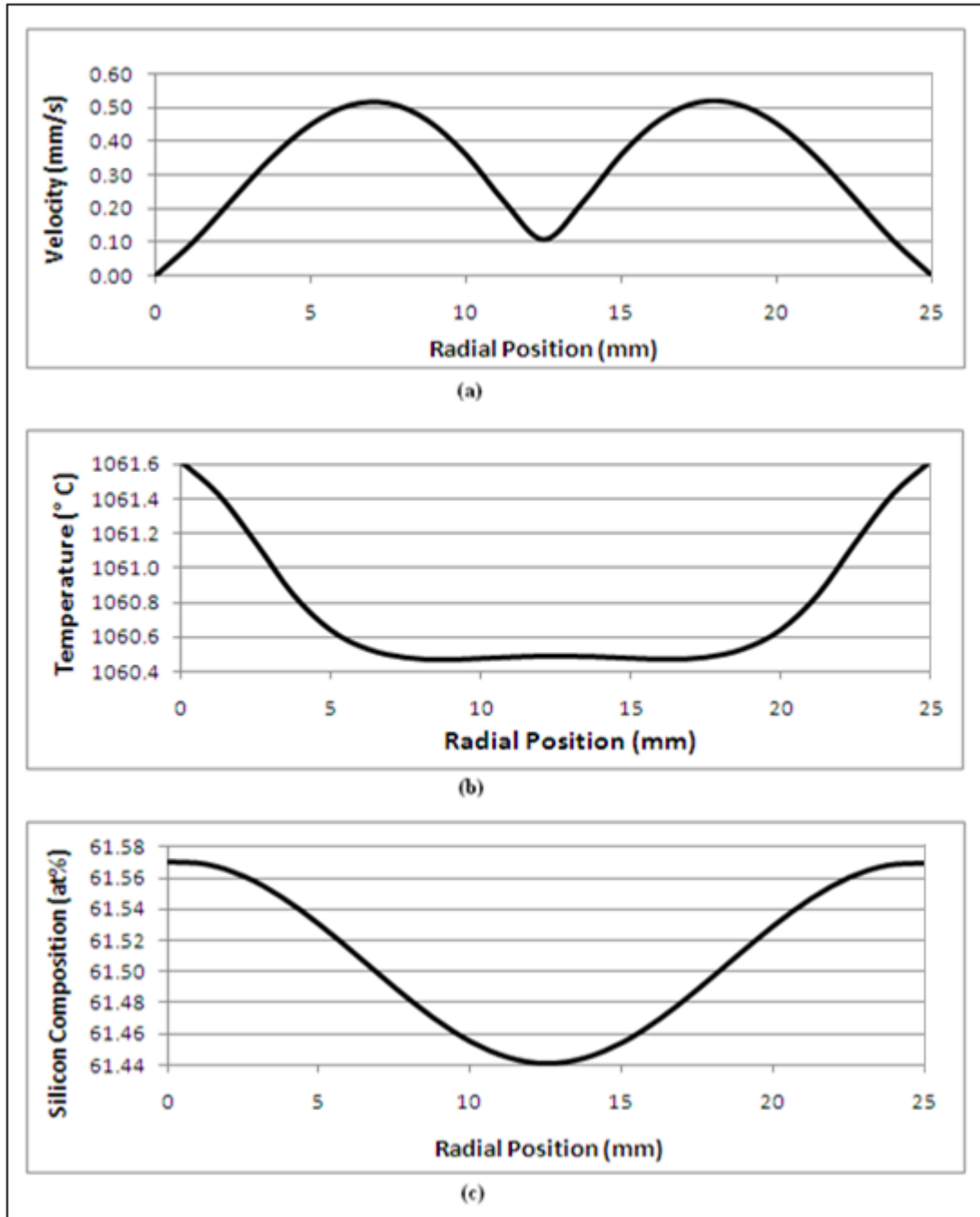


Figure 4.24 Radial line plots, under $B=200\text{mT}$ axial static magnetic field
a- Flow Velocities in horizontal plane at 1 mm above interface
b- Temperature distribution
c- Silicon composition

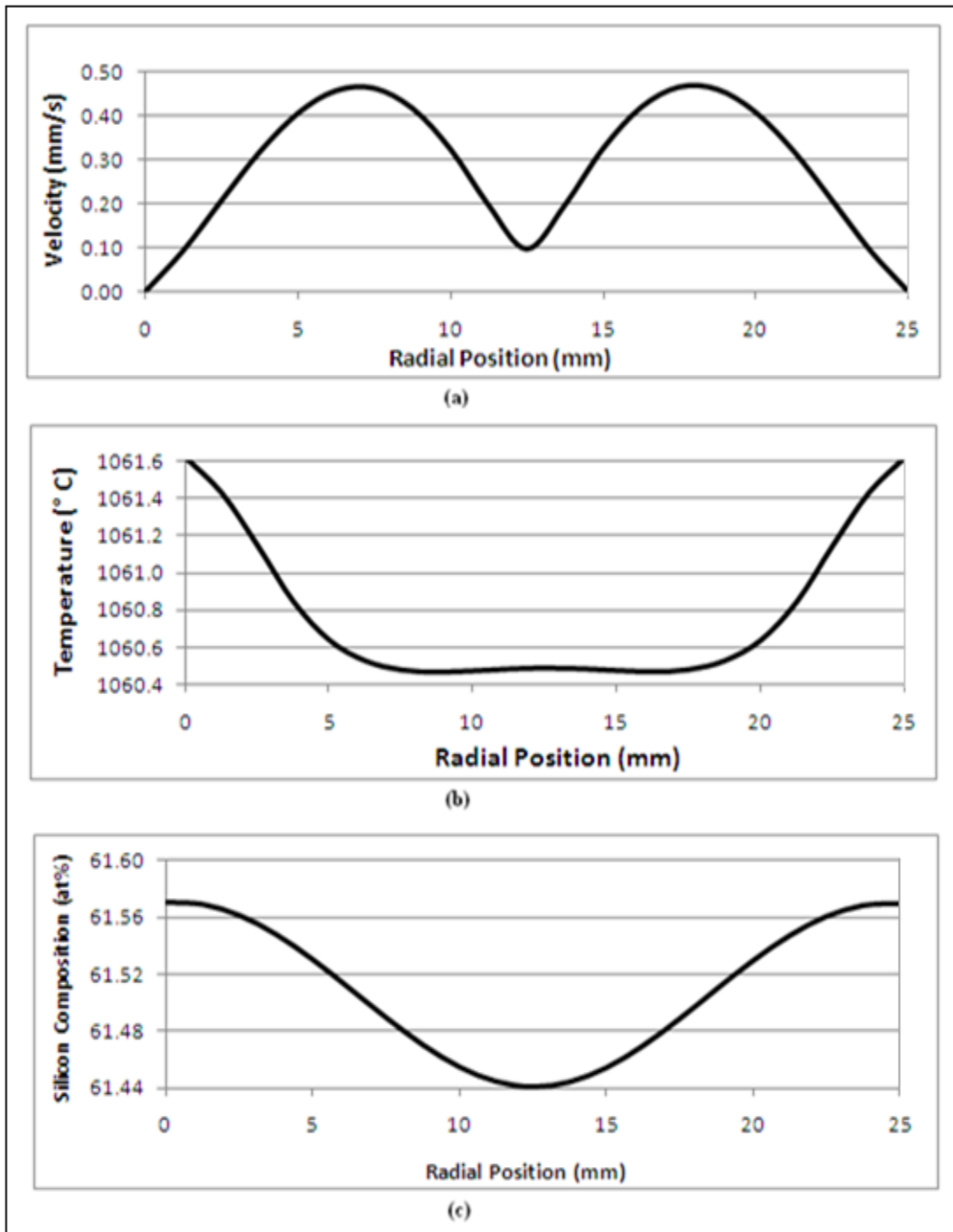


Figure 4.25 Radial line plots, under $B=1$ Tesla axial static magnetic field
a- Flow velocities in horizontal plane at 1 mm above interface
b- Temperature distribution
c- Silicon composition

4.8 Two Dimensional Model under Linear Temperature Profile in Terrestrial Condition, by simulation in (FEA)

After examining the role and effects of the non-linear temperature profile on the model, now the study would take on the application of a linear temperature profile. Knowing that in this study the crystal pulling rate is set to 0.25 mm/h which is well below the critical growth rate suggested by the Tiller criterion or Mullins-Sekerka [108] and [109] in which both criteria evaluate to approximately 10 mm/h for silicon concentration of 15 at% and temperature gradient of 50K/cm. With pulling rate and low temperature profile set in this study, it should be sufficient to avoid constitutional under cooling and to keep the growth stable in front of the interface. As it can be observed from Figure 4.26-a, under the linear temperature applied on the model the flow pattern is different from that of with non-linear, however the formation of a relatively strong flow cell in the middle and two weaker flow cell on the side of it, near the wall, is the same. It has only shifted upward. As for the intensity of it, in this setting, the flow speed is generally weaker. The flow velocity is nearly one tenth of that of the one obtained with non-linear temperature profile. In regards to the temperature distribution as it is shown in Figure 4.26-b, it is fairly uniform and has a minor deflection in the middle of the model due to the minimal convection generated by the flow. Silicon composition as seen in Figure 4.26-c is well uniform. These results are better seen in Figure 4.27 which displays the line plots of the region. Silicon composition line plot, although seems to show a linear pattern, but follows a parabolic curve; however it is a shallow curve, Figure 4.27-c shows the line equation as well.

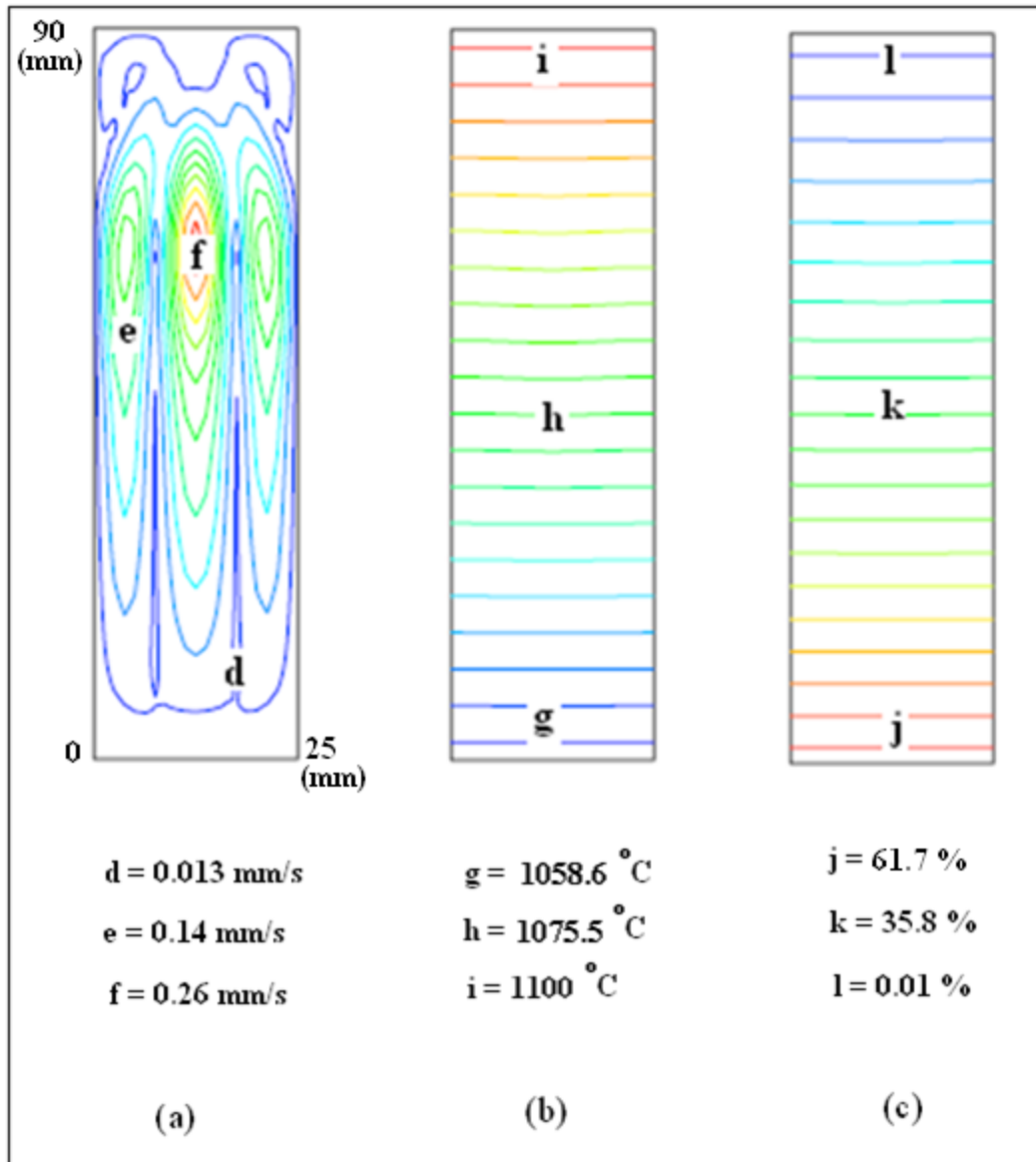


Figure 4.26 Full two dimensional model with linear temperature profile, under terrestrial condition

- a- Flow velocities in vertical plane passing through the centre of the model
- b- Temperature distribution
- c- Silicon composition

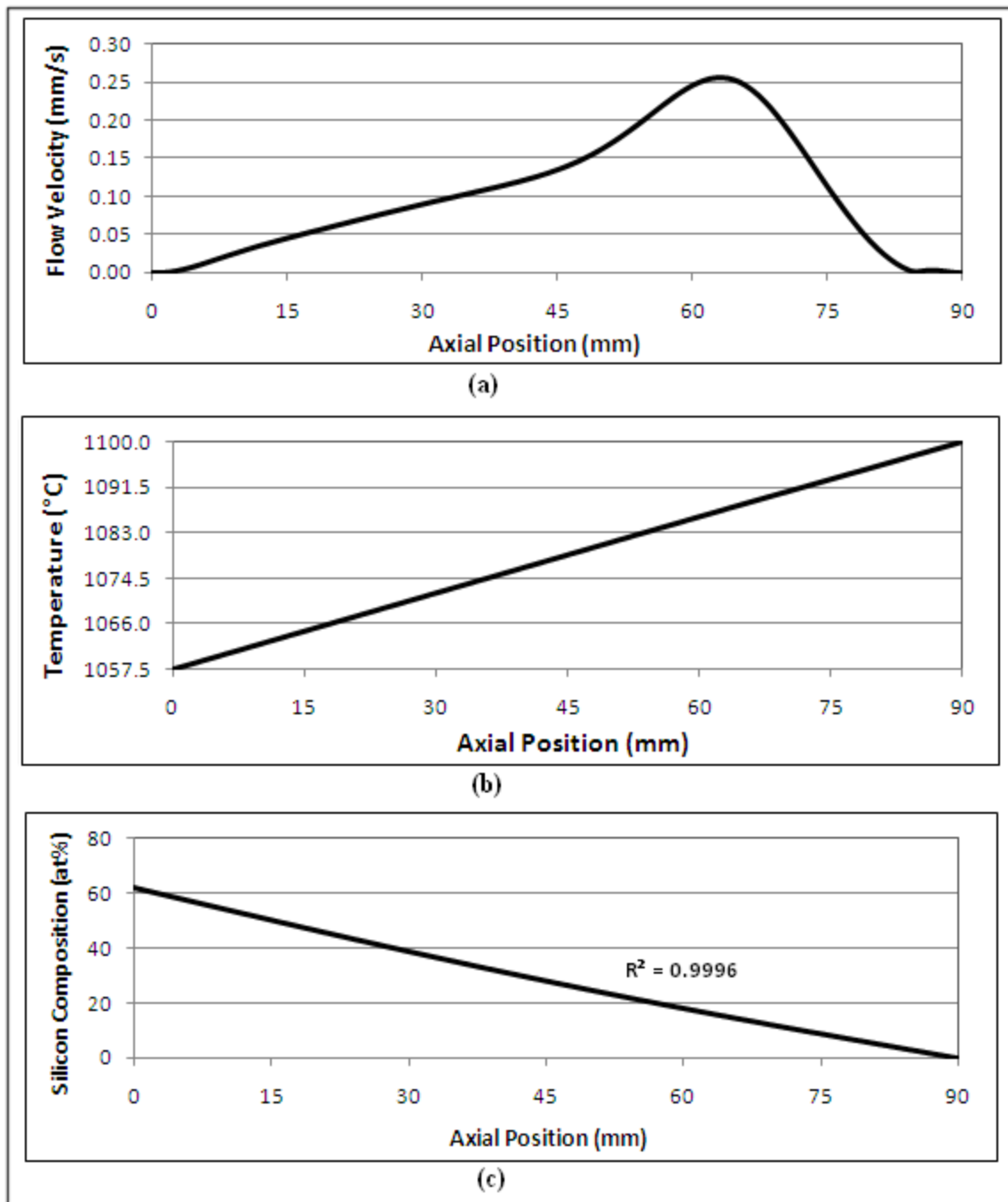


Figure 4.27 Line plots, with linear temperature profile, under terrestrial condition
a- Flow velocities in vertical plane passing through the centre of the model
b- Temperature distribution
c- Silicon composition

Figure 4.28, shows that the flow velocity is in micrometer range in radial direction and a temperature difference of about 0.001 degree along with less than 0.001% of silicon composition variation, which is a relatively stable condition for a homogeneous solidification.

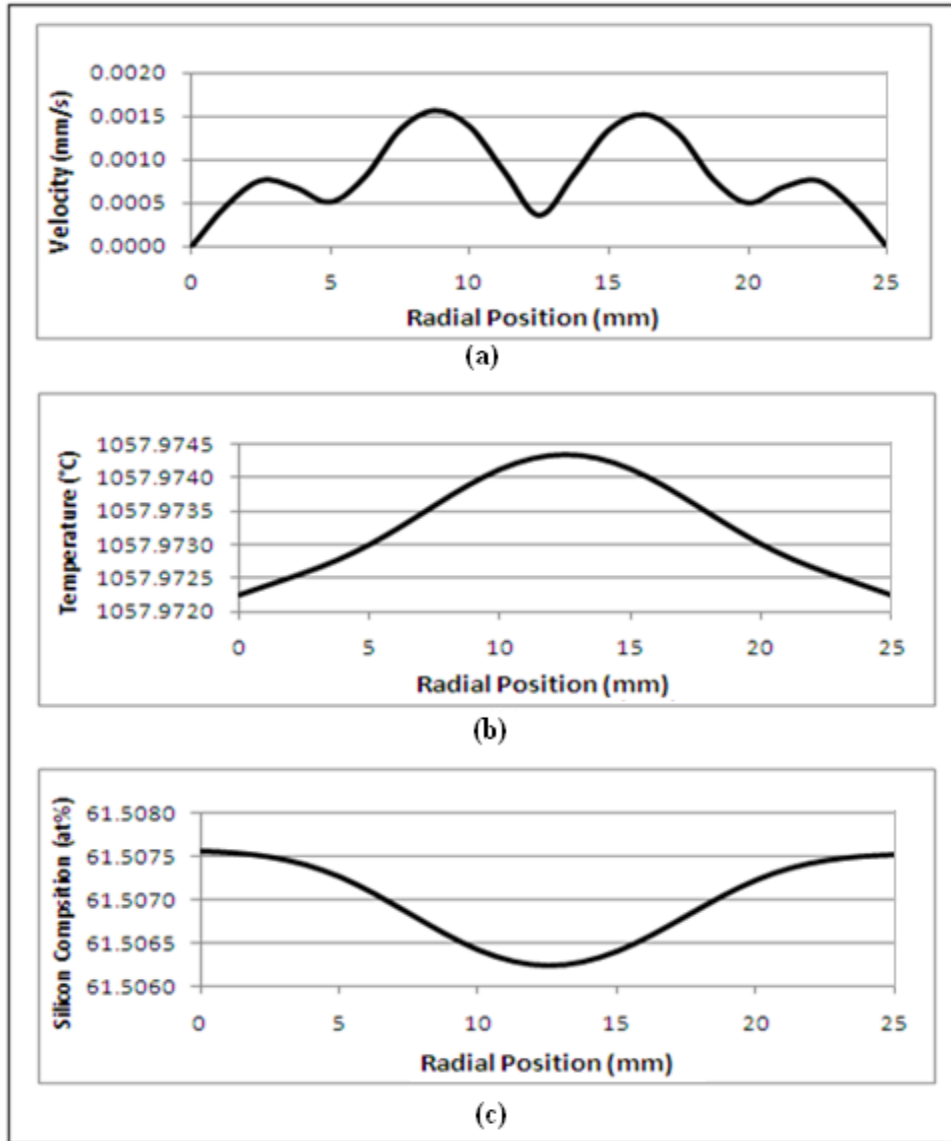


Figure 4.28 Radial line plots, linear temperature under terrestrial condition
a- Flow velocities in horizontal plane at 1 mm above interface
b- Temperature distribution
c- Silicon composition

4.9 Applied Axial Magnetic Field under Linear Temperature Profile in Terrestrial Condition, (FEA)

In this part of the study, the effect of axial static magnetic field with different intensities would be discussed. These intensities are the same as those applied in section 4.7 of this chapter. Figure 4.29 represents the flow velocities plot lines for all four magnetic field variations. It is evident that the flow velocities have been reduced only fractionally from 0.23 mm/s in case $B=1\text{mT}$ down to 0.186 mm/s in the case of $B=1\text{T}$. In fact the lower intensity (1mT) has a better effect on the flow distribution since the pattern follows a smoother curve along the axial plane in the solvent region.

In Figures 4.30 to 4.34 which show the radial plot lines of the flow velocity, temperature, and silicon composition respectively under the influence of the applied axial static field, there are not much of differences. It can be concluded that, in spite of wide range of application of axial static magnetic field in the process of some semiconductor crystal growth by other researchers who achieved some good results, in this study was not the case. This in general can be due to the size of the model (the diameter), since none of the research in literature review to the best of the author knowledge, had this diameter and combination of semiconductor alloys. Figure 4.30 displays the effect of magnetic field with intensity of 1 mT on the solvent region in radial direction on a plane cut through 1mm above the growth interface. Figure 4.31 shows the effect of magnetic field with intensity of 20 mT on the solvent region in radial direction on a plane cut through 1mm above the growth interface. Figure 4.32 reveals the effect of magnetic field with intensity of 200 mT on the solvent region in radial direction on a plane cut through 1mm above the growth interface. These results were shown by Shemirani et al. at ICTE-09 conference [110].

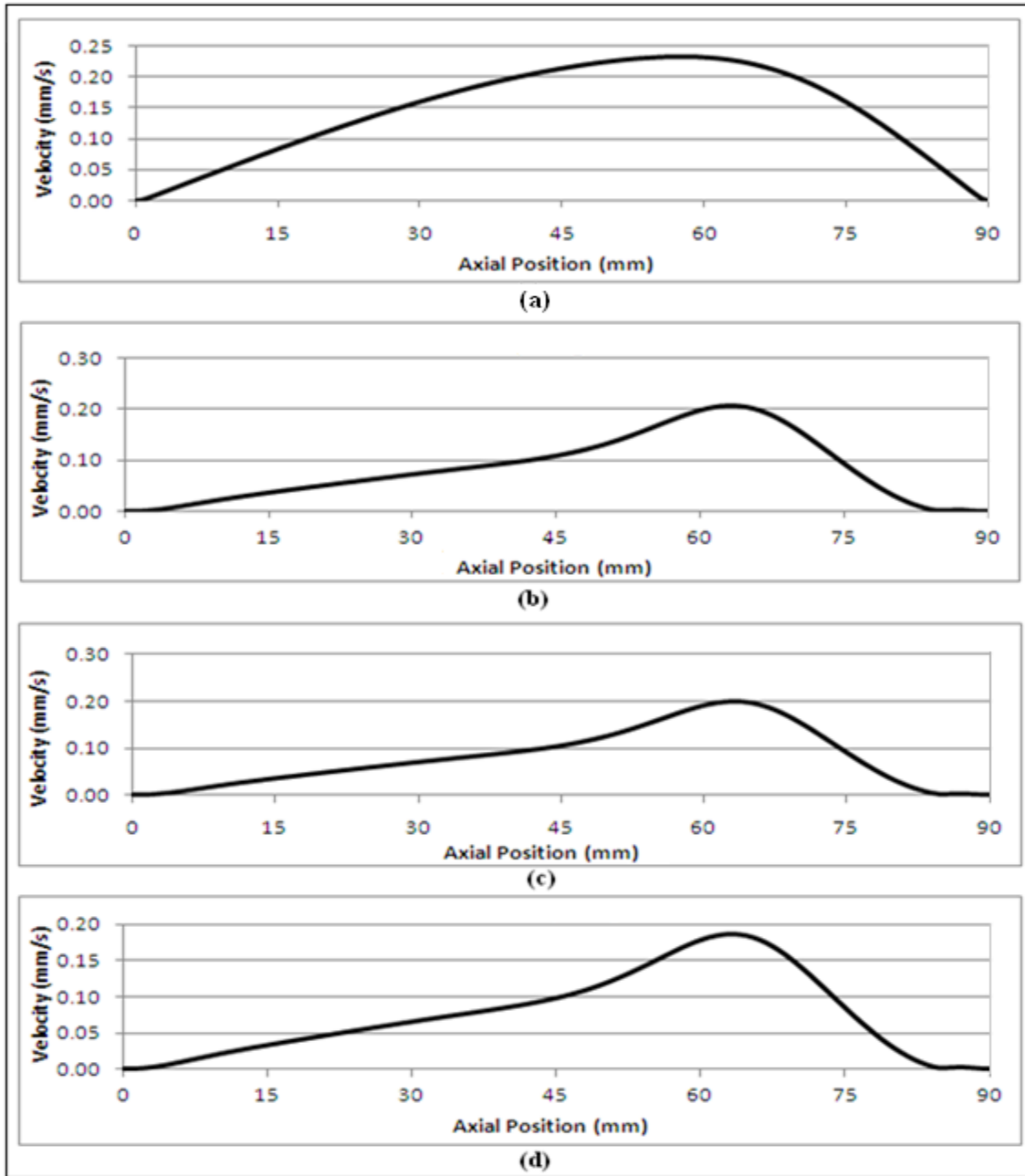


Figure 4.29 Flow velocities, under different magnetic intensities with linear temperature

- | | |
|---|---|
| a) $B = 1 \text{ mTesla}$, or $Ha = 21.70$ | b) $B = 20 \text{ mTesla}$, or $Ha = 434.02$ |
| c) $B = 200 \text{ mTesla}$, or $Ha = 4340.19$ | d) $B = 1 \text{ Tesla}$, or $Ha = 21700.93$ |

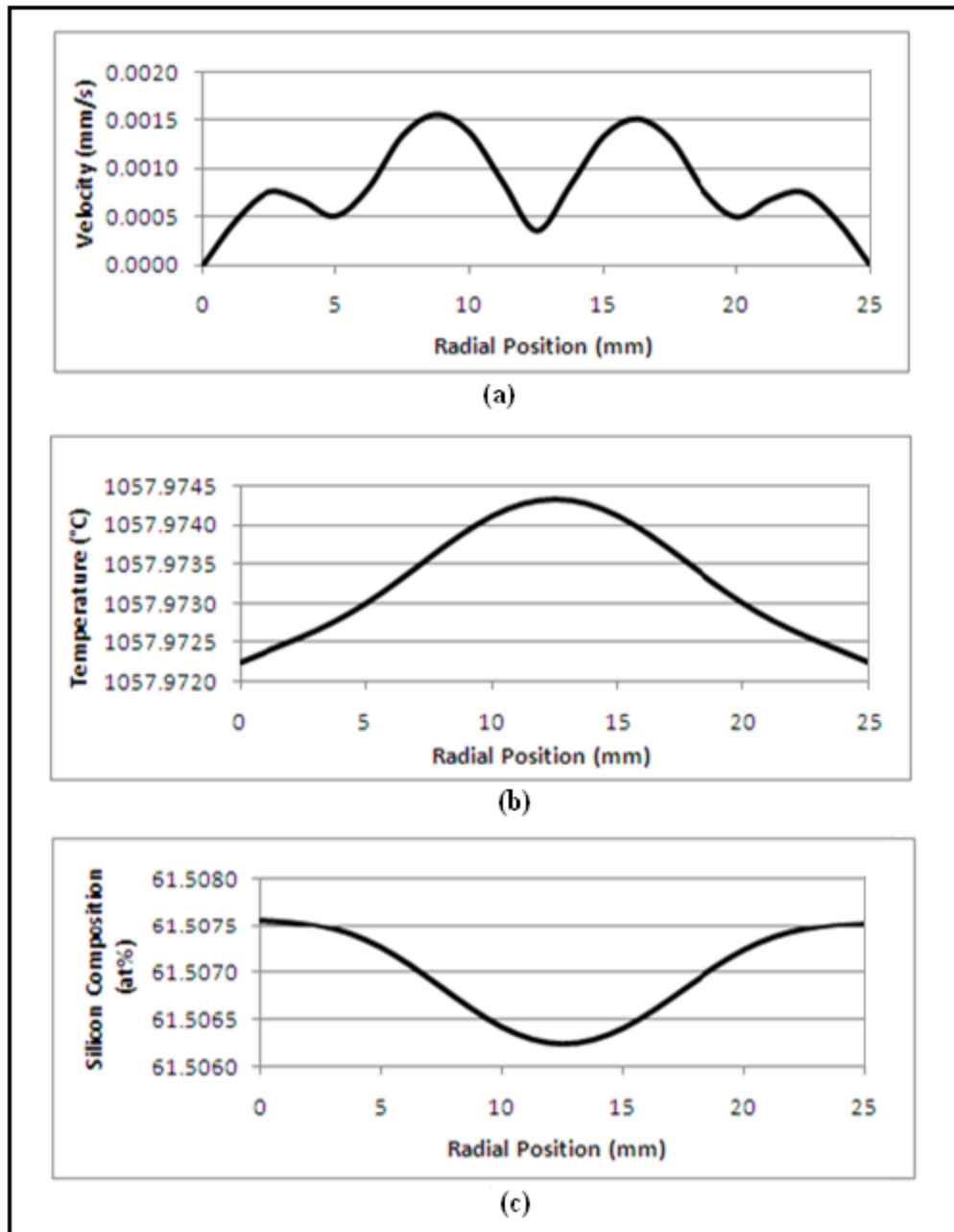


Figure 4.30 Radial line plots, under $B=1\text{mT}$ axial static magnetic field
a- Flow velocities in horizontal plane at 1 mm above interface
b- Temperature distribution
c- Silicon composition

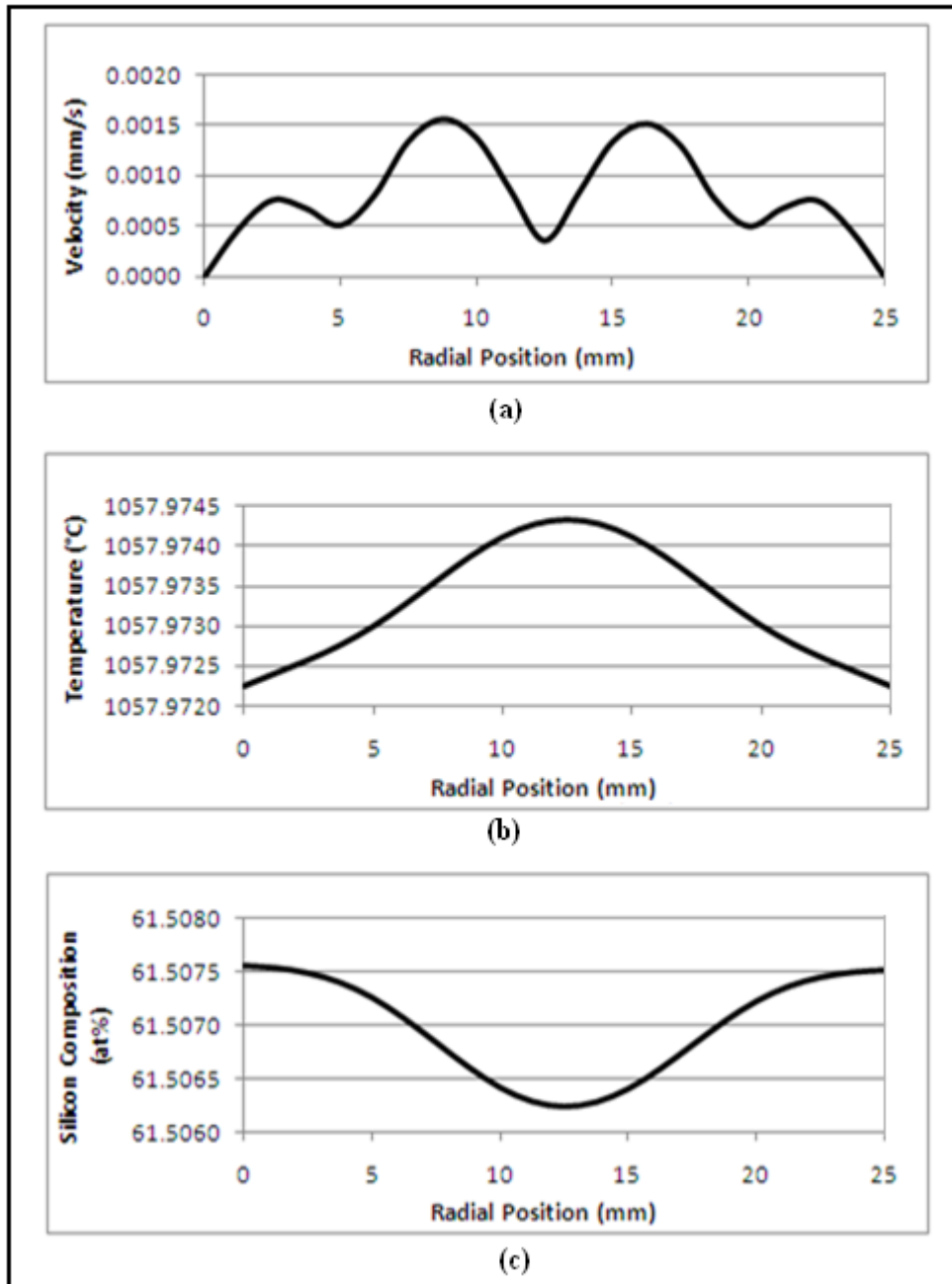


Figure 4.31 Radial line plots, under $B=20\text{mT}$ axial static magnetic field
a- Flow velocities in horizontal plane at 1 mm above interface
b- Temperature distribution
c- Silicon composition

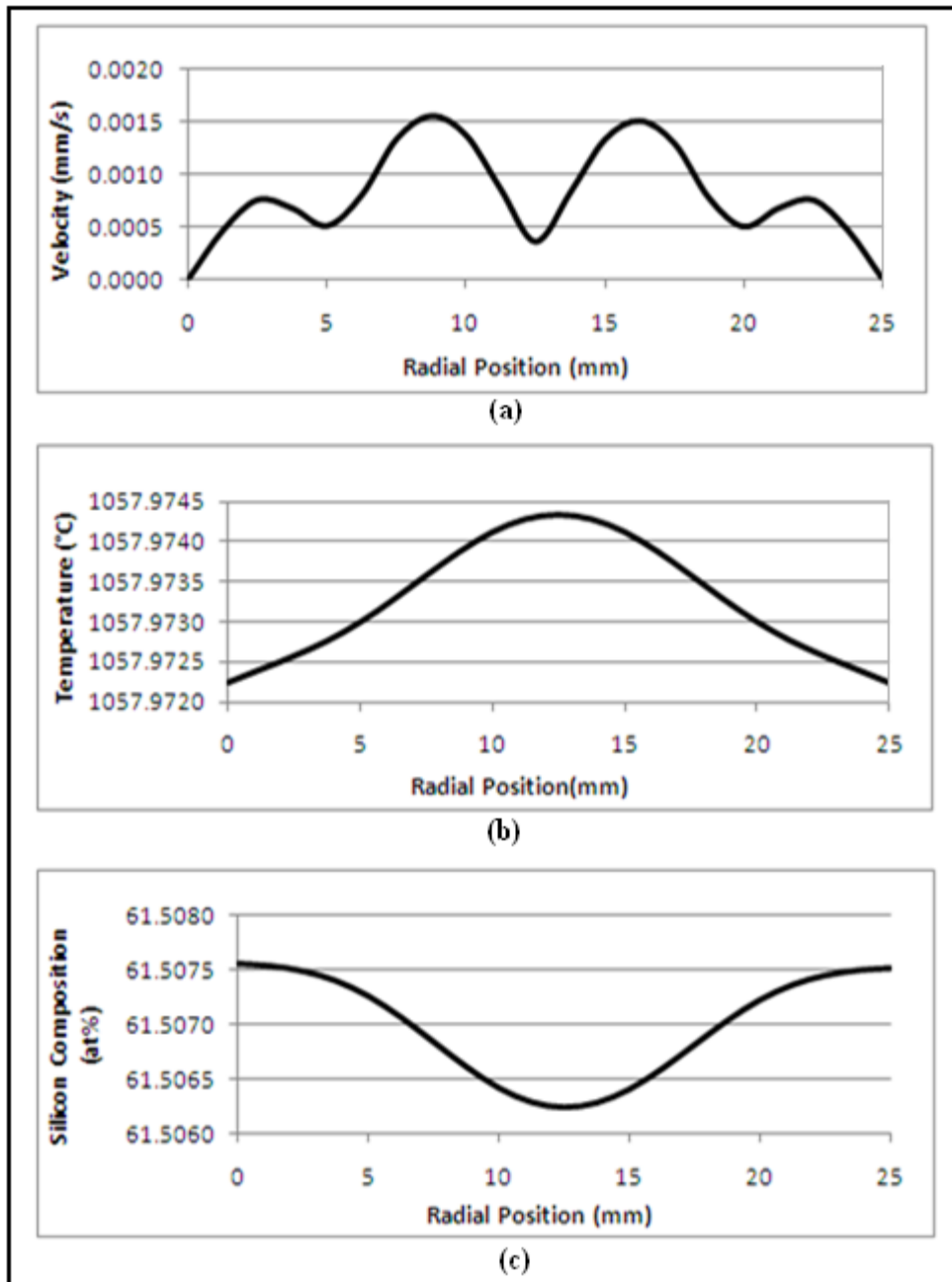


Figure 4.32 Radial line plots, under $B=200\text{mT}$ axial static magnetic field
a- Flow velocities in horizontal plane at 1 mm above interface
b- Temperature distribution
c- Silicon composition

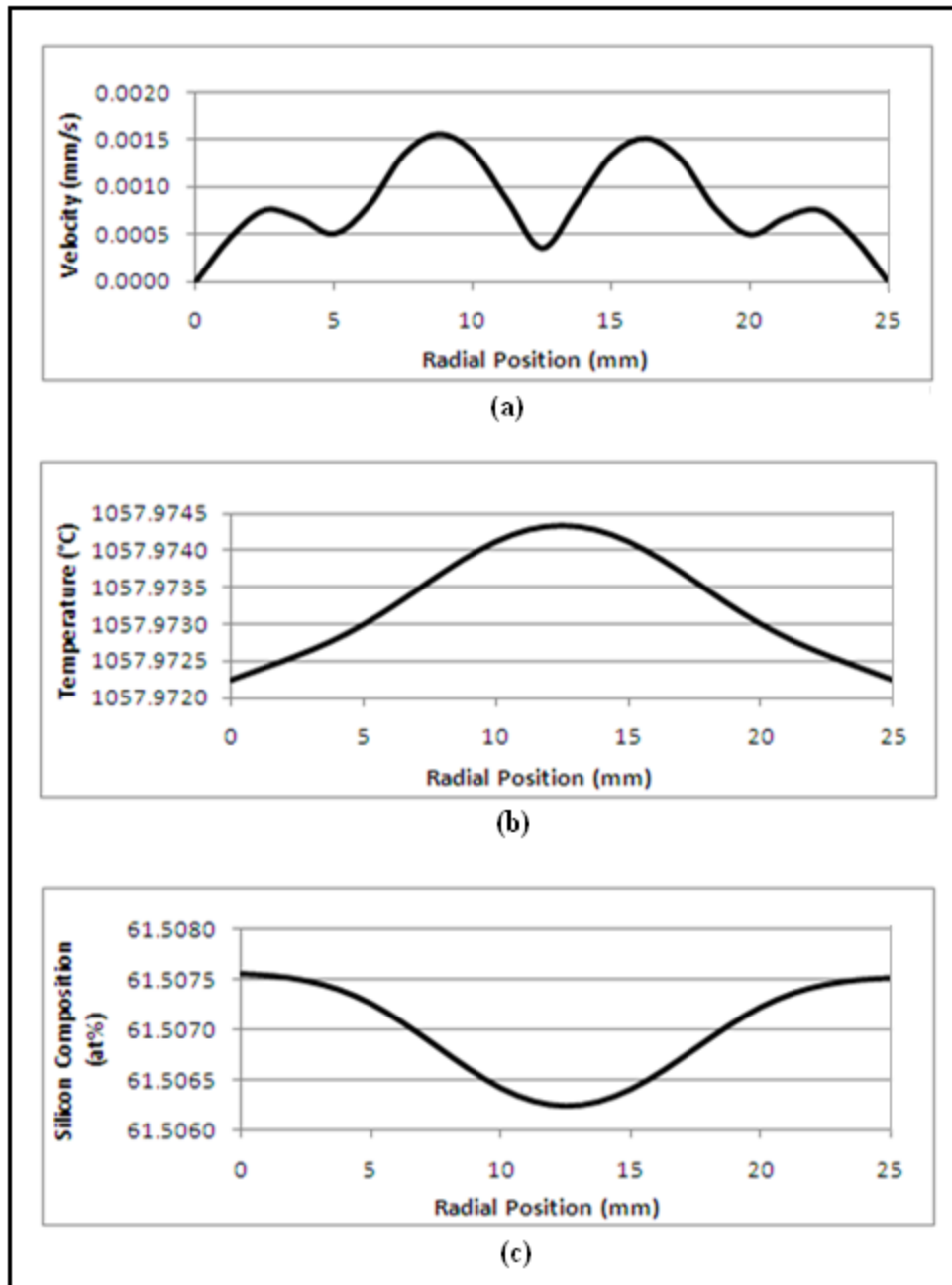


Figure 4.33 Radial line plots, under $B=1\text{T}$ axial static magnetic field
a- Flow velocities in horizontal plane at 1 mm above interface
b- Temperature distribution
c- Silicon composition

CHAPTER FIVE

The Effect of Axial and Radial Temperature Gradient

5.0 Introduction

As discussed, in order to grow crystals with better quality, precise control of heat and solute field is essential. Silicon segregation can be minimized by suppressing the melt convection. Given the chemical composition of the solvent region, the pulling rate, and thermal gradient both axially and radially are also playing a strong role in the process of crystal growth [20].

It was observed, in Chapter four, that the application of linear temperature profile provides better results. It was also shown that in the process of crystal growth, there are some challenges such as mixing the two components, supercooling, and homogeneity of grown crystal, to be overcome. As it has been shown by other researchers such as [2], [75], and [76] that they have used 60K/cm axial thermal gradient. In this chapter, the author would present an alternative approach to grow a single bulk crystal in Bridgman setting by studying different cases, with different temperature gradients, which address the aforementioned concerns.

5.1 Application of different Axial Temperature Gradient in Terrestrial Condition, by simulation in (FEA)

In this section different axial temperature gradients from 60K/cm to 30K/cm, where non-dimensional thermal Grashof (Gr_T) numbers are ranging from 230,000 down to 115,000 respectively, are presented and discussed. Figure 5.1 shows the results when

Gr = 2.3E+05. Figure-5.1-a represents the flow velocity in solvent region, in which the region has two distinct patterns, upper portion with a few stronger cells with as high as 0.243 mm/s and the lower region with a very weak flow with 0.013 mm/s. Figure 5.1-c shows the silicon concentration which clearly shows that the concentration near the interface (the bottom edge of the figure) is nearly 1% more than the desired level which is 25%. Figure 5.2-c, which depicts the silicon concentration, clearly shows that due to the strong convection in the region there is a relatively strong concentration gradient in the model and concentration has exceeded the desired 25% level right after the interface. Figure 5.3 represents results where Gr = 1.9E+05, in this case the reduction of the flow velocity, as shown in Figure 5.3-a, noticeably is reduced to a maximum of 0.167 mm/s, but still the solvent region flow is appearing into two distinct zones, upper zone with few flow cells and lower zone with a weaker flow. The concentration gradient, as it can be seen in Figure 5.4-c, is still relatively high and quickly increasing near the interface.

Since the reduction of the axial temperature gradient in the previous case resulted in less velocity in the solvent region, the next case is where Gr = 1.5E+05. Figure 5.5-a, shows that the flow velocity, now is divided into some vertical and relatively strong and a few horizontal with much less intense flow cells. As it can be seen in both Figure 5.5-a and 5.6-a, the flow velocity is from as low as 7 μ m/s to 92 μ m/s. This temperature gradient has shown that the silicon distribution is much more uniformly distributed in the region, however, it is not to the desired level especially near the interface area (near the bottom of the model), as it can be seen in Figure 5.6-c. The next temperature gradient setting would

result in $Gr = 1.3E+05$. As Figure 5.7-a, shows the flow velocity is ranged between $2\mu\text{m/s}$ in the area marked as “d” to $55\mu\text{m/s}$ in the area marked as “f”. This setting has caused the region be divided into two noticeable zones, the “d” zone which is dominated area in the solvent region and two flow cells near the side walls. The presence of a relatively large and dominant area with the weak, approximately ($2\mu\text{m/s}$) flow well defines that the flow regime is mostly governed by diffusion which is promising. Figure 5.7-c shows that lower portion of the solvent region has a 25% silicon concentration for nearly the first 20mm above the interface, this can be better seen in Figure 5.8-c. In order to see if the trend continues to enhance the situation or not, the next step is to lowering down the axial temperature gradient which is described by dimensionless number of thermal Grashof further more to $Gr = 1.22E+05$ as shown in Figure 5.9, it can be observed that the flow velocity in the solvent region is becoming relatively faster in the lower zone than the last case.

Figure 5.9-a, shows that the solvent region again contains three distinct flow cells with the stronger cell with $49\mu\text{m/s}$ velocity in the middle and two weaker cells on its side in the upper zone of the model. Figure 5.9-c, shows that this setting has a counter effect on the silicon distribution in the solvent region. This means that there is a non-uniform distribution of silicon in the solvent. Even for the first 30 mm, where it is marked by “k” and “j”, the concentration is quickly changing from 25.9% to 24.2%. The concentration is higher than desired level of 25% near the interface which is not desirable at all. This can be presented better by plot line in Figure 5.10-c. In order to see if this imperfection is a trend

by lowering the axial temperature gradient or not, the next two cases which are $Gr = 1.18E+05$ and $Gr = 1.15E+05$ are being examined. As shown in Figure 5.11-a, the flow patterns remain the same (three cells) as previous case ($Gr = 1.22E+05$) even though the flow velocity is in a lower range from 2 - 44 $\mu\text{m/s}$. As for the silicon concentration, this setting does not show a good result, both Figures 5.11-c and 5.12-c shows that there is a relatively high reduction in concentration. This time, the concentration at interface level is even less than 25% and continues to be lowered up to approximately the first 70mm of the model. Figure 5.13 and Figure 5.14 represent the results of the $Gr = 1.15E+05$ setting. This case is even worst by showing silicon distribution in the solvent region, even though the flow velocity has been reduced to as low as 44 $\mu\text{m/s}$, the silicon concentration and its distribution is unstable and non-uniform. This shows that in order to control the silicon concentration, the control of the axial temperature gradient is important and for the model under this study, the condition with $Gr = 1.3E+05$, results in a consistent and uniform silicon distribution along the vertical axis of the model as well as the radial position.

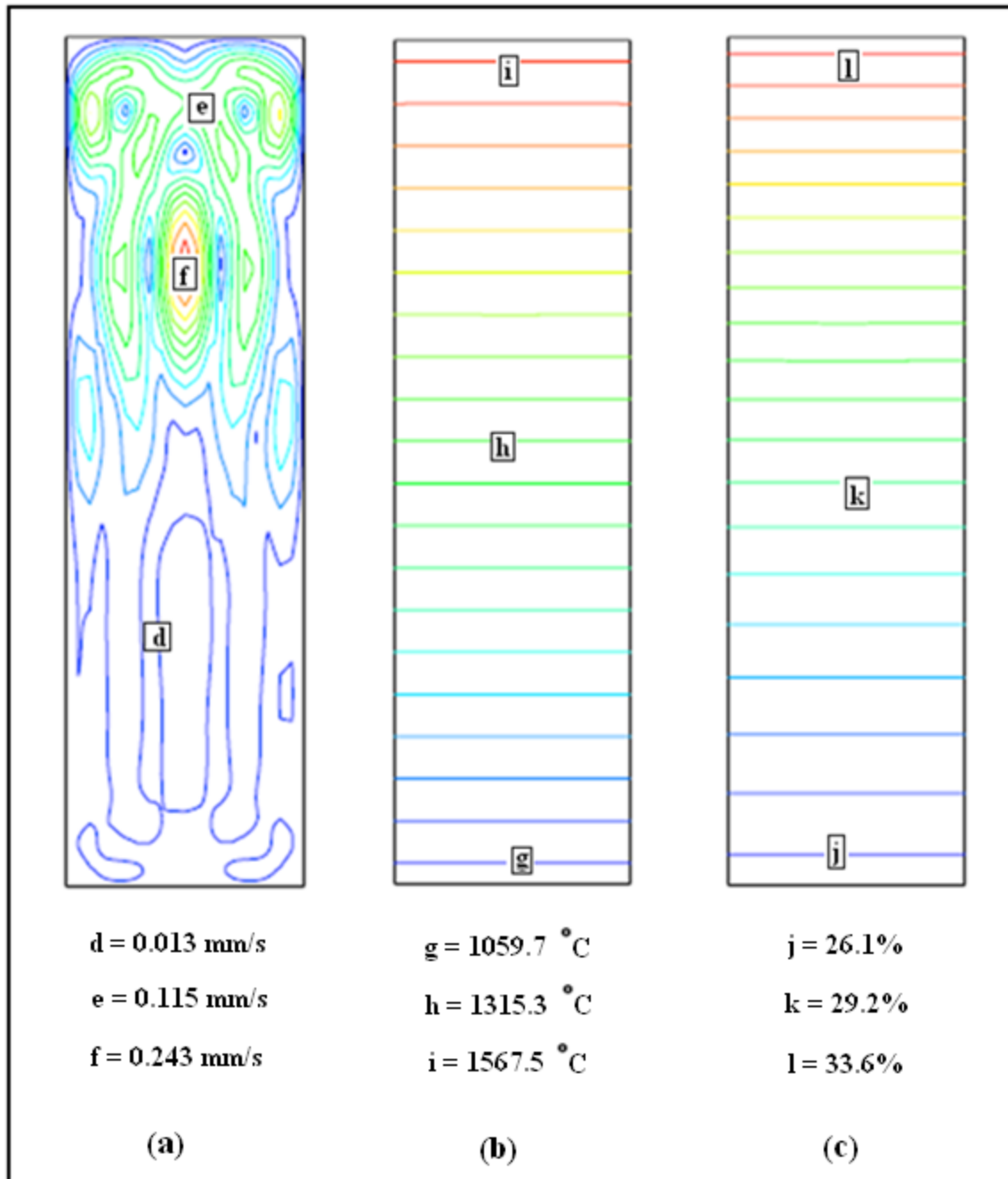


Figure 5.1 Contour plots with $Gr_T = 2.29E + 05$, terrestrial conditions
a- Flow velocities in vertical plane passing through the centre of the model
b- Temperature distribution
c- Silicon composition

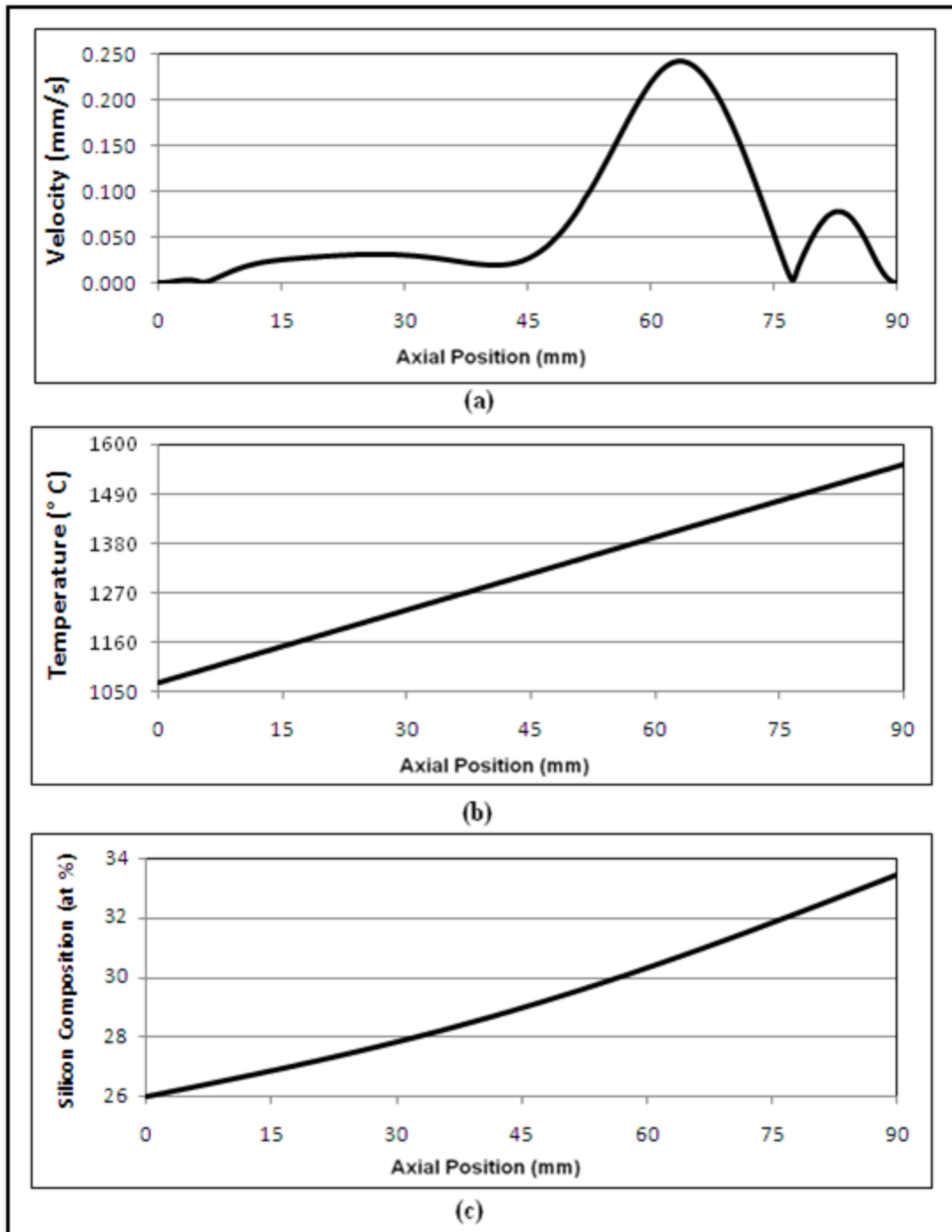


Figure 5.2 Line plots with $Gr_T = 2.29E + 05$, terrestrial conditions
a- Flow velocities in vertical plane passing through the centre of the model
b- Temperature distribution
c- Silicon composition

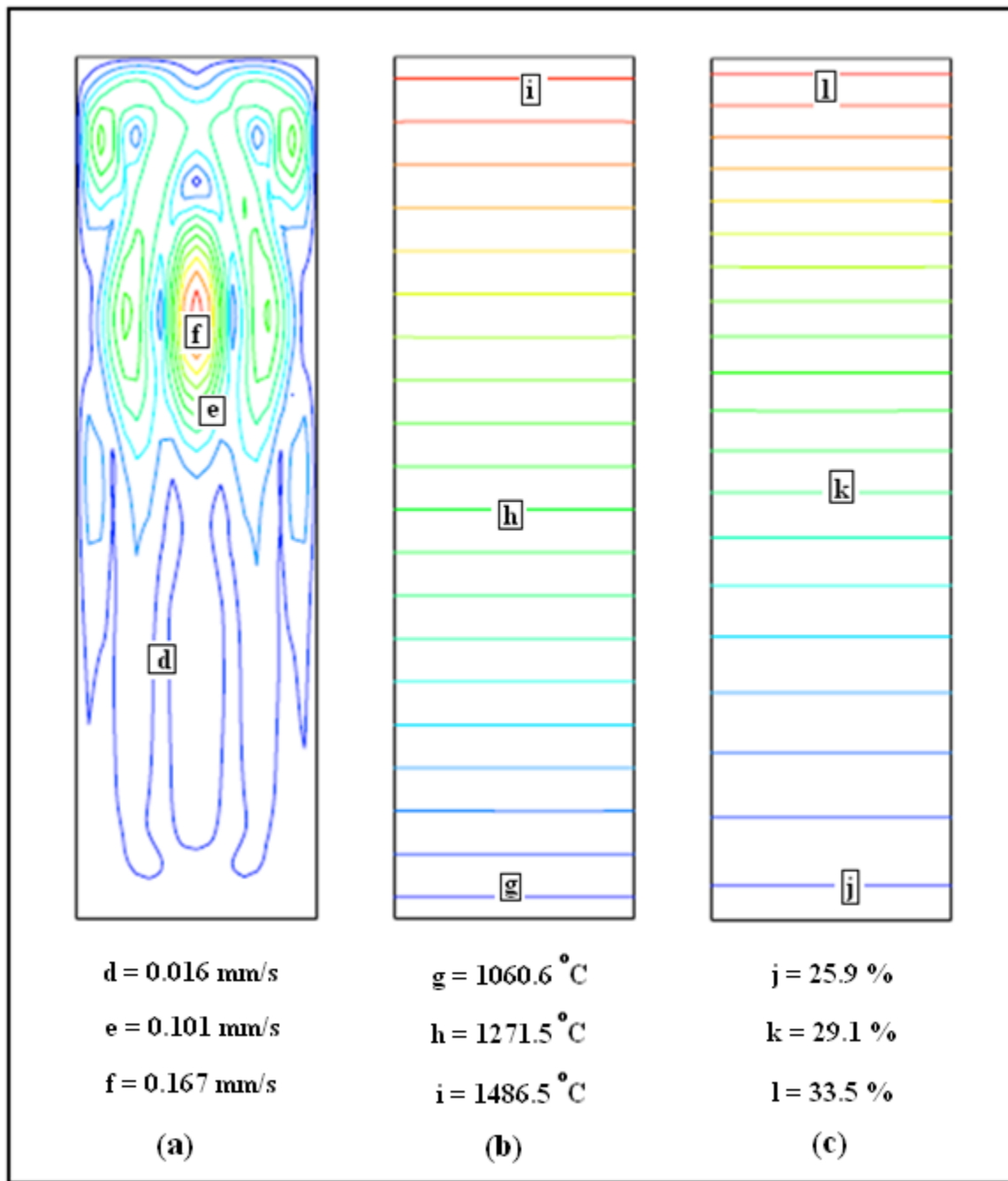


Figure 5.3 Contour plots with $Gr_T = 1.91E + 05$, terrestrial conditions
a- Flow velocities in vertical plane passing through the centre of the model
b- Temperature distribution
c- Silicon composition

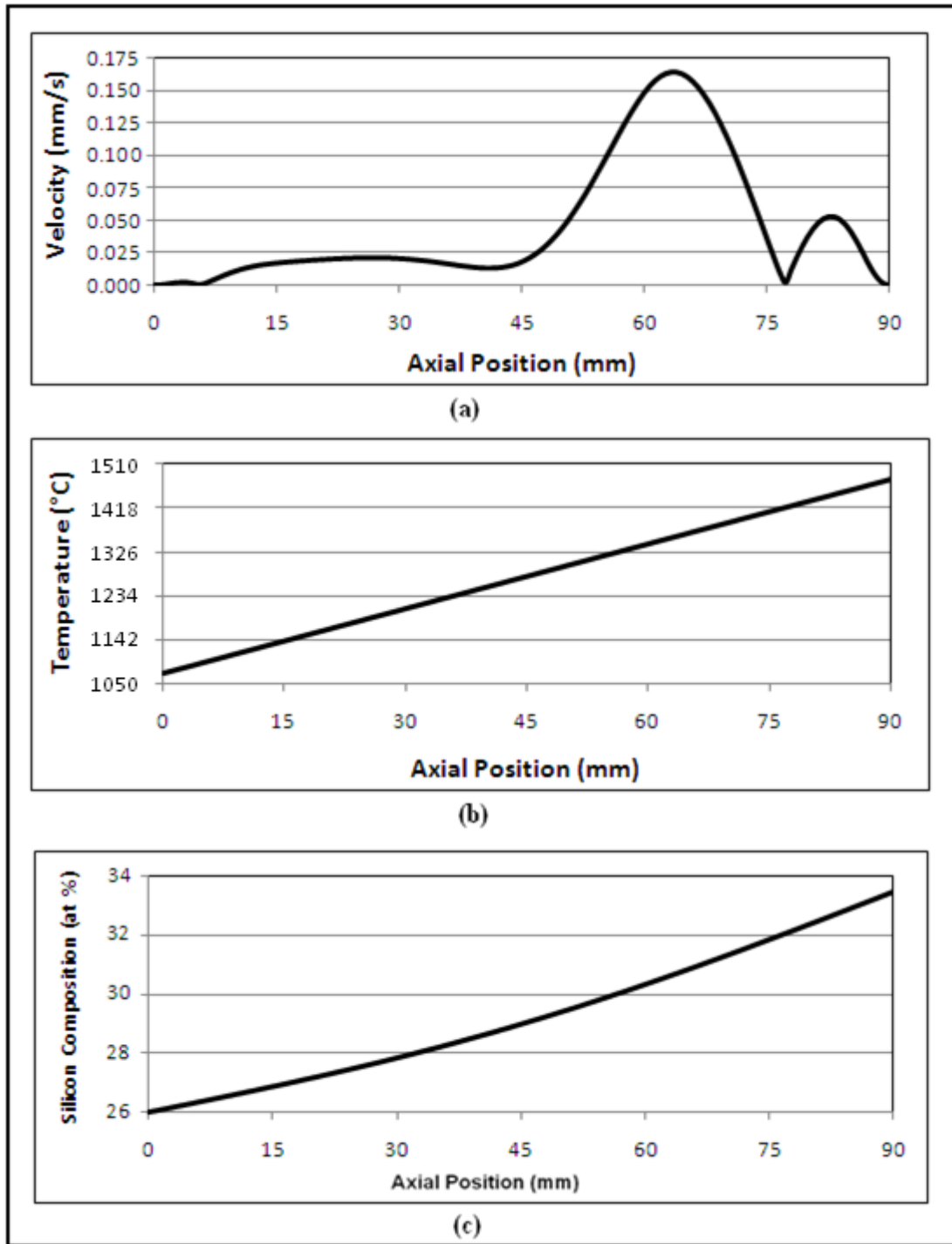


Figure 5.4 Line plots with $Gr_T = 1.91E + 05$, terrestrial conditions
a- Flow velocities in vertical plane passing through the centre of the model
b- Temperature distribution
c- Silicon composition

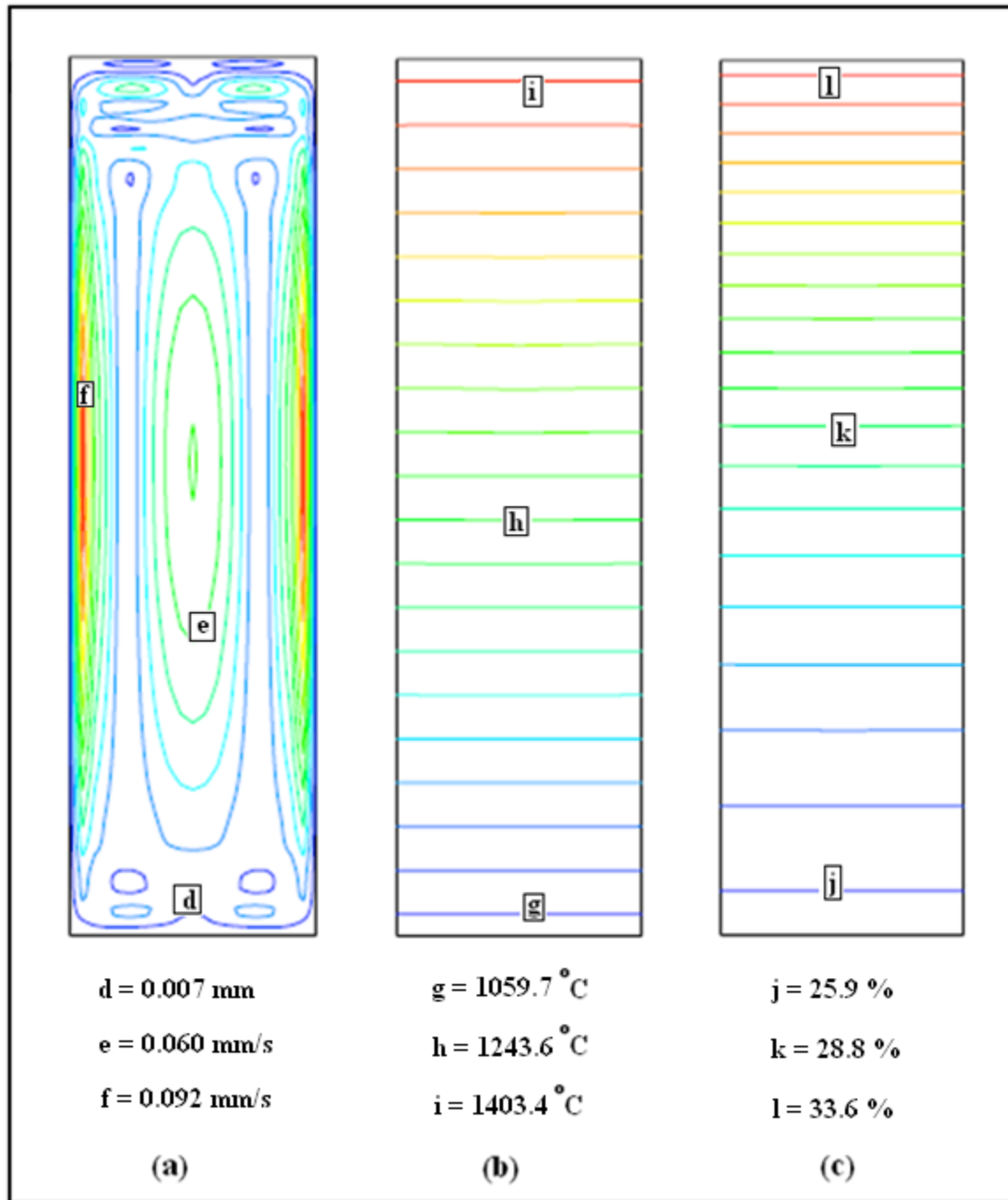


Figure 5.5 Contour plots with $Gr_T = 1.53E + 05$, terrestrial conditions
a- Flow velocities in vertical plane passing through the centre of the model
b- Temperature distribution
c- Silicon composition

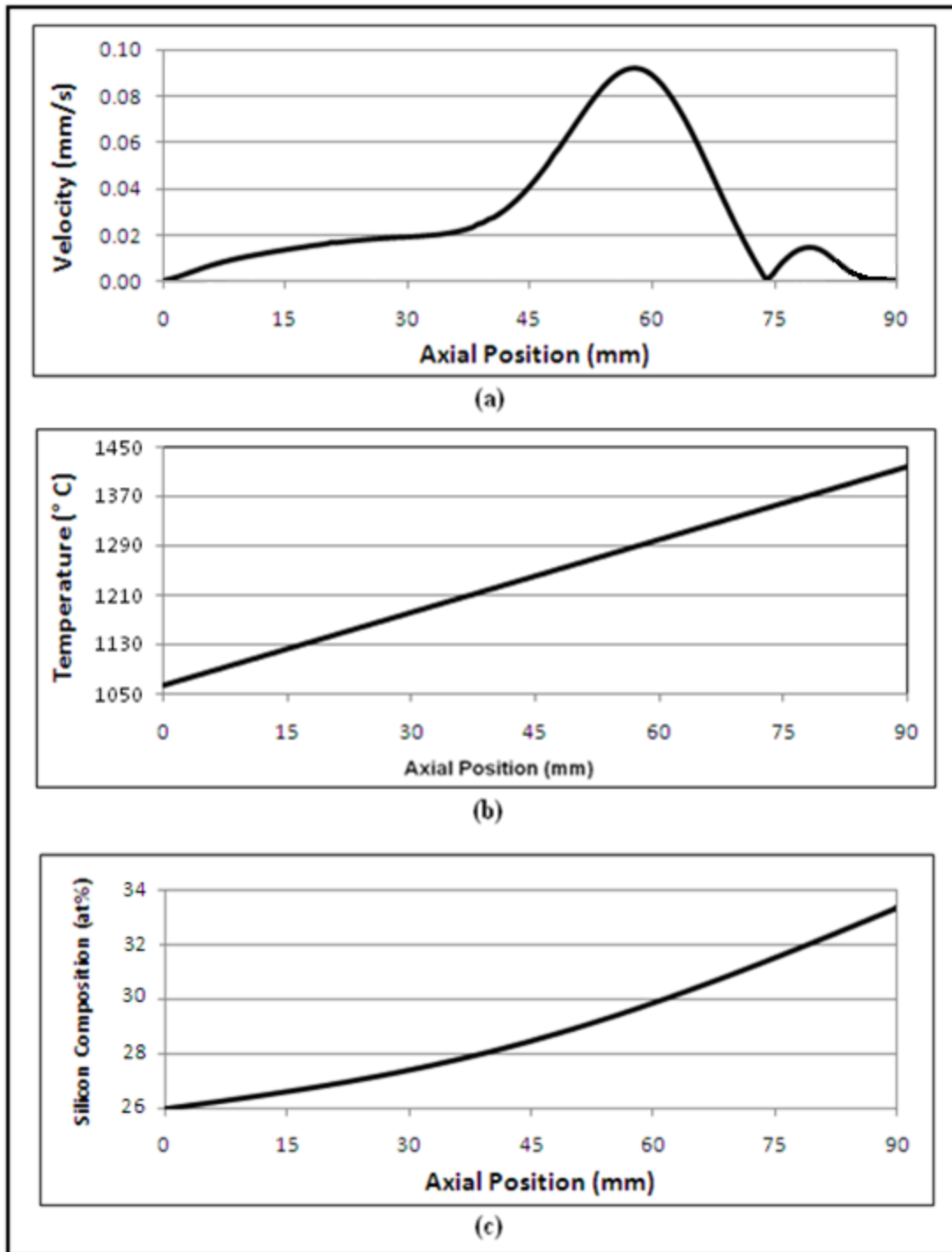


Figure 5.6 Line plots with $Gr_T = 1.53E + 05$, terrestrial conditions
a- Flow velocities in vertical plane passing through the centre of the model
b- Temperature distribution
c- Silicon composition

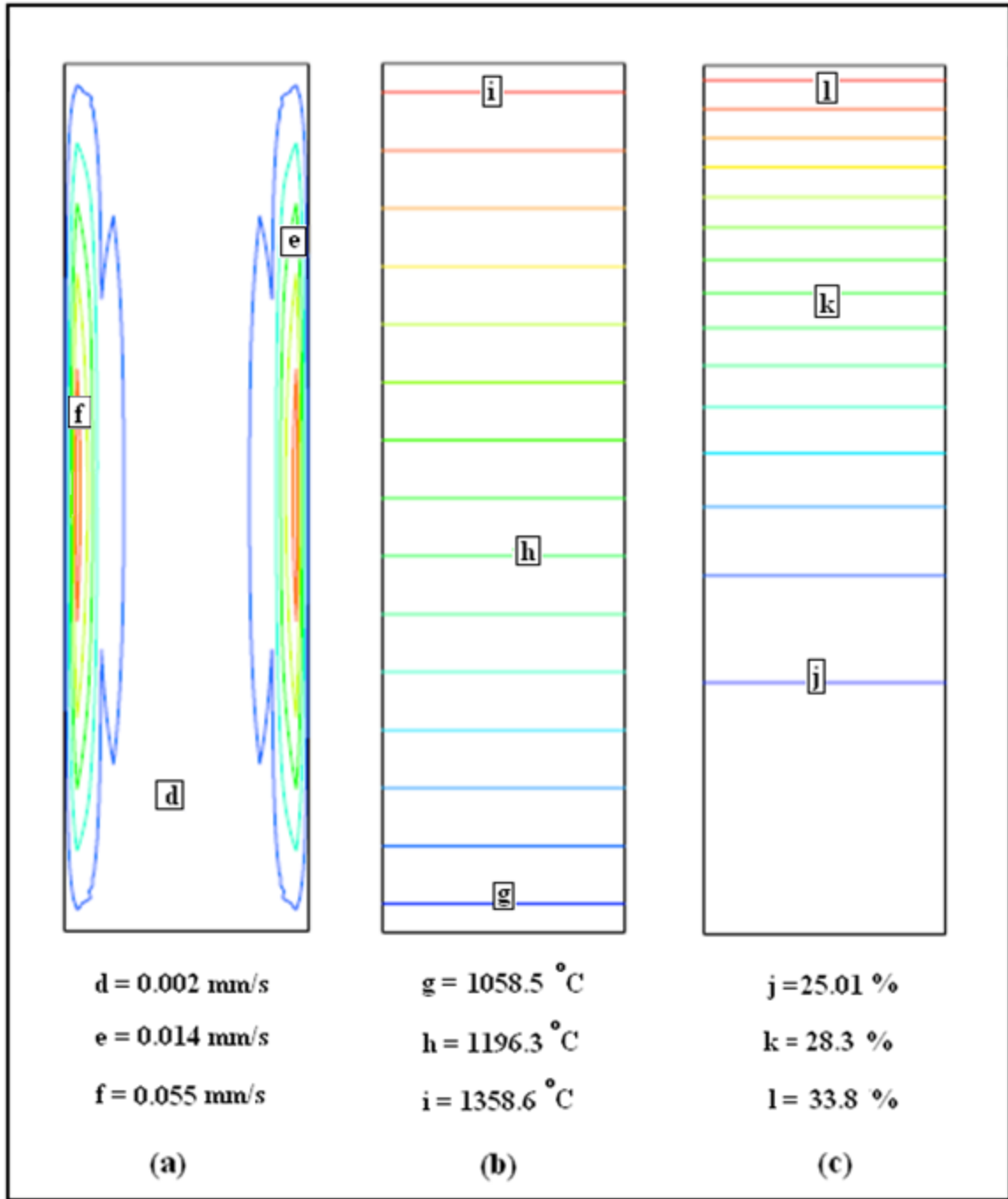


Figure 5.7 Contour plots with $Gr_T = 1.34E + 05$, terrestrial conditions
a- Flow velocities in vertical plane passing through the centre of the model
b- Temperature distribution
c- Silicon composition

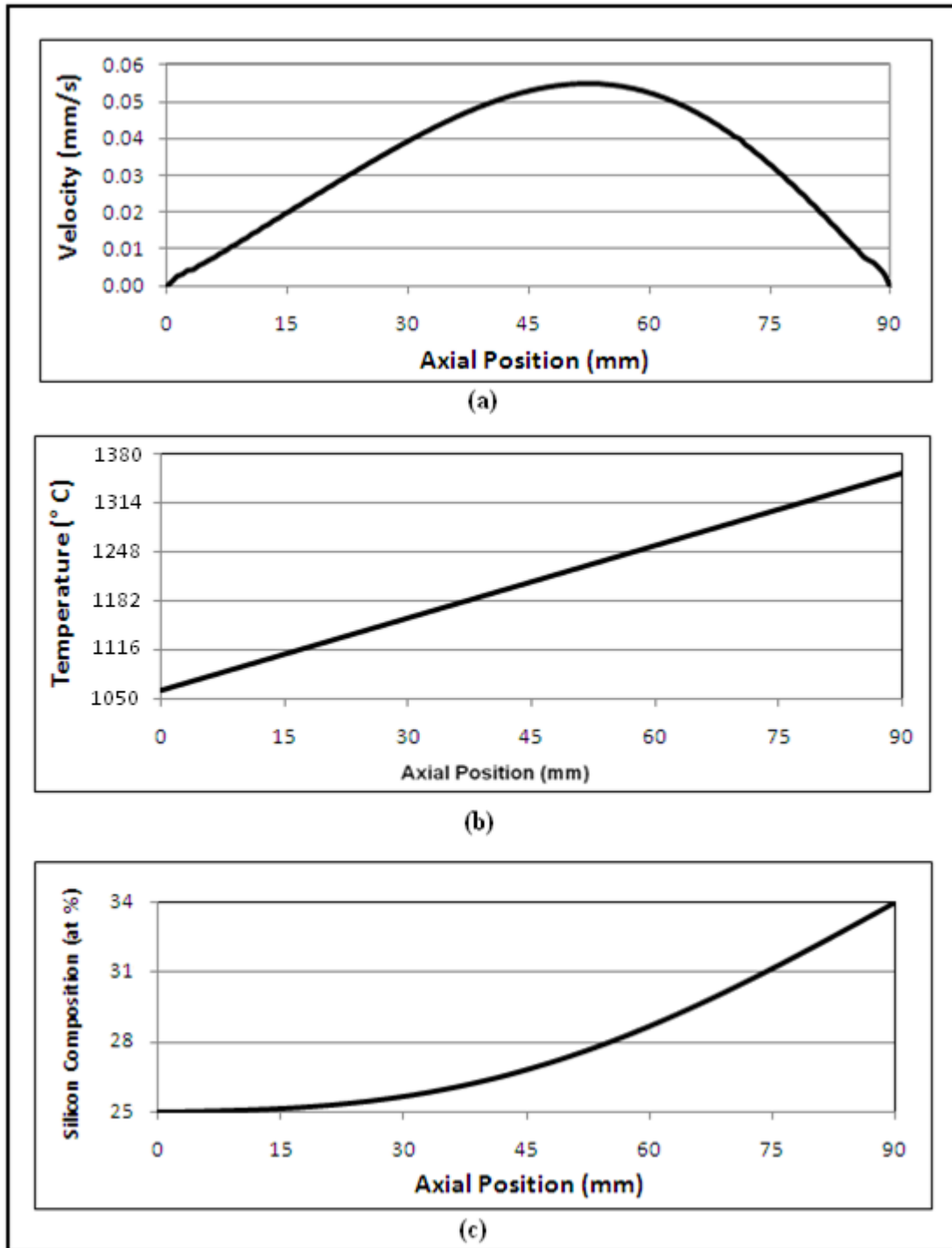


Figure 5.8 Line plots with $Gr_T = 1.34E + 05$, terrestrial conditions
a- Flow velocities in vertical plane passing through the centre of the model
b- Temperature distribution
c- Silicon composition

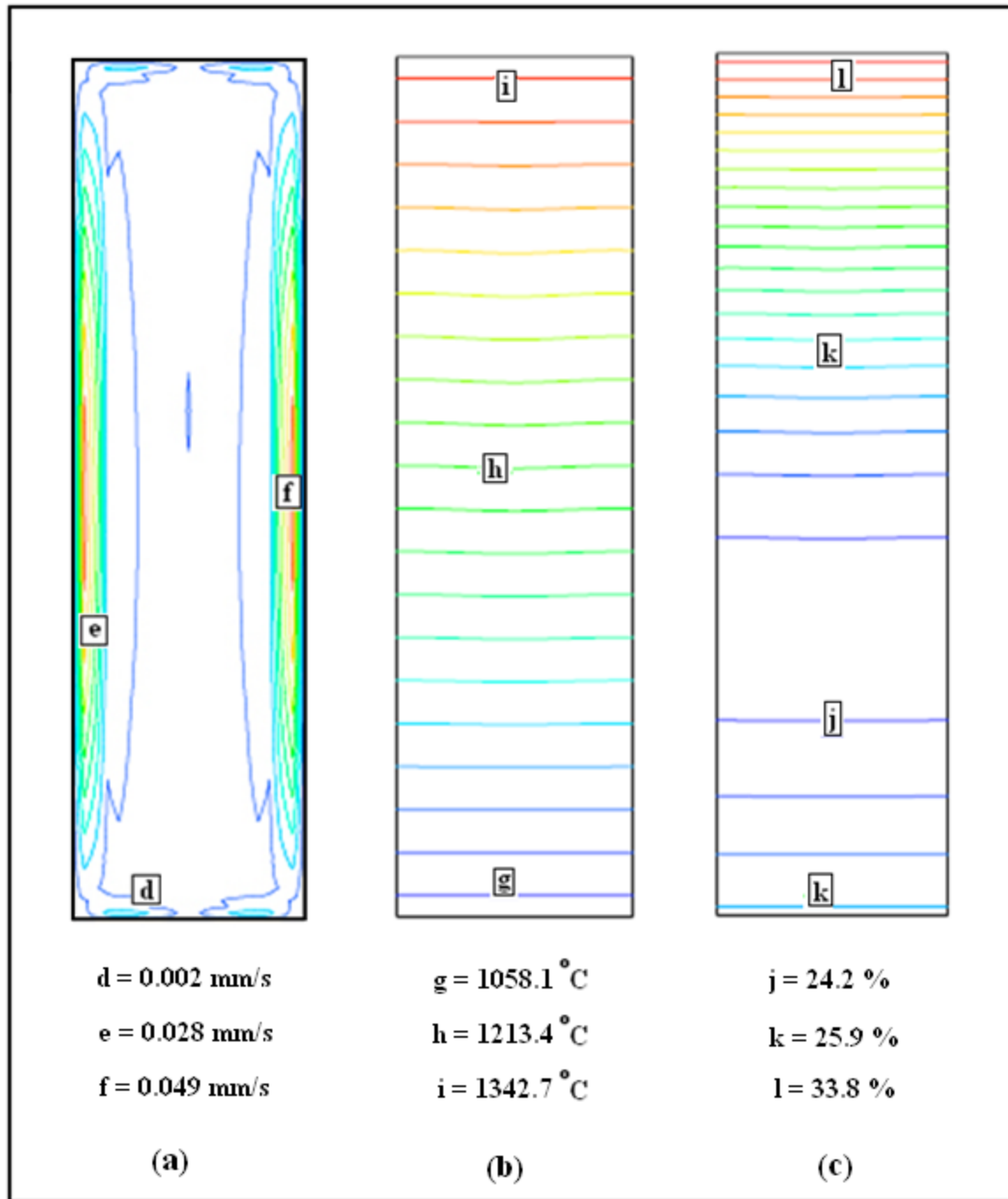


Figure 5.9 Contour plots with $Gr_T = 1.22E + 05$, terrestrial conditions
a- Flow velocities in vertical plane passing through the centre of the model
b- Temperature distribution
c- Silicon composition

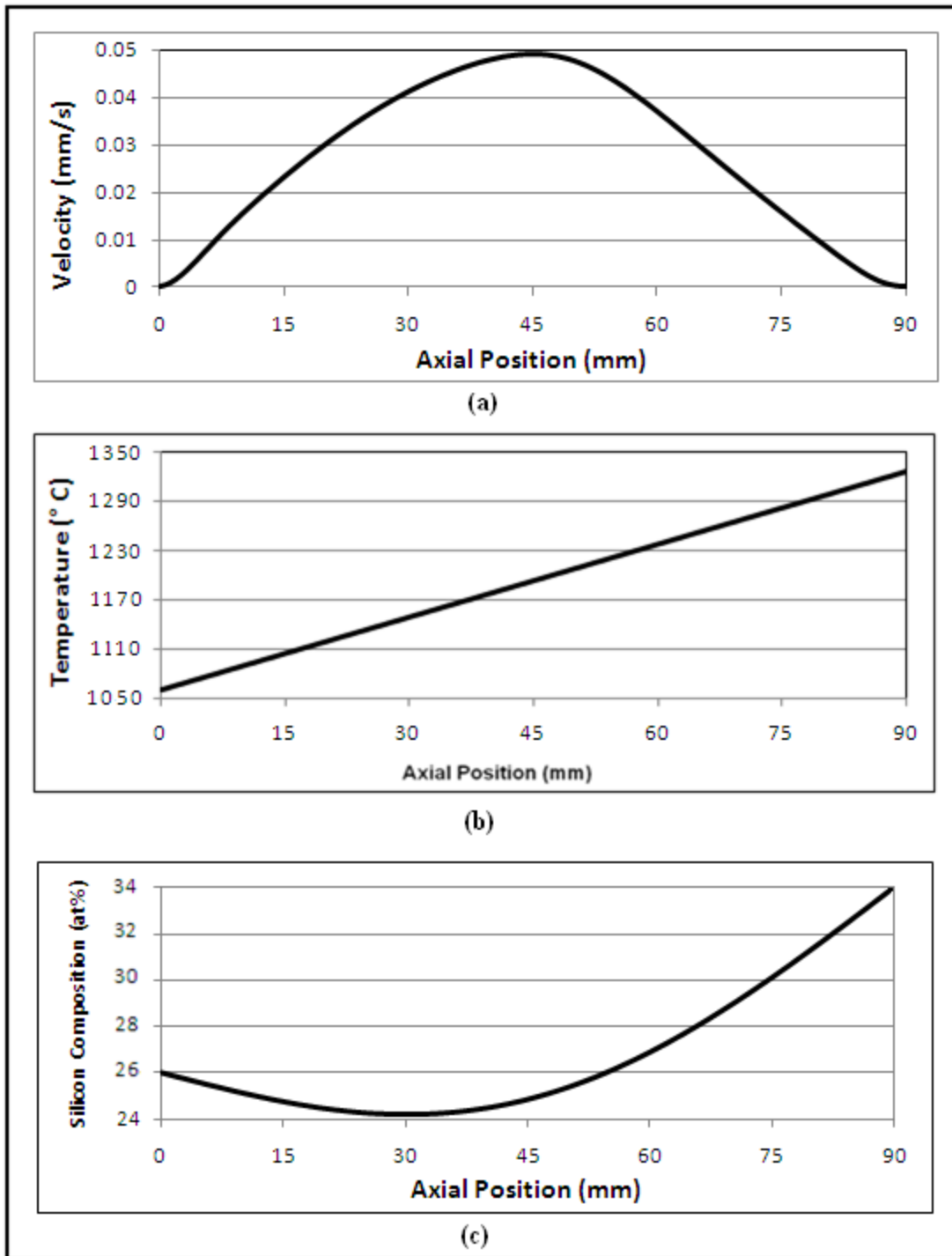


Figure 5.10 Line plots with $Gr_T = 1.22E + 05$, terrestrial conditions
a- Flow velocities in vertical plane passing through the centre of the model
b- Temperature distribution
c- Silicon composition

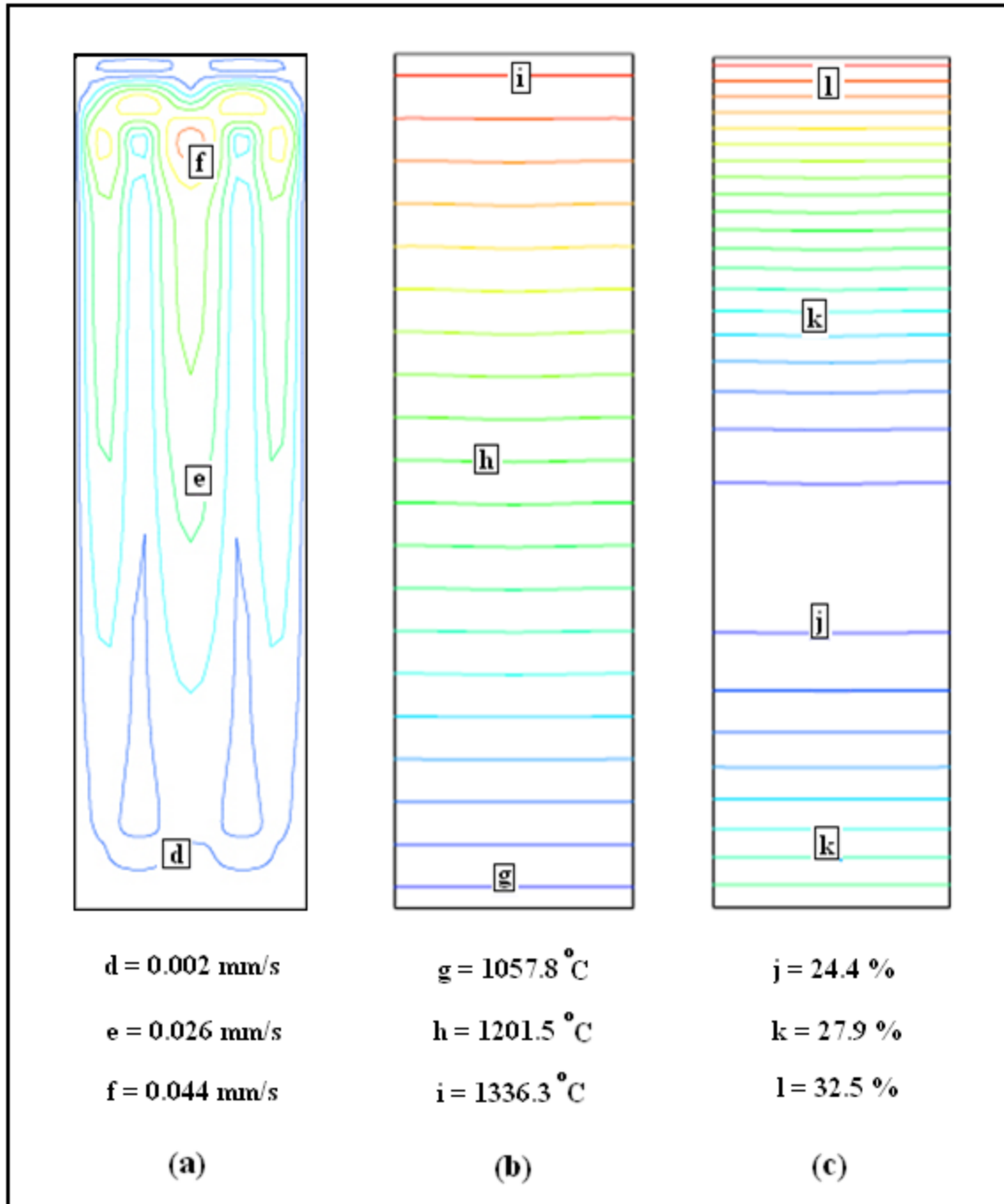


Figure 5.11 Contour plots with $Gr_T = 1.18E + 05$, terrestrial conditions
a- Flow velocities in vertical plane passing through the centre of the model
b- Temperature distribution
c- Silicon composition

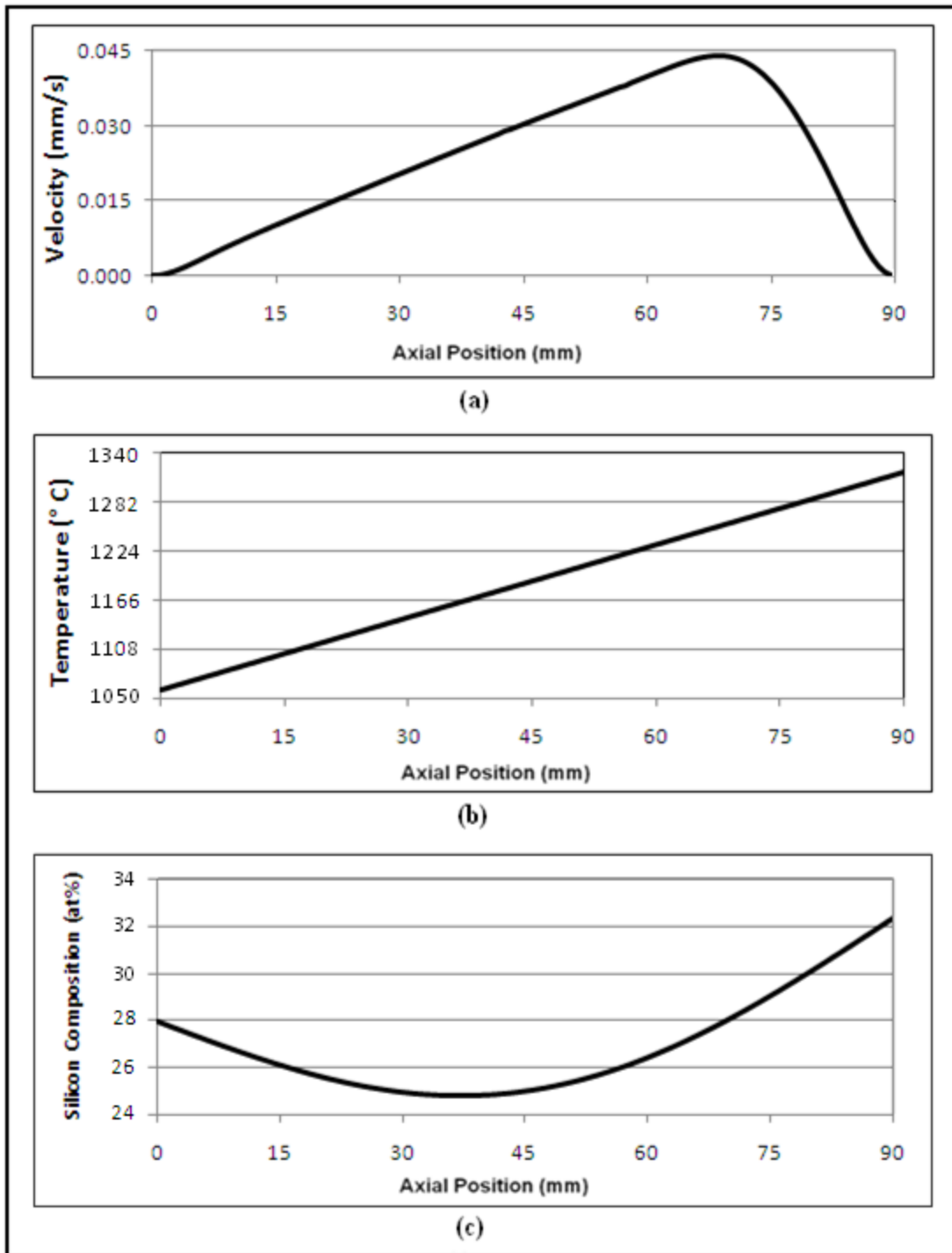


Figure 5.12 Line plots with $Gr_T = 1.18E + 05$, terrestrial conditions
a- Flow velocities in vertical plane passing through the centre of the model
b- Temperature distribution
c- Silicon composition

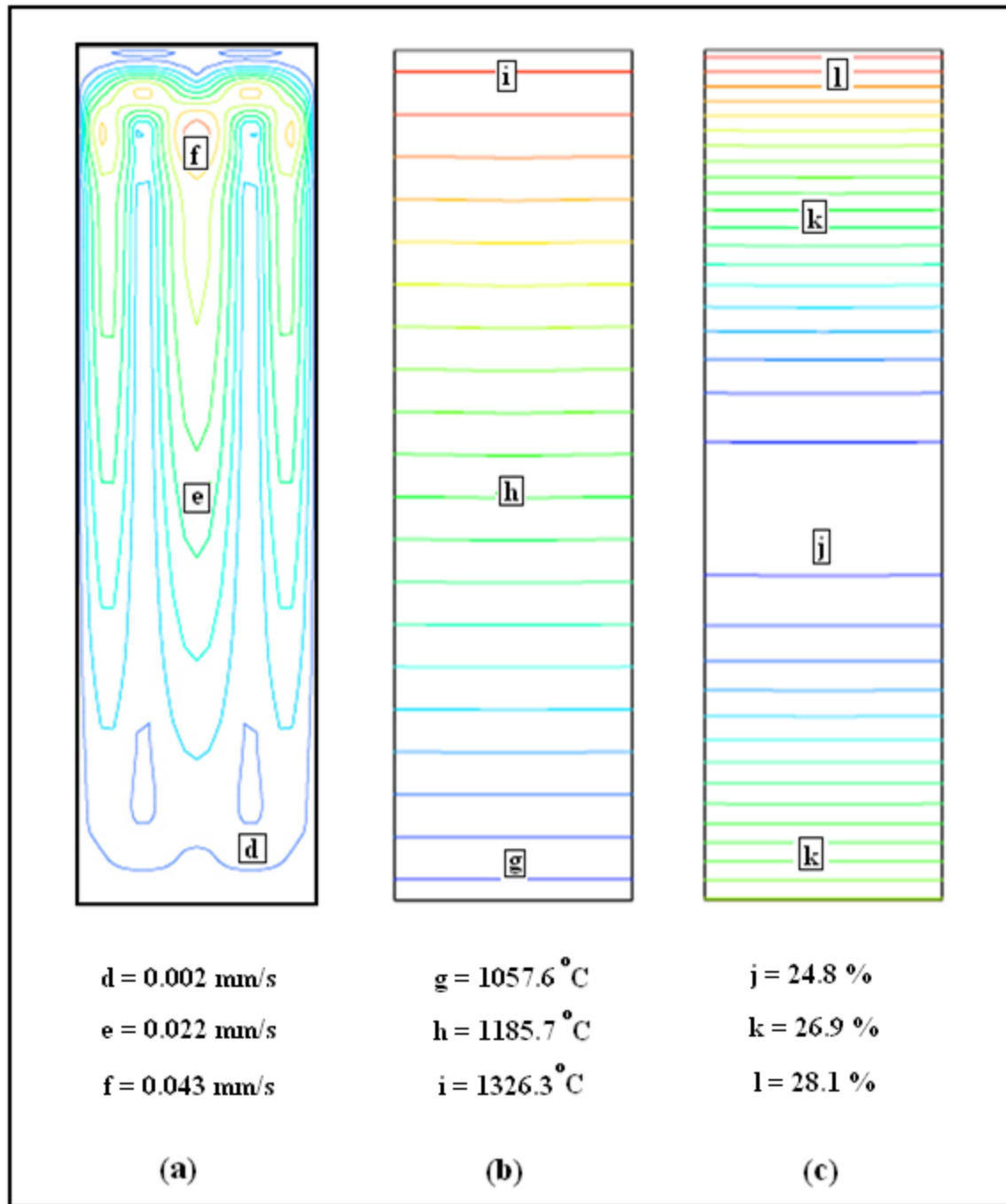


Figure 5.13 Contour plots with $Gr_T = 1.15E + 05$, terrestrial conditions
a- Flow velocities in vertical plane passing through the centre of the model
b- Temperature distribution
c- Silicon composition

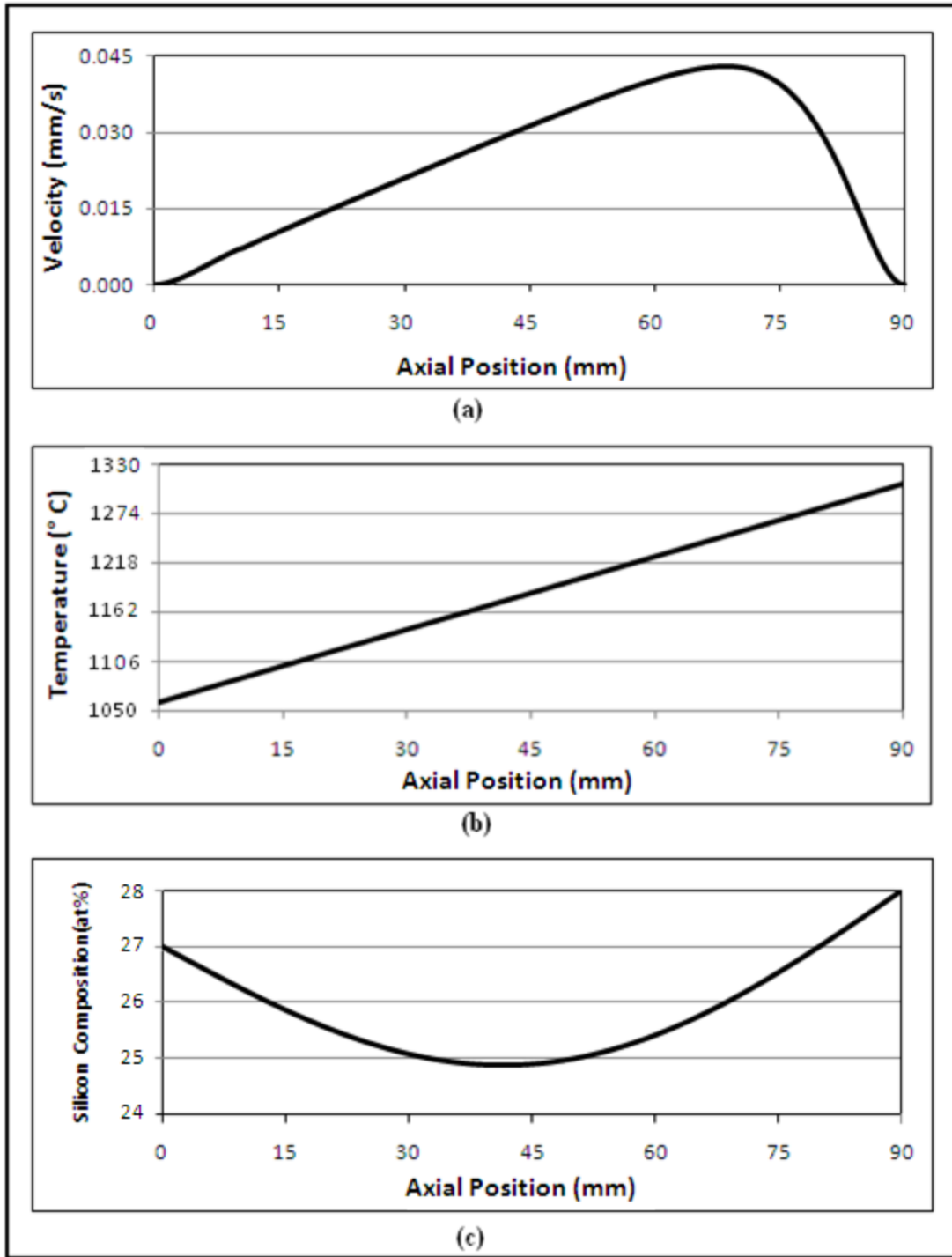


Figure 5.14 Line plots with $Gr_T = 1.15E + 05$, terrestrial conditions
a- Flow velocities in vertical plane passing through the centre of the model
b- Temperature distribution
c- Silicon composition

5.2 Detail Analysis of 35K/cm Axial Temperature Gradient Case

In order to investigate the solvent thermal conditions; both axial and radial temperature distribution, the model is dissected into different levels in the axial direction. As shown in Figure 5.15, the temperature distribution in the solvent region with axial position marker on the left and indicated radial temperature difference for each corresponding level on the right.

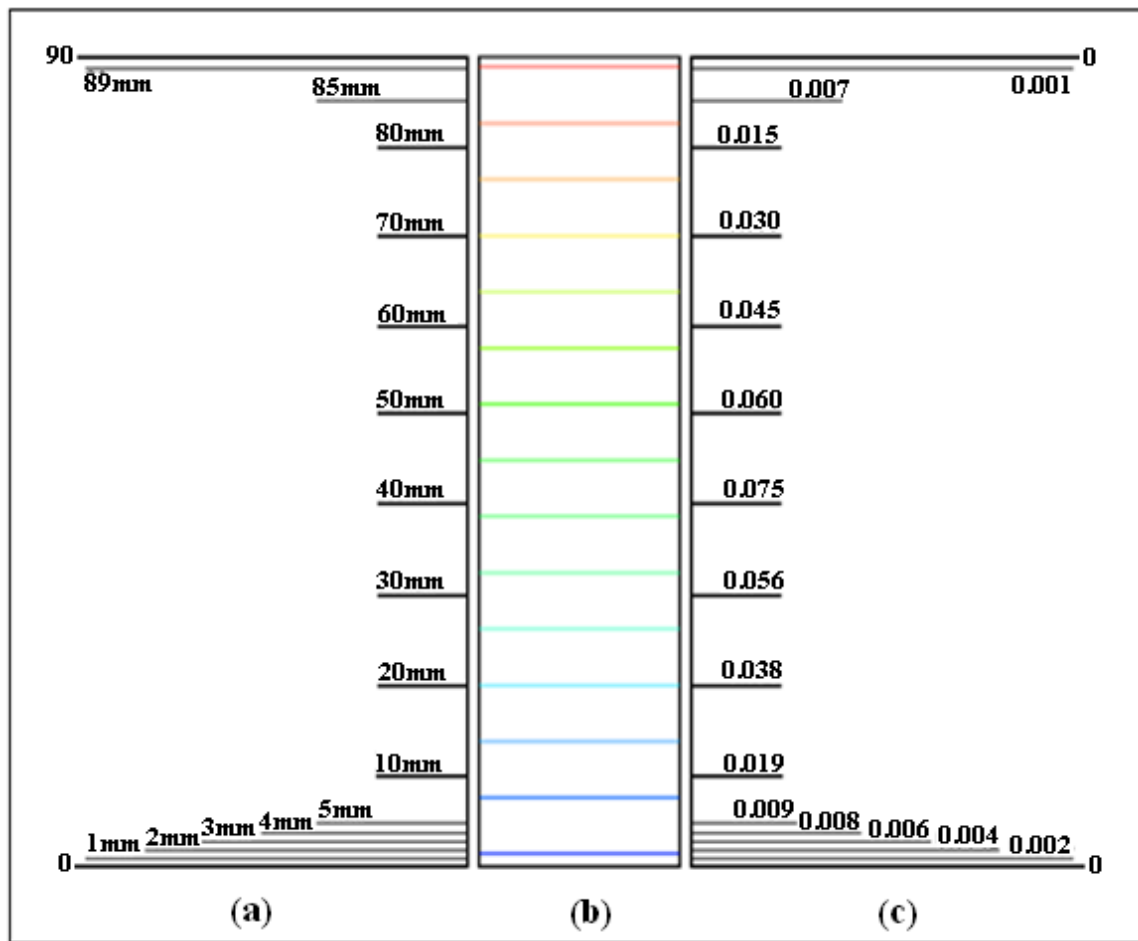


Figure 5.15 Schematic of solvent region under 35K/cm axial temperature gradient

- a- Axial position
- b- Temperature distribution contour in solvent region
- c- Radial ΔT

Figure 5.16 shows the two zones of the solvent region under the influence of the 35k/cm where $Gr_T = 1.34E + 05$. Table 5.1 and Figure 5.17 represent the radial temperature gradient in this setting for the first 5mm of the model at an interval of 1mm in the axial direction. As it can be seen in Figure 5.17-a, to 5.17-e, the radial temperature difference from $\Delta T = 0.002$ at 1 mm to $\Delta T = 0.009$ at 5 mm above the interface. Figure 5.18 shows the interval from 10 mm to 50 mm above the interface with the radial temperature difference from $\Delta T = 0.019$ at 10 mm to $\Delta T = 0.075$ at 40 mm and start to decline to $\Delta T = 0.060$ at 50 mm. As it can be seen in Figure 5.19, the radial temperature difference continues to become lower in higher intervals from as high as $\Delta T = 0.045$ at 60 mm down to $\Delta T = 0.001$ at 89 mm. So it is clear that the highest difference is at 40 mm above interface.

Table 5.1 Radial temperature gradient at different axial position

Item	Axial Position (mm)	Radial ΔT
1	0	0.000
2	1	0.002
3	2	0.004
4	3	0.006
5	4	0.008
6	5	0.009
7	10	0.019
8	20	0.038
9	30	0.056
10	40	0.075
11	50	0.060
12	60	0.045
13	70	0.030
14	80	0.015
15	85	0.007
16	89	0.001
17	90	0.000

The low radial temperature difference at lower level of the model helps the silicon distribution be more uniform and due to both low axial and radial temperature gradient in this segment of the model the undercooling will not happen. As it was shown earlier, up to 20 mm above interface, the silicon concentration remains at nearly 25% level. This trend is perceived to be continued as the solidification process continues and helps to achieve a uniform bulk single crystal. From the practical point of view, the low radial temperature gradient less than 1K/cm which is within the thermocouples accuracy in experimental settings [98] is desirable for crystal growth. In this study, this was shown to be 0.06K/cm which is very promising.

In order to get a mathematical model for the radial temperature with respect to the vertical axis of the model, a bilinear interpolation for two dimensional models (for three dimensional, a polar interpolation, Appendix-B) is applied for the two zones which were described earlier;

- a)** From solidification interface up to 40 mm level which had the highest radial ΔT , and
- b)** Above 40 mm up to the dissolution interface can be read as (5.1) and (5.2) formulas respectively, in which “r” and “z” are dimensionless values in radial and axial position.

These two are formulated and derived from the simulation results obtained in the case of 35 K/cm axial linear temperature gradient or $Gr_T = 1.34E + 05$ was applied.

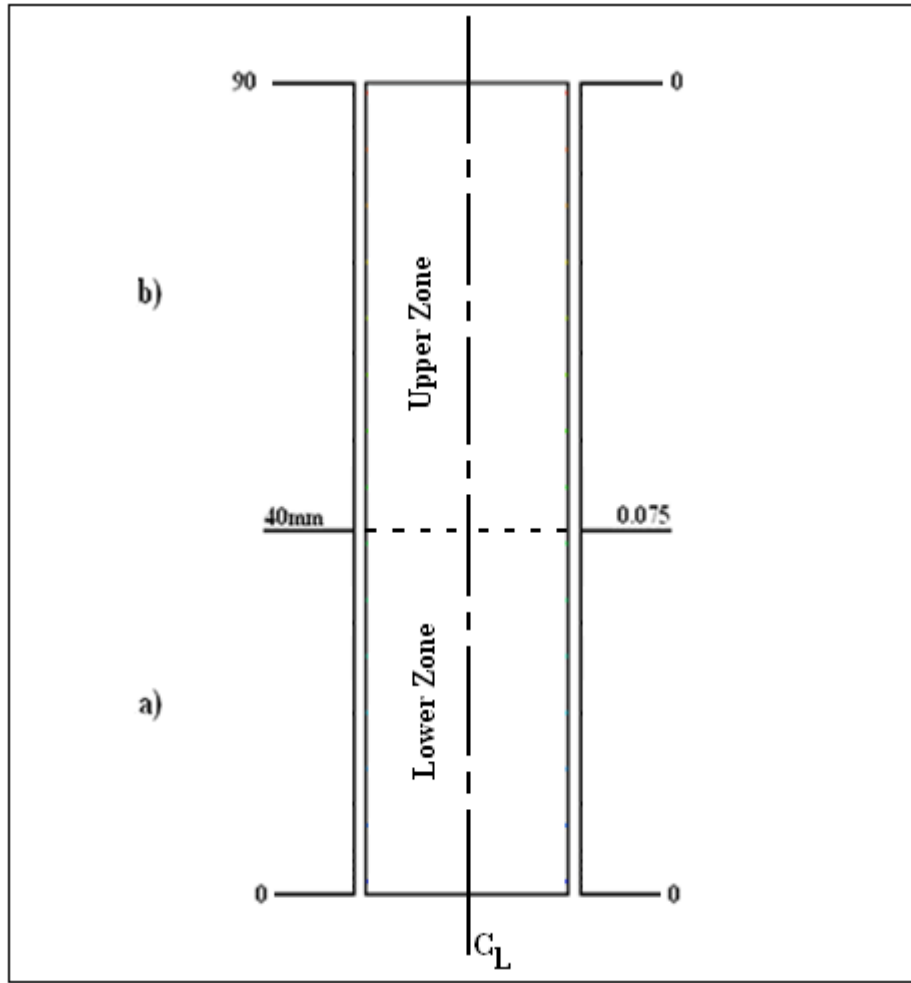


Figure 5.16 Two zones of radial temperature gradient variations in solvent region (35K/cm axial thermal gradient case)

For a);

$$\Delta T(r, z) = 0.046875z(1 - 2r) \quad (5.1)$$

And for b);

$$\Delta T(r, z) = 0.135 - 0.27r - 0.0375z + 0.075rz \quad (5.2)$$

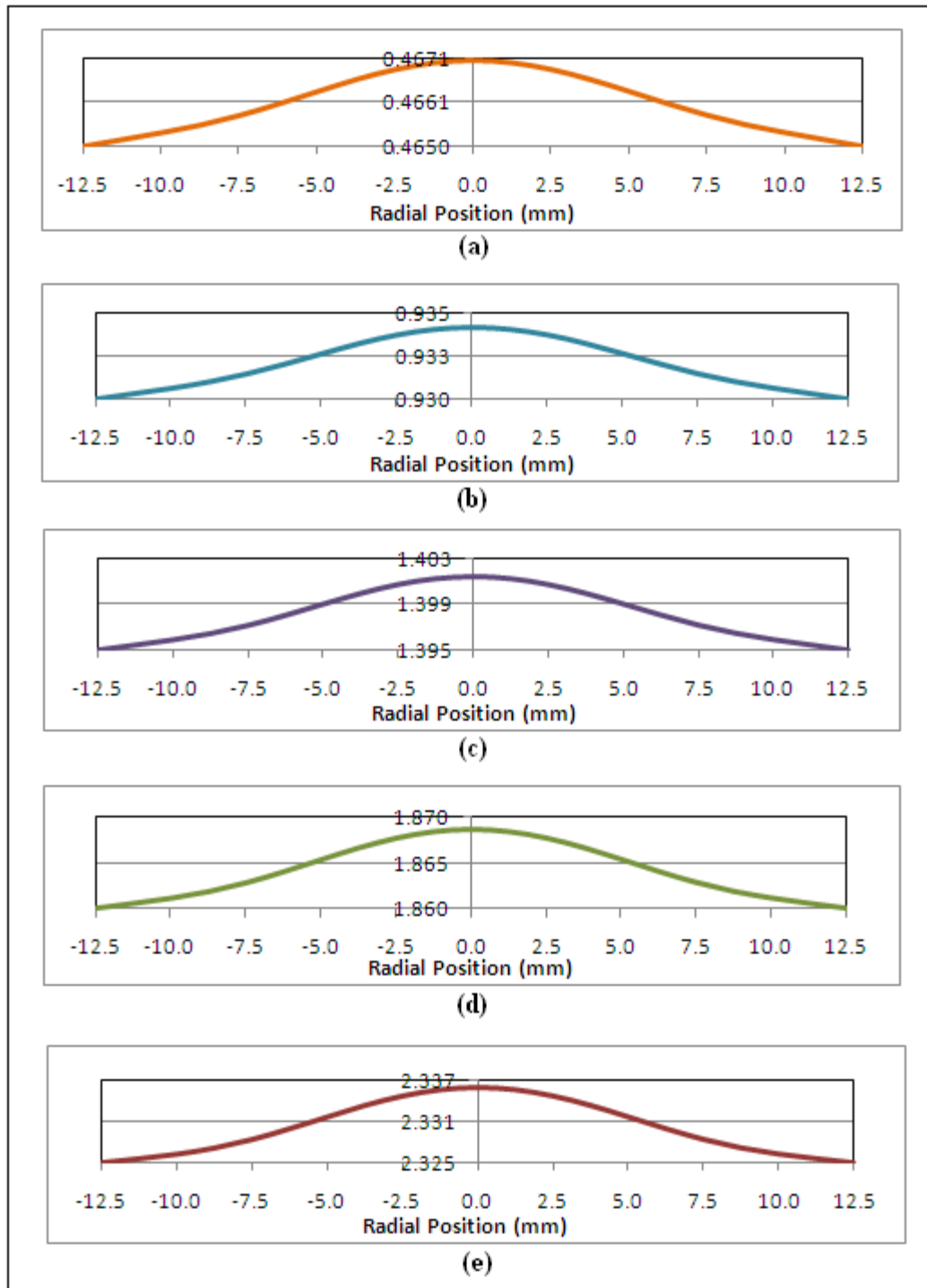


Figure 5.17 Radial temperature difference (ΔT) at the first 5 mm above interface
a) 1mm, b) 2mm, c) 3mm, d) 4mm, e) 5mm

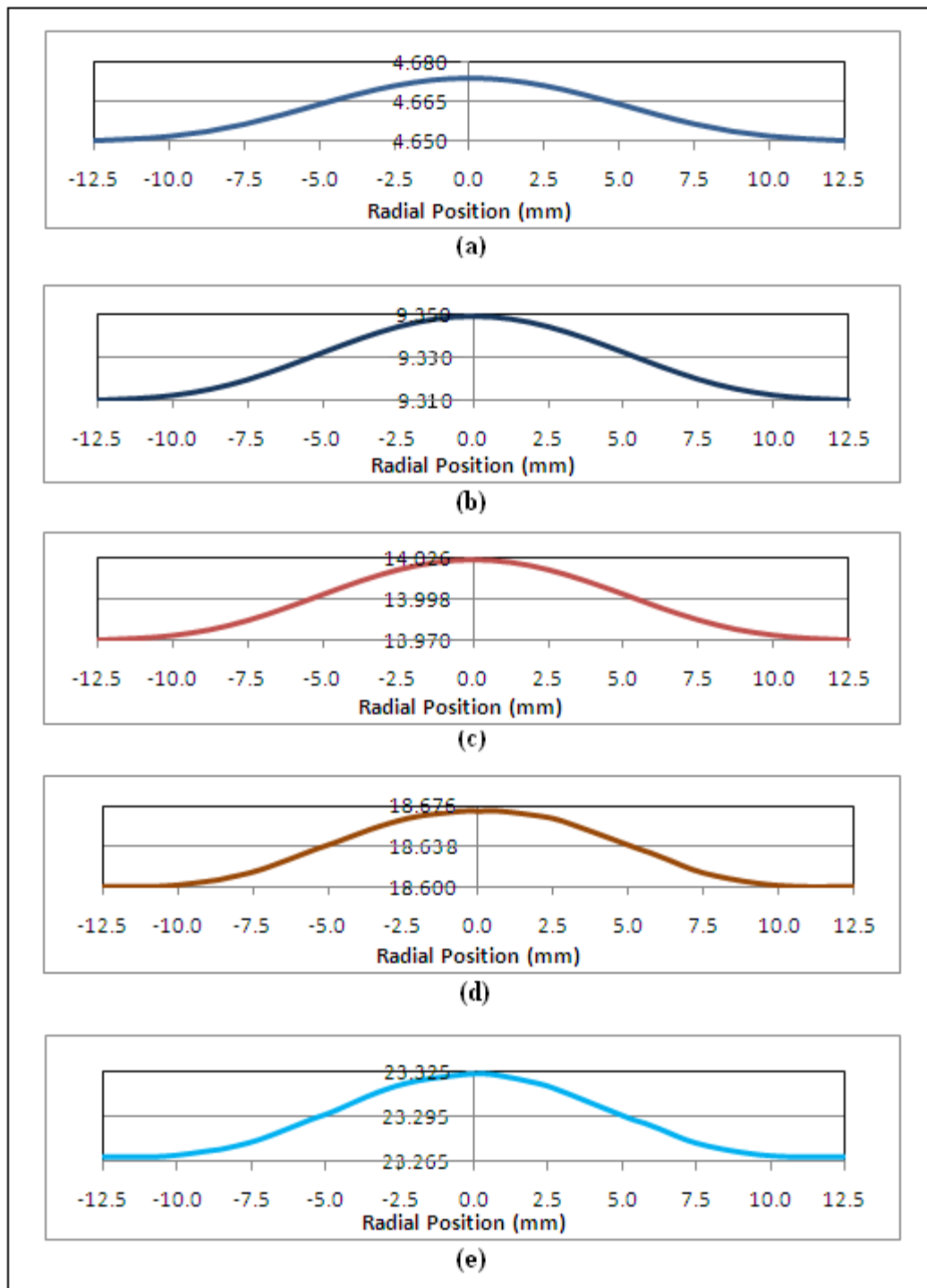


Figure 5.18 Radial temperature difference (ΔT) from 10 to 50 mm above interface
a) 10mm, b) 20mm, c) 30mm, d) 40mm, e) 50mm

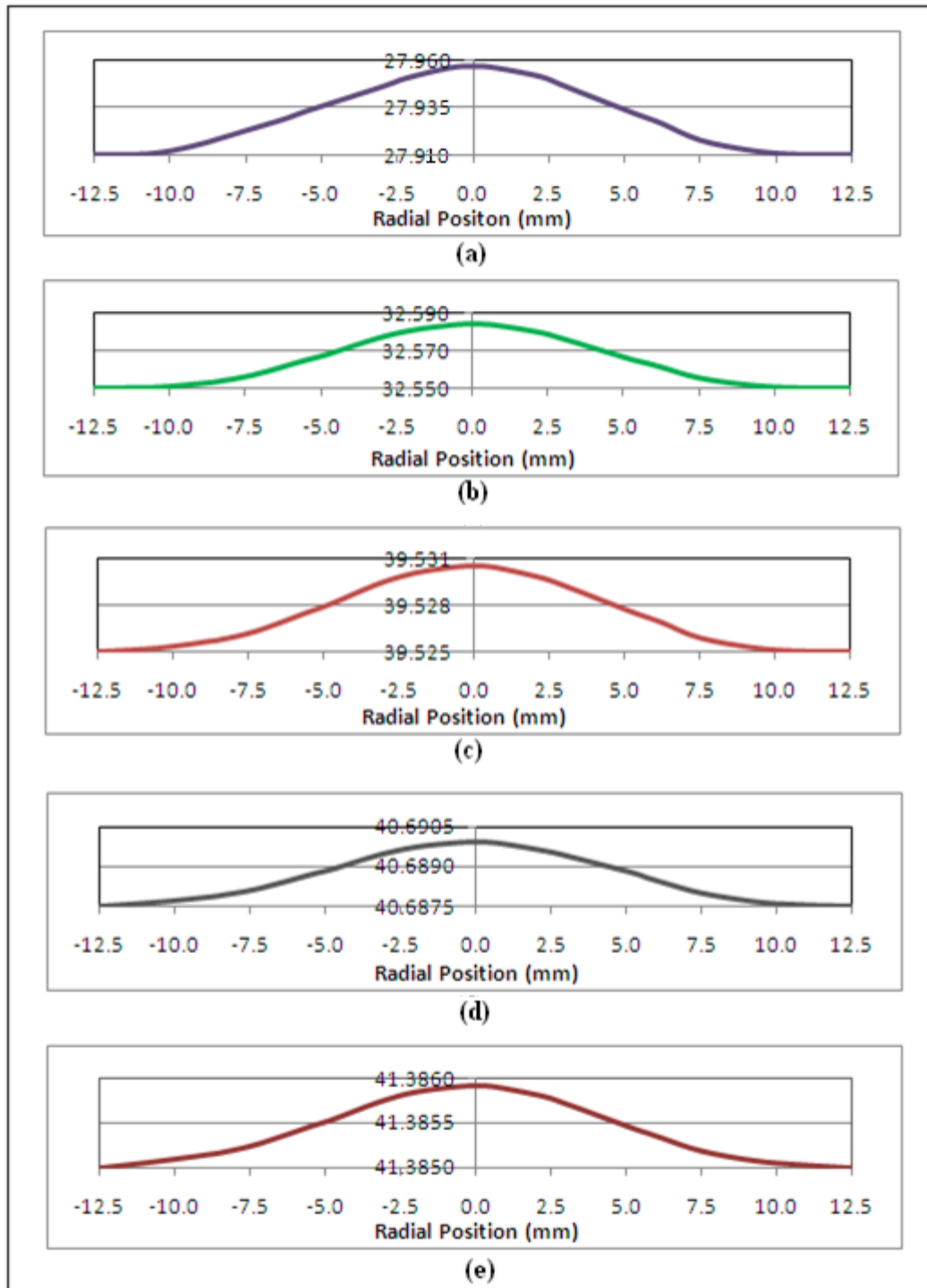


Figure 5.19 Radial temperature difference (ΔT) from 60 to 89 mm above interface
a) 60mm, b) 70mm, c) 80mm, d) 85mm, e) 89mm

Figure 5.20 represents the radial distribution of silicon in the solvent region from solid liquid interface up to 20 mm above the interface. It is clearly shown that the distribution is extremely uniform and consistent and in the desired level of 25%. This is a good indication of the absence of the strong radial temperature distribution since the excess of heat will produce the ring strain [61]. The profile is nearly flat with negligible convex in the center is the most desirable formation which also reflects the interface shape.

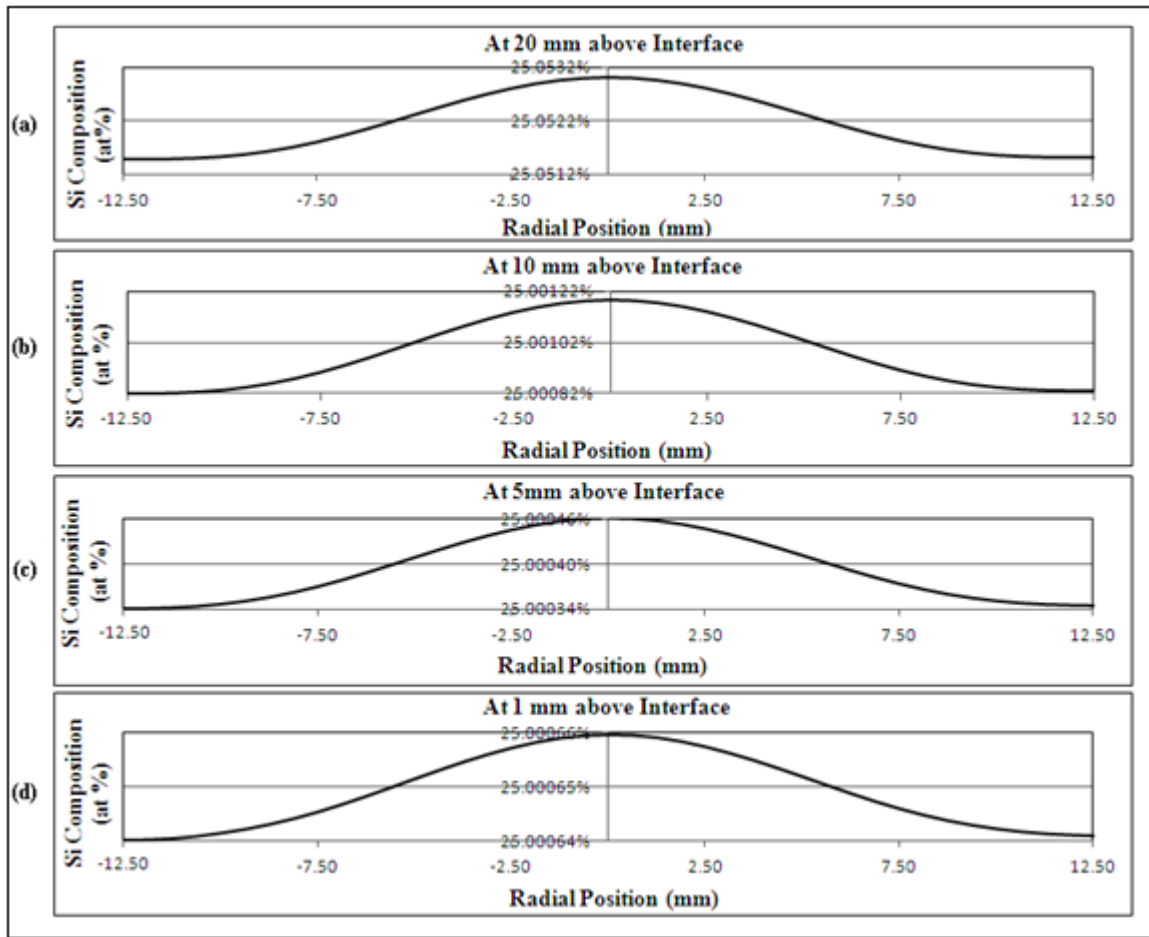


Figure 5.20 Silicon radial distributions in $Gr_T = 1.34E + 05$, (35K/cm case).

- (a) 20mm above interface
- (b) 10mm above interface
- (c) 5 mm above interface
- (d) 1 mm above interface

CHAPTER SIX

Summary, Conclusion, and Future Work

6.0 Summary

This research was focused on the growth of the single bulk crystals of Silicon Germanium using Bridgman technique. The experimental part was conducted at Dalhousie University and my role was first to conduct an extensive numerical modeling simulation both based on Finite Element Analysis and Finite Volume Analysis and second to compare the results; such as silicon distribution in the solvent region and the resulting interface shape with those released by professor Labrie at Dalhousie University. In addition, the focus was on finding the ultimate method or technique along with employing means, such as applying magnetic field, to grow large diameter single bulk crystals of silicon and germanium which not only can produce single bulk crystals but also with a reasonable physical size and timely fashioned method. The above studies point to some fundamental scientific aspects of this alloy system which are not understood to date and which underlie both the homogeneous and single crystal growth of the $\text{Si}_x\text{Ge}_{1-x}$ alloy. These aspects were the diffusion and transport of silicon and germanium in the molten alloy, and the true segregation coefficient ($k = 2.45$) of silicon (Si) in germanium (Ge) in the solvent.

On the numerical aspect, the two and three dimensional numerical simulation of thermo-solutal convection in solvent region was examined. The whole simulation scheme was applied to a cylindrical model representing the sample to investigate the aforementioned phenomena in the entire process. All the models were analyzed by Finite

Element Method simulation. One FEA model was checked with that of done by FVA for comparison purposes under the micro-gravity condition.

6.1 Conclusion

The intensity of the natural convection, which cannot be avoided, can be described with dimensionless thermal Grashof number (Gr_T). The Grashof number for mass transfer (Gr_C) was found to be from few hundreds to nearly a thousand times larger than the Grashof number for heat transfer (Gr_T) as discussed in Chapter five. This is a good evidence of the predominance of concentration-induced natural convection. As for the effects of axial magnetic field, it was found that the application of axial magnetic field, within the range of dimensionless Hartmann number (Ha) of 21.7 up to 21700, had no significant effect on the buoyancy driven convection in the solvent region, this as discussed, can mainly be the role of the large diameter of the model. All findings on this matter has been submitted to well known conferences, such as IAC-09 and are listed in the reference of this thesis. As for microgravity condition, experiment done by other researchers and also with simulation in this study by the author, the microgravity environment has shown that the removal of the gravitational force on the solvent region would result in a homogeneous solidification. Under the microgravity condition, the buoyancy effect due to concentration difference (i.e. density) was minimized; and hence, the concentration gradient in the radial direction was eliminated. As an alternative, this study has found that the radial temperature gradient plays a role (i.e the low non-dimensional thermal Grashof number equal to $1.34E+5$ for the proposed alternative, as

shown in Chapter five) in the solidification process, therefore controlling this parameter, along with other factors such as applied uniform temperature and considering a very minimal pulling rate, would help achieve a homogeneous single bulk crystal with more uniform silicon distribution in the solvent region, more specifically near the solid liquid interface and produce a flat shape interface which is most desired. This was clearly shown that the application of 35K/cm axial temperature gradient is bearing a 0.06K/cm radial temperature gradient at most at 40 mm level above the interface line in the solvent region which is outstanding.

As it was observed in both Chapter four and Chapter five, when a linear temperature gradient is applied the flow regime in the solvent region is slower, this has a markedly effect on silicon distribution. The buoyancy driven convection along with the excess temperature which causes convection as well definitely contributes to one of the major factors in presence of grain boundaries which is not desirable in the process of crystal growth. As a result in this study, the control of the applied temperature gradient along with the reduction of the pulling rate and minimizing the radial temperature is and can be a good alternative to microgravity condition. Considering the fact that although, microgravity creates one of the best conditions, but from the practical point of view and also economical scale of it, is not easy to achieve at least with today's technology. Therefore, the author believes that the findings in this study can be considered as a new approach, at least, for this setting which is $\text{Si}_{0.25}\text{Ge}_{0.75}$ alloy with large diameter (25mm). It should be admitted that production rate is relatively slow and can be considered as a disadvantage point for this proposed alternative. However, once the cost of conducting the

experiment in the space laboratory, which is tremendously high, is taken into the account, then this alternative reveals its advantage over the microgravity condition. As for the application of high magnetic field, which has been utilized by some researchers (as discussed in Chapter two, literature review) in some cases has shown good results. However, from the practical point of view either the magnetic field is not readily available (e.g. to create a magnetic field with intensity of 1 Tesla and more, there is a need of a generator as small as a basketball court to as large as a football field) or it is extremely expensive. Therefore the drawback of slowing down the pulling rate which elongates the production process is still comparatively more attractive than the other two aforementioned routes.

6.2 Future Work

All the findings in this research will open up new possibilities for the future works; the author would recommend and hope the following points to be pursued by himself or any other researchers at Ryerson University:

- To examine the same research utilizing Float Zone (FZ) technique.
- To acquire a furnace to conduct the experimental part in Ryerson Micro-gravity Laboratory.
- To apply the formulated result of this study on the sample in the above furnace.
- To explore the diffusion phenomenon in the process of crystal growth with even larger diameter of single bulk crystals.
- To investigate the residual gravity (g-jitters) effects on the solvent region in Micro-gravity condition.

APPENDIX - A

Table- A.1 Physical Properties of Silicon, Germanium and the Binary Mixture of Si_{0.25} Ge_{0.75}

Item	Variables	Description	Units	Silicon	Germanium	Si _{0.25} Ge _{0.75}
1	ρ (Liquid)	Density	g/cm ³	2.57	5.6	4.843
2	ρ (Solid)	Density	g/cm ³	2.329	5.323	4.575
3	β_C	Solutal Expansion Coefficient	1/at % Si	0.005	---	0.005
4	β_T	Thermal Expansion Coefficient	1 / °C	2.6E-6	5.9E-6	5.075E-6
5	k (solid)	Thermal Conductivity	W/cm.°K	0.15	0.06	0.083
6	k (liquid)	Thermal Conductivity	W/cm.°K	0.426	0.25	0.294
7	α_C (D)	Mass Diffusivity	cm ² /s	3.6E-4	1E-4	1.65E-4
8	α_T	Thermal Diffusivity	cm ² /s	0.85	0.36	0.44
9	T_m	Melt Temperature	°C	1413	939	1057.5
10	ν	Kinematic Viscosity	cm ² /s	3.42E-3	0.50E-3	8.88E-4
11	μ_L	Dynamic Viscosity	g/cm. s	8.8E-3	2.8E-3	4.3E-3
12	Cp (Liquid)	Specific Heat	J/g. K	0.71	0.3157	0.4145
13	Cp (solid)	Specific Heat	J/g. K	0.644	0.32	0.401

Ryerson University, Microgravity Lab

Summer 2008

Table-A.2 Silicon atomic %, Density, Segregation Coefficient, Melt Temperature

Atomic % (Si)	Density (g/cm ³)	T _{melt}	Solidus % (Si)	k (Si in Ge or Ge in Si)	Delta S/ Δ T	Delta L/ Δ T	Delta S/Delta Si composition
0	5.325	938	0.00				
0.5	5.312	946.97	3.54	7.08	0.395	0.0557	7.08
1	5.299	955.39	6.75	6.75	0.381	0.0594	6.41
1.5	5.286	963.34	9.67	6.45	0.368	0.0629	5.85
2	5.273	970.89	12.36	6.18	0.356	0.0662	5.38
2.5	5.259	978.08	14.85	5.94	0.346	0.0695	4.97
3	5.246	984.95	17.16	5.72	0.336	0.0728	4.62
3.5	5.233	991.54	19.32	5.52	0.328	0.0759	4.32
4	5.220	997.86	21.34	5.33	0.320	0.0791	4.04
4.5	5.206	1003.95	23.24	5.16	0.312	0.0821	3.80
5	5.193	1009.83	25.03	5.01	0.305	0.0850	3.59
5.5	5.180	1015.51	26.73	4.86	0.299	0.0880	3.40
6	5.166	1021.01	28.35	4.72	0.293	0.0909	3.22
6.5	5.153	1026.34	29.88	4.60	0.288	0.0938	3.07
7	5.140	1031.52	31.34	4.48	0.282	0.0965	2.92
7.5	5.126	1036.56	32.74	4.37	0.277	0.0992	2.80
8	5.113	1041.45	34.07	4.26	0.273	0.1022	2.67
8.5	5.100	1046.23	35.35	4.16	0.268	0.1046	2.57
9	5.086	1050.88	36.58	4.06	0.264	0.1075	2.46
9.5	5.073	1055.42	37.76	3.98	0.260	0.1101	2.36
10	5.059	1059.86	38.90	3.89	0.257	0.1126	2.28
10.5	5.046	1064.19	40.00	3.81	0.253	0.1155	2.19
11	5.032	1068.44	41.06	3.73	0.249	0.1176	2.12
11.5	5.019	1072.59	42.08	3.66	0.246	0.1205	2.04
12	5.005	1076.66	43.07	3.59	0.243	0.1229	1.98
12.5	4.992	1080.65	44.03	3.52	0.240	0.1253	1.92
13	4.978	1084.56	44.95	3.46	0.237	0.1279	1.86
13.5	4.964	1088.4	45.86	3.40	0.235	0.1302	1.80
14	4.951	1092.17	46.73	3.34	0.232	0.1326	1.75
14.5	4.937	1095.87	47.58	3.28	0.229	0.1351	1.70
15	4.924	1099.51	48.40	3.23	0.227	0.1374	1.65
16	4.896	1106.6	49.99	3.12	0.223	0.1410	1.58
17	4.869	1113.47	51.49	3.03	0.219	0.1456	1.51
18	4.841	1120.12	52.92	2.94	0.215	0.1504	1.43
19	4.814	1126.59	54.29	2.86	0.211	0.1546	1.37
20	4.786	1132.87	55.60	2.78	0.208	0.1592	1.31
21	4.759	1138.98	56.85	2.71	0.204	0.1637	1.25
22	4.731	1144.93	58.04	2.64	0.201	0.1681	1.20
23	4.703	1150.74	59.20	2.57	0.198	0.1721	1.15
24	4.675	1156.41	60.31	2.51	0.196	0.1764	1.11
25	4.647	1161.94	61.37	2.45	0.193	0.1808	1.07
30	4.506	1187.86	66.20	2.21	0.186	0.1929	0.96
35	4.363	1211.37	70.34	2.01	0.176	0.2127	0.83
40	4.219	1232.94	73.97	1.85	0.168	0.2318	0.73
45	4.072	1252.92	77.20	1.72	0.162	0.2503	0.65
50	3.924	1271.58	80.12	1.60	0.156	0.2680	0.58

Experimental Data released by: Dr. D. Labrie ** Dalhousie University ** Fall 2008

APPENDIX - B

Non_Dimensionalization

B.0 Introduction

As described in chapter three, the dimensionless forms of the governing equations are more suitable for the computing purposes where and when the time is of the essence.

B.1 Dimensionless form of Governing Equations

The detailed and step by step non-dimensionalization of all the governing equations is discussed as follow. Since both finite element and finite volume analysis have been utilized in this study, following would represent the non-dimensionalization steps.

B.1 Finite element

B.1.1 Navier-Stokes Equations

The dimensionless transient Navier-Stokes equation for r , ϕ and z directions are presented respectively as follow:

r-component:

Taking equation 3.2 into the consideration and applying the aforementioned dimensionless variables which are defined by scaling length (in this study is equal to the model diameter), velocity, pressure, time, concentration, electric potential and electric current in it, for L-Side, we get;

$$\rho \left(\frac{\partial U u_0}{\partial \frac{\tau L}{u_0}} + U u_0 \frac{\partial U u_0}{\partial RL} + \frac{V u_0}{RL} \frac{\partial U u_0}{\partial \Phi} + W u_0 \frac{\partial U u_0}{\partial ZL} - \frac{(V u_0)^2}{RL} \right) = \quad (B.1)$$

And for R-side, we get;

$$\begin{aligned}
& -\frac{\partial \frac{P\mu u_0}{L}}{\partial RL} + \mu \left(\frac{1}{RL} \frac{\partial}{\partial RL} \left[RL \frac{\partial U u_0}{\partial RL} \right] + \frac{1}{(RL)^2} \frac{\partial^2 U u_0}{\partial \Phi^2} + \frac{\partial^2 U u_0}{\partial (ZL)^2} - \frac{U u_0}{(RL)^2} - \frac{2}{(RL)^2} \frac{\partial U u_0}{\partial \Phi} \right) \\
& -\frac{1}{2} \sigma B_1^2 + \rho g_r [\beta_T (T - T_0) - \beta_C (C - C_0)]
\end{aligned} \tag{B.2}$$

Multiplying both sides by $\frac{L^2}{\mu u_0}$, and simplifying further and by equating common factors to

a known dimensionless number (Table-1) such as Reynolds number, we get;

$$\begin{aligned}
Re \left(\frac{\partial U}{\partial \tau} + U \frac{\partial U}{\partial R} + \frac{V}{R} \frac{\partial U}{\partial \Phi} + W \frac{\partial U}{\partial Z} - \frac{V^2}{R} \right) &= -\frac{\partial P}{\partial R} \left(\frac{\partial^2 U}{\partial R^2} + \frac{1}{R^2} \frac{\partial^2 U}{\partial \Phi^2} + \frac{\partial^2 U}{\partial Z^2} - \frac{U}{R^2} - \frac{2}{R^2} \frac{\partial V}{\partial \Phi} \right) - \\
\frac{1}{2} Ha^2 B_1^{*2} + \frac{(Gr_T)r}{Re} \theta - \frac{(Gr_C)r}{Re} C
\end{aligned} \tag{B.3}$$

Φ-component:

Taking equation 3.3 into the consideration and applying the aforementioned dimensionless variables in it, again for L-Side, we get;

$$\rho \left(\frac{\partial V u_0}{\partial \frac{\tau L}{u_0}} + U u_0 \frac{\partial V u_0}{\partial RL} + \frac{V u_0}{RL} \frac{\partial V u_0}{\partial \Phi} + W u_0 \frac{\partial V u_0}{\partial ZL} + \frac{U u_0 V u_0}{(RL)^2} \right) = \tag{B.4}$$

And for R-side, we get;

$$\begin{aligned}
& -\frac{1}{RL} \frac{\partial \frac{P\mu u_0}{L}}{\partial \Phi} + \mu \left(\frac{1}{RL} \frac{\partial}{\partial RL} \left[RL \frac{\partial V u_0}{\partial RL} \right] + \frac{\partial^2 V u_0}{\partial \Phi^2} + \frac{\partial^2 V u_0}{\partial (ZL)^2} + \frac{2}{r^2} \frac{\partial V u_0}{\partial \Phi} \right) \\
& +\frac{1}{2} \sigma B_2^2 + \rho g_\phi [\beta_T (T - T_0) - \beta_C (C - C_0)]
\end{aligned} \tag{B.5}$$

Again, multiplying both sides by $\frac{L^2}{\mu u_0}$, and simplifying further and by equating common

factors to a known dimensionless number (Table 3.1) such as Hartman number, we get;

$$Re \left(\frac{\partial V}{\partial \tau} + U \frac{\partial V}{\partial R} + \frac{V}{R} \frac{\partial V}{\partial \Phi} + W \frac{\partial V}{\partial Z} + \frac{UV}{R} \right) =$$

$$-\frac{1}{R} \frac{\partial P}{\partial \Phi} \left(\frac{\partial^2 V}{\partial R^2} + \frac{1}{R^2} \frac{\partial^2 V}{\partial \Phi^2} + \frac{\partial^2 V}{\partial Z^2} - \frac{V}{R^2} + \frac{2}{R^2} \frac{\partial V}{\partial \Phi} \right) + \frac{1}{2} Ha^2 B_2^{*2} + \frac{(Gr_T)_\Phi}{Re} - \frac{(Gr_C)_\Phi}{Re} C \quad (B.6)$$

z-component:

And taking equation 3.4 and following the same procedure, for the L-side we will have;

$$\rho \left(\frac{\partial W u_0}{\partial \frac{\tau L}{u_0}} + U u_0 \frac{\partial W u_0}{\partial RL} + \frac{V u_0}{RL} \frac{\partial W u_0}{\partial \Phi} + W u_0 \frac{\partial W u_0}{\partial ZL} \right) = \quad (B.7)$$

And for R-side, we get;

$$-\frac{\partial \frac{P \mu u_0}{L}}{\partial ZL} + \mu \left(\frac{1}{RL} \frac{\partial}{\partial RL} \left[RL \frac{\partial W u_0}{\partial RL} \right] + \frac{1}{(RL)^2} + \frac{\partial^2 W u_0}{\partial \Phi^2} + \frac{\partial^2 W u_0}{\partial (ZL)^2} \right) + 0 +$$

$$\rho g_\Phi [\beta_T (T - T_0) - \beta_C (C - C_0)] \quad (B.8)$$

Again, multiplying both sides by $\frac{L^2}{\mu u_0}$, and simplifying further and by equating common factors to a known dimensionless number (Table-1) such as Grashof number, we get;

$$Re \left(\frac{\partial W}{\partial \tau} + U \frac{\partial W}{\partial R} + \frac{V}{R} \frac{\partial W}{\partial \Phi} + W \frac{\partial W}{\partial Z} \right) = -\frac{\partial P}{\partial R} + (\nabla^2 W) + \frac{(Gr_T)_Z}{Re} \theta - \frac{(Gr_C)_Z}{Re} C \quad (B.9)$$

It should be noted that the magnetic field has no effect (external force) on the “z” component [3.4].

B.1.2 Energy Equation

When the dimensionless variables, as discussed earlier on, are introduced into the dimensional form of energy equation and after simplification, we get the following dimensionless equation in which the inverse of the product of Reynolds and Prandtl numbers represent the effect of density, specific heat and coefficient of heat conduction;

$$\left(\frac{\partial \theta}{\partial \tau} + U \frac{\partial \theta}{\partial R} + \frac{V}{R} \frac{\partial \theta}{\partial \Phi} + W \frac{\partial \theta}{\partial Z}\right) = \frac{1}{Re.Pr} \left(\frac{\partial^2 \theta}{\partial R^2} + \frac{1}{R^2} \frac{\partial^2 \theta}{\partial \Phi^2} + \frac{\partial^2 \theta}{\partial Z^2}\right) \quad (B.10)$$

B.1.3 Continuity Equation

And for the dimensionless form of the continuity equation we will have;

$$\left(\frac{\partial \rho}{\partial \tau} + \frac{1}{R} \frac{\partial}{\partial R} (RU) + \frac{1}{R} \frac{\partial V}{\partial \Phi} + W \frac{\partial W}{\partial Z}\right) = 0 \quad (B.11)$$

B.1.4 Mass Transport Equation

Once the dimensionless variables applied and required simplification done, the non-dimensional form of the mass transport equation becomes as follow;

$$\left(\frac{\partial C}{\partial \tau} + U \frac{\partial C}{\partial R} + \frac{V}{R} \frac{\partial C}{\partial \Phi} + W \frac{\partial C}{\partial Z}\right) = \frac{1}{Re.Sc} \left(\frac{\partial^2 C}{\partial R^2} + \frac{1}{R^2} \frac{\partial^2 C}{\partial \Phi^2} + \frac{\partial^2 C}{\partial Z^2}\right) \quad (B.12)$$

Where the inverse product of Reynolds number and Schmidt number represent the coefficient of solutal expansion.

B.1.5 Latent Heat Equation

$$Re \frac{Pr}{Ste} V = \frac{\partial \theta_L}{\partial Z} - \frac{K_s}{K_l} \frac{\partial \theta_s}{\partial Z} \quad (B.13)$$

Where, the term “ Pr/Ste ” is the non-dimensional value for the latent heat and “ V ” is the axial velocity of the solid-liquid interface.

B.2 Finite/Control Volume Analysis

As mentioned earlier, discretized equations for two dimensional models has been employed for verification of the result shown by the finite element purposes, programs for velocities, temperature, concentrations (species), and pressure is presented in appendix “C”. In control volume the calculation domain is divided into a number of non-overlapping control volumes such that there is one control volume surrounding each grid points. The differential equation is integrated over each control volume. Piecewise profiles expressing the variation of ϕ between the grid points are used to evaluate the required integrals. The result is the discretization equation containing the values of ϕ for a group of grid points. The discretization equation obtained in this manner expresses the conservation principle for ϕ for the finite control volume, just as the differential equation expresses it for an infinitesimal control volume. There are four basic rules that discretization equations should obey to ensure physical realism and overall balance, they are; 1) Consistency at control-volume faces which states when a face is common to two adjacent control volumes, the flux across it must be represented by the same expression in the discretization equations for the two control volumes. 2) Positive coefficients, which states all coefficients (a_p and neighbor coefficient a_{nb}) must always be positive. 3) Negative-slope linearization of the source term which states when the source term is linearized as $\bar{S} = S_C + S_P T_P$, the coefficient S_P must always be less than or equal to zero. It should be noted that for computational success, the principle of negative S_P is essential. 4) Sum of the neighbor coefficients, this rule states that $a_p = \sum a_{nb}$ for situations where the differential equation continues to remain satisfied after a constant is added to the dependent variable. The

differential equation for a portion of a two-dimensional grid as shown in Figures B.1 and B.2 is written as:

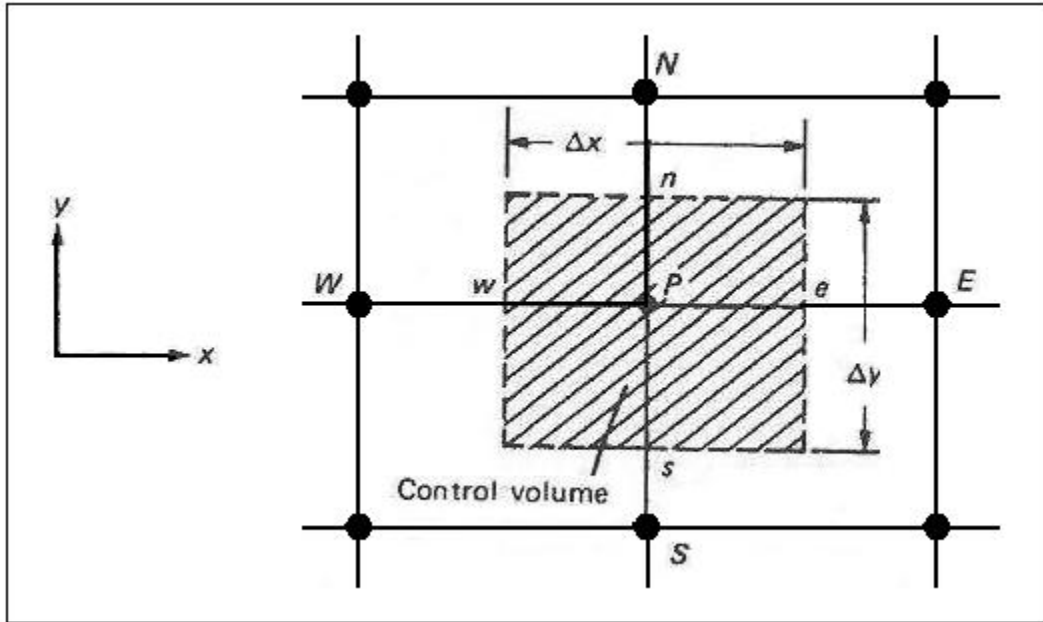


Figure B.1 Control volume grid for two dimensional models [89]

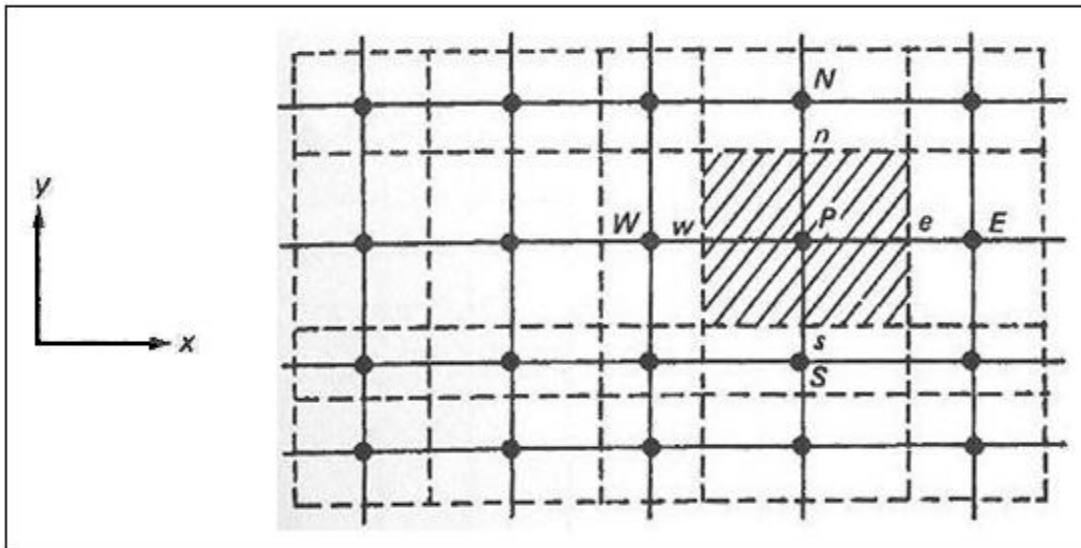


Figure B.2 Location of the control volume in the grids [89]

$$\rho c \frac{\partial T}{\partial t} = \frac{\partial}{\partial x} \left(k \frac{\partial T}{\partial x} \right) + \frac{\partial}{\partial y} \left(k \frac{\partial T}{\partial y} \right) + S \quad (\text{B.14})$$

And can be turned into discretization equation as follow:

$$a_P T_P = a_E T_E + a_W T_W + a_N T_N + a_S T_S + b \quad (\text{B.15})$$

Where

$$a_E = \frac{k_e \Delta y}{(\partial x)_e}, \quad a_W = \frac{k_w \Delta y}{(\partial x)_w}, \quad a_N = \frac{k_n \Delta y}{(\partial x)_n}, \quad a_S = \frac{k_s \Delta y}{(\partial x)_s}, \quad a_P^0 = \frac{\rho c \Delta x \Delta y}{\Delta t},$$

$b = S_C \Delta x \Delta y + a_P^0 T_P^0$, and $a_P = a_E + a_W + a_N + a_S + a_P^0 - S_P \Delta x \Delta y$ it should be noted that the product of $\Delta x \Delta y$ is the volume of the control volume in which the z value is considered as the unity.

B.2.1 Momentum Equation:

$$\frac{\partial}{\partial t} (\rho u) + \frac{\partial}{\partial x} \left(\rho u u - \mu \frac{\partial u}{\partial x} \right) + \frac{\partial}{\partial y} \left(\rho v u - \mu \frac{\partial u}{\partial y} \right) = -\frac{\partial p}{\partial x} + \rho g_x \quad (\text{B.16})$$

Where the terms $\rho u u - \mu \frac{\partial u}{\partial x} = J_x$ and $\rho v u - \mu \frac{\partial u}{\partial y} = J_y$ are the flux in x and y direction respectively. The equation 3.23 then can be written in discretized form as:

$$(\rho_e u_e - \rho_e^0 u_e^0) \frac{\Delta y (\delta x)}{\Delta t} + J_E - J_P + J'_n - J'_s = (P_P - P_E) \Delta y + \rho g_x \Delta y \delta x \quad (\text{B.17})$$

Where

$$J_E = \int_S^n J_x |_e dy; \quad J_P = \int_S^n J_x |_P dy; \quad J'_n = \int_P^E J_x |_n dy; \quad J'_s = \int_P^E J_x |_s dy$$

B.2.2 Continuity Equation

$$\frac{\partial \rho}{\partial t} + \frac{\partial}{\partial x} (\rho u) + \frac{\partial}{\partial y} (\rho v) = 0 \quad (\text{B.18})$$

This in discretized form becomes:

$$(\rho_e - \rho_e^0) \frac{\Delta y (\delta x)}{\Delta t} + F_E - F_P + F'_n - F'_s = 0 \quad (\text{B.19})$$

Where

$$F_E = (\rho u)_E y \quad ; \quad F_P = (\rho u)_P \Delta y \quad ; \quad F'_n = (\rho v)_n \delta x \quad ; \quad F'_s = (\rho v)_s \delta x$$

B.2.3 Energy Equation

$$\frac{\partial}{\partial x}(\rho T) + \frac{\partial}{\partial x}(\rho u T) + \frac{\partial}{\partial x}(\rho v T) = \frac{\partial}{\partial x} \left(\Gamma \frac{\partial T}{\partial x} \right) + \frac{\partial}{\partial y} \left(\Gamma \frac{\partial T}{\partial y} \right) + S \quad (\text{B.20})$$

Where; $S=0$, and $\Gamma = \frac{k}{c_p}$

The discretized form reads as:

$$a'_W T_W + a'_S T_S + a'_P T_P + a'_E T_E + a'_N T_N = b \quad (\text{B.21})$$

where

$$b = a_P^0 T_P^0 \quad ; \quad a_P^0 = \frac{\rho_P^0 \Delta x \Delta y}{\Delta t} \quad , \quad \text{and} \quad a_P = -(a'_E + a'_W + a'_N + a'_S) + a_P^0$$

By considering Power-Law scheme for a_E when $0 \leq P_e \leq 10$,

We have; $\frac{a_E}{D_e} = (1 - 0.1 P_e)^5$ and

$$a'_W = -\{D_w A(|P_w|) + \llbracket F_w, 0 \rrbracket\} \quad ; \quad D_w = \frac{k_w \Delta y}{c_p (\delta x)_w} \quad , \quad A(|P_w|) = \llbracket 0, (1 - 0.1 |P_w|)^5 \rrbracket$$

$$a'_S = -\{D_s A(|P_s|) + \llbracket F_s, 0 \rrbracket\} \quad ; \quad D_s = \frac{k_s \Delta y}{c_p (\delta x)_s} \quad , \quad A(|P_s|) = \llbracket 0, (1 - 0.1 |P_s|)^5 \rrbracket$$

$$a'_E = -\{D_e A(|P_e|) + \llbracket F_e, 0 \rrbracket\} \quad ; \quad D_e = \frac{k_e \Delta y}{c_p (\delta x)_e} \quad , \quad A(|P_e|) = \llbracket 0, (1 - 0.1 |P_e|)^5 \rrbracket$$

$$a'_N = -\{D_n A(|P_n|) + \llbracket F_n, 0 \rrbracket\} \quad ; \quad D_n = \frac{k_n \Delta y}{c_p (\delta x)_n} \quad , \quad A(|P_n|) = \llbracket 0, (1 - 0.1 |P_n|)^5 \rrbracket$$

Where; $D = \frac{\Gamma A}{\delta t}$, and $F = \rho u A$, and $\left(\frac{k}{c_p}\right)_e = \left(\frac{1-f_e}{\left(\frac{k}{c_p}\right)_p} + \frac{f_e}{\left(\frac{k}{c_p}\right)_E}\right)^{-1}$, and

$$\left(\frac{k}{c_p}\right)_n = \left(\frac{1-f_n}{\left(\frac{k}{c_p}\right)_p} + \frac{f_n}{\left(\frac{k}{c_p}\right)_N}\right) , \text{ and } f_e = \frac{t(\delta x)_e}{(\delta x)_P} , \text{ and } f_n = \frac{t(\delta x)_n}{(\delta x)_P}$$

B.2.4 Mass Transport (Species) Equation

$$\begin{aligned} \frac{\partial}{\partial t}(\rho r c) + \frac{\partial}{\partial r}(\rho r u c) + \frac{\partial}{\partial z}(\rho r w c) \\ = \frac{\partial}{\partial r} \left[\rho r \left(D_c \frac{\partial c}{\partial r} + D_r \frac{\partial T}{\partial r} \right) \right] + \frac{\partial}{\partial z} \left[\rho r \left(D_c \frac{\partial c}{\partial z} + D_r \frac{\partial T}{\partial z} \right) \right] \end{aligned} \quad (\text{B.22})$$

And by integrating in transient mode, we will have;

$$\begin{aligned} \iiint_t^{t+\Delta t} \frac{\partial}{\partial t}(\rho r c) dt dr dz + \iiint_t^{t+\Delta t} \frac{\partial}{\partial r}(\rho r u c) dr dz dt + \iiint_t^{t+\Delta t} \frac{\partial}{\partial z}(\rho r w c) dz dr dt = \\ \iiint_t^{t+\Delta t} \frac{\partial}{\partial r} \left(\rho r c D_c \frac{\partial c}{\partial r} \right) dr dz dt + \\ \iiint_t^{t+\Delta t} \frac{\partial}{\partial z} \left(\rho r D_c \frac{\partial c}{\partial z} \right) dz dr dt + \iiint_t^{t+\Delta t} \frac{\partial}{\partial r} \left(\rho r D_r \frac{\partial T}{\partial r} \right) dr dz dt + \\ \iiint_t^{t+\Delta t} \frac{\partial}{\partial z} \left(\rho r D_r \frac{\partial T}{\partial z} \right) dz dr dt \end{aligned} \quad (\text{B.23})$$

B.3 Two-Dimensional Interpolation

Referring to chapter five, figure 5.16, the two zones of the solvent region for interpolation are shown in figure B.3

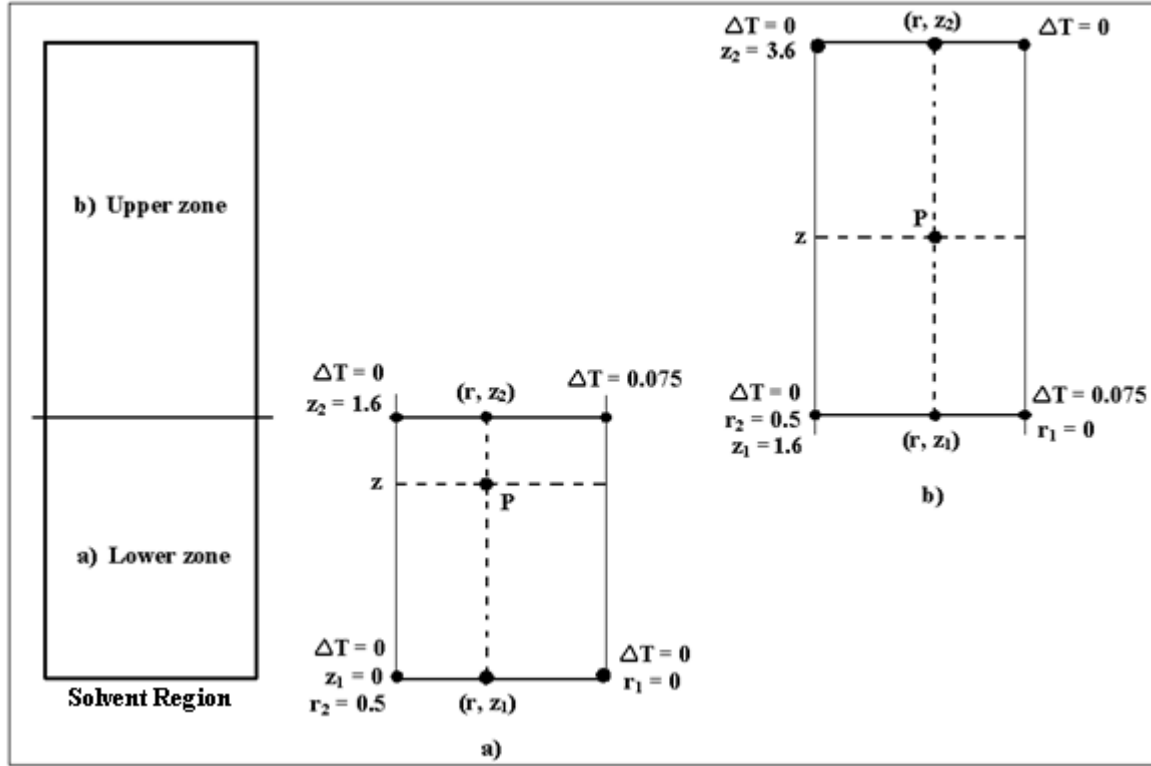


Figure B.3 Nodes for Bilinear interpolation, (dimensionless values shown)

For lower zone;

$$\Delta T(r, z) = \frac{r_2 - r}{r_2 - r_1} \Delta T(r_1, z_1) + \frac{r - r_1}{r_2 - r_1} \Delta T(r_2, z_1) \quad (\text{B.24})$$

For upper zone;

$$\Delta T(r, z) = \frac{z_2 - z}{z_2 - z_1} \Delta T(r, z_1) + \frac{z - z_1}{z_2 - z_1} \Delta T(r, z_2) \quad (\text{B.25})$$

B.4 Three-Dimensional Interpolation

Considering a point in the cylindrical coordinate such as; (r_i, θ_j, z_k) ,

Where;

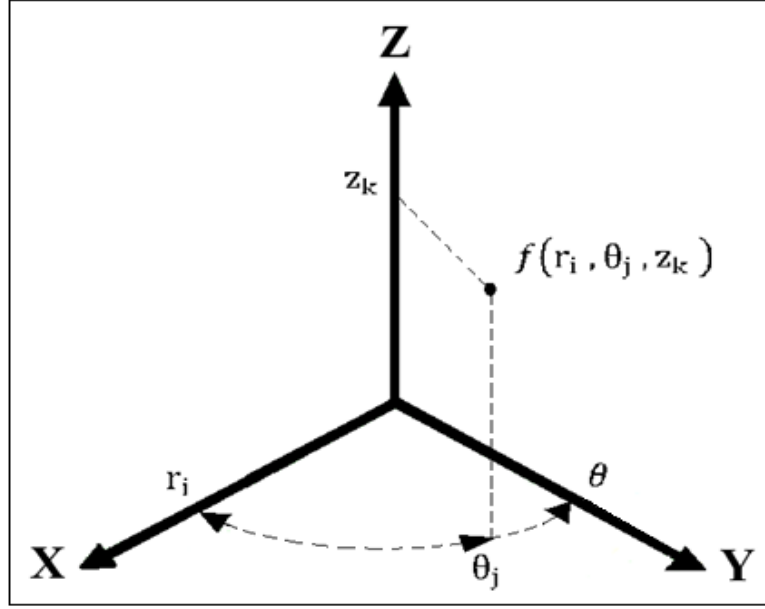


Figure B.4 Cylindrical coordinate system

And $0 \leq i \leq n_i$, $0 \leq j \leq n_j$, $0 \leq k \leq n_k$, $n_i = n_j = n_k$

We have:

$$f(r, \theta, z) = \sum_{i,j,k} f(r_i, \theta_j, z_k) l_i(r) l_j(\theta) l_k(z) \quad (\text{B.26})$$

With;

$$l_i(r) = \frac{\prod_{p=0}^{n_i} (r - r_p)}{\prod_{p=0}^{n_i} (r_i - r_p)} , \quad l_j(\theta) = \frac{\prod_{p=0}^{n_j} (\theta - \theta_p)}{\prod_{p=0}^{n_j} (\theta_j - \theta_p)} , \quad \text{and} \quad l_k(z) = \frac{\prod_{p=0}^{n_k} (z - z_p)}{\prod_{p=0}^{n_k} (z_k - z_p)}$$

and $p \neq i$, $p \neq j$, $p \neq k$

B.5 Magnetic Field Vectors

The orientation of the applied magnetic force vectors in the coordinate system is shown in Figure B.5 below.

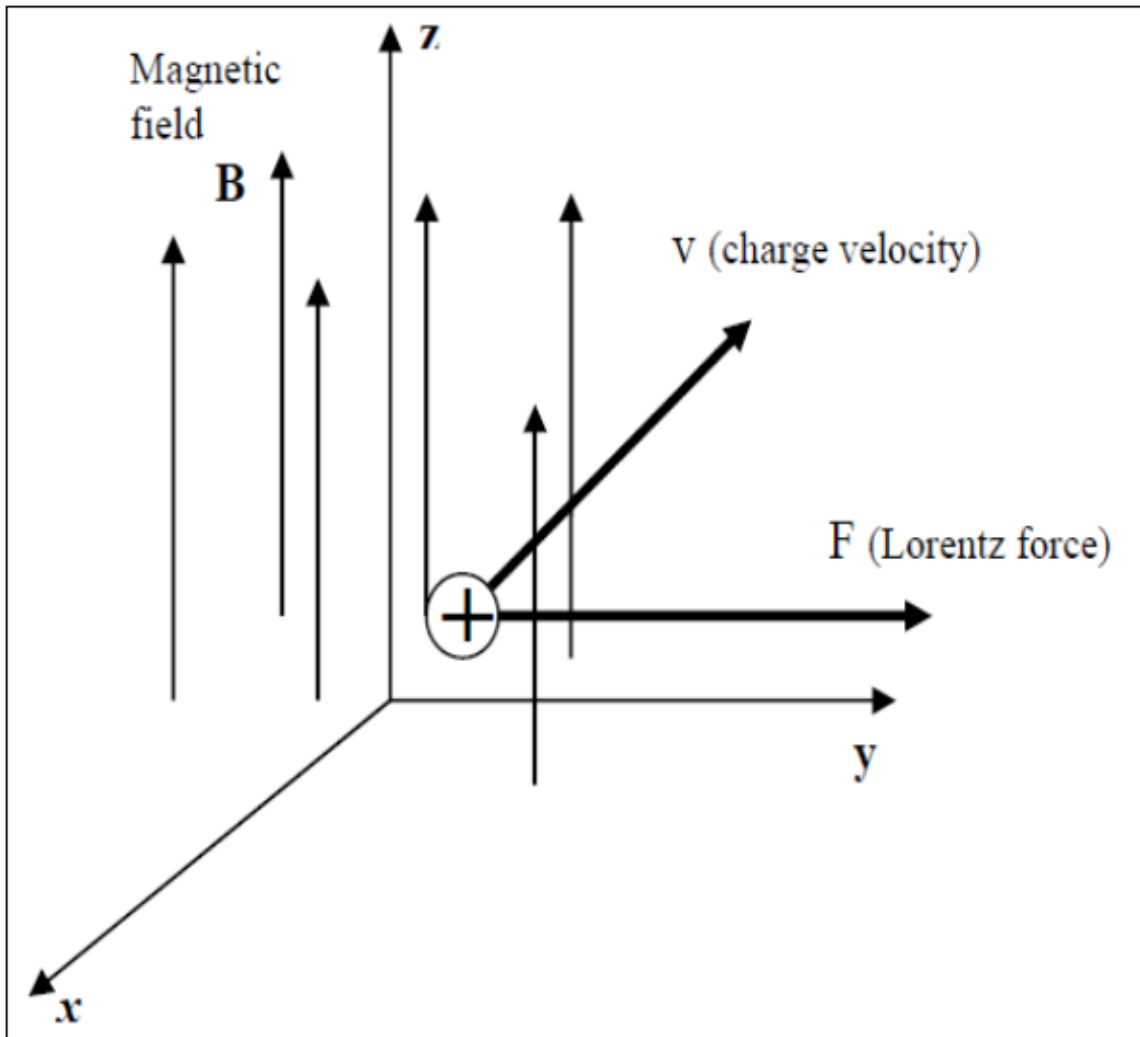


Figure B.5 Magnetic field vectors orientation

APPENDIX - C

C.1 Finite Element Input Files For Three Dimensional Model in Terrestrial Condition

The input files are revised as per application, as follow;

1. Three Dimensional Model in Terrestrial Condition under non-linear heating profile
2. Three Dimensional Model in Microgravity ($g = 10^{-6} g_0$) under non-linear heating profile
3. Axi-symmetric Model under non-linear heating profile
4. Two Dimensional Model in Terrestrial Condition under non-linear heating profile
5. Two Dimensional Model in Terrestrial Condition under linear heating profile

C.1.1

CONVERSION OF NEUTRAL FILE TO FIDAP Database

```
/
FICONV( NEUTRAL )
INPUT( FILE="3dnlft.FDNEUT" )
OUTPUT( DELETE )
END
/
TITLE
3d9nlt-(3-D, full cylinder 9cm melt section)
/
FIPREP
/   PROBLEM SETUP
/
PROBLEM (3-D, LAMINAR, NONLINEAR, BUOYANCY, BUOYANCY=1,
TRANSIENT)
EXECUTION( NEWJOB )
PRINTOUT( NONE )
DATAPRINT( CONTROL )
/
/   CONTINUUM ENTITIES
/
ENTITY ( NAME = "solvent", FLUID, PROPERTY = "solvent" )
```

```

/
/   BOUNDARY ENTITIES
/
ENTITY ( NAME = "bot", PLOT )
ENTITY ( NAME = "skin", SHELL )
ENTITY ( NAME = "dis", PLOT )
/
/   LOCAL COORDINATE SYSTEMS DEFINED
/
/COORDINATE ( SYSTEM = 2, MATRIX,CARTESIAN )
/
/   SOLUTION PARAMETERS
/
SOLUTION( SEGREGATED = 450 )
PRESSURE( MIXED = 1.E-8, DISCONTINUOUS )
/RELAX( HYBRID )
OPTIONS( UPWINDING)
UPWIND(1STO)
/SCALE( VALUE = 1 )
TIMEINT(BACK, dt=0.002, FIXED, nsteps=1800, tend= 3.6)
/POSTPROCESS( NBLOCKS = )
/
/   MATERIAL PROPERTIES
/
/ Partial list of Material Properties data
/
DENSITY( SET = "solvent", CONSTANT = 314.13,TYP2, TEMPERATURE,
SPECIES =1 )
VISCOSITY( SET = "solvent", CONSTANT = 1 )
CONDUCTIVITY( SET = "solvent", CONSTANT = 1 )
SPECIFICHEAT( SET = "solvent", CONSTANT = 6.06E-3, LATENT=12.12,
TMELT=0 )
VOLUMEXPANSION(SET = "solvent", CONSTANT = 1, TEMPERATURE)
GRAVITY(MAGNITUDE = 1)
/
/
SEGREGATIONCOEFFICIENT(SET = "bot", CONSTANT = 2.45)
/
/   INITIAL AND BOUNDARY CONDITIONS
/
/ICNODE( SPECIES =1, CONSTANT = 0.25, ENTITY = "solvent" )
/
BCNODE( SPECIES =1, CONSTANT = 0.75, ENTITY = "bot" )
BCNODE( SPECIES =1, CONSTANT = 0.0, ENTITY = "dis" )

```

```

/BCNODE( , CONSTANT = 0, ENTITY = "bot" )
/BCNODE( , CONSTANT = 0, ENTITY = "dis" )
BCNODE( VELOCITY, CONSTANT = 0, ENTITY = "skin" )
BCNODE( VELOCITY, CONSTANT = 0, ENTITY = "bot" )
BCNODE( VELOCITY, CONSTANT = 0, ENTITY = "dis" )
/
BCNODE( TEMPERATURE, CONSTANT = 0, ENTITY = "bot" )
BCNODE( TEMPERATURE, CONSTANT = 42.5, ENTITY = "dis" )
BCNODE( TEMPERATURE, POLYNOMIAL = 6, ENTITY = "skin" )
1.4255 66.017 0 0 1 -92.161 0 0 2 67.826 0 0 3 -27.247 0 0 4 5.586 0 0 5 -0.4548 0 0 6
/
END
/
CREATE( FIPREP,DELETE )
PARAMETER( LIST )
CREATE( FISOLV )
/RUN( FISOLV, FOREGROUND )

```

C.1.2

```

FICONV( NEUTRAL )
INPUT( FILE="3dmgnlt.FDNEUT" )
OUTPUT( DELETE )
END
/
TITLE
3dmgnlt
/
/(3-D, full cylinder, 9cm melt section, microgravity)
/
FIPREP
/
/      PROBLEM SETUP
/
PROBLEM (3-D, LAMINAR, NONLINEAR, BUOYANCY, BUOYANCY=1,
TRANSIENT)
EXECUTION( NEWJOB )
PRINTOUT( NONE )
DATAPRINT( CONTROL )
/
/      CONTINUUM ENTITIES
/
ENTITY ( NAME = "solvent", FLUID, PROPERTY = "solvent" )
/

```

```

/      BOUNDARY ENTITIES
/
ENTITY ( NAME = "bot", PLOT )
ENTITY ( NAME = "skin", SHELL )
ENTITY ( NAME = "dis", PLOT )
/
/      LOCAL COORDINATE SYSTEMS DEFINED
/
/COORDINATE ( SYSTEM = 2, MATRIX,CARTESIAN )
/
/
/      SOLUTION PARAMETERS
/
SOLUTION( SEGREGATED = 450 )
PRESSURE( MIXED = 1.E-8, DISCONTINUOUS )
/RELAX( HYBRID )
OPTIONS( UPWINDING)
UPWIND(1STO)
/SCALE( VALUE = 1 )
TIMEINT(BACK, dt=0.002, FIXED, nsteps=1800, tend= 3.6)
/POSTPROCESS( NBLOCKS = )
/
/      MATERIAL PROPERTIES
/
/ Partial list of Material Properties data
/
DENSITY( SET = "solvent", CONSTANT = 314.13,TYP2, TEMPERATURE,
SPECIES =1 )
VISCOSITY( SET = "solvent", CONSTANT = 1 )
CONDUCTIVITY( SET = "solvent", CONSTANT = 1 )
SPECIFICHEAT( SET = "solvent", CONSTANT = 6.06E-3, LATENT=12.12,
TMELT=0 )
VOLUMEXPANSION(SET = "solvent", CONSTANT = 1, TEMPERATURE)
GRAVITY(MAGNITUDE = 1E-6)
/
/
SEGREGATIONCOEFFICIENT(SET = "bot", CONSTANT = 2.45)
/
/      INITIAL AND BOUNDARY CONDITIONS
/
/ICNODE( SPECIES =1, CONSTANT = 0.25, ENTITY = "solvent" )
/
BCNODE( SPECIES =1, CONSTANT = 0.75, ENTITY = "bot" )
BCNODE( SPECIES =1, CONSTANT = 0.0, ENTITY = "dis" )

```

```

/BCNODE( , CONSTANT = 0, ENTITY = "bot" )
/BCNODE( , CONSTANT = 0, ENTITY = "dis" )
BCNODE( VELOCITY, CONSTANT = 0, ENTITY = "skin" )
BCNODE( VELOCITY, CONSTANT = 0, ENTITY = "bot" )
BCNODE( VELOCITY, CONSTANT = 0, ENTITY = "dis" )
/
BCNODE( TEMPERATURE, CONSTANT = 0, ENTITY = "bot" )
BCNODE( TEMPERATURE, CONSTANT = 42.5, ENTITY = "dis" )
BCNODE( TEMPERATURE, POLYNOMIAL = 6, ENTITY = "skin" )
1.4255 66.017 0 0 1 -92.161 0 0 2 67.826 0 0 3 -27.247 0 0 4 5.586 0 0 5 -0.4548 0 0 6
/
/
END
/
CREATE( FIPREP,DELETE )
PARAMETER( LIST )
CREATE( FISOLV )
/RUN( FISOLV, FOREGROUND )

```

C.1.3

```

FICONV( NEUTRAL )
INPUT( FILE="ax2d9.FDNEUT" )
OUTPUT( DELETE )
END
/
TITLE
ax2d9-(Axi-Symmetric, 9cm melt section, non-linear temp.,Micro-gravity)
/
FIPREP
/
/
/    PROBLEM SETUP
/
PROBLEM (AXI-SYMMETRIC, LAMINAR, NONLINEAR, BUOYANCY,
BUOYANCY=1, TRANSIENT)
EXECUTION( NEWJOB )
PRINTOUT( NONE )
DATAPRINT( CONTROL )
/
/    CONTINUUM ENTITIES
/
ENTITY ( NAME = "solvent", FLUID, PROPERTY = "solvent" )
/

```

```

/      BOUNDARY ENTITIES
/
ENTITY ( NAME = "bot", PLOT )
ENTITY ( NAME = "rskin", PLOT )
ENTITY ( NAME = "dis", PLOT )
ENTITY ( NAME = "symm", PLOT )
/
/      LOCAL COORDINATE SYSTEMS DEFINED
/
/COORDINATE ( SYSTEM = 2, MATRIX,CARTESIAN )
/
/
/      SOLUTION PARAMETERS
/
SOLUTION( SEGREGATED = 450 )
PRESSURE( MIXED = 1.E-8, DISCONTINUOUS )
/RELAX( HYBRID )
OPTIONS( UPWINDING)
UPWIND(1STO)
/SCALE( VALUE = 1 )
TIMEINT(BACK, dt=0.002, FIXED, nsteps=1800, tend= 3.6)
/POSTPROCESS( NBLOCKS = )
/
/      MATERIAL PROPERTIES
/
/ Partial list of Material Properties data
/
DENSITY( SET = "solvent", CONSTANT = 314.13,TYP2, TEMPERATURE,
SPECIES =1 )
VISCOSITY( SET = "solvent", CONSTANT = 1 )
CONDUCTIVITY( SET = "solvent", CONSTANT = 1 )
SPECIFICHEAT( SET = "solvent", CONSTANT = 6.06E-3, LATENT=12.12,
TMELT=0 )
VOLUMEXPANSION(SET = "solvent", CONSTANT = 1, TEMPERATURE)
GRAVITY(MAGNITUDE = 1E-6)
/
/
SEGREGATIONCOEFFICIENT(SET = "bot", CONSTANT = 2.45)
/
/      INITIAL AND BOUNDARY CONDITIONS
/
/ICNODE( , CONSTANT = 0, ALL )
/
BCNODE( SPECIES =1, CONSTANT = 0.75, ENTITY = "bot" )

```

```

BCNODE( SPECIES =1, CONSTANT = 0.0, ENTITY = "dis" )
/
BCNODE( VELOCITY, CONSTANT = 0, ENTITY = "rskin" )
BCNODE( VELOCITY, CONSTANT = 0, ENTITY = "bot" )
BCNODE( VELOCITY, CONSTANT = 0, ENTITY = "dis" )
/
BCNODE( TEMPERATURE, CONSTANT = 0, ENTITY = "bot" )
BCNODE( TEMPERATURE, CONSTANT = 42.5, ENTITY = "dis" )
BCNODE( TEMPERATURE, POLYNOMIAL = 6, ENTITY = "rskin" )
0.0344 140.52 0 1 0 -193.9 0 2 0 140.04 0 3 0 -54.837 0 4 0 10.951 0 5 0 -0.8706 0 6 0
/
/
END
/
CREATE( FIPREP,DELETE )
PARAMETER( LIST )
CREATE( FISOLV )
/RUN( FISOLV, FOREGROUND )

```

C.1.4

```

FICONV( NEUTRAL )
INPUT( FILE="2d9nlt.FDNEUT" )
OUTPUT( DELETE )
END
/
TITLE
2d9nlt-(2-D, full cylinder, 9cm melt section,non-linear-Temp)
/
/
FIPREP
/
/      PROBLEM SETUP
/
PROBLEM (2-D, LAMINAR, NONLINEAR, BUOYANCY,BUOYANCY=1,
TRANSIENT)
EXECUTION( NEWJOB )
PRINTOUT( NONE )
DATAPRINT( CONTROL )
/
/      CONTINUUM ENTITIES
/
ENTITY ( NAME = "solvent", FLUID, PROPERTY = "solvent" )
/

```



```

/      BOUNDARY ENTITIES
/
ENTITY ( NAME = "bot", PLOT )
ENTITY ( NAME = "rskin", PLOT )
ENTITY ( NAME = "dis", PLOT )
ENTITY ( NAME = "lskin", PLOT )
/
/      LOCAL COORDINATE SYSTEMS DEFINED
/
/COORDINATE (SYSTEM = 2, MATRIX, CARTESIAN )
/
/
/      SOLUTION PARAMETERS
/
SOLUTION( SEGREGATED = 450 )
PRESSURE( MIXED = 1.E-8, DISCONTINUOUS )
/RELAX( HYBRID )
OPTIONS( UPWINDING)
UPWIND(1STO)
/SCALE( VALUE = 1 )
TIMEINT(BACK, dt=0.002, FIXED, nsteps=1800, tend= 3.6)
/POSTPROCESS( NBLOCKS = )
/
/      MATERIAL PROPERTIES
/
/ Partial list of Material Properties data
/
DENSITY( SET = "solvent", CONSTANT = 314.13,TYP2, TEMPERATURE,
SPECIES =1 )
VISCOSITY( SET = "solvent", CONSTANT = 1 )
CONDUCTIVITY( SET = "solvent", CONSTANT = 1 )
SPECIFICHEAT( SET = "solvent", CONSTANT = 6.06E-3, LATENT=12.12,
TMELT=0 )
VOLUMEXPANSION(SET = "solvent", CONSTANT = 1, TEMPERATURE)
GRAVITY(MAGNITUDE = 1)
/
/
SEGREGATIONCOEFFICIENT(SET = "bot", CONSTANT = 2.45)
/
/      INITIAL AND BOUNDARY CONDITIONS
/
/ICNODE( , CONSTANT = 0, ALL )
/
BCNODE( SPECIES =1, CONSTANT = 0.75, ENTITY = "bot" )

```

```

BCNODE( SPECIES =1, CONSTANT = 0.0, ENTITY = "dis" )
/
BCNODE( VELOCITY, CONSTANT = 0, ENTITY = "rskin" )
BCNODE( VELOCITY, CONSTANT = 0, ENTITY = "bot" )
BCNODE( VELOCITY, CONSTANT = 0, ENTITY = "dis" )
BCNODE( VELOCITY, CONSTANT = 0, ENTITY = "lskin" )
/
BCNODE( TEMPERATURE, CONSTANT = 0, ENTITY = "bot" )
BCNODE( TEMPERATURE, CONSTANT = 42.5, ENTITY = "dis" )
BCNODE( TEMPERATURE, POLYNOMIAL = 6, ENTITY = "rskin" )
0.0344 140.52 0 1 0 -193.9 0 2 0 140.04 0 3 0 -54.837 0 4 0 10.951 0 5 0 -0.8706 0 6 0
BCNODE( TEMPERATURE, POLYNOMIAL = 6, ENTITY = "lskin" )
0.0344 140.52 0 1 0 -193.9 0 2 0 140.04 0 3 0 -54.837 0 4 0 10.951 0 5 0 -0.8706 0 6 0
/
/
END
/
CREATE( FIPREP,DELETE )
PARAMETER( LIST )
CREATE( FISOLV )
/RUN( FISOLV, FOREGROUND )

```

C.1.5

```

FICONV( NEUTRAL )
INPUT( FILE="2d9lt.FDNEUT" )
OUTPUT( DELETE )
END
/
TITLE
2d9lt-(2-D, full cylinder, 9cm melt section, LINEAR-Temp)
/
/
FIPREP
/
/    PROBLEM SETUP
/
PROBLEM (2-D, LAMINAR, NONLINEAR, BUOYANCY,BUOYANCY=1,
TRANSIENT)
EXECUTION( NEWJOB )
PRINTOUT( NONE )
DATAPRINT( CONTROL )
/

```

```

/      CONTINUUM ENTITIES
/
ENTITY ( NAME = "solvent", FLUID, PROPERTY = "solvent" )
/
/      BOUNDARY ENTITIES
/
ENTITY ( NAME = "bot", PLOT )
ENTITY ( NAME = "rskin", PLOT )
ENTITY ( NAME = "dis", PLOT )
ENTITY ( NAME = "lskin", PLOT )
/
/      LOCAL COORDINATE SYSTEMS DEFINED
/
/COORDINATE ( SYSTEM = 2, MATRIX,CARTESIAN )
/
/
/      SOLUTION PARAMETERS
/
SOLUTION( SEGREGATED = 450 )
PRESSURE( MIXED = 1.E-8, DISCONTINUOUS )
/RELAX( HYBRID )
OPTIONS( UPWINDING)
UPWIND(1STO)
/SCALE( VALUE = 1 )
TIMEINT(BACK, dt=0.002, FIXED, nsteps=1800, tend= 3.6)
/
/POSTPROCESS( NBLOCKS = )
/
/      MATERIAL PROPERTIES
/
/ Partial list of Material Properties data
/
DENSITY( SET = "solvent", CONSTANT = 314.13,TYP2, TEMPERATURE,
SPECIES =1 )
VISCOSITY( SET = "solvent", CONSTANT = 1 )
CONDUCTIVITY( SET = "solvent", CONSTANT = 1 )
SPECIFICHEAT( SET = "solvent", CONSTANT = 6.06E-3, LATENT=12.12,
TMELT=0 )
VOLUMEXPANSION(SET = "solvent", CONSTANT = 1, TEMPERATURE)
GRAVITY(MAGNITUDE = 1)
/
/
SEGREGATIONCOEFFICIENT(SET = "bot", CONSTANT = 2.45)
/

```

```

/      INITIAL AND BOUNDARY CONDITIONS
/
/
/ICNODE( , CONSTANT = 0, ALL )
/
BCNODE( SPECIES =1, CONSTANT = 0.75, ENTITY = "bot" )
BCNODE( SPECIES =1, CONSTANT = 0.0, ENTITY = "dis" )
/
BCNODE( VELOCITY, CONSTANT = 0, ENTITY = "rskin" )
BCNODE( VELOCITY, CONSTANT = 0, ENTITY = "bot" )
BCNODE( VELOCITY, CONSTANT = 0, ENTITY = "dis" )
BCNODE( VELOCITY, CONSTANT = 0, ENTITY = "lskin" )
/
BCNODE( TEMPERATURE, CONSTANT = 0, ENTITY = "bot" )
BCNODE( TEMPERATURE, CONSTANT = 42.5, ENTITY = "dis" )
BCNODE( TEMPERATURE, POLYNOMIAL = 1, ENTITY = "rskin" )
0 11.806 0 1 0
BCNODE( TEMPERATURE, POLYNOMIAL = 1, ENTITY = "lskin" )
0 11.806 0 1 0
/
/
END
/
CREATE( FIPREP,DELETE )
PARAMETER( LIST )
CREATE( FISOLV )
/RUN( FISOLV, FOREGROUND )

```

C.2 Finite Element Input Files For Applied Magnetic Field in Terrestrial Condition

The input files are adjusted as per application in Terrestrial Condition, as follow;

1. Two Dimensional Model under non-linear temperature & Various Applied
Magnetic Field
2. Two Dimensional Model under linear temperature & Various Applied Magnetic
Field

(All magnetic fields revised accordingly, here two samples are shown)

```

C.2.1
FICONV( NEUTRAL )
INPUT( FILE="2dnlt1mT.FDNEUT" )
OUTPUT( DELETE )
END
/
TITLE
2dnlt1mT-(2-D, full cylinder, 9cm melt section, non-linear temp., B=1mT)
/
/
FIPREP
/
/      PROBLEM SETUP
/
PROBLEM (2-D, LAMINAR, NONLINEAR, BUOYANCY,BUOYANCY=1,
TRANSIENT)
EXECUTION( NEWJOB )
PRINTOUT( NONE )
DATAPRINT( CONTROL )
/
/      CONTINUUM ENTITIES
/
ENTITY ( NAME = "solvent", FLUID, PROPERTY = "solvent" )
/
/      BOUNDARY ENTITIES
/
ENTITY ( NAME = "bot", PLOT )
ENTITY ( NAME = "rskin", PLOT )
ENTITY ( NAME = "dis", PLOT )
ENTITY ( NAME = "lskin", PLOT )
/
/      LOCAL COORDINATE SYSTEMS DEFINED
/
/COORDINATE ( SYSTEM = 2, MATRIX,CARTESIAN )
/
/
/      SOLUTION PARAMETERS
/
SOLUTION( SEGREGATED = 450 )
PRESSURE( MIXED = 1.E-8, DISCONTINUOUS )
/RELAX( HYBRID )
OPTIONS( UPWINDING)
UPWIND(1STO)
/SCALE( VALUE = 1 )

```

```

TIMEINT(BACK, dt=0.002, FIXED, nsteps=1800, tend= 3.6)
/POSTPROCESS( NBLOCKS = )
/
/ MATERIAL PROPERTIES
/
/ Partial list of Material Properties data
/
DENSITY( SET = "solvent", CONSTANT = 314.13,TYP2, TEMPERATURE,
SPECIES =1 )
VISCOSITY( SET = "solvent", CONSTANT = 1 )
CONDUCTIVITY( SET = "solvent", CONSTANT = 1 )
SPECIFICHEAT( SET = "solvent", CONSTANT = 6.06E-3, LATENT=12.12,
TMELT=0 )
VOLUMEXPANSION(SET = "solvent", CONSTANT = 1, TEMPERATURE)
GRAVITY(MAGNITUDE = 1)
/
/
SEGREGATIONCOEFFICIENT(SET = "bot", CONSTANT = 2.45)
/
/
BODYFORCE(ENTITY = "solvent", LORENTZ = 2, VXB=1, FRC=2.907)
/
/ INITIAL AND BOUNDARY CONDITIONS
/
/ICNODE( , CONSTANT = 0, ALL )
/
BCNODE( SPECIES =1, CONSTANT = 0.75, ENTITY = "bot" )
BCNODE( SPECIES =1, CONSTANT = 0.0, ENTITY = "dis" )
/
BCNODE( VELOCITY, CONSTANT = 0, ENTITY = "rskin" )
BCNODE( VELOCITY, CONSTANT = 0, ENTITY = "bot" )
BCNODE( VELOCITY, CONSTANT = 0, ENTITY = "dis" )
BCNODE( VELOCITY, CONSTANT = 0, ENTITY = "lskin" )
/
BCNODE( TEMPERATURE, CONSTANT = 0, ENTITY = "bot" )
BCNODE( TEMPERATURE, CONSTANT = 42.5, ENTITY = "dis" )
BCNODE( TEMPERATURE, POLYNOMIAL = 6, ENTITY = "rskin" )
0.0344 140.52 0 1 0 -193.9 0 2 0 140.04 0 3 0 -54.837 0 4 0 10.951 0 5 0 -0.8706 0 6 0
BCNODE( TEMPERATURE, POLYNOMIAL = 6, ENTITY = "lskin" )
0.0344 140.52 0 1 0 -193.9 0 2 0 140.04 0 3 0 -54.837 0 4 0 10.951 0 5 0 -0.8706 0 6 0
/
/
END
/

```

```

CREATE( FIPREP,DELETE )
PARAMETER( LIST )
CREATE( FISOLV )
/RUN( FISOLV, FOREGROUND )

```

C.2.2

```

FICONV( NEUTRAL )
INPUT( FILE="2dlt1mT.FDNEUT" )
OUTPUT( DELETE )
END
/
TITLE
2dlt1mT-(2-D, full cylinder, 9cm melt section, linear-Temp-B=1mT)
/
/
FIPREP
/
/      PROBLEM SETUP
/
PROBLEM (2-D, LAMINAR, NONLINEAR, BUOYANCY, BUOYANCY=1,
TRANSIENT)
EXECUTION( NEWJOB )
PRINTOUT( NONE )
DATAPRINT( CONTROL )
/
/      CONTINUUM ENTITIES
/
ENTITY ( NAME = "solvent", FLUID, PROPERTY = "solvent" )
/
/      BOUNDARY ENTITIES
/
ENTITY ( NAME = "bot", PLOT )
ENTITY ( NAME = "rskin", PLOT )
ENTITY ( NAME = "dis", PLOT )
ENTITY ( NAME = "lskin", PLOT )
/
/      LOCAL COORDINATE SYSTEMS DEFINED
/
/COORDINATE ( SYSTEM = 2, MATRIX,CARTESIAN )
/
/

```

```

/      SOLUTION PARAMETERS
/
SOLUTION( SEGREGATED = 450 )
PRESSURE( MIXED = 1.E-8, DISCONTINUOUS )
/RELAX( HYBRID )
OPTIONS( UPWINDING)
UPWIND(1STO)
/SCALE( VALUE = 1 )
TIMEINT(BACK, dt=0.002, FIXED, nsteps=1800, tend= 3.6)
/
/POSTPROCESS( NBLOCKS = )
/
/      MATERIAL PROPERTIES
/
/ Partial list of Material Properties data
/
DENSITY( SET ="solvent",CONSTANT =314.13,TYP2,TEMPERATURE, SPECIES
=1)
VISCOSITY( SET = "solvent", CONSTANT = 1 )
CONDUCTIVITY( SET = "solvent", CONSTANT = 1 )
SPECIFICHEAT( SET = "solvent", CONSTANT = 6.06E-3, LATENT=12.12,
TMELT=0 )
VOLUMEXPANSION(SET = "solvent", CONSTANT = 1, TEMPERATURE)
GRAVITY(MAGNITUDE = 1)
/
/
SEGREGATIONCOEFFICIENT(SET = "bot", CONSTANT = 2.45)
/
/      INITIAL AND BOUNDARY CONDITIONS
/
/
BODYFORCE(ENTITY = "solvent", LORENTZ = 2, VXB=1, FRC=2.907)
/
/ICNODE( , CONSTANT = 0, ALL )
/
BCNODE( SPECIES =1, CONSTANT = 0.75, ENTITY = "bot" )
BCNODE( SPECIES =1, CONSTANT = 0.0, ENTITY = "dis" )
/
BCNODE( VELOCITY, CONSTANT = 0, ENTITY = "rskin" )
BCNODE( VELOCITY, CONSTANT = 0, ENTITY = "bot" )
BCNODE( VELOCITY, CONSTANT = 0, ENTITY = "dis" )
BCNODE( VELOCITY, CONSTANT = 0, ENTITY = "lskin" )
/
BCNODE( TEMPERATURE, CONSTANT = 0, ENTITY = "bot" )

```



```

BCNODE( TEMPERATURE, CONSTANT = 42.5, ENTITY = "dis" )
BCNODE( TEMPERATURE, POLYNOMIAL = 1, ENTITY = "rskin" )
0 11.806 0 1 0
BCNODE( TEMPERATURE, POLYNOMIAL = 1, ENTITY = "lskin" )
0 11.806 0 1 0
/
/
END
/
CREATE( FIPREP,DELETE )
PARAMETER( LIST )
CREATE( FISOLV )
/RUN( FISOLV, FOREGROUND )

```

C.3 Finite Element Input Files for Alternative approach in Terrestrial Condition

```

FICONV( NEUTRAL )
INPUT( FILE="2dlt35k.FDNEUT" )
OUTPUT( DELETE )
END
/
TITLE
2dlt35k/(2-D,full cylinder,9cm melt,**LINEAR-Temp, $\Delta\theta=35K$ )
/
/
FIPREP
/
/    PROBLEM SETUP
/
PROBLEM (2-D, LAMINAR, NONLINEAR, BUOYANCY, BUOYANCY=1,
TRANSIENT)
EXECUTION( NEWJOB )
PRINTOUT( NONE )
DATAPRINT( CONTROL )
/
/    CONTINUUM ENTITIES
/
ENTITY ( NAME = "solvent", FLUID, PROPERTY = "solvent" )
/
/    BOUNDARY ENTITIES
/
ENTITY ( NAME = "bot", PLOT )

```

```

ENTITY ( NAME = "rskin", PLOT )
ENTITY ( NAME = "dis", PLOT )
ENTITY ( NAME = "lskin", PLOT )
/
/   LOCAL COORDINATE SYSTEMS DEFINED
/
/COORDINATE ( SYSTEM = 2, MATRIX,CARTESIAN )
/
/
/   SOLUTION PARAMETERS
/
SOLUTION( SEGREGATED = 450 )
PRESSURE( MIXED = 1.E-8, DISCONTINUOUS )
/RELAX( HYBRID )
OPTIONS( UPWINDING)
UPWIND(1STO)
/SCALE( VALUE = 1 )
TIMEINT(BACK, dt=0.002, VARI, NOFIXED=20, nsteps=1800, tend= 3.6)
/
/
/   MATERIAL PROPERTIES
/
/ Partial list of Material Properties data
/
DENSITY( SET = "solvent", CONSTANT = 314.13,TYP2, TEMPERATURE,
SPECIES =1 )
VISCOSITY( SET = "solvent", CONSTANT = 1 )
CONDUCTIVITY( SET = "solvent", CONSTANT = 1 )
SPECIFICHEAT( SET = "solvent", CONSTANT = 6.06E-3, LATENT=12.12,
TMELT=0 )
VOLUMEXPANSION(SET = "solvent", CONSTANT = 1, TEMPERATURE)
GRAVITY(MAGNITUDE = 1)
/
/
/SEGREGATIONCOEFFICIENT(SET = "bot", CONSTANT = 2.45)
/
/   INITIAL AND BOUNDARY CONDITIONS
/
/
/
/BODYFORCE(ENTITY = "solvent", LORENTZ = 1, VXB=1, FX=145350)
/
/ICNODE( , CONSTANT = 0, ALL )
/
BCNODE( SPECIES =1, CONSTANT = 0.25, ENTITY = "bot" )

```

```

BCNODE( SPECIES =1, CONSTANT = 0.34, ENTITY = "dis" )
/
BCNODE( VELOCITY, CONSTANT = 0, ENTITY = "rskin" )
BCNODE( VELOCITY, CONSTANT = 0, ENTITY = "bot" )
BCNODE( VELOCITY, CONSTANT = 0, ENTITY = "dis" )
BCNODE( VELOCITY, CONSTANT = 0, ENTITY = "lskin" )
/
BCNODE( TEMPERATURE, CONSTANT = 0, ENTITY = "bot" )
BCNODE( TEMPERATURE, CONSTANT = 41.85, ENTITY = "dis" )
BCNODE( TEMPERATURE, POLYNOMIAL = 1, ENTITY = "rskin" )
0 11.625 0 1 0
BCNODE( TEMPERATURE, POLYNOMIAL = 1, ENTITY = "lskin" )
0 11.625 0 1 0
/
/
END
/
CREATE( FIPREP,DELETE )
PARAMETER( LIST )
CREATE( FISOLV )
/RUN( FISOLV, FOREGROUND )

```

C.4 Finite Volume Input Files under Non-linear Temperature in Microgravity Condition

```

*****
0          /* Initia 1: existing restart file, 0: none
0          /* I_THERMAL 1: Thermodiff accounted for; 0: not !

```

0 /* I_BARODIFF 1: Barodiff accounted for; 0: not !
10 /* N. of time steps -MTM- or load steps
1.0d+03 /* Time step or load step - DT (steady state: t=75000s)
1 /* Impression sur disque - NIMP
0 /* ISORTIE en 1: mass fraction, 0: molar fraction
1 /* Impression sur ecran - LIMP
5000 /* Maximum number of iterations per time step - MAX_ITER
1.0d-06 /* Convergence criterion - Epsilon (min (relative errors
(u,v,p,T,c) from iteration 1 to 2)<=Epsilon)

0.0d0 /* Horizontal temperature gradient (K/m)
0.0d0 /* Verical temperature gradient (K/m)

0.00625d+00 0.045d+00 1330.65d+00 /* X0_T, Z0_T, T0 (X0_T,Z0_T) T0(K)
0.00625d+00 0.045d+00 0.0d+06 /* X0_P, Z0_P, P0 (X0_P,Z0_P) P0(Pa)

2 /* number of components/pseudocomponents

0.0d+00 0.0d+00 0.00625d+00 0.045d+00 /* X0_C, Z0_C at the reference point

0.623d0 /* Si molar fraction
0.377d0 /* Ge molar fraction

0.1d0 /* permeability (m**2, 1darc=0.987 10**-12)
1.d0 /* porosity (dimensionless)

0.0d0 0.0d0 1.0d0 0.1d0 /* radiation (1:yes, 0:no radiation) emissivity
0.0d0 0.0d0 /* convection(1:yes, 0: no convection) convective heat coeff.

303.15d0 /* environment temperature
1.d0 /* temp relaxation factor(=1: no relaxation):relaxtemp

0.5d0 /*velocity relaxation factor (=1: no relaxation):relaxvel
0.8d0 /*pressure relaxation factor (=1: no relaxation):relaxp

1.d0 /*concentration relaxation factor (=1: no relaxation):relaxconc
1.0d0 /*density relaxation factor (=1: no relaxation):relaxdens

0.d0 1.d0 /* g: gravity acceleration (used to activate g_exp=g*gexp)
9.81d0 0.d0 /* gravs: static gravity (residual-g)
0.d0 /* gravi: g-jitter amplitude
0.d0 /* alpha (deg.): angle of orientation of gravs relative to negative z

0.d0 /* theta (deg.): angle of orientation of gravi relative to negative z
0.d0 /* freq: frequency of the g-jitter

414.5D0 /* reference specific heat (J/kg-K)
29.4D0 /* reference thermal conductivity (W/m-K)

1444.8407D0 /* temperature on the hot wall (K)
1444.8407D0 /* temperature on the cold wall (K)

***** Comments on data.in *****

/* INITIA=0 ==> homogeneous composition as intial guess
 INITIA=1 ==> inital guess from a previous run; one should copy,
 in this case field.out in field.in

/* T0(X0_T,Z0_T)=Temperature (X0_C,Z0_C)
/* P0(X0_P,Z0_P)=Pressure (X0_C,Z0_C)

/* I_THERMAL = 0 <==> no thermal diffusion
 I_THERMAL = 1 <==> with thermal diffusion

/* Permeability=0 <==> convection-free

/* Horizontal temperature gradient (K/m) : >0 ==> the left side is colder than
 the right side

/* Verical temperature gradient (K/m): <0 ==> higher temperature in the bottom

/* relaxation factor 0 < relax < 1 : underrelaxation

/* advised relaxation: pressure 0.8 velocity 0.5

C*****
 SUBROUTINE COINIT(V_X, V_Z, C, P, T, C0, P0, T0, RHO_MOLE,
 & X0_C, Z0_C, X0_P, Z0_P,
 & I0_C, K0_C, I0_P, K0_P,
 & TDE,TDN,X0_T,Z0_T,
 & N_COMP,N_MAX,
 & XC,ZC,LM,NM,KX,KZ)
C*****

PARAMETER(JRED=20)
IMPLICIT REAL*8(A-H,O-Z)

COMMON /INIT/ INITIA
COMMON /TIME_STEP/ DT,DT0
COMMON /TOTAL_TIME/ TIME
COMMON /TEMP_WALLS/ THOT, TCOLD
COMMON /MEAN_DENSITY/ RHO_MEAN,RHO_MOLE_MEAN
COMMON /PROP_MEAN/ CP_MEAN, TK_MEAN, VISC_MEAN
COMMON /MEAN_TEMP/ T_MEAN

DIMENSION P(0:KX,0:KZ)
DIMENSION V_X(0:KX,0:KZ),V_Z(0:KX,0:KZ)
DIMENSION T(0:KX,0:KZ),C(N_MAX,0:KX,0:KZ)
DIMENSION C0(N_MAX)
DIMENSION RHO_MOLE(0:KX,0:KZ)
DIMENSION XC(0:KX),ZC(0:KZ)

C TSTART=(THOT+TCOLD)/2.0D0
TSTART=T_MEAN

C----- CONDITION FOR READING INITIAL FIELD -----

I0_T=0
I0_P=0
I0_C=0

K0_T=0
K0_P=0
K0_C=0

DO I=0,LM+1
IF(XC(I).LE.X0_T) I0_T=I
IF(XC(I).LE.X0_P) I0_P=I
IF(XC(I).LE.X0_C) I0_C=I
ENDDO

DO K=0,NM+1
IF(ZC(K).LE.Z0_T) K0_T=K
IF(ZC(K).LE.Z0_P) K0_P=K
IF(ZC(K).LE.Z0_C) K0_C=K
ENDDO

```

      IF (INITIA.EQ.0) THEN
        DO I=0,LM+1
          DO K=0,NM+1
            P(I,K)=P0
            V_X(I,K)=1.0D-20  !0.0D0
            V_Z(I,K)=1.0D-20  !0.0D0
          ENDDO
        ENDDO

        DO I=0,LM+1
          DO K=0,NM+1
            DO II=1,N_COMP-1
              C(II,I,K)=C0(II)/2.
              C(II,I,K)=.0
            ENDDO
          ENDDO
        ENDDO

c
      C ---- CONDITIONS AT TOP AND BOTTOM ENDS
      C=====
        DO I=0,LM+1
          DO II=1,N_COMP-1
            C(II,I,0)=0.623
          ENDDO
        ENDDO

        DO I=0,LM+1
          DO II=1,N_COMP-1
            C(II,I,NM+1)=0.0
          ENDDO
        ENDDO
      C=====

      ENDIF

      DO I=0,LM+1
        DO K=0,NM+1
          T(I,K)=TSTART
        ENDDO
      ENDDO

```

```

C      ***** BC on top and bottom walls *****

      DO i=0,LM+1
c          T(i,0)= 1162.6 + 273.15
c          T(i,nm+1)= 1181.8 + 273.15
          T(i,0)= 1162.4 + 273.15
          T(i,nm+1)= 1180.9814 + 273.15
      ENDDO

c      goto 002
c----- bc on outer shell -----

      DO K=1,NM
          Z1=ZC(K)*100
          Z2=Z1*Z1
          Z3=Z2*Z1
          Z4=Z3*Z1
          Z5=Z4*Z1
          Z6=Z5*Z1
c my profile
c          T(LM+1,K)=0.0069*Z5 - 0.1835*Z4 + 1.8781*Z3 +
c      &          - 9.2281*Z2 + 21.492*Z1 + 1162.4 + 273.15

c1          T(LM+1,K)=0.0069*Z5 - 0.1835*Z4 + 1.8781*Z3 +
c1      &          - 9.2281*Z2 + 21.492*Z1 + 1162.4 + 273.15

c2          T(LM+1,K)=-0.0019*Z6 + 0.0572*Z5 - 0.6975*Z4 + 4.3409*
c2      &          Z3 - 14.746*Z2 + 26.407*Z1 + 1161.4 + 273.15

c-----mehdi #1-----

c          T(LM+1,K)=- (2e+9)*Z6 + (6e+8)*Z5 - (7e+7)*Z4 + (5e+6)*
c3      &          Z3 - 152387*Z2 + 2699.9*Z1 + 1162.6 + 273.15

c-----

c-----mehdi #2-----

c          T(LM+1,K)=- (2E-9)*Z6 + (5E-7)*Z5 - (6E-5)*Z4 + 0.0041*

```



```
c      &                                Z3 - 0.1434*Z2 + 2.6345*Z1 + 1160.4 +273.15
```

```
c-----
```

```
c-----mehdi #3-----
```

```

                                T(LM+1,K)=- (4E-9)*Z6 + (1E-6)*Z5 - 0.0001*Z4 + 0.009*
      &                                Z3 - 0.3102*Z2 + 5.621*Z1 + 1057.5 + 273.15
c-----
```

```
c      print*, xc(lm+1), ' ', zc(k), ' ', T(LM+1,K)-273.15
```

```
      ENDDO
```

```
c-----
```

```
002    continue
```

```
      IF (INITIA.EQ.1) THEN
```

```
          OPEN(UNIT=JRED,FILE='field.in',STATUS='UNKNOWN')
```

```
          REWIND JRED
```

```
          READ(JRED,*) TIME,DT0,T_MEAN,P0,RHO_MEAN
```

```
          READ(JRED,*)
```

```
RHO_MOLE_MEAN,CP_MEAN,TK_MEAN,VISC_MEAN
```

```
          READ(JRED,*) ((V_X(I,K),I=0,LM+1),K=0,NM+1)
```

```
          READ(JRED,*) ((V_Z(I,K),I=0,LM+1),K=0,NM+1)
```

```
          READ(JRED,*) ((P(I,K),I=0,LM+1),K=0,NM+1)
```

```
          READ(JRED,*) ((T(I,K),I=0,LM+1),K=0,NM+1)
```

```
          DO II=1,N_COMP-1
```

```
              READ(JRED,*) ((C(II,I,K),I=0,LM+1),K=0,NM+1)
```

```
          ENDDO
```

```
          CLOSE(JRED)
```

```
      ENDIF
```

```
      DO I=0,LM+1
```

```
          DO K=0,NM+1
```

```
              C(N_COMP,I,K)=1.0D0
```

```
              DO II=1,N_COMP-1
```

```

                                C(N_COMP,I,K)=C(N_COMP,I,K)-C(II,I,K)
                                ENDDO
                                ENDDO
                                ENDDO

                                RETURN
                                END

```

```

C*****
SUBROUTINE ZVELOCITY(V_X, V_Z, P, VISC, RHO, RHO_0,
&                   I0_C, K0_C, C0,
&                   XWEST, XEST, CENTRE, ZSUD, ZNORD, SM,
&                   DXC, DXG, DZC, DZG, XC, XG, ZC, ZG,
&                   II, N_MAX, N_COMP, KX, KZ, LM, NM,
&                   V_Z0,RELAXVEL,T,Z,C_MEAN)
C*****

PARAMETER(NN1=101)

IMPLICIT REAL*8(A-H,O-Z)

DIMENSION T(0:KX,0:KZ),Z(N_MAX,0:KX,0:KZ)

DIMENSION V_X(0:KX,0:KZ)
DIMENSION V_Z(0:KX,0:KZ), V_Z0(0:KX,0:KZ)

DIMENSION P(0:KX,0:KZ)

DIMENSION RHO(0:KX,0:KZ), RHO_0(0:KX,0:KZ)

DIMENSION VISC(0:KX,0:KZ), C0(N_MAX)

DIMENSION XWEST(0:KX,0:KZ),XEST(0:KX,0:KZ)
DIMENSION CENTRE(0:KX,0:KZ),SM(0:KX,0:KZ)
DIMENSION ZSUD(0:KX,0:KZ),ZNORD(0:KX,0:KZ)

DIMENSION DXC(0:KX),DXG(0:KX),XC(0:KX),XG(0:KX)
DIMENSION DZC(0:KZ),DZG(0:KZ),ZC(0:KZ),ZG(0:KZ)

```

```

COMMON /TIME_STEP/ DT,DT0
COMMON /TOTAL_TIME/TIME
COMMON /GRAVITY/G, GRAVS, GRAVI, ALPHA, THETA, FREQ
COMMON /MEAN_DENSITY/ RHO_MEAN,RHO_MOLE_MEAN
COMMON /MEAN_TEMP/ T_MEAN

```

```

COMMON /FOURIER_COEF1/ AX(NN1),AY(NN1),AZ(NN1)
COMMON /FOURIER_COEF2/ BX(NN1),BY(NN1),BZ(NN1)
COMMON /FOURIER_FREQ/ FX(NN1),FY(NN1),FZ(NN1)
COMMON /NUMBER_COEF/ KK1

```

```

PI=DACOS(-1.D0)
  BETAT=5.075d-6
  BETAC=0.005

```

```

C   ** boundary conditions **
C   ** **

```

```

DO I=0,LM+1
  DO K=0,NM+1
    XWEST(I,K)=0.0d0
    XEST(I,K)=0.0d0
    CENTRE(I,K)=1.0d0
    ZSUD(I,K)=0.0d0
    ZNORD(I,K)=0.0d0
    SM(I,K)=V_Z0(I,K)
  ENDDO
ENDDO

```

```

C
C   ----- Gravity z-component -----
C   ****

```

```

      GZ = -GRAVS*DCOS(ALPHA) +
&      -GRAVI*DCOS(THETA)*DSIN(2.D0*PI*FREQ*TIME)

```

```

C   ****

```

```

DO I=1,LM
  DO K=1,NM-1

```

```

C      ***** interpolation coeff *****

```

```

      deltax = dxg(i)
      delz = dzc(k+1)

```

```

c      -----

```

```

      deltaz_s = dzg(k)
      deltaz_n = dzg(k+1)

```

```

c      -----

```

```

      delx_w = dxc(i)
      delx_e = dxc(i+1)

```

```

      fw = (xg(i)-xc(i-1))/dxc(i)
      fe = (xc(i+1)-xg(i+1))/dxc(i+1)
      fs = (zg(k)-zc(k-1))/dzc(k)
      fn = (zc(k+1)-zg(k+1))/dzc(k+1)

```

```

      f_S = (zc(k)-zg(k))/dzg(k)
      f_N = (zg(k+2)-zc(k+1))/dzg(k+1)

```

```

      x_E=xc(i)
      x_W=xc(i-1)
      x_Mean = (x_E + x_W)/2.

```

```

C      -----

```

```

      RHO_S = RHO(I,K)
      RHO_N = RHO(I,K+1)
      RHO_WS = RHO(I,K)*fw + RHO(I-1,K)*(1.d0-fw)
      RHO_WN = RHO(I,K+1)*fw + RHO(I-1,K+1)*(1.d0-fw)
      RHO_W = RHO_WS*fn + RHO_WN*(1.d0-fn)
      RHO_ES = RHO(I,K)*fe + RHO(I+1,K)*(1.d0-fe)
      RHO_EN = RHO(I,K+1)*fe + RHO(I+1,K+1)*(1.d0-fe)
      RHO_E = RHO_ES*fn + RHO_EN*(1.d0-fn)

```

```

C      -----

```

```

      rho0n=rho(i,k)*fn + rho(i,k+1)*(1.d0-fn)

```

```

C      rho0n=rho_0(i,k)*fn + rho_0(i,k+1)*(1.d0-fn)

```

```

      temp = t(i,k)*fn + t(i,k+1)*(1.d0-fn)
      c_ij = z(1,i,k)*fn + z(1,i,k+1)*(1.d0-fn)

```

```

C          -----
          VISC_S = VISC(I,K)
          VISC_N = VISC(I,K+1)
          VISC_WS = VISC(I,K)*fw + VISC(I-1,K)*(1.d0-fw)
          VISC_WN = VISC(I,K+1)*fw + VISC(I-1,K+1)*(1.d0-fw)
          VISC_W = VISC_WS*fn + VISC_WN*(1.d0-fn)
          VISC_ES = VISC(I,K)*fe + VISC(I+1,K)*(1.d0-fe)
          VISC_EN = VISC(I,K+1)*fe + VISC(I+1,K+1)*(1.d0-fe)
          VISC_E = VISC_ES*fn + VISC_EN*(1.d0-fn)

C          -----
          diffcond_n = visc_n*deltax/deltaz_n
&
& *x_Mean
          diffcond_s = visc_s*deltax/deltaz_s
&
& *x_Mean
          diffcond_e = visc_e*delz/delx_e
&
& *x_E
          diffcond_w = visc_w*delz/delx_w
&
& *x_W

c          -----
          v_n = v_z(i,k)*f_N + v_z(i,k+1)*(1.d0-f_N)
          v_s = v_z(i,k)*f_S + v_z(i,k-1)*(1.d0-f_S)
          u_e = v_x(i,k)*fn + v_x(i,k+1)*(1.d0-fn)
          u_w = v_x(i-1,k)*fn + v_x(i-1,k+1)*(1.d0-fn)

c          -----
          flowrate_w = rho_w*u_w*delz
&
& *x_W
          flowrate_e = rho_e*u_e*delz
&
& *x_E
          flowrate_s = rho_s*v_s*deltax
&
& *x_Mean
          flowrate_n = rho_n*v_n*deltax
&
& *x_Mean

c          -----
          reynolds_w = flowrate_w/diffcond_w
          reynolds_e = flowrate_e/diffcond_e
          reynolds_s = flowrate_s/diffcond_s
          reynolds_n = flowrate_n/diffcond_n

C          *****
C          ** PARTIE DES COEFFICIENTS DUE AUX TERME NON LINEAIRE ****
C
          TNL_W = dmax1(flowrate_w,0.d0)

```

```

TNL_E = dmax1(-flowrate_e,0.d0)
TNL_S = dmax1(flowrate_s,0.d0)
TNL_N = dmax1(-flowrate_n,0.d0)

C      *****
C      ** PARTIE DES COEFFICIENTS DUE AU TERME VISQUEUX *****

      TV_W = diffcond_w*dmax1(0.d0,
&                                     (1.d0-
0.1d0*dabs(reynolds_w))*5.)
      TV_E = diffcond_e*dmax1(0.d0,
&                                     (1.d0-
0.1d0*dabs(reynolds_e))*5.)
      TV_S = diffcond_s*dmax1(0.d0,
&                                     (1.d0-
0.1d0*dabs(reynolds_s))*5.)
      TV_N = diffcond_n*dmax1(0.d0,
&                                     (1.d0-
0.1d0*dabs(reynolds_n))*5.)

C      *****
C      ** Second Member *****

c      SM_P = (P(I,K)-P(I,K+1))*deltax
c &                                     *x_Mean

      SM_P = 0.0

      XWEST(I,K) = -(TNL_W + TV_W)
      XEST(I,K) = -(TNL_E + TV_E)
      ZSUD(I,K) = -(TNL_S + TV_S)
      ZNORD(I,K) = -(TNL_N + TV_N)

      A0P = RHO_0(I,K)*DELTAX*DELZ/DT
&                                     *x_Mean

      CENTRE(I,K) =(-(XWEST(I,K)+ XEST(I,K)+
&                                     + ZSUD(I,K)
+ZNORD(I,K))+A0P)/RELAXVEL

      SM(I,K) = A0P*V_Z0(I,K) + SM_P +
&               + CENTRE(I,K)*(1.0D0-RELAXVEL)*V_Z(I,K)
&               + GZ*DELZ*DELTAX*(RHO0N)

```

```

&          * (-BETAT*(TEMP-T_MEAN)+
&          BETAC*(C_IJ-C_MEAN)
&
)*x_Mean

```

```

      ENDDO
    ENDDO

```

```

c----- bc on axis -----

```

```

      DO k=0,NM+1
        i=0
        v_z(i,k)=v_z(i+1,k)
c        centre(i,k)=1.0d0
        sm(i,k)=v_z(i+1,k)
      ENDDO

```

```

c----- bc on axis end

```

```

c      DT=DT1

```

```

      RETURN
      END

```

```

C*****

```

```

      SUBROUTINE TEMPERATURE(T, T_0, V_X, V_Z, TK, CP,
&      I0_C, K0_C, C0, RHO, RHO_0,
&      XWEST, XEST, CENTRE, ZSUD, ZNORD, SM,
&      DXC, DXG, DZC, DZG, xc, xg, zc, zg,
&      II, N_MAX, N_COMP, KX, KZ, LM, NM,
&      TENV, RAY, CONV, EMISS, HC,RELAXT)

```

```

C*****

```

```

      IMPLICIT REAL*8(A-H,O-Z)

```

```

      DIMENSION V_X(0:KX,0:KZ)
      DIMENSION V_Z(0:KX,0:KZ)

```

```

      DIMENSION RHO(0:KX,0:KZ)
      DIMENSION RHO_0(0:KX,0:KZ)

```

```

      DIMENSION T_0(0:KX,0:KZ),T(0:KX,0:KZ)

```

```

      DIMENSION TK(0:KX,0:KZ)

```

DIMENSION CP(0:KX,0:KZ)

Data sb/5.67d-08/

! Stefan-Boltzmann constant (W.m-2.K-4)

DO I=0,LM+1

DO K=0,NM+1

XWEST(I,K)=0.0d0

XEST(I,K)=0.0d0

CENTRE(I,K)=1.0d0

ZSUD(I,K)=0.0d0

ZNORD(I,K)=0.0d0

SM(I,K)=T(I,K)

ENDDO

ENDDO

C *****

DO I=1,LM

DO K=1,NM

C *** interpolation coeff *******

deltax = dxg(i)

deltaz = dzg(k)

c -----

delx_w = dxc(i)

delx_e = dxc(i+1)

delz_s = dzc(k)

delz_n = dzc(k+1)

c -----

fw = (xg(i)-xc(i-1))/dxc(i)

fe = (xc(i+1)-xg(i+1))/dxc(i+1)

fs = (zg(k)-zc(k-1))/dzc(k)

fn = (zc(k+1)-zg(k+1))/dzc(k+1)

xe=xg(i+1)

xw=xg(i)

xmean = (xe + xw)/2.

c print*,i, k, xe, xmean

C-----

C-----

RHO_W = RHO(I,K)*fw + RHO(I-1,K)*(1.d0-fw)

RHO_E = RHO(I,K)*fe + RHO(I+1,K)*(1.d0-fe)

RHO_S = RHO(I,K)*fs + RHO(I,K-1)*(1.d0-fs)

RHO_N = RHO(I,K)*fn + RHO(I,K+1)*(1.d0-fn)


```

C          -----
C-----
      GOTO 30
      TK_w = 1.d0/((1.d0-fw)/TK(I,K) + fw/TK(I-1,K))
      TK_e = 1.d0/((1.d0-fe)/TK(I,K) + fe/TK(I+1,K))
      TK_s = 1.d0/((1.d0-fs)/TK(I,K) + fs/TK(I,K-1))
      TK_n = 1.d0/((1.d0-fn)/TK(I,K) + fn/TK(I,K+1))
C-----
      CP_w = 1.d0/((1.d0-fw)/CP(I,K) + fw/CP(I-1,K))
      CP_e = 1.d0/((1.d0-fe)/CP(I,K) + fe/CP(I+1,K))
      CP_s = 1.d0/((1.d0-fs)/CP(I,K) + fs/CP(I,K-1))
      CP_n = 1.d0/((1.d0-fn)/CP(I,K) + fn/CP(I,K+1))
C-----
      diffcond_w = (TK_w/cp_w)*(deltaz/delx_w)
      diffcond_e = (TK_e/cp_e)*(deltaz/delx_e)
      diffcond_s = (TK_s/cp_s)*(deltax/delz_s)
      diffcond_n = (TK_n/cp_n)*(deltax/delz_n)
c          -----
30      CONTINUE
      TKoverCP_w = 1.d0/((1.d0-fw)/(TK(I,K)/CP(I,K)) +
&                                     fw/(TK(I-1,K)/CP(I-1,K)))
      TKoverCP_e = 1.d0/((1.d0-fe)/(TK(I,K)/CP(I,K)) +
&                                     fe/(TK(I+1,K)/CP(I+1,K)))
      TKoverCP_s = 1.d0/((1.d0-fs)/(TK(I,K)/CP(I,K)) +
&                                     fs/(TK(I,K-1)/CP(I,K-1)))
      TKoverCP_n = 1.d0/((1.d0-fn)/(TK(I,K)/CP(I,K)) +
&                                     fn/(TK(I,K+1)/CP(I,K+1)))
C-----
      diffcond_w = TKoverCP_w*(deltaz/delx_w)*xw
      diffcond_e = TKoverCP_e*(deltaz/delx_e)*xe
      diffcond_s = TKoverCP_s*(deltax/delz_s)*xmean
      diffcond_n = TKoverCP_n*(deltax/delz_n)*xmean
c          -----
      flowrate_w = rho_w*v_x(i-1,k)*deltaz*xw
      flowrate_e = rho_e*v_x(i,k)*deltaz *xe
      flowrate_s = rho_s*v_z(i,k-1)*deltax *xmean
      flowrate_n = rho_n*v_z(i,k)*deltax*xmean
c          -----
      peclet_w = flowrate_w/diffcond_w
      peclet_e = flowrate_e/diffcond_e
      peclet_s = flowrate_s/diffcond_s
      peclet_n = flowrate_n/diffcond_n

```

C

```
TNL_W = dmax1(flowrate_w,0.d0)
TNL_E = dmax1(-flowrate_e,0.d0)
TNL_S = dmax1(flowrate_s,0.d0)
TNL_N = dmax1(-flowrate_n,0.d0)
```

```
TV_W = diffcond_w*dmax1(0.d0,(1.d0-0.1d0*dabs(peclet_w))**5.)
TV_E = diffcond_e*dmax1(0.d0,(1.d0-0.1d0*dabs(peclet_e))**5.)
```

```
TV_S = diffcond_s*dmax1(0.d0,(1.d0-0.1d0*dabs(peclet_s))**5.)
TV_N = diffcond_n*dmax1(0.d0,(1.d0-0.1d0*dabs(peclet_n))**5.)
```

C

```
RHO_W = RHO(I,K)*fw + RHO(I-1,K)*(1.0d0-fw)
RHO_E = RHO(I,K)*fe + RHO(I+1,K)*(1.0d0-fe)
RHO_S = RHO(I,K)*fs + RHO(I,K-1)*(1.0d0-fs)
RHO_N = RHO(I,K)*fn + RHO(I,K+1)*(1.0d0-fn)
```

c

&

```
diffcond_w = rho_w*d_w*deltaz/delx_w
              *xw
```

&

```
diffcond_e = rho_e*d_e*deltaz/delx_e
              *xe
```

&

```
diffcond_s = rho_s*d_s*deltax/delz_s
              *xmean
```

&

```
diffcond_n = rho_n*d_n*deltax/delz_n
              *xmean
```

c

&

```
flowrate_w = rho_w*v_x(i-1,k)*deltaz
              *xw
```

&

```
flowrate_e = rho_e*v_x(i,k)*deltaz
              *xe
```

&

```
flowrate_s = rho_s*v_z(i,k-1)*deltax
              *xmean
```

&

```
flowrate_n = rho_n*v_z(i,k)*deltax
              *xmean
```

C

```
XWEST(I,K) = -(TNL_W + TV_W)
XEST(I,K) = -(TNL_E + TV_E)
ZSUD(I,K) = -(TNL_S + TV_S)
ZNORD(I,K) = -(TNL_N + TV_N)
```

&

```
a0p = RHO_0(I,K)*deltax*deltaz/DT
      *xmean
```

```

&          CENTRE(I,K) = (-(XWEST(I,K)+ XEST(I,K) +
          ZSUD(I,K) + ZNORD(I,K)) + a0p)*(1.d0/relaxt)

SM(I,K) =a0p*T_0(I,K) +
&          (1.d0-relaxt)*centre(i,k)*T(I,K)

c      print*
c      print*, 'i k xw xe xm=', i, k, xw, xe, xmean
c      print*, 'w e s n=', XWEST(I,K), XEST(I,K), ZSUD(I,K), ZNORD(I,K)
c      print*, 'a0 centre sm t_0=', A0P, CENTRE(I,K), SM(I,K), T_0(I,K)
c      print*
c      read*

      ENDDO
ENDDO
goto 001
C      ***** BC on axis and skin *****
      DO k=1,NM
        i=0
        fe = (xc(i+1)-xg(i+1))/dxc(i+1)
        delx_e = dxc(i+1)
        deltaz = dzg(k)

c          xe=xg(i)
c          xmean = (xg(i) + xg(i-1))/2.

        xe=xg(i+1)
        xmean = (xg(i) + xg(i+1))/2.

c      print*, k, xe, xmean
C      -----
          RHO_E = RHO(I,K)*fe + RHO(I+1,K)*(1.d0-fe)
          TKoverCP_e = 1.d0/((1.d0-fe)/(TK(I,K)/CP(I,K)) +
&          fe/(TK(I+1,K)/CP(I+1,K)))

          diffcond_e = TKoverCP_e*(deltaz/delx_e)
&          *xe

          flowrate_e = rho_e*v_x(i,k)*deltaz
&          *xe
          peclet_e = flowrate_e/diffcond_e
c      goto 002
C      PRINT*, XC(0), zc(0), T(0,0)-273.15
      DO k=1,NM

```

```

      T(0,K) = T(1,K)
      SM(0,K)= T(1,K)

C      PRINT*, XC(0), zc(k), T(0,k)-273.15

      ENDDO ! K=1,NM
C      PRINT*, XC(0), zc(nm+1), T(0,nm+1)-273.15
002    continue

      goto 003
c----- bc on outer shell -----

      DO K=0,NM+1
          Z1=ZC(K)*100
          Z2=Z1*Z1
          Z3=Z2*Z1
          Z4=Z3*Z1
          Z5=Z4*Z1
          Z6=Z5*Z1
          T(LM+1,K)=0.0069*Z5 - 0.1835*Z4 + 1.8781*Z3 +
&                  - 9.2281*Z2 + 21.492*Z1 + 1162.4 + 273.15
c          T(LM+1,K)=-0.0019*Z6 + 0.0572*Z5 - 0.6975*Z4 + 4.3409*
c      &          Z3 - 14.746*Z2 + 26.407*Z1 + 1161.4 + 273.15
          SM(LM+1,K)= T(LM+1,K)

      ENDDO
003    continue
004    continue
      RETURN
      END

C*****
      SUBROUTINE CONCENTRATION (CHI, T, P, V_X, V_Z,
&          D, D_P, D_T,
&          I0_C, K0_C, C0,
&          RHO_MOLE, RHO_MOLE_0, RHO, RHO_0,
&          XWEST, XEST, CENTRE, ZSUD, ZNORD, SM,
&          DXC, DXG, DZC, DZG, XC, XG, ZC, ZG,
&          II, N_MAX, N_COMP, KX, KZ, LM, NM,
&          ZN,RELAXCONC)
C*****
C ATTENTION: SI HARMONIC INTERPOLATION EMPLOYED
C*****

      IMPLICIT REAL*8(A-H,O-Z)

```

DIMENSION CHI(N_MAX,0:KX,0:KZ)
DIMENSION ZN(N_MAX,0:KX,0:KZ)

DIMENSION V_X(0:KX,0:KZ)
DIMENSION V_Z(0:KX,0:KZ)

DIMENSION RHO_MOLE(0:KX,0:KZ)
DIMENSION RHO_MOLE_0(0:KX,0:KZ)

DIMENSION RHO(0:KX,0:KZ), RHO_0(0:KX,0:KZ)

DIMENSION P(0:KX,0:KZ),T(0:KX,0:KZ)

DIMENSION D(N_MAX,N_MAX,0:KX,0:KZ)
DIMENSION D_P(N_MAX,0:KX,0:KZ)
DIMENSION D_T(N_MAX,0:KX,0:KZ)

DIMENSION XWEST(0:KX,0:KZ),XEST(0:KX,0:KZ)
DIMENSION CENTRE(0:KX,0:KZ),SM(0:KX,0:KZ)
DIMENSION ZSUD(0:KX,0:KZ),ZNORD(0:KX,0:KZ)

DIMENSION DXC(0:KX),DXG(0:KX),XC(0:KX),XG(0:KX)
DIMENSION DZC(0:KZ),DZG(0:KZ),ZC(0:KZ),ZG(0:KZ)

COMMON /TIME_STEP/ DT,DT0

C COMMON /PARA/ PERME, PORO

c print*,'cv coeff Calc: hit [Enter]/[Return] to continue'
c read*

DO I=0,LM+1
DO K=0,NM+1
XWEST(I,K)=0.0d0
XEST(I,K)=0.0d0
CENTRE(I,K)=1.0d0
ZSUD(I,K)=0.0d0
ZNORD(I,K)=0.0d0
c SM(I,K)=CHI(IL,I,K)
SM(I,K)=ZN(IL,I,K)
ENDDO
ENDDO

```

C      *****
DO      I=1,LM
        DO      K=1,NM

C      ***** interpolation coeff *****
        deltax = dxg(i)
        deltaz = dzg(k)

c      -----
        delx_w = dxc(i)
        delx_e = dxc(i+1)
        delz_s = dzc(k)
        delz_n = dzc(k+1)

c      -----
        fe = (xc(i+1)-xg(i+1))/dxc(i+1)
        fw = (xg(i)-xc(i-1))/dxc(i)
        fs = (zg(k)-zc(k-1))/dzc(k)
        fn = (zc(k+1)-zg(k+1))/dzc(k+1)

c      xe=xg(i)
c      xw=xg(i-1)
c      xmean = (xg(i) + xg(i-1))/2.

        xe=xg(i+1)
        xw=xg(i)
        xmean = (xe + xw)/2.

c      -----
        D_W = D(II,II,I,K)*fw + D(II,II,I-1,K)*(1.0d0-fw)
        D_E = D(II,II,I,K)*fe + D(II,II,I+1,K)*(1.0d0-fe)
        D_S = D(II,II,I,K)*fs + D(II,II,I,K-1)*(1.0d0-fs)
        D_N = D(II,II,I,K)*fn + D(II,II,I,K+1)*(1.0d0-fn)

c      print*, 'i k xw xe xm=', i, k, xw, xe, xmean
c      print*, 'fw fe fs fn=', fw, fe, fs, fn
c      print*, 'd_w d_e d_s d_n=', d_w, d_e, d_s, d_n
c      read*

c      -----
        DT_W = D_T(II,I,K)*fw + D_T(II,I-1,K)*(1.0d0-fw)
        DT_E = D_T(II,I,K)*fe + D_T(II,I+1,K)*(1.0d0-fe)
        DT_S = D_T(II,I,K)*fs + D_T(II,I,K-1)*(1.0d0-fs)

```

```

DT_N = D_T(II,I,K)*fn + D_T(II,I,K+1)*(1.0d0-fn)
c -----
DP_W = D_P(II,I,K)*fw + D_P(II,I-1,K)*(1.0d0-fw)
DP_E = D_P(II,I,K)*fe + D_P(II,I+1,K)*(1.0d0-fe)
DP_S = D_P(II,I,K)*fs + D_P(II,I,K-1)*(1.0d0-fs)
DP_N = D_P(II,I,K)*fn + D_P(II,I,K+1)*(1.0d0-fn)
c -----
RHO_W = RHO(I,K)*fw + RHO(I-1,K)*(1.0d0-fw)
RHO_E = RHO(I,K)*fe + RHO(I+1,K)*(1.0d0-fe)
RHO_S = RHO(I,K)*fs + RHO(I,K-1)*(1.0d0-fs)
RHO_N = RHO(I,K)*fn + RHO(I,K+1)*(1.0d0-fn)
c -----
diffcond_w = rho_w*d_w*deltaz/delx_w
& *xw
diffcond_e = rho_e*d_e*deltaz/delx_e
& *xe
diffcond_s = rho_s*d_s*deltax/delz_s
& *xmean
diffcond_n = rho_n*d_n*deltax/delz_n
& *xmean
c -----
flowrate_w = rho_w*v_x(i-1,k)*deltaz
& *xw
flowrate_e = rho_e*v_x(i,k)*deltaz
& *xe
flowrate_s = rho_s*v_z(i,k-1)*deltax
& *xmean
flowrate_n = rho_n*v_z(i,k)*deltax
& *xmean
c -----
peclet_w = flowrate_w/diffcond_w
peclet_e = flowrate_e/diffcond_e
peclet_s = flowrate_s/diffcond_s
peclet_n = flowrate_n/diffcond_n

C *****
C ** PART OF COEFFICIENTS DUE TO THE NONLINEAR TERM ****
C

TNL_W = dmax1(flowrate_w,0.0d0)
TNL_E = dmax1(-flowrate_e,0.0d0)
TNL_S = dmax1(flowrate_s,0.0d0)
TNL_N = dmax1(-flowrate_n,0.0d0)

```

```

C *****
C ** PART OF COEFFICIENTS DUE TO THE VISCOUS TERM *****

      TV_W = diffcond_w*dmax1(0.0d0,(1.0d0-
& 0.1d0*dabs(peclet_w))**5.)
      TV_E = diffcond_e*dmax1(0.0d0,(1.0d0-
& 0.1d0*dabs(peclet_e))**5.)
      TV_S = diffcond_s*dmax1(0.0d0,(1.0d0-
& 0.1d0*dabs(peclet_s))**5.)
      TV_N = diffcond_n*dmax1(0.0d0,(1.0d0-
& 0.1d0*dabs(peclet_n))**5.)

c  print*, 'i k xw xe xm= ', i, k, xw, xe, xmean
c  print*, 'fw fe fs fn= ', fw, fe, fs, fn
c  print*, 'tv_w tv_e tv_s tv_n= ', tv_w, tv_e, tv_s, tv_n
c  read*

C *****
C ** Second Member *****

      SM_T_W = - RHO_W*DT_W*(T(I,K)-T(I-1,K))*deltaz/delx_w
&
&      *xw
      SM_T_E = + RHO_E*DT_E*(T(I+1,K)-T(I,K))*deltaz/delx_e
&
&      *xe
      SM_T_S = - RHO_S*DT_S*(T(I,K)-T(I,K-1))*deltax/delz_s
&
&      *xmean
      SM_T_N = + RHO_N*DT_N*(T(I,K+1)-T(I,K))*deltax/delz_n
&
&      *xmean
c  -----
      SM_P_W = - RHO_W*DP_W*(P(I,K)-P(I-1,K))*deltaz/delx_w
&
&      *xw
      SM_P_E = + RHO_E*DP_E*(P(I+1,K)-P(I,K))*deltaz/delx_e
&
&      *xe
      SM_P_S = - RHO_S*DP_S*(P(I,K)-P(I,K-1))*deltax/delz_s

```



```

&
      *xmean
      SM_P_N = + RHO_N*DP_N*(P(I,K+1)-P(I,K))*deltax/delz_n
&
      *xmean
C      ---      Cross Diffusion ---

      SM_X_W=0.0D0
      SM_X_E=0.0D0
      SM_X_S=0.0D0
      SM_X_N=0.0D0
      SM_X_C=0.0D0

      DO      KK=1,N_COMP-1
      IF(KK.NE.II) THEN
            D_W =(D(II,KK,I,K)*fw + D(II,KK,I-1,K)*(1.0d0-
fw))
&
            *xw
            D_E =(D(II,KK,I,K)*fe + D(II,KK,I+1,K)*(1.0d0-
fe))
&
            *xe
            D_S =(D(II,KK,I,K)*fs + D(II,KK,I,K-1)*(1.0d0-
fs))
&
            *xmean
            D_N =(D(II,KK,I,K)*fn + D(II,KK,I,K+1)*(1.0d0-
fn))
&
            *xmean
            SM_X_W = SM_X_W - RHO_W*D_W*
            (CHI(KK,I,K)-CHI(KK,I-
1,K))*deltaz/delx_w
&
            SM_X_E = SM_X_E + RHO_E*D_E*
            (CHI(KK,I+1,K)-
CHI(KK,I,K))*deltaz/delx_e
&
            SM_X_S = SM_X_S - RHO_S*D_S*
            (CHI(KK,I,K)-CHI(KK,I,K-
1))*deltax/delz_s
&
            SM_X_N = SM_X_N + RHO_N*D_N*
            (CHI(KK,I,K+1)-
CHI(KK,I,K))*deltax/delz_n
&
            ENDIF
      ENDDO

      XWEST(I,K) = -(TNL_W + TV_W)

```

```

XEST(I,K) = -(TNL_E + TV_E)
ZSUD(I,K) = -(TNL_S + TV_S)
ZNORD(I,K) = -(TNL_N + TV_N)

A0P = RHO_0(I,K)*DELTAX*DELTAZ/DT
&
XWEST(I,K)+XEST(I,K)+
&
+ A0P)
SM(I,K)=A0P*ZN(II,I,K)+
&
+ SM_T_W + SM_T_E + SM_T_S + SM_T_N +
&
+ SM_X_W + SM_X_E + SM_X_S + SM_X_N +
&
+ (SM_P_W + SM_P_E + SM_P_S + SM_P_N)+
&
+ (1.0d0-
RELAXCONC)*CENTRE(I,K)*CHI(II,I,K)

c    print*, 'i k xw xe xm=', i, k, xw, xe, xmean
c    print*, 'w e s n=', XWEST(I,K), XEST(I,K), ZSUD(I,K), ZNORD(I,K)
c    print*, 'a0 centre sm zmn=', A0P, CENTRE(I,K), SM(I,K), ZN(II,I,K)
c    read*

ENDDO
ENDDO

C    ***** BC on (the axis and) the right wall *****

DO    K=1,NM

C    ----- wall
=====

i=lm+1
fw = (xg(i)-xc(i-1))/dxc(i)
delx_w = dxc(i)
deltaz = dzg(k)

xw=xg(i-1)
xmean = (xg(i) + xg(i-1))/2.

C    -----

```

```

D_W=D(IL,IL,I,K)*fw+D(IL,IL,I-1,K)*(1.0d0-fw)
DP_W = D_P(IL,I,K)*fw+D_P(IL,I-1,K)*(1.0d0-fw)
DT_W = D_T(IL,I,K)*fw+D_T(IL,I-1,K)*(1.0d0-fw)
RHO_W = RHO(I,K)*fw + RHO(I-1,K)*(1.0d0-fw)

diffcond_w = rho_w*d_w*deltaz/delx_w
&
c -----
&
c -----
flowrate_w = rho_w*v_x(i-1,k)*deltaz
&
c -----
peclet_w = flowrate_w/diffcond_w

TNL_W = 0.0d0
TV_W = diffcond_w

C *****
C ** Second Member *****

SM_T_W = - RHO_W*DT_W*(T(I,K)-T(I-1,K))*deltaz/delx_w
&
c -----
&
SM_P_W = - RHO_W*DP_W*(P(I,K)-P(I-1,K))*deltaz/delx_w
&
C --- Cross Diffusion ---

SM_X_W=0.0D0
DO KK=1,N_COMP-1

IF(KK.NE.II) THEN
&
&
&
SM_X_W = SM_X_W - RHO_W*D_W*
(CHI(KK,I,K)-CHI(KK,I-
1,K))*deltaz/delx_w
ENDIF
ENDDO

```

```

XWEST(I,K) = -(TNL_W + TV_W)
A0P = 0.0

CENTRE(I,K)=(1.d0/RELAXCONC)*(-(XWEST(I,K)+XEST(I,K)+
&
+ a0p)                                + ZSUD(I,K) + ZNORD(I,K))

SM(I,K)=a0p*ZN(II,I,K) + SM_T_W + SM_X_W +SM_P_W +
&
(1.0d0-
RELAXCONC)*CENTRE(I,K)*CHI(II,I,K)
ENDDO ! k=1,nm

goto 001
C *****

C ---- CONDITIONS AT TOP AND BOTTOM ENDS
C=====
DO I=0,LM+1
  K=0
c DO II=1,N_COMP-1
    CHI(II,I,K)=ZN(II,I,K)
    SM(I,K)= ZN(II,I,K)
c ENDDO
ENDDO

DO I=0,LM+1
  K=NM+1
c DO II=1,N_COMP-1
    CHI(II,I,K)=ZN(II,I,K)
    SM(I,K)= ZN(II,I,K)
c ENDDO
ENDDO
001 continue

C===== BC AT THE AXIS =====
DO K=1,NM
c DO II=1,N_COMP-1
c CHI(II,0,K)=CHI(II,1,K)
c SM(0,K)=CHI(II,1,K)
c ENDDO
ENDDO

```

```
C=====
c      print*,'cv coeff Calc- END: hit [Enter]/[Return] to continue'
c      read*

      RETURN
      END
```


REFERENCES

- [1] E.R. Johnson and S. M. Christian, Phys. Rev. 95, (1954) 560.
- [2] D.J. Paul, Advanced Materials 11(3), (1999) 191-204.
- [3] J.D. Cressler, IEEE Spectrum, (March 1995) 49-55.
- [4] Y.J. Mii, Y.H. Xie, E.A. Fitzgerald, D. Monroe, F.A. Thiel, B.E. Weir, and L.C. Feldman, Appl. Phys. Lett. 59, (1991) 1611-1613.
- [5] M. Jutzi, and M. Berroth, "SiGe-Based Photodetectors for Optical communications. Properties of Silicon Germanium and SiGe : Carbon", (eds. Erich Kasper and Klar a Lyutovich) INSPEC, (2000) p-342, London.
- [6] A. Spleet, Th. Zinke, B. Schuppert, K. Petermann, and et al., SPIE Vol. 2550, (1998) 224-234.
- [7] G. Bremond, A. Daami, A. Laugier, W. Seif er, M. Kittler, Mat. Res. Soc. Symp. Proc. Vol 485, (1998) 43-48.
- [8] K. Said, J. Poor tmans, M. Caymax , Thin Solid Films 337 (1999) 85-89.
- [9] S. A. Healy, and M. A. Green, Solar Energy Materials and Solar Cells 28, (1992) 273-284.
- [10] K. Nakajima, S. Kodama, S. Miyashita, G. Sazaki and S. Hiyamizu, J. Crystal Growth 205, (1999) 270-276.
- [11] A.E. Fitzgerald, Y.-H. Xie, D. Monroe, P.J. Silverman and M. J. Kuo, A.R. Kortan, , J. Vac. Sci. Tech. B 10(4), (1992) 1807-1819.
- [12] C.M. Bhandari and D.M. Rowe, Contemp. Phys. 21, (1980) 219-242.
- [13] G.A. Slack and M.A. Hussain, J. Appl. Phys. 70, (1991) 2694-2718.
- [14] M.L. Kozhukh, I.N. Belokurova, S.B. Vahrushev, A.N. Titkov and I.L. Shul'pina, Nuclear Instruments and Methods 213, (1983) 483-487.
- [15] J. Schilz and V.N. Romanenko, Journal of Materials Science: Material in Electronics 6, (1995) 265-279.
- [16] N.V. Abrasimov, S.N. Rossolenko, W. Thieme, A. Gerhardt and W. Schroder, J. Crystal Growth 174, (1997) 182-186.
- [17] A. Matsui, I. Yonenaga and K. Sumino, J. of Crys. growth 183, (1998) 109-116.

- [18] J. Wollweber, D. Schulz and W. Schroder, J. of Crys. growth 163, (1996) 243-248.
- [19] P. Dold, A. Barz, S. Recha, K. Pressel, M. Franz and K.W. Benz, J. Crystal Growth 192, (1998) 125-135.
- [20] N. Duhanian, T. Duffar, C. Marin, E. Dieguez, J.P. Garandet, P. Dantan, G. Guiffant, J. Crystal Growth, 275(3-4), (2005) 422-432.
- [21] S. M. Chatoh, B. Damaschke and K. Samwer, Thermophysical Properties of Si, Ge, SiGe melts under Microgravity, ESA Project Report, (April 2007).
- [22] G. Frohberg, Y. Malmejac, Mass Transport by Diffusion, in: Fluid Sciences and Materials Science in Space, ed., H. U. Walter, Springer Verlag, (1987) 159-190.
- [23] S. M. Chatoth, B. Damaschke and K. Samwer, Thermophysical Properties of Si, Ge, Si-Ge Melts under Microgravity, ESA Project Report, (April 2007).
- [24] I. Stich, R. Car, and M. Parrinello. Phys. Rev. B, 44(9), (1991) 4262–4274.
- [25] Lehoczky, S., Szofran, F. R., Gillies, D. C. : *Growth of solid solution single crystals” Second United States Microgravity Payload. Six Month Sciences Report.* NASA MSC, (1994).
- [26] Labrie, D., George, A. E., Jamieson, M., Obruchkov, S., Healey, J. P., Paton, B.E. Saghir, M. Z., International Journal of Materials and product Technology, Vol.22, No.1/2/3, (2005) pp. 105-121.
- [27] J. R. Chelikowsky, N. Troullier, and N. Binggeli. Phys. Rev. B, 49 (1), (1994) 114–119.
- [28] Muller, G., Ostrogorsky, A., Handbook of crystal Growth, Elsevier Science, (1994) pp. 711-819.
- [29] Voronkov, V.V., Journal of Crystal Growth, 310, (2008) pp. 130.
- [30] Dash, W. C., Journal of Applied Physics, 30, (1958) pp. 459.
- [31] Plaskett, T. S., Trans. AIME 233, (1965) pp. 809.
- [32] Abe, T.; Samizo, T.; Maruyama, S., Jpn. J. of Appl. Physics, 5, (1966) pp. 458.
- [33] *Abundances of the Elements in the Earth’s Crust*, Hyper physics, Georgia State University.
- [34] O’Mara, William C., *Handbook of Semiconductor Silicon Technology* William Andrew Inc., (1990) pp. 349–352. ISBN 0815512376.

- [35] U.S. Geological Survey (2008). "Germanium—Statistics and Information". *U.S. Geological Survey, Mineral Commodity Summaries*. Retrieved (2008) pp. 08-28.
- [36] Moskalyk, R. R. "Review of germanium processing worldwide". *Minerals Engineering* 17, (2004) 393–402. doi:10.1016/j.min.eng., (2003) 11.014.
- [37] Brown, Jr., Robert D. (2000) "Germanium" (pdf). U.S. Geological Survey. Retrieved (2008), 09-22.
- [38] R.W. Olesinski, G.J. Abbaschian, " Bulletin of Alloy Phase Diagram" 5th edition, (1984).
- [39] M. Shemirani, MAsc. Thesis, Ryerson University, (2008)
- [40] Helmers, L., Schilz, J., Bahr, G., Kaysser, W. A., *Journal of Crystal Growth*, 154, (1995) pp. 60-67.
- [41] Schilz, J., Romanenko, V.N., "Review, Bulk growth of Silicon-Germanium Solid Solutions" *Journal of Material Science, Materials in Electronics*, Vol.6, (1995) pp. 265-279.
- [42] Dold, P., Barz, A., Recha, S., Pressel, K., Franz, M., Benz, K. W. *Journal of Crystal Growth*, 192, (1998) pp. 125-135.
- [43] Walker, J. S. *Journal of Crystal Growth*, 192, (1998) pp. 318-327.
- [44] Feonychev, A. I., Bondareva, N. V., *Journal of Engineering Physics and Thermodynamics*. Vol. 77, N0.4, (2004) pp. 731-742.
- [45] Okano, Y., Nishino, S., Ohkubo, S., Dost, S. *Journal of Crystal Growth*, 237- 239, (2002) pp. 1779-1784.
- [46] Martinez-Tomas, M. C., Munoz-Sanjose, V., Reig, C., *Journal of Crystal Growth*, 243, (2002) pp. 463-475.
- [47] Labrie, D., George, A. E., Jamieson, M., Obruchkov, S., Healey, J. P., Paton, A. E. *International Journal of Materials and Product Technology*, Vol.22, No.1/2/3, (2005) pp. 105-121.
- [48] Labrie, D., George, A. E., Jamieson, M., Obruchkov, S., Healey, J. P., Paton, A. E., Saghir, M. Z., *Jor. Vac. Sci. Technol. A* 22(3), May/Jun. (2004) pp. 962-965
- [49] Makriyannis, T. J., Saghir, M. Z., *International Journal of Materials and Product Technology*, Vol.22, No 1/2/3, (2005) pp. 135-150.
- [50] Saghir, M. Z., Makriyannis, T. J., Labrie, D., *Journal of Fluid Engineering*, Vol.126, (2004) pp. 223-228.
- [51] Lan, C. W, Yang, D. T., *Modeling Simul. Mat'l. Sci. Eng.* Vol. 3, (1995) pp. 71-92.
- [52] Yeckel, A., Derby, J. J., *Journal of Crystal Growth*, 263, (2004) pp. 40-52.
- [53] Saghir, M. Z., Jaber, T. J., Labrie, D., *International Journal of Materials and Product Technology*, Vol.0, Nos.0/0, (2006) pp. 1-15.

- [54] Yesiyurt, S., Vujisic, L., Motakef, S., Szofran, F. R., Volz, M. P., *Journal of Crystal Growth*, 207, (1999) pp. 278-291.
- [55] Lehoczky, S., Szofran, F. R., Gillies, D. C., *Second United States Microgravity Payload. Six-Month Sciences Report, NASA MSC*, (1994).
- [56] Muller, G., Ostrogorsky, A., *Handbook of crystal Growth*, Elsevier Science, (1994) pp. 711-819.
- [57] Marin, C., Ostrogorsky, A. G., *Journal of Crystal Growth*, 211, (2000) pp. 378-383.
- [58] Li, B. Q., *Int'l. J. of Heat and Mass transfer*, Vol. 39, No. 14, (1996) pp.2853-2860.
- [59] Mitric, A., Duffar, T., *Journal of Crystal Growth*, 310, (2008) pp. 1511-1517.
- [60] Naumann, R. J., Lehoczky, S. K., *Journal of Crystal Growth*, 61, (1983) pp. 173.
- [61] Meyer, S., Ostrogorsky, A. G., *Journal of Crystal Growth*, 171, (1997) pp. 566-576.
- [62] Ruiz, X., Ermakov, M. K., *Journal of Crystal Growth*, 275, (2005) pp. e21-e27.
- [63] Ermakov, M. K., Ermakova, M. S., Ruiz, X., *Proceedings of the Fifth International Conference on Single Crystal Growth and Heat and Mass Transfer*, Obninsk, Russian Federation, (2003).
- [64] Volz, M. P., Walker, J. S., Schweizer, M., Cobb, S. D., Szofran, F. R., *Journal of Crystal Growth*, 282, (2005) pp. 305-312.
- [65] Duhanian, N., Duffar, T., Marin, C., Dieguez, E., Garrandet, J.P., Dantan, P., Guiffant, G., *Journal of Crystal Growth*, 275, (2005) pp 422-432.
- [66] Wagner, J. W., *Journal of Electrochemical Society*, 117, (1970) pp. 1193.
- [67] Plaskett, T. S., Woods, J. F., *Journal of Crystal Growth*, 11, (1971) pp. 341.
- [68] Capper, P., Gosney, J. J., Jones, C. L., Quelch, M. J. T., *Journal of Crystal Growth*, Vol. 63, (1983) pp. 154.
- [69] Foster, L. M., *The preparation of III-V compound semiconductor alloys*, in W. R. Wilcox, R. A. Lefever (Eds), *Preparation and Properties of Solid State Materials*, Marcel Dekker, New York, (1977).
- [70] Lendvay, E., *Prog. Cryst. Growth Charact.* 8, (1984) pp. 371.
- [71] Andrews, R. N., Szofran, F. R., Lehoczky, S. L., *Journal of Crystal Growth*, 92, (1988) pp. 445.
- [72] Cobb, S. D., Andrews, R. N., Szofran, F. R., Lehoczky, S. L., *Journal of Crystal Growth*, 110, (1991) pp. 415.
- [73] Szofran, F.R., Lehoczky, S.L., *Journal of Crystal Growth*, vol. 70, (1984) pp. 349.
- [74] Sha, Y.G., Su, C.H., Alexander, H.A., Lehoczky, S.L., Wang, J.C., *Journal of Crystal Growth*, vol. 174, (1997) pp. 267.
- [75] Nishijama, Y., Nakajima, K., Otsubo, K., Ishikawa, H., vol. 197, (1999) pp. 769.

- [76] Corriel, S., Sekerka, F., Journal of Crys. Growth, vol. 46, (1997) pp. 479.
- [77] Barat, C., Duffar, T., Garandet, J. P., Jour. of Crystal Growth, 194, (1998) pp. 149.
- [78] Duffar, T., Dusserre, P., Picca, F., Lacroix, S., Giacometti, N., Journal of Crystal Growth, 211, (2000) pp. 434.
- [79] Duffar, T., “A review of the fundamental of dewetting”, EPM Laboratory, ENSHMG, (2001), BP 95, F-38402 Saint Martin d’Heres, France
- [80] Palosz, W., Volz, M. P., Cobb, S., Motakef, S., Szofran, F. R., Journal of Crystal Growth, 277, (2005) pp. 124-132.
- [81] Steian, C., Duffar, T., Journal of Crystal Growth, 266, (2004) pp. 190-199.
- [82] Ruiz, X., Academy of Sciences, 1077: 96-114 © New York. Doi: 10.1196/annuals.1362.010, (2006).
- [83] Li, K., Li, B. Q., Handa, J., International Journal of Numerical Methods for Heat & Fluid Flow, Vol. 15, No 8, (2005) pp. 872-893.
- [84] Hoshikawa, K., Japan. Journal of Applied Physics, No. 21, (1982) pp. 9.
- [85] Nikitin, S. A., Poleshaev, V. I., Fedyushkin, A. I., Journal of Crystal Growth, 52, (1981) pp. 471.
- [86] Chang, C. J., Brown, R. A., Journal of Crystal Growth 63, (1983) pp. 343.
- [87] Burton, J. A., Prim, R. C., Slichter, W. P., Journal of Chem. Phys., (1987) 1953.
- [88] Fu, T. W., Wilcox, W. R., Journal of Crystal Growth, 48, (1980) pp. 416.
- [89] Jasinsky, T., Witt, A. F., Journal of Crystal Growth, 67, (1984) pp. 173.
- [90] S. V. Patankar, “Numerical Heat Transfer and Fluid Flow”, (1980), ISBN 0-89116-522-3
- [91] FIDAP User manual, vol. 8.7.2, (1999) and Fluent User manual, (2004)
- [92] C. K. Ghaddar, C. K. Lee, S. Motakef, and D. C. Gillies, “ Numerical simulation of the THM growth of CdTe in presence of rotating magnetic field (RMF), Journal Of Crystal Growth, vol. 205, (1999) pp. 97.
- [93] C.W. Lan, I.F. Lee, B.C. Yeh, “Three Dimensional analysis of flow segregation in vertical Bridgman crystal growth under axial and transversal magnetic fields”, Journal of crystal growth, vol. 254, (2003) pp. 503-515.
- [94] L. Helmers, J. Schilz. G. Bahr, W. A. Kaysse, “Macrosegregation during Bridgman growth of GeSi mixed crystals”, J. Cryst. Growth, vol. 154, (1995) pp. 60-67.
- [95] R.V. Giles, Fluid mechanics and Hydraulics, third edition, (1995), Chap. 6, p82.
- [96] F.M. White, Fluid Mechanics, Sixth edition, (2008), Chap. 5, p287.
- [97] Ye, B. Tabarrok, D. Walsh, Journal of crystal growth, vol. 169, (1996) p 525.

- [98] H. Weimann, J. Amon, T. Jung, G. Muller, J. of Crys. Growth, 180 (1997) p560.
- [99] N. Ma, J. walker, Journal of Fluid Mechanic, 15 (2001) p 50.
- [100] L. Abidi, Z. Saghir, D. Labrie, Jour. Of Mat'l. & Product Tech. 22 (2005) p2.
- [101] M. Shemirani, Z. Saghir, J. Woodacre, D. Labrie, "A study of the solid-liquid interface shape during the growth of SiGe in microgravity utilizing Bridgman method", 60th International Astronautical Conference, IAC-09, (2009), S. Korea.
- [102] A. Kidess, N. Armours, S. Dost, Jour. of Crys. Growth, 312 (2010) p1402.
- [103] N. Dropka, W. Miller, R. Menzel, U. Rehse, Journal of Crystal Growth, 312, (2010) p1407.
- [104] N. Armour, S. Dost, Journal of Crystal Growth, vol. 306, (2007) p 200.
- [105] M. Shemirani, Z. Saghir, H. Sheibani, " Thermo-solutal convection in horizontal Bridgman growth of SiGe in the presence of magnetic field", International Symp., CHMT-09, (2009), Tunisia.
- [106] M. Shemirani, M. Chacha, Z. Saghir, Proceedings of the 8th International Conference, HEFAT-011, (2011), Mauritius.
- [107] W.A. Tiller, K.A. Jackson, J.W.Rutter, B. Chalmers, Acta Met.1, (1953) p 428.
- [108] S.R. Coriell, G.B. McFadden, Handbook of Crys. Growth, (1993), Ch.1B, p801.
- [109] M. Shemirani, Z. Saghir, Proceeding of the 4th International Conference, ICTE-09, (2009), UAE.